

Correlations in semiconductor quantum dots

by
Marek Korkusinski

Thesis
presented to the Faculty of Graduate and Postdoctoral Studies
of the University of Ottawa
in partial fulfilment of the requirements for the Degree of
DOCTOR OF PHILOSOPHY IN PHYSICS

June 8, 2004

Ottawa – Carleton Institute of Physics
University of Ottawa
Ottawa, Ontario, Canada

©Marek Korkusinski, Ottawa, Ontario, Canada, 2004

Abstract

In this Thesis, I present a theoretical study of correlation effects in strongly interacting electronic and electron-hole systems confined in semiconductor quantum dots. I focus on three systems: N electrons in a two-dimensional parabolic confinement in the absence and in the presence of a magnetic field, an electron-hole pair confined in a vertically coupled double-quantum-dot molecule, and a charged exciton in a quantum-ring confinement in a magnetic field.

To analyse these systems I use the exact diagonalisation technique in the effective-mass approximation. This approach consists of three steps: construction of a basis set of particle configurations, writing the Hamiltonian in this basis in a matrix form, and numerical diagonalisation of this matrix. Each of these steps is described in detail in the text.

Using the exact diagonalisation technique I identify the properties of the systems due to correlations and formulate predictions of how these properties could be observed experimentally. I confront these predictions with results of recent photoluminescence and transport measurements.

First I treat the system of N electrons in a parabolic confinement in the absence of magnetic field and demonstrate how its properties, such as magnetic moments, can be engineered as a function of the system parameters and the size of the Hilbert space.

Next I analyse the evolution of the ground state of this system as a function of the magnetic field. In the phase diagram of the system I identify the spin-singlet $\nu = 2$

phase and discuss how correlations influence its phase boundaries both as a function of the magnetic field and the number of electrons.

I also demonstrate that in higher magnetic fields electronic correlations lead to the appearance of spin-depolarised phases, whose stability regions separate the weakly correlated phases with higher spin. Further on, I consider electron-hole systems. I show that the Coulomb interaction leads to entanglement of the states of an electron and a hole confined in a pair of vertically coupled quantum dots.

Finally I consider the system of two electrons and one hole (a negatively charged exciton) confined in a quantum ring and in the presence of the magnetic field. I show that the energy of a single electron in the ring geometry exhibits the Aharonov-Bohm oscillations as a function of the magnetic field. In the case of the negatively charged exciton these oscillations are nearly absent due to correlations among particles, and as a result the photoluminescence spectra of the charged complex are dominated by the energy of the final-state electron. The Aharonov-Bohm oscillations of the energy of a single electron are thus observed directly in the optical spectra.

Sommaire

Une étude théorique des corrélations électroniques dans des points quantiques semi-conducteurs où les électrons et les trous interagissent fortement entre eux est présentée. Trois systèmes en particulier sont considérés: N électrons confinés dans un potentiel parabolique bi-dimensionnel en absence et en présence d'un champ magnétique, une paire électron-trou isolée dans deux points quantiques couplés verticalement, et un complexe excitonique formé dans un anneau quantique soumis à un champ magnétique externe.

Une technique de diagonalisation exacte dans l'approximation de la masse effective est employée pour analyser ces systèmes. Cette approche se divise en trois étapes : la construction d'une base d'états dans l'espace des configurations possibles pour les particules, l'écriture en forme matricielle du Hamiltonien dans la base construite, et la diagonalisation numérique de la matrice. Chacune de ces étapes est expliquée en détails dans cette thèse.

En utilisant cette technique, nous étudions les effets des corrélations sur les propriétés électroniques des systèmes en question et formulons des prédictions théoriques permettant l'observation expérimentale de ces effets. Ces prédictions sont confrontées à des résultats récents obtenus par mesures optique et de transport électrique dans ces systèmes.

On démontre tout d'abord comment les propriétés électroniques de N électrons confinés en deux dimensions dans un potentiel parabolique, comme par exemple le moment magnétique, peuvent être ajustées, en absence de champ magnétique, en fonction des paramètres du système et de la taille de l'espace d'Hilbert.

On analyse ensuite l'évolution en champ magnétique de l'état fondamental. Une phase de spin singulet $\nu = 2$ est identifiée dans le diagramme de phase et l'influence des corrélations sur cette phase est étudiée en fonction du champ magnétique et du nombre d'électrons. On démontre aussi qu'à plus fort champ magnétique, les corrélations électroniques induisent de nouvelles phases dépolarisées en spin dont les régions de stabilité séparent les phases polarisées mais moins corrélées.

On montre, en second lieu, comment l'interaction de Coulomb enchevêtre l'état d'un électron avec celui d'un trou, tous deux confinés dans une paire de points quantiques couplés verticalement.

Finalement, on considère un complexe excitonique composé de deux électrons et d'un trou (exciton chargé) formé dans un anneau quantique en présence d'un champ magnétique. On montre que les oscillations d'Aharanov-Bohm, présentes dans le spectre à une particule, disparaissent dans celui de l'exciton chargé. Cet effet, dû aux corrélations entre les trois particules, implique que le spectre de photoluminescence de l'exciton chargé est dominé par l'énergie de l'électron non apparié. Les oscillations d'Aharanov-Bohm de cet électron peuvent être alors observées optiquement.

Acknowledgements

I would like to express my deepest gratitude to all the people that made the completion of this thesis possible.

First and foremost, I thank Dr. Pawel Hawrylak, my research supervisor, for making my Ph.D. studies in Canada possible, teaching me everything I know about how to do research, and putting up with me for all these years. His personal involvement led to the creation of a unique group of coworkers, with a harmonious atmosphere and enough challenges to ensure the growth of all of its members.

I thank all my colleagues, past and present. They are, in order of appearance: Dr. Shuhei Yoshida, Dr. Andreas Wensauer, Dr. Jordan Kyriakidis, Dr. Brandon van Zyl, Dr. Shun-Jen Cheng, Dr. Weidong Sheng, Dr. Marian Florescu, Alexandra Olaya Castro, Rowan Thomson, Juan Ignacio Climente Plasencia, Wojciech Dybalski, Dr. Ramin Abolfath. You have always been fantastic coworkers and friends. It is amazing how such very different people can find ways of working together so smoothly and entirely without conflicts, which, especially in the scientific community, is not that easy to achieve.

I also thank our experimentalist colleagues: Dr. Andy Sachrajda, Dr. Mariusz Ciorga, Michel Pioro-Ladrière, who endured patiently my theoretical ramblings on many occasions. I thank Michel for his help with the French version of the abstract of this Thesis.

I extend my gratitude to the Institute for Microstructural Sciences, National Research Council of Canada, with which I was affiliated as a visitor during the four years of my studies. All the results described in this work were obtained using the Institute's com-

puting facilities, and hereby I wish to thank Claude Cantin and Dr. Geof Aers for their patience and understanding in this context (they know best what I mean).

And, last but not least, I thank my Parents, Anna and Jacek Korkusiński, and my Brother Aleksander, for their unwavering support over these thousands of kilometres of land and sea between us. Unfortunately, my Father's time in this world ended before this thesis was submitted. I wish to dedicate this work to Him and to all my Family.

Contents

Abstract	i
Sommaire	iii
Acknowledgements	v
List of Acronyms	x
List of Figures	xvi
Plan of the Thesis and Statement of Originality	1
1 Introduction	8
1.1 Elementary properties of quantum dots	8
1.2 Quantum-dot density of states	10
1.3 Fabrication of quantum dots	15
1.3.1 Gated quantum-dot devices	16
1.3.2 Self-assembled quantum dots	22
1.3.3 Quantum rings	30
1.4 Spectroscopy	33
1.4.1 Photoluminescence experiment	33

1.4.2	Tunnelling experiment	35
1.5	Electronic correlations in QDs: overview of the field and scientific contributions of this thesis	41
2	Single-particle states in typical quantum-dot confinements	48
2.1	Parabolic lateral confinement	49
2.2	Confinement of the quantum disk	57
2.2.1	Quantum disk in the absence of the magnetic field	58
2.2.2	Quantum disk in finite magnetic fields	61
2.3	Confinement of the quantum ring	68
3	Methods of analysis of confined many-particle systems	72
3.1	The problem of many interacting particles in a QD confinement	73
3.1.1	The many-particle Hamiltonian	73
3.1.2	Coulomb matrix elements in the harmonic-oscillator basis	75
3.2	The Hartree-Fock method	81
3.3	The exact diagonalisation approach	84
3.3.1	Notation and choice of basis	85
3.3.2	Exact diagonalisation method optimised for parabolic lateral confinements	89
3.3.3	Creation of the Hamiltonian matrix	95
3.3.4	Diagonalisation of large and sparse matrices	102
3.4	Other methods accounting for electronic correlations	118
3.4.1	Spin density functional theory	120
3.4.2	Monte Carlo methods	125
4	Electronic correlations as a function of the confinement energy	132

5	Electronic correlations as a function of the magnetic field	140
5.1	Collapse of the $\nu = 2$ phase of the quantum Hall droplet	141
5.2	Pairing of spin excitations in high magnetic fields	152
6	Correlations in a coupled quantum-dot molecule	158
6.1	Single-particle states of the QD molecule	159
6.2	Entangled states of an electron-hole complex in the QD molecule	172
7	Negatively charged exciton on a quantum ring	176
8	Conclusions	182
A	Curriculum Vitae	198

List of Acronyms

2DEG	two-dimensional electron gas
CI	configuration interaction (method)
CM	centre of mass
DFT	density functional theory
DOS	density of states
FD	Fock-Darwin (spectrum)
IMS	Institute for Microstructural Sciences, National Research Council of Canada
IQHE	integer quantum Hall effect
FQHE	fractional quantum Hall effect
LL	Landau level
LLL	lowest Landau level
MDD	maximum-density droplet
PL	photoluminescence
QD	quantum dot
QDIP	quantum-dot infrared photodetector
QDMC	quantum diffusion Monte Carlo
QMC	quantum Monte Carlo
QWIP	quantum-well infrared photodetector
SAD	self-assembled dot
SDFT	spin density functional theory
SET	single-electron transistor
WL	wetting layer

List of Figures

1.1	Four semiconductor structures of different dimensionality: bulk (a), quantum well (b), quantum wire (c), and quantum dot (d). The narrower (wider)-bandgap material is marked by the dark (light) colour	11
1.2	Energy as a function of wave vector (left-hand panels) and the density of states as a function of energy in the conduction band (right-hand panels) of a bulk material (a), quantum well (b), and quantum wire (c). The vertical axis shows the energy, while the horizontal axes - the length of the wave vector or the density of states, respectively. The density of states of a quantum dot is also shown (d)	13
1.3	SEM micrograph of the vertical quantum dot device and a schematic diagram of the structure of the sample (Adapted from Ref. [123])	18
1.4	(a) Composition of the GaAs/AlGaAs heterojunction with the 2DEG. (b) Profile of the edge of the conduction band along the growth axis of the heterojunction. (c) Scanning electron micrograph of the surface of the sample with metallic gates. (d) Calculated electrostatic potential created by gates as experienced by electrons in the 2DEG layer (Parts (a) and (b) adapted from Ref. [116]; part (c) courtesy of A.S. Sachrajda at IMS NRC)	20

1.5	Atomic force micrographs of InAs self-assembled quantum dots for InAs coverage of 1.6 (a), 1.7 (b), and 1.8 monolayers (Adapted from Ref. [98]). Figure (d) shows a transmission electron micrograph of an InAs SAD (photo courtesy of J.P. McCaffrey at IMS NRC [85])	24
1.6	Growth of quantum disks using the indium flush technique (From Ref. [126])	25
1.7	Cross-sectional TEM image of a stack of quantum disks grown using the indium flush technique. Image on the top right-hand side shows a magnification of the main micrograph (From Ref. [126])	27
1.8	(a) Schematic illustration of the diffusion process in the growth on patterned substrates. This process leads to formation of templates, on top of which several (b) or only one quantum dot (c) can be grown. In these scanning electron microscopy images the base of the pyramid is 400 nm long (Adapted from Ref. [130])	28
1.9	(a) Scanning electron micrograph of the quantum ring structure. The circular shape seen on top is the metallic mask produced by lithography before etching. (b) Schematic diagram of the structure; the carriers are confined in the areas marked by circles (Adapted from Ref. [15])	31
1.10	Schematic representation of energy levels in the lateral quantum dot (see text for details) (Adapted from Ref. [107])	36
1.11	A typical addition spectrum of a gated quantum dot shown as a function of the magnetic field. Forty-five Coulomb blockade peaks are shown, with the charging energy manually removed (From Ref. [32])	39
2.1	Energy spectrum of a single particle in a two-dimensional parabolic potential versus the magnetic field. I show the energies of twenty eigenstates which in the absence of the magnetic field form four lowest shells (see text for details). In this figure, the parabolic frequency $\hbar\omega_0 = 6$ meV, and the Landé factor $g = -4.4$	54

- 2.2 Energy spectrum of a single particle in a rigid-wall quantum disk potential versus the magnetic field. The width of the disk is $W = 20 \text{ \AA}$, and its radius is $R = 200 \text{ \AA}$. I show the energies of twenty eigenstates which in the absence of the magnetic field form four lowest shells (see text for details). In this figure the Landé factor $g = -4.4$. Inset shows the geometry of the disk confinement 67
- 2.3 Energy of a single electron confined in a quantum-ring potential as a function of the number of flux quanta. The colour lines show energies of states with definite angular momenta m (given by numbers on the graph); the black line shows the ground-state energy 70
- 3.1 Relative error of the steepest descent (solid line) and the conjugate gradient (dashed line) methods as a function of the iteration number. 115
- 4.1 The configuration of the three-electron system with quantum numbers $|L, S_z\rangle = |-1, -1/2\rangle$ (a) and $|0, -3/2\rangle$ (b). The graph (c) shows the expectation values of the total energy of the system as a function of the confinement energy Ω_0 for the low-spin state (green line) and the high-spin state (red line) 135
- 4.2 (a) Number of configurations in the low-spin subspace ($L = -1, S_z = -1/2$ - green bars) and in the high-spin subspace ($L = 0, S_z = -3/2$ - red bars) for a three-electron system as a function of the number of single-particle shells N_S . Inset shows ratios between these numbers. (b) Critical confinement energies Ω_0^T marking the low-spin - high-spin transition as a function of the number of shells N_S . For $N_S = 3$ there is no transition . . 138

5.1	(a) Magnetic field evolution of the single-particle spectrum of the parabolic quantum dot (Zeeman energy artificially enhanced). Circles denote the edge spin flip of a droplet with even (empty) and odd (full) number of electrons; squares denote the centre spin flip. (b) Configuration of noninteracting electrons corresponding to the $\nu = 2$ phase	142
5.2	Phase diagrams obtained in the lowest Landau level approximation (dotted lines), using the Hartree-Fock approximation (solid lines), from single electron-hole pair excitation spectre (dot-dashed lines), using the SDFt approach (dashed lines), and from exact diagonalisation study (full circles)	149
5.3	Charge distribution corresponding to the $\nu = 2$ phase (a), the first spin-flip configuration (b), the correlated biexciton (c), the internal spin-flip phase (d) and the second spin-flip configuration for an eight-electron parabolic dot	153
5.4	Phase diagram of the even-electron droplet as a function of the number of electrons and the magnetic field. In this calculation $\hbar\omega_0 = 6$ meV and the Zeeman energy $E_Z = 0$	156
6.1	(a) Schematic picture of the vertically coupled double-dot molecule; (b) illustration of effective potentials in the adiabatic calculation of electronic states for the vertical motion (left-hand panel) and for the planar motion (right-hand panel) (see text for details)	160
6.2	Vertical cross section of the spatial variation of hydrostatic (a) and biaxial (b) strain components through the centre of the double-disk InAs/GaAs system	166
6.3	Band edge alignment along the symmetry axis of the system (dotted lines - unstrained, solid lines - with strain)	169

- 6.4 Electronic energy levels for a double-disk structure with confinement $V_0 = 600$ meV and electronic effective mass $m^* = 0.053 m_0$. WL denotes the states of the wetting layer. Numbers in braces denote quantum numbers (n, m, l) of the states. $l = +$ denotes a symmetric state (solid lines), while $l = -$ denotes an antisymmetric state (dashed lines) 171

Plan of the Thesis

and Statement of Originality

In this Thesis I present a theoretical study of correlation effects in strongly interacting electronic and electron-hole systems confined in semiconductor nanostructures. The problem of interest can be posed rigorously by writing the Hamiltonian of a system of N particles confined in a potential $V(x, y, z)$ of a nanostructure:

$$\hat{H} = \sum_{i=1}^N \left[\frac{1}{2m_i^*} \left(\hat{\mathbf{p}}_i - \frac{q_i}{c} \mathbf{A}_i \right)^2 + V_i(\mathbf{r}_i) \right] + \sum_{i \neq j}^N \frac{q_i q_j}{\varepsilon |\mathbf{r}_i - \mathbf{r}_j|}. \quad (1)$$

Here, $\hat{\mathbf{p}}_i$, \mathbf{r}_i , q_i , and m_i^* are respectively: the momentum and position operators and the charge and effective mass of the i -th particle, \mathbf{A} is the magnetic vector potential, c is the speed of light, and ε is the dielectric constant of the material.

The first term in this Hamiltonian describes the problem of a single particle moving in the potential well V of the nanostructure in the presence of an external magnetic field. This problem is at most three-dimensional, and in most cases it can be solved exactly, using analytical or numerical methods.

What makes the Hamiltonian difficult to analyse is the second term, which describes the Coulomb interactions. Now the particles are no longer independent and one needs to build the basis of the Hilbert space for the problem out of configurations of all N particles. The size of this basis grows factorially with the number N . This makes the problem of interacting particles too difficult to solve exactly on present-day computers.

Approximate methods have been developed to approach the problem. For example, in mean-fields treatments, such as the Hartree-Fock theory, the wave function of the system is postulated in the form of a single Slater determinant:

$$\Psi(\mathbf{r}_1\sigma_1, \dots, \mathbf{r}_N\sigma_N) = \begin{vmatrix} \phi_1(\mathbf{r}_1)\chi_{\sigma_1}(\mathbf{r}_1) & \dots & \phi_1(\mathbf{r}_N)\chi_{\sigma_1}(\mathbf{r}_N) \\ \vdots & & \vdots \\ \phi_N(\mathbf{r}_1)\chi_{\sigma_N}(\mathbf{r}_1) & \dots & \phi_N(\mathbf{r}_N)\chi_{\sigma_N}(\mathbf{r}_N) \end{vmatrix}, \quad (2)$$

built out of effective single-particle orbital and spin wave functions $\phi_i(\mathbf{r})\chi_{\sigma_i}(\mathbf{r})$. The total energy is then formulated as a functional of these effective orbitals, and then minimised self-consistently by adjusting these orbitals one by one until convergence. This means in practice that the system is modelled on a single-particle level, but now each particle moves not only in the potential $V(x, y, z)$ of the nanostructure, but also in the mean effective field created by all other particles.

Note that in this approach, allowing to approximate only the ground-state energy of the system, each particle interacts with all other particles not as with point-like objects, but rather through a smeared-out effective potential, which accounts for the total Coulomb direct and exchange interactions. The mean-field theories usually work well in weakly interacting systems, i.e., systems, where the first term of the Hamiltonian (1) plays the dominant role, and the second term is just a perturbation. In such systems the ground state can indeed be well approximated by a single Slater determinant. However, the confinement $V(x, y, z)$ of semiconductor nanostructures can be chosen in such a way that the characteristic energy scale of the single-particle problem is the same as that of interactions, or even smaller. To show this, let us examine the two-dimensional parabolic confinement potential, used frequently in this work:

$$V(r) = \frac{1}{2}m^*\omega_0^2r^2, \quad (3)$$

with the characteristic frequency ω_0 . I will prove later on that the energy gaps between the levels of its single-particle spectrum are of order of $\hbar\omega_0$, while interactions scale as

$\frac{e^2}{\varepsilon} \sqrt{\frac{2m^*}{\hbar^2}} \sqrt{\hbar\omega_0}$ (\hbar is the Dirac's constant, ε is the dielectric constant of the material, and m^* and e are the electronic effective mass and charge, respectively). Thus the ratio λ of the characteristic interaction and single-particle energies is $\lambda = \frac{e^2}{\varepsilon} \sqrt{\frac{2m^*}{\hbar^2}} \frac{1}{\sqrt{\omega_0}}$, and can be made larger than 1 for ω_0 small enough (for instance, in GaAs, $m^* = 0.067 m_0$ and $\varepsilon = 12.4$, and $\lambda > 1$ for $\hbar\omega_0 < 23.7$ meV, a value easily obtained experimentally). The properties of these strongly interacting systems cannot be fully understood in terms of quasiparticles (particles dressed in interactions), because in this regime the particles are correlated and manifest collective behaviour. To account for these phenomena, the wave function should also contain terms dependent explicitly on differences between electronic coordinates, which is not fully included in the mean-field treatment. This is achieved by writing the eigenstates (ground and excited) of the Hamiltonian (1) not as a single Slater determinant, but rather as linear combinations of many such objects. In order to establish what these linear combinations should be, one needs to move to more sophisticated, nonperturbative approaches. The goal of this Thesis is to use such approaches to examine correlation effects in these systems, and contrast them with those due to the Coulomb direct and exchange terms.

I choose to study the correlation effects in semiconductor nanostructures, because such systems can be realised experimentally, offering a possibility of direct verification of my findings. The nanostructures I focus on in this context are quantum dots and quantum rings. I start this work with a general introduction to these zero-dimensional structures, from fundamental concepts to specific realisations (Chapter 1). In this Chapter I also present a review of the available literature treating the subject of many interacting particles confined in them. As I have pointed out, proper treatment of correlations in these systems cannot be accomplished within the mean-field approaches, but requires sophisticated methods and tools of mathematical and computational physics. My presentation of these tools starts in Chapter 2 with a description of single-particle properties of typical nanostructures. Having done that, in Chapter 3 I formulate the problem of many

interacting particles confined in nanostructures and describe the exact diagonalisation method, capable of capturing the physics of such systems in an exact (nonperturbative) manner. This level of complexity of my theories is necessary to account for the correlation effects in the system, although I acknowledge the existence of other methods, capable of accomplishing this task in an approximate manner. Only then do I proceed to the main body of my work. In Chapter 4 I analyse the properties of systems of many electrons confined in parabolic quantum dots and I show that properties of such systems, such as their magnetic moments, can be engineered. This engineering is accomplished by controlling the Hilbert space of the many-particle system, which, in turn, is achieved by tuning the single-particle properties of the dots. In Chapter 5 I analyse many-electron systems under parabolic confinement and in an external magnetic field, and I show how the electronic correlations modify the evolution of these systems as a function of the number of electrons, the magnetic field, the Zeeman energy, etc. Then I move on to electron-hole systems, and in Chapter 6 I consider a single electron-hole pair confined in the vertically coupled double-quantum-dot molecule. I show that the Coulomb interactions of the carriers lead to the appearance of a special kind of correlation, known as entanglement. I continue the analysis of electron-hole systems in Chapter 7, where I demonstrate how correlations can lead to suppression of Aharonov-Bohm oscillations of an exciton and a negatively charged exciton confined in a quantum ring. I conclude the thesis with a brief summary in Chapter 8.

All the calculations presented in the text were carried out under the supervision of Dr. Pawel Hawrylak, the Group Leader of the Quantum Theory Group at the Institute for Microstructural Sciences, National Research Council in Ottawa. Since many of the methods are numerical in nature, this Group adopted a specific procedure to prove their correctness: apart from the cases where the result was obvious, it had to be reproduced independently by two or more people. Note the word “independently”: in this case it means that each of the persons involved had to parametrise the model in their own

way, write their own computer programs, and prepare their own presentation of results. Therefore I feel that I can, in good faith, claim the results presented herein as my own, however not without crediting the coworkers and colleagues, who have helped to put this research on solid scientific ground. They are:

- Dr. Pawel Hawrylak, of the Institute of Microstructural Sciences, National Research Council of Canada, Ottawa - the Group Leader, who directed all of our research, ultimately supervising and reproducing all the results;
- Dr. Andreas Wensauer, formerly at the Physics Department, University of Regensburg, Germany, now at Framatome Inc., Erlangen, Germany, a visitor at IMS, and a co-developer of the exact diagonalisation tools used to analyze the spectra of lateral gated quantum dot devices;
- Dr. Jordan Kyriakidis, formerly a Research Associate at IMS, now an Assistant Professor at the Physics Department, Dalhousie University, Halifax, NS, who was involved in analyzing the electronic spectra of deformed lateral dots;
- Dr. Shun-Jen Cheng, formerly a Research Associate at IMS, now an Assistant Professor at National Chiao Tung University in Taiwan, who worked on the excitonic spectra of deformed self-assembled dots and dots in high magnetic fields;
- Dr. Weidong Sheng, a Research Associate at IMS, who has worked on microscopic models of electron and hole states in self-assembled quantum dots;
- Juan Ignacio Climente Plasencia, now a Ph.D. Student at the Physics Department, Universitat Jaume I, Castelló, Valencia, Spain, who worked on double-hole spectra of self-assembled dots.

I am indebted to all these coworkers and colleagues.

Most of our original results have already been published in refereed journals (see Appendix A for the full list of papers), which prompted me to build this Thesis as a

collection of articles, rather than write a separate monograph. Out of the full list I have chosen eight papers, which, in my opinion, present a consistent line of research into correlations in nanostructured materials. These papers are:

1. A. Wensauer, M. Korkusiński, and P. Hawrylak, “Configuration interaction method for Fock-Darwin states”, *Solid State Commun.* **130**, 115 (2004);
2. M. Korkusiński, W. Sheng, and P. Hawrylak, “Designing quantum systems in self-assembled quantum dots”, *Phys. Stat. Sol. (b)* **238**, 246 (2003);
3. A. Wensauer, M. Korkusiński, and P. Hawrylak, “Theory of spin-singlet filling factor $\nu = 2$ quantum Hall droplet”, *Phys. Rev. B* **67**, 035325 (2003);
4. M. Korkusiński, P. Hawrylak, M. Ciorga, M. Pioro-Ladrière, and A.S. Sachrajda, “Pairing of spin excitations in lateral quantum dots”, submitted for publication in *Phys. Rev. Lett.*;
5. M. Korkusiński and P. Hawrylak, “Electronic structure of vertically stacked self-assembled quantum disks”, *Phys. Rev. B* **63**, 195311 (2001);
6. M. Korkusiński, P. Hawrylak, M. Bayer, G. Ortner, A. Forchel, S. Fafard, and Z. Wasilewski, “Entangled states of electron-hole complex in a single InAs/GaAs coupled quantum dot molecule”, *Physica E* **13**, 610 (2002);
7. M. Korkusiński, P. Hawrylak, and M. Bayer, “Negatively charged exciton on a quantum ring”, *Phys. Stat. Sol. (b)* **234**, 274 (2002);
8. M. Bayer, M. Korkusiński, P. Hawrylak, T. Gutbrod, M. Michel, and A. Forchel, “Optical detection of the Aharonov-Bohm effect on a charged particle in a nanoscale quantum ring”, *Phys. Rev. Lett.* **90**, 186801 (2003).

As can be seen from this list, all these papers resulted from joint effort. The first four of them are strictly theoretical in nature, and, in the best possible faith, I declare that I have

contributed to their entire content within the collaborative procedure outlined above, with only one exception: the spin density functional calculations presented in the third paper are due to Dr. Andreas Wensauer, and I have not reproduced them on my own. As for the last four papers, they cover both theoretical and experimental aspects of the research, but the emphasis is put on a detailed presentation of the theory, and experimental results are only invoked to confirm it. Being a theorist, I have not contributed to the experimental aspects of these publications, but I declare my full involvement in the theories presented there - again, within the collaborative procedure described earlier.

Searches of available literature have revealed a number of publications tackling problems similar to those presented in this Thesis, and using similar methods; I review some of these publications in order to put our results in the appropriate perspective. I find, however, that in each of these cases my work is sufficiently distinct to be considered unique and original.

Chapter 1

Introduction

1.1 Elementary properties of quantum dots

Quantum dots (QDs) can be defined as solid-state structures capable of confining electrons and holes in all spatial directions. They are frequently modelled as three-dimensional wells of confining potential, or “quantum boxes” (usually with walls of finite height); the confinement is usually produced electrostatically or by appropriate material engineering. Typical dimensions of QDs range from a few to several hundreds of nanometres, which results in distinct quantisation of the single-particle energy spectrum of trapped carriers: the energy gaps between levels are typically of the order of several microelectronvolts to several tens of millielectronvolts (meV). At this point one frequently draws an analogy between the QDs and atoms, in which electrons are confined by the positive potential of the nucleus, and their energy levels form well-separated shells. This analogy is quite useful, and QDs are often called “artificial atoms” [8, 62]. Indeed, as mentioned before, in QDs, as in atoms, the wave functions of charge carriers are confined in the vicinity of the dot centre, and the corresponding eigenenergies form a discrete spectrum. If the QD is of a sufficiently high symmetry, these levels can form shells with increasing degeneracy. Also, it is possible to obtain dots with well-controllable number of confined carriers, from one to

hundreds, and indeed reproduce a Mendeleev periodic table of “QD elements” [32, 121]. The carriers can relax or be promoted from one level to another subject to selection rules similar to those found in atoms. There are, however, notable differences between the artificial atoms and their natural counterparts. First of all, quantum dots can confine holes as well as electrons, while the positive potential of atomic nucleus can only confine the negative carriers. Further, the lateral confinement in QDs is usually smooth, and in many cases approximately parabolic, in contrast to the Coulomb potential of atoms, possessing a singularity at the nucleus. Also, QDs are composed of thousands of atoms or more. This size leads to a smaller interlevel separation (tens of meV at most), compared to that of atoms, where the shells are separated by a few eV. Moreover, the lateral confinement (Coulomb potential) in atoms is fixed and defined by the electrostatic charge of the nucleus, which makes it difficult to change the number of electrons confined by it. In contrast, in certain types of dots the QD lateral confinement can be tuned, and the same device can contain from zero to hundreds of confined electrons (I shall discuss these devices later on).

The first successful attempts at creating QDs date back to the early 1980’s [62]. Since then fabrication technologies have progressed rapidly, and today it is possible to manufacture dots of various shapes and sizes, and to tailor almost all the properties indicated above. It is then not surprising that QDs have become an area of interest both in the domain of fundamental research and device physics. This thesis will cover in detail only a small section of this ever-increasing field. For the reader interested in a general introduction to QDs, QD devices and terminology in their full variety I suggest three books: by Bimberg, Grundmann, and Ledentsov [20], Jacak, Hawrylak, and Wójs [62], and Michler [85], and review articles by Ashoori [8], Kastner [65], and Chakraborty [30].

1.2 Quantum-dot density of states

Control over the number of confined carriers seems to be of particular importance in the physics of quantum dots. Therefore, many important realisations of QDs employ semiconductor structures, where the number of mobile carriers can be controlled by means of appropriate doping, illumination, etc., and this work will focus on such structures exclusively. For this reason, at this point I will introduce an alternative treatment of the QD energy quantisation using the language of the density of states (DOS). At the same time, the notion of “zero-dimensional states” is presented here more rigorously and put in context of other structures with reduced dimensionality, such as quantum wells and wires. The description given in this Section is similar to that presented in Ref. [62].

In my simplified description of the influence of the reduced dimensionality on DOS I shall assume my semiconductor materials to be isotropic, with parabolic energy bands and spherical energy isosurfaces, and I shall consider the electrons in conduction bands only. In this case, in order to calculate the DOS as a function of the wave vector k I will consider the number of electronic states $n(k)$ contained in an infinitesimal region $d^m k$ at the wave vector \mathbf{k} , where $m = 3, 2$ or 1 is the dimensionality of the material (the case of zero-dimensional structures will be considered separately). The DOS will be then calculated as [7]

$$\text{DOS}(k) = \frac{dn(k)}{dk}. \quad (1.1)$$

This expression may contain an extra factor of two if the spin degeneracy of levels is taken into account.

Usually the DOS is calculated as a function of energy in the band, and to make contact with this formulation, I shall make use of the well-known formula for energy as a function of the wave vector:

$$E(k) = \frac{\hbar^2 k^2}{2m^*}, \quad (1.2)$$

where m^* is the effective mass of the electron, and k is the length of the wave vector \mathbf{k} .

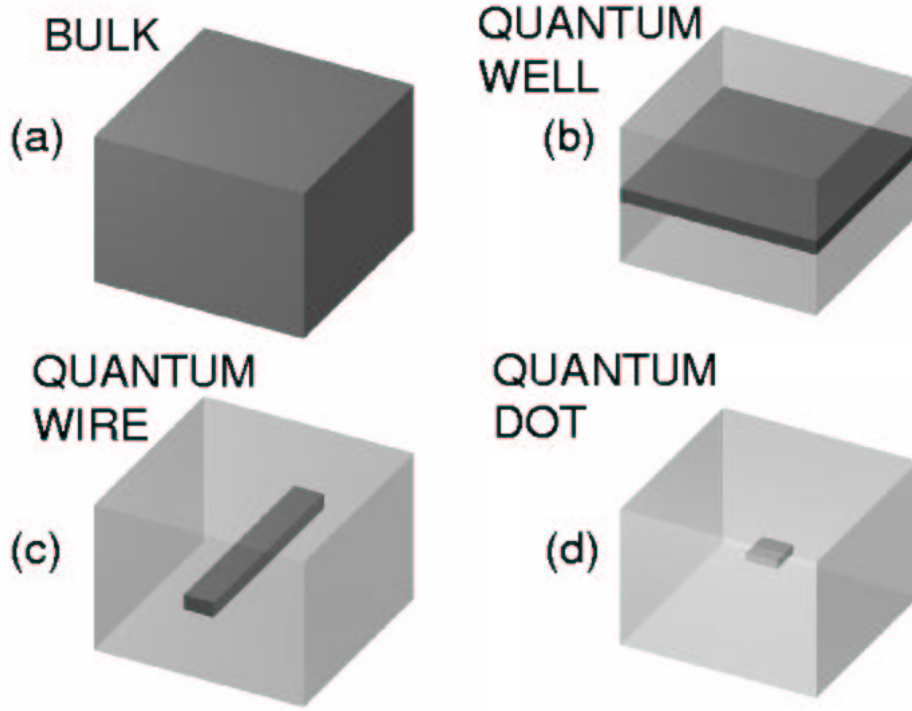


Figure 1.1: Four semiconductor structures of different dimensionality: bulk (a), quantum well (b), quantum wire (c), and quantum dot (d). The narrower (wider)-bandgap material is marked by the dark (light) colour

By combining the two formulae one can calculate

$$\text{DOS}(E) = \frac{dn(E)}{dE}. \quad (1.3)$$

Let us now consider four semiconductor structures, presented in Figure 1.1. Part (a) of this Figure shows a macroscopic sample of bulk semiconductor material. If the dimensions of this sample are infinite, the single-particle energy spectrum in the conduction and the valence bands is continuous, and spherical coordinates can be introduced in Eq. (1.1). Thus the function $n(k)$ gives the number of states contained between two spherical surfaces, one with radius k , and another, with radius $k + dk$, and is

$$n^{3D}(k) = \frac{1}{(2\pi)^3} 4\pi k^2 dk. \quad (1.4)$$

As a result, the DOS as a function of energy in the band attains a well-known square-root form:

$$\text{DOS}^{3D}(E) = \frac{1}{(2\pi)^2} \left(\frac{2m^*}{\hbar^2} \right)^{3/2} \sqrt{E}. \quad (1.5)$$

The energy as a function of the electronic wave vector k is shown in the left-hand panel, and the DOS as a function of energy - in the right-hand panel of Fig. 1.2 (a). Finite dimensions of the sample introduce boundary conditions resulting in quantisation of energy levels, but if the dimensions are sufficiently large, the spacing of levels is very small. The spectrum becomes quasi-continuous, and the changes to DOS are negligible.

If a layer of a narrower-bandgap material is sandwiched between two thick layers of a wider-bandgap material, one creates a quantum well, shown in Fig. 1.1 (b). If the edge of the conduction band in the well material is below the band edge of the barrier, the mobile carriers in the structure are trapped inside the well. They are still free to move in the plane, but their motion across the structure is strongly quantised. Thus the energy spectrum consists of distinct quantum-well energy levels E_0, E_1, \dots , on top of which there is a quasi-continuous spectrum corresponding to the planar motion. In the left-hand panel of Fig. 1.2 (b) I show this energy spectrum as a function of the in-plane wave vector. In this case the function $n(k)$ describes the number of states of each subband contained between two circular boundaries, one with the radius k , and the other with the radius $k + dk$, and is

$$n^{2D}(k) = \frac{1}{(2\pi)^2} 2\pi k dk. \quad (1.6)$$

The resulting total DOS of the quantum well is zero for energies below E_0 , and then exhibits a steplike dependence on energy, with steps beginning at energies E_i , i.e., the quantum-well subband edges:

$$\text{DOS}^{2D}(E) = \sum_i \frac{1}{2\pi} \frac{m^*}{\hbar^2} H(E - E_i), \quad (1.7)$$

where the Heaviside's function $H(x) = 1$ for $x \geq 0$ and 0 otherwise, and i enumerates the quantum-well subbands. This DOS is shown in the right-hand panel of Fig. 1.2 (b).

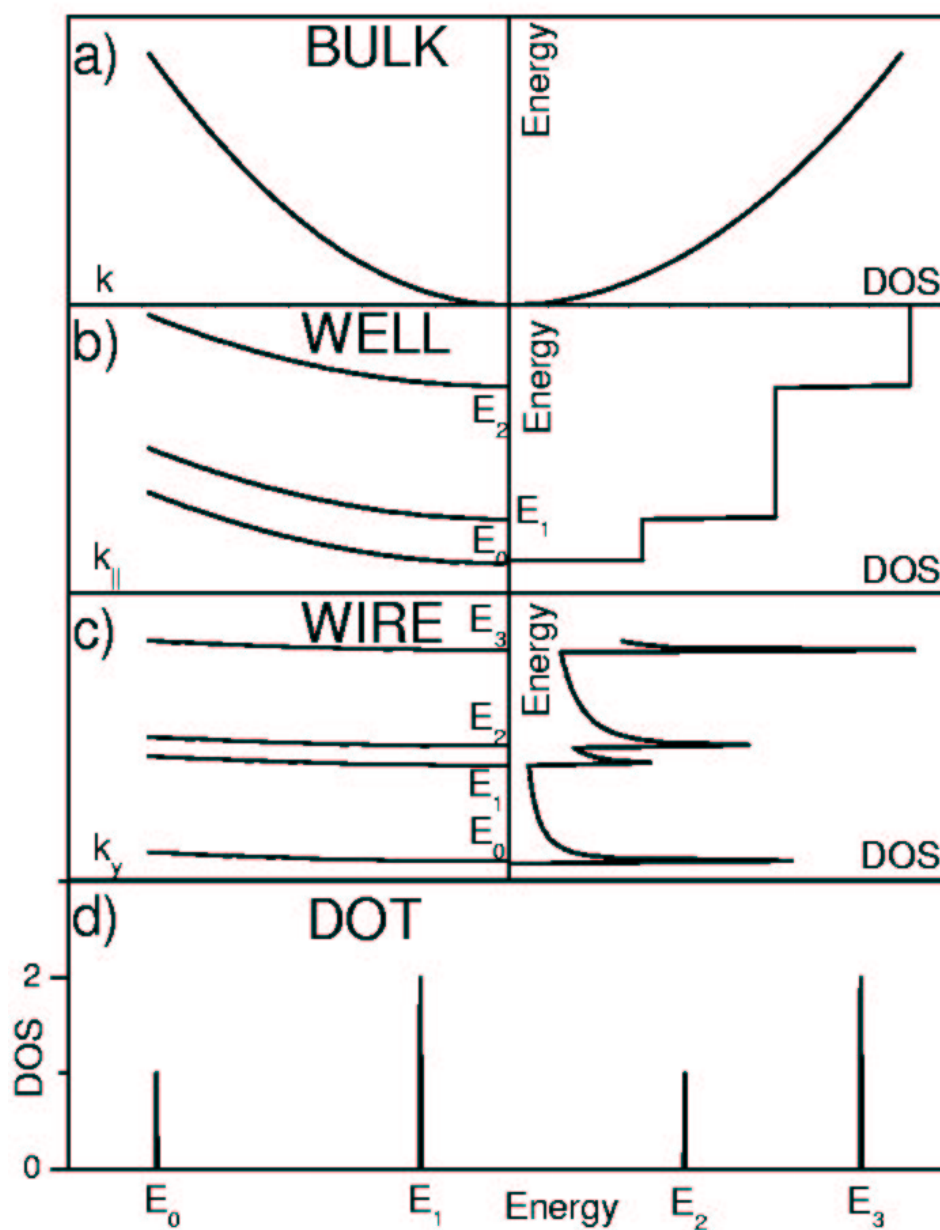


Figure 1.2: Energy as a function of wave vector (left-hand panels) and the density of states as a function of energy in the conduction band (right-hand panels) of a bulk material (a), quantum well (b), and quantum wire (c). The vertical axis shows the energy, while the horizontal axes - the length of the wave vector or the density of states, respectively. The density of states of a quantum dot is also shown (d)

A quantum wire, shown schematically in Fig. 1.1(c), is formed when the motion of the carriers is restricted in two directions, while they are free to move along the third direction (say, along the y axis). The electronic energy spectrum consists now of a ladder of discrete quantum-wire modes, on top of which there is a quasi-continuous one-dimensional spectrum corresponding to the motion along the wire. I show this spectrum as a function of the electronic wave vector in the left-hand panel of Fig. 1.2 (c). In this case the function $n(k)$ for each subband describes the number of states contained in a one-dimensional section of the reciprocal space between the wave vector k and $k + dk$, and is

$$n^{1D}(k) = \frac{1}{2\pi} dk. \quad (1.8)$$

The total quantum-wire DOS consists of a series of inverse-square-root peaks centered at the edges of the quantum-wire subbands:

$$\text{DOS}^{1D}(E) = \sum_i \frac{1}{4\pi} \left(\frac{2m^*}{\hbar^2} \right)^{1/2} \frac{1}{\sqrt{(E - E_i)}} H(E - E_i). \quad (1.9)$$

This function is shown in the right-hand panel of Fig. 1.2 (c).

Finally, the zero-dimensional structure - a QD - is created when the well material is surrounded by the barrier on all sides, as shown in Fig. 1.1 (d). Here the electronic spectrum consists of discrete states, and the DOS is composed of delta function peaks at the QD energies; the height of these peaks corresponds to the degeneracy of the levels. In Fig.1.2 (d) I show a QD DOS for a dot whose base is a square and height is small compared to the lateral dimension. Due to this dimensional disparity, the energy scale introduced by the stronger, vertical quantisation will be different from that due to the lateral confinement: one expects a ladder of widely spaced vertical energy levels, on top of which there are the modes of the lateral motion, still discrete, but spaced much more closely. In fact, if the QD height is sufficiently small, the energy of the second vertical subband is already above the barrier, so the bound states contain the lowest vertical mode only. Furthermore, due to the square symmetry of the QD base, one expects the first excited state of this system to be doubly degenerate, which is reflected in the height

of the corresponding delta peak in Fig. 1.2 (d). This schematic picture is, of course, only valid in the region of energies corresponding to the QD bound states (below the barrier). Energies above the barrier correspond to the continuum states. At this point one might compare the DOS of these propagating states to that of the bulk material. Indeed, the wave functions of the states above the barrier will be distorted by the presence of the QD, but these distortions do not lead to major changes in the square-root dependence of the DOS on energy. Of particular interest is the case in which the wave function is distorted just so that its part inside the QD fits smoothly to the undistorted function in the barrier. If interrogated outside the QD, the state behaves then as if there was no QD at all (in other words, the scattering cross-section of the QD for this particular energy is zero). This is the Ramsauer-Townsend effect [110], well known in scattering theory, and the propagating states with this property are called resonances. These resonances can be thought of as an “echo” of the QD potential, experienced by the states above the barrier, and their corresponding wave functions must carry symmetries characteristic for the QD. They are of interest in device physics, and in particular in quantum-dot infrared photodetectors, briefly mentioned in the next section.

1.3 Fabrication of quantum dots

This Thesis is devoted to presenting my theoretical understanding of many-body systems confined by the potential of nanostructures. I would like to apply my theories to real systems, and obtain experimental verification of my results. To this end it is necessary to model the behaviour of the particles in realistic, experimentally attainable confinements. Perhaps the best way to understand the most important properties of these confinements is to present the techniques of nanostructure fabrication. In two decades of technological progress in this area several such techniques were developed. The starting point in some of them is a semiconductor quantum well (see Fig. 1.1(b)). One can further process

such a sample with lithography and etching to obtain free-standing nanopillars with a small amount of quantum well material located somewhere along their height [38, 103]. One can also evaporate an array of miniature metallic electrodes onto the surface, and subsequently polarise them with voltage - the resulting electrostatic field propagates down to the quantum well layer and creates the lateral confinement [115]. The third method here would involve a selective illumination of the surface by an intense laser beam. This causes interdiffusion of the well and barrier materials within the illuminated spot, which leads to modulation of the thickness of the quantum well and creation of dots [25]. A completely different method - selective epitaxy - involves growing a bulk substrate of the barrier material with a mask on its surface. Then, using lithographical methods, one creates small openings in the mask, and then one deposits the material of the quantum well. The well material will adsorb on the substrate only in the openings, so, as a result, we obtain an array of small islands [45, 73].

Although using all these methods it is possible to obtain QDs in a variety of shapes and sizes, recent years have brought new techniques, allowing for far more advanced QD engineering. I will cover in detail three such techniques: gated QD devices, growth of QDs by self-assembly, and fabrication of quantum rings by lithography and etching.

1.3.1 Gated quantum-dot devices

This type of QD design is particularly important in the context of my research into electronic correlations. In this design the potential of the nanostructure confines only one type of carriers, i.e., electrons, and the number of confined carriers is controlled electrostatically by applying voltage to metallic gates. The experimental technique most frequently used to probe these dots is transport spectroscopy, in which information about the system is derived from the properties of tunnelling current induced to flow through the device. I shall discuss the principles of tunnelling spectroscopy in the next Section; now let us only describe how these devices are built and operated.

There are two variants of the design. In the first one the lateral confinement for electrons is created by means of material engineering (by lithography and etching techniques) and using a metallic gate to control electronic population of the system. The first such device was fabricated by Ashoori *et al.* in 1992 [9], and the properties of the system of electrons localised on it were analysed theoretically by Hawrylak in 1993 [51]. Another device was created by D.G. Austing in the group of Seigo Tarucha at NTT Japan [4, 11, 92, 121, 122].

Here the gates are used not only to induce the tunnelling current, but also to change the lateral confinement of electrons by squeezing them electrostatically to a smaller area. The common feature of both designs is the fact that the tunnelling current flows vertically, i.e., along the axis of rotational symmetry of a disk-like quantum dot. This is why these structures are called **vertical quantum dots**. Let us briefly describe the second of the two devices.

A SEM micrograph and a schematic diagram of the sample is shown in Fig. 1.3. Its most important part, providing the vertical confinement for electrons, is the double-barrier heterostructure (DBH) seen in the centre of the diagram; the lateral confinement is produced by the lateral surface of the pillar and controlled by the gate. The sample is composed of the following elements. The substrate material is the n-doped GaAs, seen at the bottom of the diagram. Doping introduces electrons into the conduction band of this layer, so that we have mobile carriers that can be injected into the quantum dot. On top of this substrate the DBH is created using epitaxy. Each of the two barriers (denoted by darker regions in Fig. 1.3) is made of $\text{Al}_{0.22}\text{Ga}_{0.78}\text{As}$; the thickness of bottom barrier is 7.5 nm, and that of the top barrier is 9.0 nm. The material of the 12.0-nm-thick well between the barriers is $\text{In}_{0.05}\text{Ga}_{0.95}\text{As}$; the small amount of indium present in this layer causes the edge of its conduction band to be below that in the GaAs substrate. The DBH is then covered by a thick layer of n-doped GaAs, on top of which a metallic gate is deposited. A pillar, with the radius of about $0.5\ \mu\text{m}$, is formed using lithography and etching, and

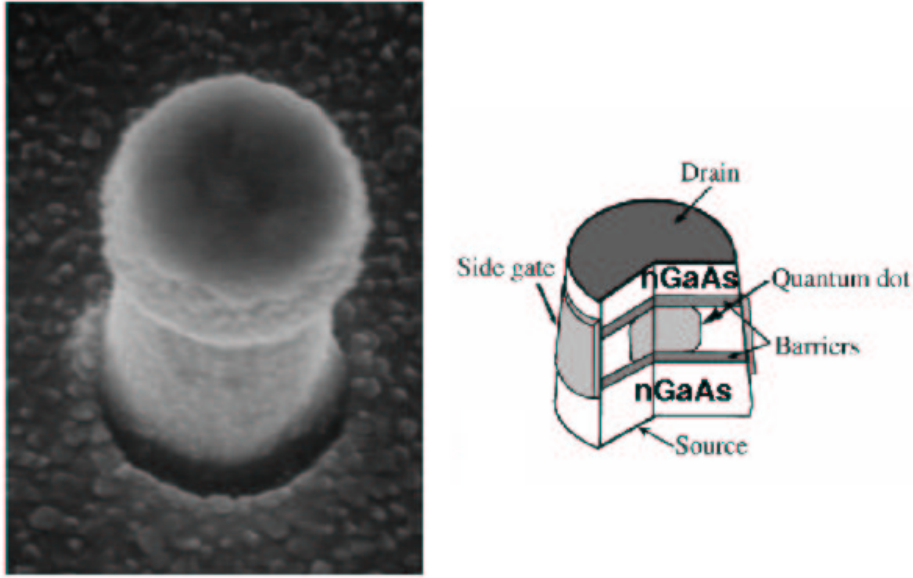


Figure 1.3: SEM micrograph of the vertical quantum dot device and a schematic diagram of the structure of the sample (Adapted from Ref. [123])

a metallic gate is also deposited on the lateral surface of the pillar, close to the DBH. In the tunnelling experiment a small voltage is applied to the top gate, which causes the electrons from the bottom nGaAs layer (the *source*) to tunnel into the dot and out to the top nGaAs layer (the *drain*). The tunnelling current is measured as a function of the voltage on the side gate and typically as a function of an external magnetic field applied along the rotational symmetry axis of the system.

Let us now move on to the second design of gated QDs: the **lateral gated quantum-dot device**. I am aware of several experimental groups working with the lateral dots, for instance the groups of Charles Marcus [81] and Robert Westervelt [129] at Harvard University, Marc Kastner at MIT [63], Klaus von Klitzing at MPI Stuttgart [66], and Leo Kouwenhoven at Delft in the Netherlands [68]. Here, however, I shall present a device built by A.S. Sachrajda and co-workers in the Quantum Physics Group at IMS NRC [31, 32, 33], because it was used to obtain experimental verification of my theoretical

results. To the best of my knowledge, this was the first device in which the number of confined electrons was known and controlled (from zero to about fifty). This was also the first device whose design allowed for the spin blockade spectroscopy (I shall describe this spectroscopic technique in detail in the next Section).

Fabrication of the lateral QD device consists of two stages. The first stage involves epitaxial growth of a GaAs/AlGaAs heterojunction. A schematic diagram of the sample composition is presented in Fig. 1.4(a). First, a thick ($1\text{--}3\ \mu\text{m}$) layer of GaAs is deposited epitaxially on a substrate. Then, a heterointerface is formed by depositing undoped AlGaAs on top of the structure. The growth of AlGaAs is terminated after reaching the optimal spacer thickness, marked in Fig. 1.4(b) by the vertical line. Thicker n-doped AlGaAs and GaAs layers are subsequently deposited on top. This growth sequence results in the alignment of the conduction band edge shown in Fig. 1.4(b). As we move within GaAs along the z axis, closer and closer to the AlGaAs material, we see conduction band bending and formation of a triangular quantum well at the interface. This well is filled with electrons coming from ionised donor atoms (white circles). The well is narrow enough so that the electrons populate only its lowest subband. The spacer, made of undoped AlGaAs separates the doped AlGaAs region from the interface to insure high quality of the 2DEG in the well (and, in particular, high mobility of electrons).

The triangular quantum well at the interface confines the electrons only in vertical direction (along the z axis). The lateral confinement, i.e., the confinement in the plane of the 2DEG, is created by means of metallic gates, deposited lithographically on the surface of the sample. A scanning electron micrograph of the gates is shown in Fig. 1.4 (c). In this design there are typically four gates. The two large side gates and the small top gate provide the electrostatic lateral confinement, while the small bottom gate (the “plunger” gate) serves to tune the QD energy spectrum in the tunnelling experiment. Under negative voltage, all of these gates create an electrostatic potential, which propagates down to the 2DEG layer and depletes it locally of electrons, forming a soft lateral confinement, whose

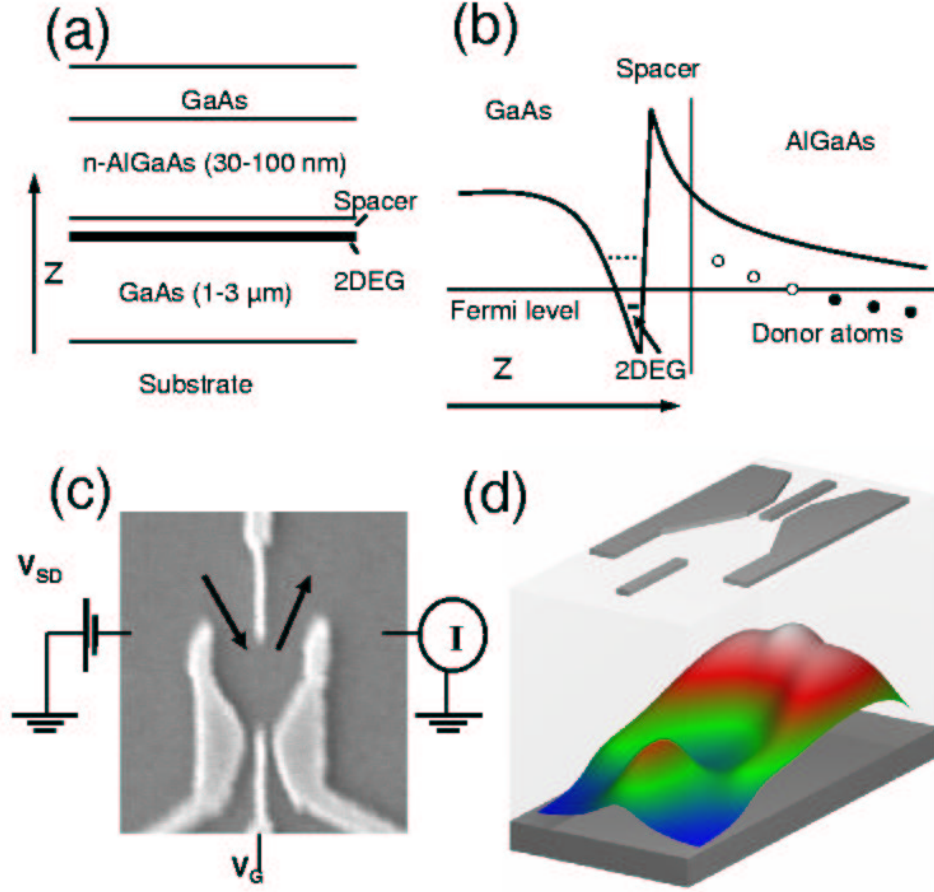


Figure 1.4: (a) Composition of the GaAs/AlGaAs heterojunction with the 2DEG. (b) Profile of the edge of the conduction band along the growth axis of the heterojunction. (c) Scanning electron micrograph of the surface of the sample with metallic gates. (d) Calculated electrostatic potential created by gates as experienced by electrons in the 2DEG layer (Parts (a) and (b) adapted from Ref. [116]; part (c) courtesy of A.S. Sachrajda at IMS NRC)

size is of order of $0.5 \mu\text{m}$. This electrostatic potential, calculated [70] for typical gate voltages, is shown in Fig. 1.4(d). By tuning the gate voltages one can empty the dot of electrons, and then add them, one by one, in a fully controllable manner [31].

In this design, the source and the drain are the 2DEG electronic reservoirs to the left and to the right of the QD, so that the external voltage is applied laterally across the device, as shown in Fig. 1.4(c). Electrons tunnel in and out of the QD across the quantum point contacts defined by the top gate and one of the side gates, respectively (along black arrows in Fig. 1.4(c)). The tunnelling current is measured as a function of the voltage on the plunger gate V_G and the magnetic field perpendicular to the device. The function of this gate is to change the QD size by pushing it towards the top gate (increasing the slope of the large potential maximum shown in Fig. 1.4(d)).

In the lateral design the current tunnelling through the QD can be made to be spin-polarised. This occurs when an external magnetic field is applied perpendicularly to the surface of the sample (i.e., perpendicularly to the 2DEG). Note that the left and right reservoirs of electrons (the source and the drain) are both 2DEGs, and the tunnelling of electrons into and out of the QD involves the 2DEG edge states. Upon application of the external magnetic field, the Zeeman energy distinguishing between the two spin species translates into spatial separation of these edge states, so that the states close to both point contacts carry predominantly electrons with the same spin [31]. It is possible for electrons with the opposite spin to tunnel into the QD, however the probability for this to occur is small due to the fact that these electrons have to tunnel through a wider barrier. The spin-polarised injection and detection of the tunnelling current will play a major role in one of the main chapters of this thesis.

Note that the vertical device maintains a good circular symmetry irrespective of the potential applied to the side gate. The lateral device, on the other hand, produces a non-circular confinement, and the degree of this noncircularity varies with gate voltages. For these reasons, the shell structure of the single-particle spectrum of the QD can manifest

itself more clearly in vertical devices [121], while in the analysis of the results obtained with the lateral device the more complicated nature of the potential (due to its lower symmetry) often has to be taken into account [70].

The gated quantum-dot devices are relatively large (their typical size is of order of hundreds of nanometres), and therefore the shells of the single-particle energy spectrum are relatively close in energy (typical gaps are of order of several meV). These characteristic energies are smaller than the energy equivalent of the room temperature, and, in fact, the experiments on gated dots are usually conducted in millikelvin temperatures in a dilution fridge. The separation of single-particle states can be tuned by appropriately changing the voltage on the gates. Thus, the coefficient λ , defined in the beginning of this Thesis as the ratio of the characteristic interaction and single-particle energies, can be tuned as well, and one can obtain system with large electron-electron interactions. Due to the small interlevel gaps, the single-particle energy scale of the gated QDs can also be significantly tuned by an external magnetic field of order of several Tesla, leading to a nontrivial evolution of the system with the increase of the field. These issues will be discussed at length in this Thesis.

Gated quantum dots are also interesting in the context of the single-electron transistor [64] and Kondo physics (see Refs. [47, 117] and references therein). Finally, gated QD devices are seen as extremely promising candidates for quantum bits and quantum logic gates in quantum computing proposals. The most important theoretical paper in this field was published by Loss and DiVincenzo in 1998 [79]. In it, the authors consider using coupled gated QD devices to create entangled states of electrons.

1.3.2 Self-assembled quantum dots

Let us now move on to describing a different type of QD design, leading to formation of a confinement trapping both electrons and holes, and based on the self-assembly process. Self-assembly of QDs can be achieved by exploiting the Stranski-Krastanow phase tran-

sition occurring in the growth of highly strained semiconductor heterostructures [118]. I shall describe some details of this procedure following Petroff and DenBaars [98].

Let us consider a situation when a crystal of one semiconductor material is grown epitaxially on the surface of another material, and these two materials differ in their lattice constants. If this difference is very large, the deposited material will form an epitaxial layer full of crystallographic defects. However, if this difference is of order of 1-10%, the deposited material will initially form a layer of good quality, but highly strained. The degree of strain will increase as the layer becomes thicker, and, upon reaching a critical thickness (usually of order of a few monolayers), the planar growth of the layer will stop, and small islands of deposited material will start forming on top of the residual “wetting layer”. This is the Stranski-Krastanow phase transition. The growth that follows this transition is a kinetic process driven by the strain energy. To minimise this energy, the material from larger dots will tend to diffuse along the wetting layer towards the smaller dots, thus leading to a better uniformity of the island sizes. If we deposit more material, it will also diffuse and end up being incorporated by the islands, which will grow both in height and diameter. Having obtained islands (dots) with desired dimensions, one can interrupt the growth and cap the structure with a “cladding layer” of the substrate material.

The islands will function as QDs only if the substrate material has a higher bandgap than the island material. In this context, GaAs or $\text{Al}_x\text{Ga}_{1-x}\text{As}$ is frequently used as the barrier, on top of which $\text{In}_x\text{Ga}_{1-x}\text{As}$ or $\text{In}_y\text{Al}_{1-y}\text{As}$ is deposited to form dots. Depending on molar fractions, the lattice mismatch between the barrier and dot materials is of order of 1-8%, making it possible to grow high-quality self-assembled dots (SADs). For example, the change from the two-dimensional to the three-dimensional growth mode upon reaching the critical thickness is illustrated in Fig. 1.5. In this case InAs is being deposited on the GaAs substrate, and the critical thickness of the dot material is about 1.7 monolayers. Dots seen in Fig. 1.5 have diameters of order of $30 \text{ nm} \pm 5\%$ and heights of order of 10 nm

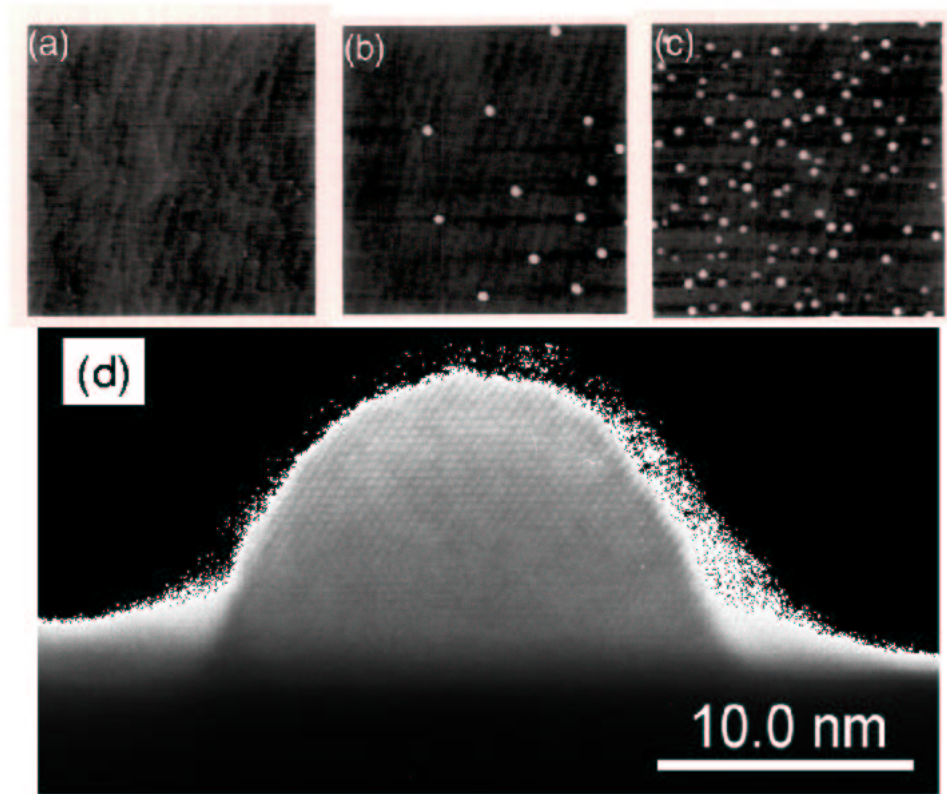


Figure 1.5: Atomic force micrographs of InAs self-assembled quantum dots for InAs coverage of 1.6 (a), 1.7 (b), and 1.8 monolayers (Adapted from Ref. [98]). Figure (d) shows a transmission electron micrograph of an InAs SAD (photo courtesy of J.P. McCaffrey at IMS NRC [85])

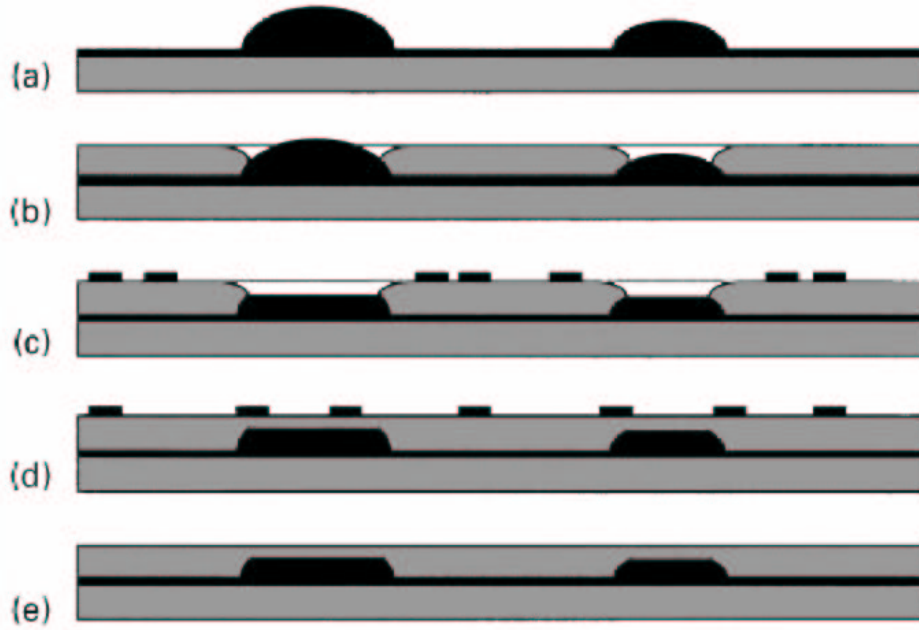


Figure 1.6: Growth of quantum disks using the indium flush technique (From Ref. [126])

$\pm 4\%$. Additionally, in Fig. 1.5 (d) I show a transmission electron micrograph of a SAD grown at the Institute for Microstructural Sciences, NRC Canada.

By choosing the misfit strain one can tune the sizes of SADs, since a smaller misfit leads to a smaller amount of strain, larger critical thickness and, ultimately, larger dots. Also, depending on the conditions of the growth itself, one can obtain SADs in a variety of shapes (e.g., pyramids with a square base [82], lenses [41, 101], hemispheres with hexagonal base [98]).

In recent years, Wasilewski *et al.* at IMS [126] developed a technique allowing for further control over the shape of SADs. The sequence of sample processing steps in this method is shown schematically in Fig. 1.6. First, SADs are grown in the Stranski-Krastanow mode along the lines laid out above, and in this example InAs is used as the dot material. As already mentioned, this growth leads to the formation of an array of dots with similar, but not identical diameters and heights, as shown in Fig. 1.6 (a). Then, the cladding layer is deposited on top of the sample, but this growth is interrupted, so that

dots are not completely covered with the barrier material (Fig. 1.6 (b)). This situation is energetically unfavourable from the point of view of total strain energy, since the indium atoms on the still exposed surface of dots experience a large stress from the surrounding GaAs barrier material. To lower this energy, indium atoms begin migrating from the dots onto the cladding layer, and gallium atoms from the cladding layer onto the dot, which results in a decrease of the dot height and capping of all dots (Fig. 1.6(c) and (d)). Note that this process of migration of atoms results in truncation of dots to uniform height. The next step, called the “indium flush”, involves increasing the sample temperature, so that indium deposited on the surface of the cladding layer is desorbed (Fig. 1.6(e)). As a result, one obtains an array of randomly distributed dots, with variations in diameter, but with uniform heights. The growth can be further continued, i.e., upon deposition of the layer of barrier material of chosen thickness, evaporation of InAs can start again. The process of island growth will then start again, but now positions of QDs in the new layer will be aligned with positions of QDs already grown. This is due to the strain field, created by the QDs, and propagating upwards through the cladding layer of the barrier material. Thus one obtains stacks of coupled quantum disks, shown in Fig. 1.7.

Typically, the SADs can confine both electrons and holes, making it possible to examine the many-body systems composed of particles carrying both positive and negative charges. These systems can be probed by optical spectroscopic techniques, which I will briefly describe later on. However, the interaction effects are difficult to resolve in sufficient detail when working with arrays of QDs presented in the above discussion. This is due to the fact that the sizes of all dots are not exactly identical, but rather form a narrow distribution. As a result, different dots have slightly different single-particle energy spectra, and the corresponding spectroscopic features, obtained as a superposition of signals from the entire array, are broadened (this effect is called “inhomogeneous broadening”). To eliminate this broadening, a single QD must be isolated for a spectroscopic study. There are several techniques which can be used to this end. One of them involves cover-

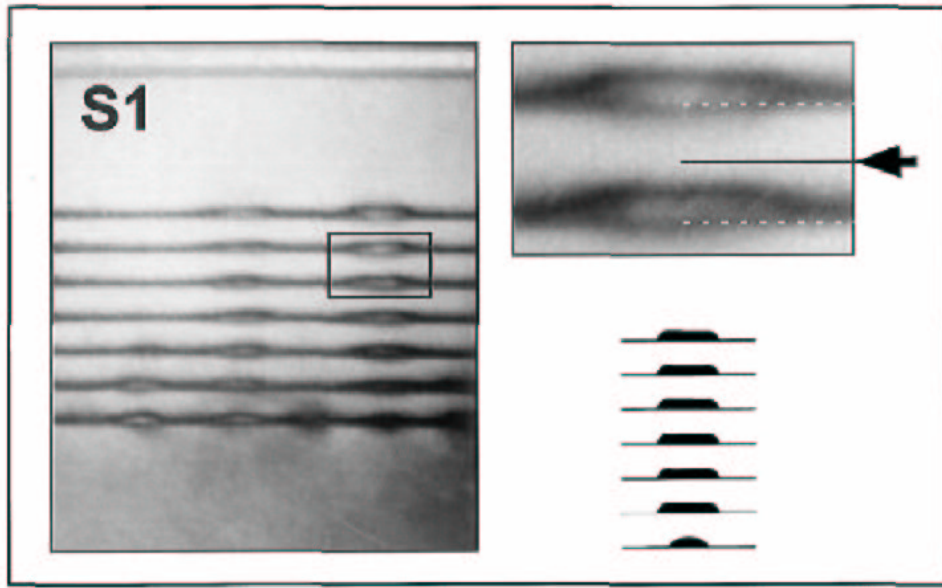


Figure 1.7: Cross-sectional TEM image of a stack of quantum disks grown using the indium flush technique. Image on the top right-hand side shows a magnification of the main micrograph (From Ref. [126])

ing the capped sample of the SAD array with a metallic thin film and creating openings in this film. If the opening is sufficiently small, it may be possible to address exactly one QD below. Another method involves covering a selected area of the QD array with a mask and etching away everything around it [14, 16]. This leads to a formation of a “mesa” structure, which, if it is small enough, may contain exactly one QD (or exactly one stack of QDs created using the indium flush method) in its interior.

Control over the position of a QD can also be achieved by patterning the substrate, on which the dots are grown. Here I shall describe a technique developed recently by Williams and co-workers at IMS [130]. The general principle of this method is illustrated in Fig. 1.8(a). First, a planar substrate (in this case InP) is grown as described previously. Then, a mask is deposited on top of the surface, and rectangular or square openings (with dimensions W of several hundred nanometres) are defined in it by lithography and etching (Fig. 1.8(a)). Then, deposition of the substrate material is resumed, but the material

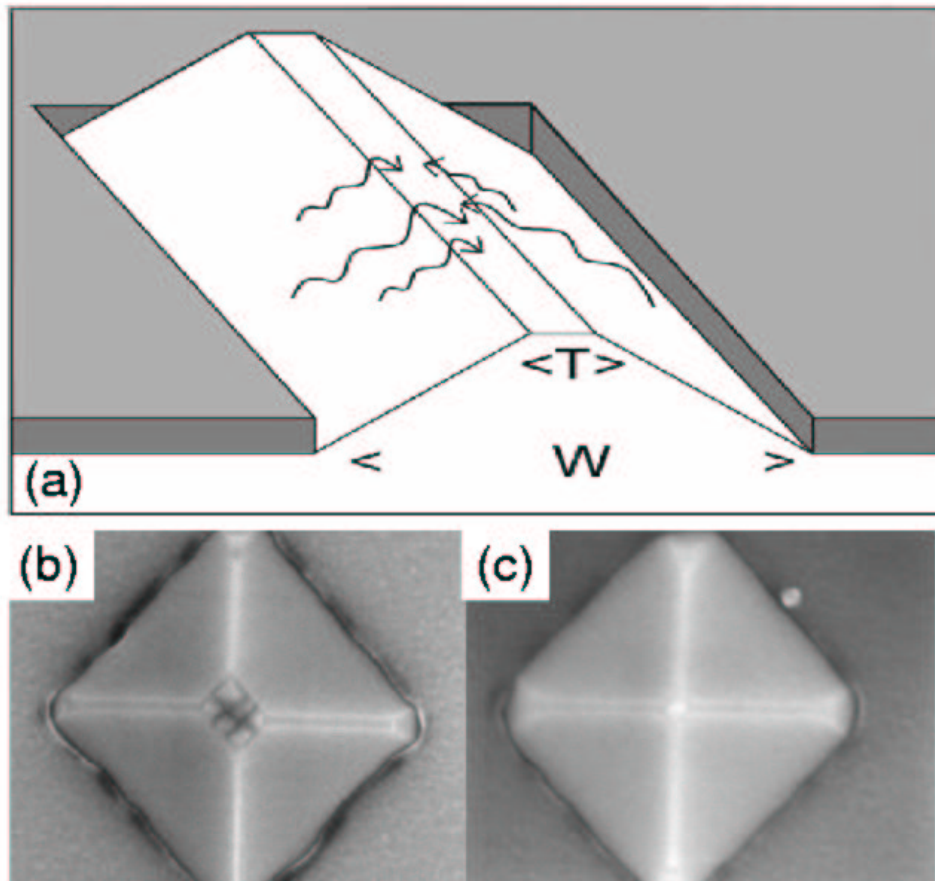


Figure 1.8: (a) Schematic illustration of the diffusion process in the growth on patterned substrates. This process leads to formation of templates, on top of which several (b) or only one quantum dot (c) can be grown. In these scanning electron microscopy images the base of the pyramid is 400 nm long (Adapted from Ref. [130])

adsorbs only in the openings. The substrate grows forming ridges or pyramids with walls corresponding to low-index crystallographic planes. This growth is continued until the width T of the area on top of the ridge is narrow enough to contain only one or two QDs. At this point the growth of the substrate is stopped, and deposition of the QD material begins. The QD material does not adsorb on top of the mask, and diffuses onto the sides of the ridge. However, the adsorption rate of the material to the substrate in this crystallographic orientation is very low. The deposited atoms continue diffusing across the structure, as shown in Fig. 1.8(a), until they reach the top of the pattern, where they finally adsorb.

Upon reaching the critical thickness the Stranski-Krastanow transition takes place, which leads to the growth of SADs on top of the pattern. As demonstrated in Fig. 1.8(b) and (c), the number of grown SADs depends on the size of the plateau. By careful engineering and growth control of the ridge it is possible to localise precisely one InAs SAD on top of the InP pyramid.

As mentioned before, QDs grown by self-assembly have diameters of order of a few tens of nanometres, and heights of a few nanometres. For typical materials used for barriers and dots, the depth of the confinement potential in the conduction band (or the height of the wall of the “quantum box”) is of order of 600 - 800 meV. This means in practice that the lateral confinement of the QD is strong, and its single-particle energy spectrum consists of a small number of levels (typically fewer than 15), usually grouped into degenerate shells; the energy gaps between shells are of order of tens of meV. Introduction of charge carriers into such QDs can be achieved by optical excitation, but also by introducing doping in the barrier. The latter technique allows to fill QDs with electrons (or holes, depending on the kind of doping) without illumination. These systems are then ideal to study formation, dynamics and recombination of excitons and neutral or charged excitonic complexes (for reviews and references on that subject, see Refs. [62, 85]). Another important area of fundamental research involves enclosing such excitonic QDs in photonic cavities. In so

doing, both excitonic and photonic modes are confined and strongly coupled to each other (this is the Purcell effect [46]; for additional review and references see Ref. [55]).

The rapid progress in fabrication technologies of SADs is also driven by their possible applications, particularly in quantum optics. Single self-assembled QDs are used as detectors of infrared radiation (quantum dot infrared photodetectors, QDIPs) [10, 76], optical memories [97], single-photon sources [86, 88, 108] important for quantum cryptography [18, 24]. Arrays of SADs are also used as optically active regions in high-efficiency lasers. To date, successful prototypes of QD lasers have been demonstrated to work with low injection currents and high quantum efficiency even at room temperatures [42]. There are also proposals to use the intraband transitions in coupled QDs to generate terahertz radiation [5, 6, 131].

1.3.3 Quantum rings

I shall now describe another structure capable of confining electrons and holes, but with a topology different than that of the SADs - a quantum ring. The ring geometry is of interest, because it allows to access and manipulate the phase of a charge carrier confined in it by an external magnetic field, applied in parallel to the rotational axis of the system. As I will show later in this Thesis, this leads to the appearance of persistent currents and Aharonov-Bohm oscillations of the system's energy as a function of the number of flux quanta threading the ring.

Quantum ring nanostructures can be fabricated using self-assembly techniques [78], but here I will describe another method, involving lithography and etching. This is because I shall compare the results of my theoretical treatment of the many-body systems in the ring geometry to measurements performed on nanostructures obtained using this technique. My description follows that presented by Bayer *et al.* in Ref. [15]. A scanning electron micrograph of the sample is shown in Fig. 1.9(a). The inner radius of the sample is about 15 nm, while the outer radius is 45 nm. Composition of this sample is shown

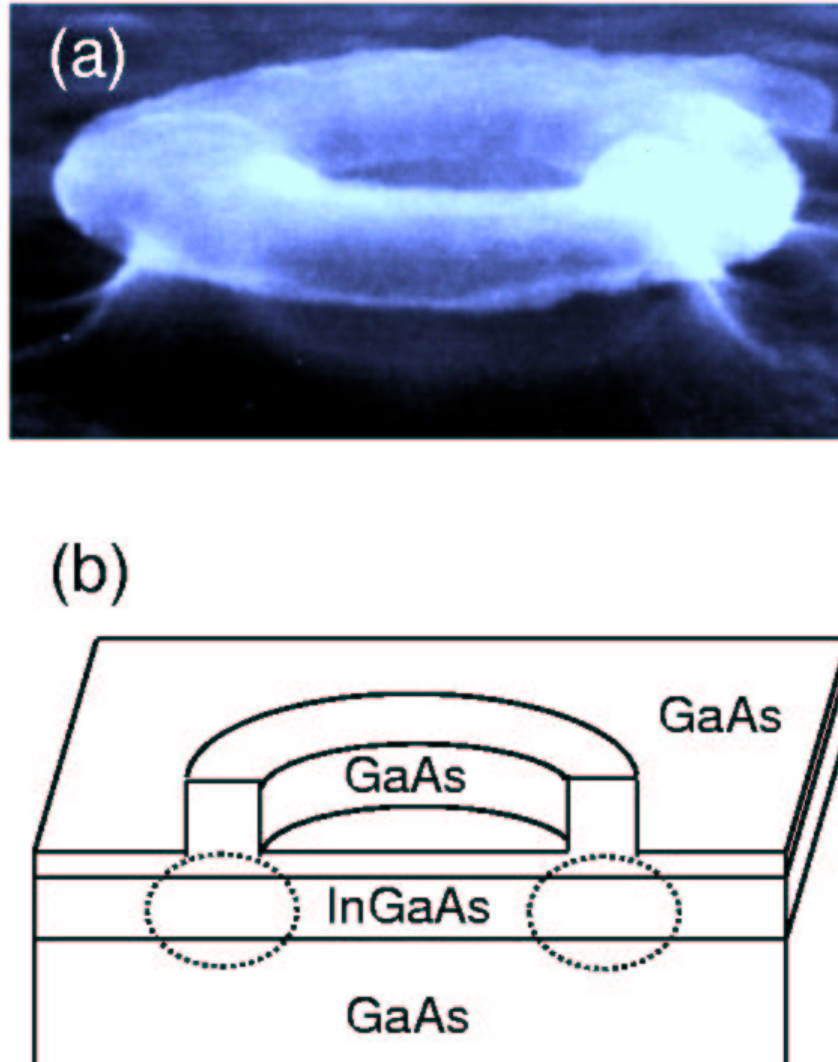


Figure 1.9: (a) Scanning electron micrograph of the quantum ring structure. The circular shape seen on top is the metallic mask produced by lithography before etching. (b) Schematic diagram of the structure; the carriers are confined in the areas marked by circles (Adapted from Ref. [15])

schematically in Fig. 1.9 (b).

To create the disk confinement, a 7-nm-thick layer of the $\text{In}_{0.1}\text{Ga}_{0.9}\text{As}$ quantum well material is lithographically deposited on top of the GaAs barrier material, and then capped by a 20-nm-thick layer of GaAs. Then, a ring-shaped metallic mask is deposited lithographically on top, and the structure is processed with etching. The etching removes only the GaAs material not covered by the mask and is stopped before reaching the InGaAs layer, so that the quantum well material is covered by a thin capping layer of GaAs everywhere except under the mask, where the GaAs layer is thick.

Let us now describe how the lateral confinement is formed. In regions where the GaAs layer was etched, the band profile along the vertical direction corresponds to an InGaAs quantum well with asymmetric barriers: on the bottom side of the well we have the GaAs material, but on the top side we have a very thin layer of the barrier material followed by vacuum. On the other hand, in the region underneath the GaAs ring the InGaAs well has a symmetric profile, being surrounded by a thick layer of GaAs material on both sides. The difference in height of the top barrier (very high in the etched area, lower under the GaAs cap) and the additional strain field produced by the GaAs ring creates a shallow lateral confinement, with a height of a few tens of meV, inside the InGaAs well. Note that the carriers are confined *not* in the ring structure seen in Fig. 1.9 (a), but rather underneath it (in the regions marked with circles in Fig. 1.9 (b)).

The control over ring radius R in the experiments with magnetic field is of particular importance. I will show in Section 2.3 that the magnetic field enters the single-particle energies in the system through the number of flux quanta $N_\phi \sim \pi R^2 / \pi \ell^2$, where $\ell \sim 1/\sqrt{B}$ is the magnetic length. Thus N_ϕ depends linearly on the magnetic field, but the proportionality coefficient scales as R^2 . For rings with large radii it is thus sufficient to use small magnetic fields to obtain large values of N_ϕ . On the other hand, the radii should be sufficiently small to produce distinct quantisation of single-particle energy levels. The rings fabricated by lithography and etching can be easily engineered to satisfy all these

conditions, since their radii can be naturally varied over a wide range by depositing a smaller or larger metallic mask. However, the existence of open surfaces appears to worsen the optical quality of the structures. This problem does not appear in self-assembled rings [78], but here the control of their shapes and sizes is much more difficult.

1.4 Spectroscopy

In the previous Sections I have described how the semiconductor quantum dots are created and how they can be populated with carriers. I will now move on to describing how these systems can be probed experimentally and how to interpret the results of these measurements. Understanding of these issues is important, since I seek experimental verification of my theories.

In this Section I shall describe two spectroscopic techniques. The first one - the photoluminescence spectroscopy - is used to study the electron-hole systems confined in quantum dots and rings. The second technique - the tunnelling current spectroscopy - is used to probe the many-electron systems confined in gated quantum dots, and I will discuss it in the particular case of the lateral QD design.

1.4.1 Photoluminescence experiment

As already mentioned, the self-assembled QDs and quantum rings are typically capable of confining both electrons and holes. That is why the experimental tool most commonly used in their study is photoluminescence (PL) spectroscopy. Here I shall describe only its fundamental principles; the interested reader will find reviews and references in Ref. [62, 85].

In order to obtain the PL signal, the QD must be first populated with electron-hole pairs (excitons). This is achieved by illuminating the sample with photons, whose energy is sufficient to promote electrons from the valence band to the conduction band in the barrier

material. Electrons and holes thus created diffuse across the sample and become confined in QDs, creating a system of many, strongly interacting charge carriers of both signs. The number of carriers trapped inside the QD depends on the power of the exciting laser. These complexes have a finite lifetime, since electrons will recombine with holes to lower the total energy of the system. In the absence of non-radiative recombination centres, such as impurities, the electron-hole pairs recombine radiatively, emitting photons, which are detected.

Information about the properties of the many-exciton system is obtained from the analysis of energies of the emitted photons. The emission spectrum of a dot with N excitons is given in by the Fermi's golden rule, which, in the dipole approximation, can be written as

$$A(\omega, N, i) = \frac{2\pi}{\hbar} \sum_f |\langle f, (N-1) | e\hat{\mathbf{e}} \cdot \mathbf{r} | i, N \rangle|^2 \delta(E_i - E_f - \hbar\omega), \quad (1.10)$$

where $\hat{\mathbf{e}}$ is the polarisation of the photon. Here, $|i, N\rangle$ denotes the initial state of the N -exciton system. On the other hand, $|f, (N-1)\rangle$ denotes the final state of the $N-1$ -exciton system, which remains after the recombination of a single exciton. Note that the state $|f, (N-1)\rangle$ can be the ground state or one of the excited states of $N-1$ excitons. Due to the delta function in the above formula, the energy $\hbar\omega$ of detected photons, or the position of the PL peak on the energy axis, is equal to the energy difference between the initial state $|i, N\rangle$ and one of the final states $|f, (N-1)\rangle$.

The dipole matrix element present in the above formula gives the intensity of each emission line. The magnitude of this element depends on the initial and final wave functions of the system. Thus, the height of PL peaks provides information about the symmetries of many-particle wave functions, complementing the information about their energy, derived from peak positions.

The PL spectroscopy of single QDs is described in great detail in articles by Bayer *et al.* [16] and Hawrylak [50]. In these papers the authors model the systems of interacting electrons and holes in the absence of the magnetic field, and identify how these interac-

tion manifest themselves in PL spectra. A detailed analysis of interactions in excitonic artificial atoms in a magnetic field is given in Ref. [34], where the magnetic-field-induced degeneracies in the single-particle energy spectrum allow the study of interactions in the context of the so-called “hidden symmetries”.

1.4.2 Tunnelling experiment

Let us now move on to describing the tunnelling current spectroscopy. This technique is used to examine the properties of many-electron gated quantum dots, and I shall describe how it is applied to lateral devices.

In Section 1.3.1 I have described that the lateral QD is created electrostatically by locally depleting the 2DEG of electrons. The 2DEGs on either side of such local lateral confinement are reservoirs of electrons. Upon application of a small voltage across the device, the electrons from, say, the left lead - the source - can tunnel into the dot, then tunnel out on the other side of the device and be collected by the other 2DEG - the drain. Since the tunnelling electron experiences the repulsion of all electrons already confined in the dot, this type of spectroscopy is called the Coulomb blockade (CB) spectroscopy. A detailed review of this experimental technique can be found in Ref. [69], here I shall only summarise its most important properties. My description follows that of Sachrajda *et al.* in Ref. [107].

In Fig. 1.10 I present a schematic diagram of the lateral quantum dot device. The two tall tunnelling barriers are created by the side gates of the lateral device. The plunger gate, represented by the voltage symbol V_P , is used to adjust the confinement of the dot, thereby shifting the QD states with respect to the Fermi energy μ_L of the source S and drain D .

Inside the dot there are several states lying below the Fermi level of the leads and occupied by electrons (full circles), and several states lying above μ_L and unoccupied (empty circles). In the simple charging model, the gap between the last occupied and the

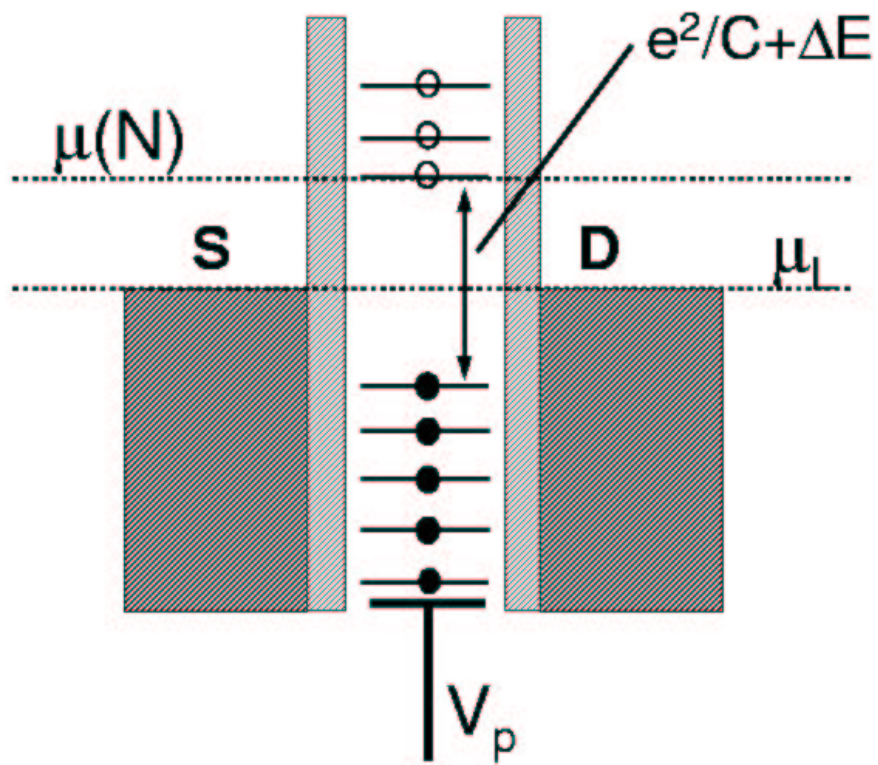


Figure 1.10: Schematic representation of energy levels in the lateral quantum dot (see text for details) (Adapted from Ref. [107])

first unoccupied QD level is equal to $e^2/C + \Delta E$, where C is the total capacitance of the QD. The capacitance C describes the effects of interactions of electrons inside the dot with each other and with the environment. Thus, if one wants to add another electron into the dot, one has to overcome the charging energy e^2/C . In lateral devices considered here this energy dominates the energy landscape of the system. The energy ΔE reflects the characteristic properties of the QD spectrum, and contains terms due to the discrete nature of QD single-particle states, effects of exchange and correlations. The goal of this technique is to examine the dependence of this term on the parameters of the system: confinement, external magnetic field, number of electrons.

Let us now formulate the conditions that have to be fulfilled for the current to flow. Let us denote the total energy of the system of n electrons in the left lead (the source) by $E_L(n)$, and the total energy of the system of N electrons in the quantum dot by $E_{QD}(N)$. The tunnelling of a single electron will be observed only if in this process the total energy of the leads plus total energy of the QD is conserved, i.e., when

$$E_L(n) + E_{QD}(N) = E_L(n-1) + E_{QD}(N+1). \quad (1.11)$$

Upon rearranging the terms in the above equation one gets

$$E_L(n) - E_L(n-1) = E_{QD}(N+1) - E_{QD}(N). \quad (1.12)$$

The left-hand side of this equation is the electrochemical potential of the lead: $\mu_L(n) = E_L(n) - E_L(n-1)$. Since the lead contains a very large number of electrons (of order of 10^{11}), this quantity does not depend on the number of electrons: $\mu_L(n) \equiv \mu_L$.

The right-hand side of the equation (1.12) is the electrochemical potential of the QD: $\mu_{QD}(N) = E_{QD}(N+1) - E_{QD}(N)$. It depends on the energy of the initial state of the system (with N electrons) and on the energy of its final state (with $N+1$ electrons), and thus carries information about the many-particle properties of the system of many interacting electrons confined in the device. The electrochemical potential $\mu_{QD}(N)$ is a discrete function of the number of electrons and a smooth function of the plunger gate

voltage V_P .

Let us now consider the alignment of energy levels presented in Fig. 1.10. In this case the electrochemical potential of the lead falls in the middle of the Coulomb gap between QD states. Thus the current cannot flow due to the Coulomb blockade. However, by tuning the plunger gate voltage V_P the electrochemical potential $\mu_{QD}(N)$ of the QD can be shifted down, and, for some gate voltage, aligned with the Fermi level μ_L of the leads. If this alignment is achieved, one electron from the source can tunnel back and forth through the left barrier. In the Fig. 1.10, to the right of the QD we also see the drain, whose Fermi energy is equal to that of the source. Therefore, upon alignment of all electrochemical potentials the electron will be able to tunnel from the source through the dot to the drain. If a small voltage is applied across the device (between the source and the drain), this tunnelling can be detected as a current flowing through the dot. Thus, if the current is measured as a function of the plunger gate voltage, one registers a series of peaks for voltages V_P , for which the electrochemical potentials are aligned. In such instances the number of electrons on the dot is undetermined. For the intermediate voltages, for which the condition (1.12) is not satisfied, the current is blocked, and the QD contains a well-defined number of electrons.

A typical addition spectrum, i.e., the current measured as a function of the gate voltage, and additionally as a function of the magnetic field, is presented in Fig. 1.11. The gate voltage is shown on the vertical axis, and the magnetic field - on the horizontal axis. One sees a collection of lines, denoting peaks of the tunnelling current. Each consecutive line marks the fulfilment of the tunnelling condition for the QD electrochemical potential $\mu_{QD}(N)$ with one more electron confined in the dot. The lines exhibit a series of features (kinks), which are signatures of changes of the ground state of the N -electron dot or of the $N + 1$ -electron dot. My goal is to reproduce this structure of kinks theoretically.

Before I conclude this description, I shall mention two possible modifications of this experimental technique. I have described the principles of the CB spectroscopy in the

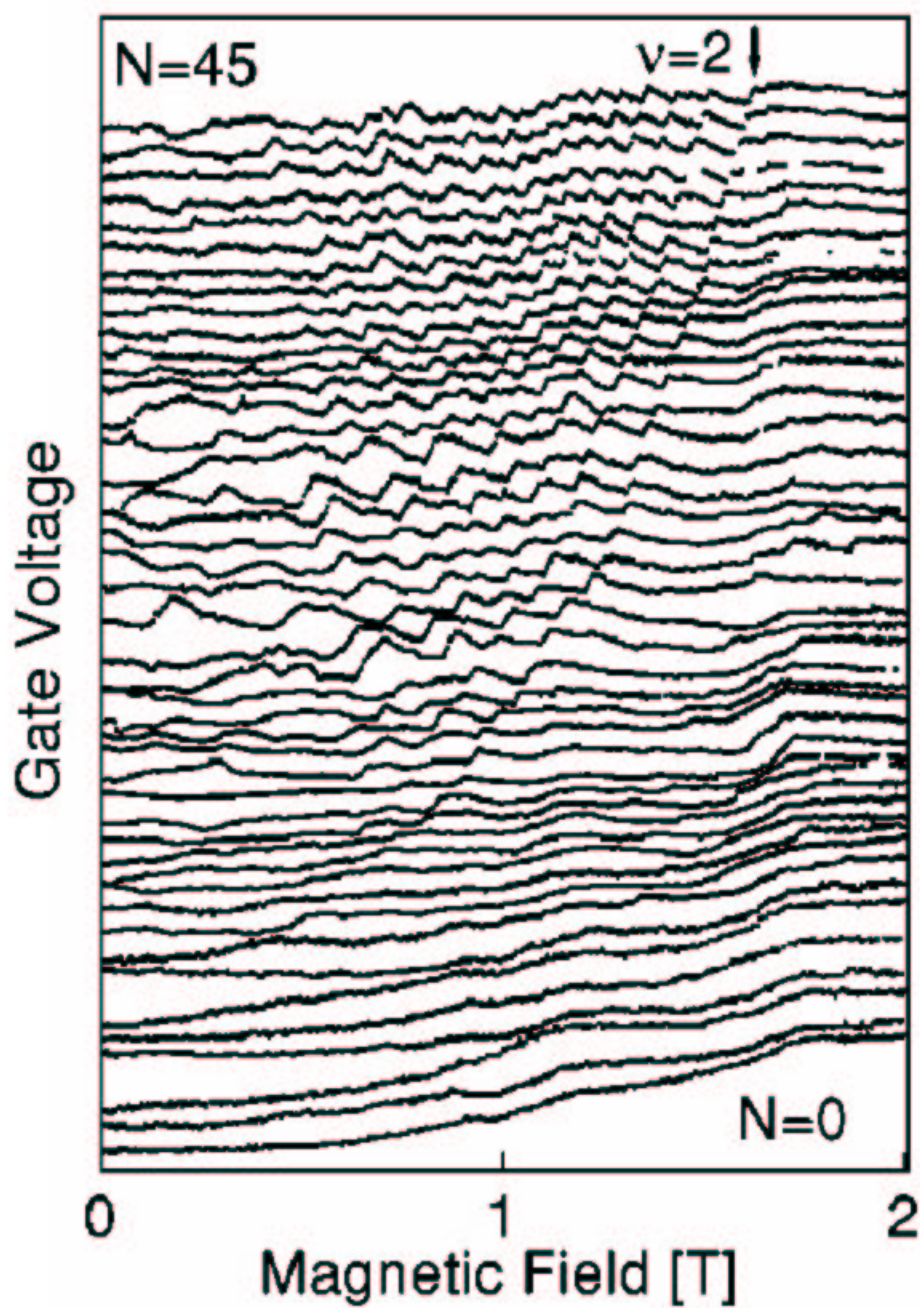


Figure 1.11: A typical addition spectrum of a gated quantum dot shown as a function of the magnetic field. Forty-five Coulomb blockade peaks are shown, with the charging energy manually removed (From Ref. [32])

low source-drain voltage regime, since I have assumed that the Fermi level of the source was aligned with the Fermi level of the drain. In this mode the tunnelling electron probes only the ground state of the $N + 1$ -electron dot. The spectrum presented in Fig. 1.11 was measured exactly in this mode, with the source-drain voltage of order of several μeV . However, a larger voltage (but smaller than the charging energy e^2/C) can also be applied across the QD. In this case the electron tunnelling from the source will probe not only the ground state, but also the excited states of the system. Also, on tunnelling from the QD to the drain, the electron may leave the N -electron dot in its ground or excited state. I shall compare my results to an experiment performed in this mode in one of the main chapters of this Thesis.

Up to now I have considered the electron tunnelling through the dot as a charged particle, experiencing the Coulomb repulsion from all the electrons confined in the dot. But this particle also has spin, and, as I have described in Section 1.3.1, in the case of lateral devices in an external magnetic field the tunnelling current consists predominantly of electrons with the same spin (say, spin down). In this case the fulfilment of the condition (1.12) is necessary, but not sufficient for the current to flow. The electrons will be able to tunnel onto the QD only if the final state of the $N + 1$ -electron dot can be created from the initial state of the N -electron dot by adding one electron spin down. If it is not possible, the current will not flow, and this phenomenon is called spin blockade. In practice the tunnelling current is not completely spin-polarised, and instead of the full spin blockade one only sees a modulation of the amplitude of the current. But this is sufficient to derive information about the spin of the system, which is complementary to that obtained from the positions of the CB peaks. Results of the spin-blockade experiments will also be discussed in this Thesis.

1.5 Electronic correlations in QDs: overview of the field and scientific contributions of this thesis

In the previous Sections I have defined the main subject of this Thesis: systems of many strongly interacting particles confined by semiconductor nanostructures. In particular, I am interested in identifying the manifestations of correlations, which requires a nonperturbative treatment, and comparing them to those of the direct and exchange Coulomb interactions, which can be captured by simpler mean-field approaches. I choose to treat interacting systems confined in nanostructures, because these systems can be probed experimentally both in the regime of strong and weak interactions, which allows to obtain experimental verification of my theories. This is possible because the properties of the atomic-like QD spectrum (in the language of quantum chemistry) or, equivalently, the QD DOS (in the solid-state terminology) can be *engineered*. There are several degrees of freedom: one can, within certain limits, change QD dimensions and symmetry, thereby influencing the energy separation and degeneracy of the single-particle states (separation and height of the DOS peaks) [11, 70, 105]. By building higher dots one can also bring the states belonging to the second vertical subband down in energy, thereby introducing new symmetry elements into the spectrum [58]. By choosing appropriate materials for the barrier and the well, one can tune the band offsets, thereby influencing the depth of the confinement, which gives control over the QD wave function penetration inside the barrier. Positioning two or more QDs close to each other allows for their quantum-mechanical coupling and leads to formation of an artificial molecule [2, 14, 96, 106, 114]. Finally one can also fill some types of QDs with a precisely known number of electrons. I will proceed by analysing the properties of the system of confined interacting particles as a function of these parameters, calculating characteristic quantities that can be measured, and comparing my results to the available experimental data, if such data exist. But, before I move on to discussing my results, I shall present a brief overview of the state of

scientific knowledge on the subject.

Collective behaviour of particles in strongly interacting systems leads to a number of nontrivial phenomena, from magnetism to superconductivity. Because of that it is not surprising that significant theoretical and experimental attention has been devoted to them for many years. Interest in collective phenomena in structures with lowered dimensionality has been particularly strong since 1982, when Tsui, Störmer, and Gossard [124] observed the appearance of unusual features in transport spectra of the two-dimensional electron gas under a magnetic field, interpreted as a new state of matter, whose appearance is due to electronic correlations. This effect, named fractional quantum Hall effect (FQHE), was intensively studied, both theoretically and experimentally (for reviews and references see a recent paper by Murthy *et al.* [89]). Here I shall mention two papers, written by Robert Laughlin [72], which opened the way towards theoretical understanding of the system and won their author the Nobel prize in 1998. In these papers the three-electron problem in a strong magnetic field is solved exactly with the assumption of a truncated Hilbert space. This solution is further extrapolated in a variational manner to systems with more electrons. As a result of these calculations, Laughlin postulated the existence of so-called incompressible correlated electronic states. He discusses one case in detail - the filling factor $\nu = 1/3$ phase, or, in other words, the case in which there are three magnetic flux quanta per each electron. In the words of Laughlin, these incompressible ground states of the system are “new states of matter”, and they are somewhat reminiscent of the superconducting state in that they enable a dissipationless electrical conductivity. Laughlin predicted a series of such states decreasing in density and terminated by the Wigner crystalline phase.

Research into correlations in zero-dimensional nanostructures - quantum dots and rings - proceeds in several directions.

One direction of research involves examining properties of an N -electron system confined in a QD at zero magnetic field. The control parameter in this research is the ratio λ

of characteristic single-particle energy gaps to characteristic interaction energies, already defined in the beginning of this Thesis. Calculations in this domain were carried out using exact diagonalisation for $N = 3, 4$ [36, 87], and quantum Monte Carlo [40], spin density functional [102], and unrestricted Hartree-Fock theories for larger systems [133]. Mikhailov [87], for instance, finds that tuning the interaction parameter λ results in changes in the ground state of the three-electron system in a parabolic dot. If λ is sufficiently small, i.e., if the single-particle energy quantisation dominates the energy spectrum of the system, the ground-state configuration can be constructed by distributing the quasi-particles dressed in interactions on single-particle QD orbitals, subject only to the Pauli exclusion principle. In this regime the ground state of the three-electron system has total spin $S = 1/2$, since two electrons are placed on the lowest single-particle state with opposite spin, and one unpaired electron is confined on the first excited single-particle state. However, there exists a critical value λ_c of the interaction parameter, for which Mikhailov finds a transition in the QD ground state. The new ground state has maximal total spin possible, $S = 3/2$, and has the nature of a rotating Wigner molecule. This is demonstrated by examining the electronic pair correlation function, which appears to suggest that the electrons assume positions in the corners of a rotating equilateral triangle. Similar results are also obtained for larger systems [40, 102, 133]. I shall analyse transitions similar to those mentioned above, i.e., transitions from weakly correlated to strongly correlated phases of an electronic droplet as a function of the system parameters and the size of the Hilbert space in Chapter 4.

Wigner crystallisation is also observed in the presence of the magnetic field [48, 90, 119, 134]. Of particular interest is the case of the so-called maximum-density droplet (MDD), i.e., the system, in which all electrons are spin-polarised and occupy the consecutive single-particle orbitals on the lowest Landau level (in the language of the integer QHE, this is the $\nu = 1$ state). It has been shown [80], that this state is the ground state of the system for a finite region of magnetic fields. If the magnetic field becomes too low, electrons start

populating the Landau level with spin up. However, if the magnetic field is increased beyond the stability of MDD, holes appear in the centre of the dot, and the charge density of the system assumes the shape of a ring (falls to zero in the QD centre). This phenomenon was considered from the point of view of the Wigner crystallisation [48, 119]. In a study of pair-distribution functions derived from the ground states of QDs in high magnetic field, it was found that the structure of electronic quantum Wigner molecules is similar to the lowest-energy configurations expected for classical charged particles.

The second broad direction of research involves studies of magnetic-field evolution of electronic quantum dots. In the literature there is a large number of publications on the subject, presenting results of calculations carried out both at zero and finite magnetic fields using various methods: mean-field Hartree-Fock [17, 134], density-functional theory [11, 59, 75, 111, 128], quantum Monte Carlo [22, 49], and exact diagonalisation [54, 83]. All these methods suggest that for QDs with an even number of electrons there exists a region of magnetic fields, in which the ground state of the system is the so-called $\nu = 2$ spin-singlet phase in the terminology of the integer quantum Hall effect. Now, as the magnetic field is increased, one observes transitions in the ground state of the QD: electrons flip their spin one by one and the radius of the droplet increases until the fully spin-polarised maximum-density droplet is formed. If the magnetic field is increased even further, one expects the formation of QD-equivalents of incompressible states, discussed earlier in the context of the fractional quantum Hall effect. The sequence of spin flips can be completely understood without correlations, using simple arguments based on the competition between the single-particle energy quantisation and the interaction energies (direct and exchange). However, if correlations are taken into account, this sequence of phases turns out to be richer: the total spin of the system does not increase in the steplike manner, but rather exhibits oscillatory behaviour: each spin-flip event is preceded by a complete spin depolarisation. Similar spin oscillations take place also in the regime of magnetic field beyond the stability of the MDD: transitions between incompressible states

(fully polarised) are preceded by spin depolarisations. I find two theoretical treatments of these effects. First, presented by Imamura *et al.* [61], treats the correlated electron states in QDs as “electron molecules”, which leads to interpretation of electronic spin wave functions as spin configurations in molecules, including the so-called resonating valence-bond states. The second treatment, put forward by Oaknin *et al.*, [91], describes the spin-depolarised states as spin-texture excitations (skyrmions), carrying topological and real charge equal to one. Excitations of the electronic droplet are thus charged skyrmions, which the authors express as condensates of interacting spin excitons. I shall discuss these phenomena in detail using the language of exact diagonalisation. This description, initiated by Hawrylak *et al.* in Ref. [53], will also include a discussion of stability of the correlated, spin-depolarised phases as a function of the system parameters (number of electrons, strength of confining potential, etc.). At this point I shall mention that in the experiments reported in literature the effects of direct and exchange Coulomb interactions were clearly identified [31, 33, 92, 121, 122], but, to the best of my knowledge, the spin depolarisations due to electronic correlations have not been accounted for. It is only in recent research, carried out by the Quantum Physics Group and the Quantum Theory Group (with the author of this thesis as a member) at the IMS NRC that these spin oscillations were clearly identified and traced back to the correlated behaviour of electrons confined in the lateral gated QD device (see Chapter 5).

Finally, the third research direction involves a specific type of correlations, manifesting itself in entangled states of systems of particles. The issue of entanglement is of particular interest for the rapidly developing field of quantum computation (see e.g. [43]). In quantum computers information is stored and processed using quantum bits (qubits), the quantum counterparts of classical bits. The difference between these two is such that classical bits can only store two states: $|0\rangle$ or $|1\rangle$, while qubits can be in any linear superposition $\alpha|0\rangle + \beta|1\rangle$, subject only to normalisation constraints. But information stored in the form of such quantum state has to be processed using quantum principles as well.

This is accomplished with quantum logic gates, built out of two coupled qubits; ability to perform single- and two-qubit operations is sufficient to build a quantum computer. It is said that the state of the system is *entangled*, if the total state of the array of qubits cannot be written as a simple tensor product of states of each individual qubit. If one-electron gated quantum dots are taken as qubits, as suggested by Loss and DiVincenzo [39, 79], the state of an array of such coupled qubits is thus a highly correlated state of many electrons. In this work I shall explore a different qubit design: as two qubits I will take an electron and a hole, both confined in the same double-dot structure, consisting of two vertically coupled self-assembled dots. I will show that the entanglement is created in such systems by the Coulomb electron-hole interaction (Chapter 6).

I shall also analyse the electron-hole correlations outside the context of quantum computation. In Chapter 7 I shall consider the problem of a negatively charged exciton (X^- , composed of two electrons and one hole) confined in a quantum ring and subject to an external magnetic field directed along the rotational axis of the ring. It is well known that the ground state energy of a single electron in this geometry exhibits the Aharonov-Bohm oscillations (for reviews and references see Ref. [27]). The X^- complex is charged (carries the charge of an electron), so one would expect this complex to exhibit the Aharonov-Bohm oscillations as well. As I shall demonstrate, this is true in the regime of weak interactions, i.e., when the radius of the ring is sufficiently small. In the regime of strong interactions the electron-hole correlations lead to suppression of the Aharonov-Bohm oscillations of X^- . Of interest is thus a photoluminescence experiment, in which the X^- complex recombines, emitting one photon and leaving one electron still confined in the ring. When calculated as a function of the magnetic field, the energy of such photon exhibits clear Aharonov-Bohm oscillations due to the oscillatory character of the energy of the final-state electron. Thus one can observe *optically* the oscillations of the energy of the *single electron*, and this is possible only due to the correlated character of the X^- complex.

However, before I can move on to considering all these problems, I must carefully introduce the tools of my analysis. I start by calculating the single-particle states of nanostructures with various geometries: parabolic and disk-shaped QDs and the quantum ring. Then I shall move on to describing selected computational methods of many-body physics capable of capturing the correlation effects. My method of choice is the exact diagonalisation technique. This approach involves three steps: construction of a basis set of the Hilbert space, writing the Hamiltonian in this basis in a matrix form, and numerical diagonalisation of this matrix. I shall describe each of these steps in detail. I shall also compare the exact diagonalisation with other computational techniques, such as the spin density functional theory and the quantum Monte Carlo approach.

Chapter 2

Single-particle states in typical quantum-dot confinements

Before I can move on to describing the many-particle properties of QDs, I first need to understand their single-particle spectra. In Chapter 1 I have shown that QDs can be fabricated in a variety of sizes and shapes, and the lateral confinement produced by each of them possesses its own characteristic symmetry properties. Detailed calculations, fully accounting for all the details of particular structures, are complicated and require large computational effort [26, 28, 70, 99, 112]. In this work, however, I shall approximate the complicated QD confinements by model potentials, capturing the fundamental physics, but at the same time making it possible to understand it in simple terms. I shall consider three fundamental classes of “ideal” QD geometries: (i) parabolic QDs, (ii) disk-shaped QDs, and (iii) quantum rings. It turns out, in fact, that these potentials are reasonably good approximations of the real QD potentials, so much so that in most cases it is sufficient to treat the peculiarities of each QD as small perturbations to the ideal shape [34, 70]. The two-dimensional parabolic potential is commonly used in modelling of gated quantum dot devices, both vertical [92, 121, 122] and lateral [31, 32, 33]. It has

also been successfully applied to lens-shaped self-assembled QDs (obtained without using the indium-flush technique) [34, 50, 57]. In this work, however, when talking about SADs I shall refer to the indium-flushed structures, whose geometry is approximated better by the disk-shaped potential. Finally, when discussing the quantum ring geometry I shall assume that this ring is of infinitesimal thickness, i.e., it is a one-dimensional circular system. This Chapter is devoted to describing and comparing the single-particle energy spectra of these three fundamental lateral confinements.

2.1 Parabolic lateral confinement

First I consider two-dimensional parabolic confinement in the presence of an external magnetic field $\mathbf{B} = [0, 0, B]$ perpendicular to the plane in which the potential is defined (by default, the XY plane). The Hamiltonian of a single electron in this case attains the following form:

$$\hat{H} = \frac{1}{2m^*} \left(\hat{\mathbf{p}} + \frac{e}{c} \hat{\mathbf{A}} \right)^2 + \frac{1}{2} m^* \omega_0^2 r^2 - g \mu_B B \sigma, \quad (2.1)$$

where m^* and e is the electron's effective mass and charge, respectively ($e > 0$; the negative sign of the charge is accounted for by the “+” sign in the first term), c is the velocity of light, and ω_0 is the characteristic frequency of the confining potential (CGS units are used). The last term of this Hamiltonian is the Zeeman term, with g being the Landé factor, $\mu_B = e\hbar/2m_e$ - the Bohr magneton, and $\sigma = \pm\frac{1}{2}$ - the z component of the electronic spin. Since the Zeeman term depends only on the spin component of the electronic wave function, I shall neglect it in the following calculations, and return to it in the discussion of results.

The problem at hand has been solved by Fock [44] and Darwin [37], and this is why the single-particle energy spectrum of such a parabolic potential is called the *Fock-Darwin spectrum*. The cited authors solved the Schrödinger equation with the Hamiltonian (2.1) in real space. I shall follow a different path, involving the harmonic-oscillator raising and

lowering operators. My description is similar to that given in Refs. [51, 62, 127].

To proceed I must first define the form of the vector potential \mathbf{A} . I choose the symmetric gauge: $\mathbf{A} = [-By/2, Bx/2, 0]$. To prove that this potential indeed corresponds to the vertical magnetic field \mathbf{B} as specified above, I calculate

$$\nabla \times \mathbf{A} = \begin{vmatrix} \hat{i} & \hat{j} & \hat{k} \\ \frac{\partial}{\partial x} & \frac{\partial}{\partial y} & \frac{\partial}{\partial z} \\ -By/2 & Bx/2 & 0 \end{vmatrix} = \hat{k}(B + B)/2 = [0, 0, B]. \quad (2.2)$$

Let us expand the expression $(\hat{\mathbf{p}} + \frac{e}{c}\hat{\mathbf{A}})^2$ using the above vector potential:

$$\left(\hat{\mathbf{p}} + \frac{e}{c}\hat{\mathbf{A}}\right)^2 = \hat{\mathbf{p}}^2 + \frac{eB}{2c}(-p_x y + p_y x) + \frac{eB}{2c}(-y p_x + x p_y) + \frac{e^2 B^2}{4c^2}(x^2 + y^2).$$

Let us now define the cyclotron frequency $\omega_c = eB/m^*c$ (for GaAs, the cyclotron energy $\hbar\omega_c \approx 1.728$ meV for the magnetic field $B = 1$ T, and scales linearly with the field).

Taking into account that $yp_x = p_x y$ and $xp_y = p_y x$, I get

$$\left(\hat{\mathbf{p}} + \frac{e}{c}\hat{\mathbf{A}}\right)^2 = \hat{\mathbf{p}}^2 + \frac{1}{4}(m^*)^2 \omega_c^2 \mathbf{r}^2 + m^* \omega_c \hat{l}_z,$$

where $\hat{l}_z = p_y x - p_x y$ is the z -th component of the angular momentum operator. The Hamiltonian can be now written in the following form:

$$\hat{H} = \frac{1}{2m^*} \hat{\mathbf{p}}^2 + \frac{1}{2} m^* \left(\omega_0^2 + \frac{1}{4} \omega_c^2 \right) \mathbf{r}^2 + \frac{1}{2} \omega_c \hat{l}_z. \quad (2.3)$$

Using the notation $(\omega_0^2 + \frac{1}{4} \omega_c^2) = \omega_h^2$ (“hybrid frequency”), I get

$$\hat{H} = \frac{1}{2m^*} \hat{\mathbf{p}}^2 + \frac{1}{2} m^* \omega_h^2 \mathbf{r}^2 + \frac{1}{2} \omega_c \hat{l}_z. \quad (2.4)$$

Let us further introduce complex variables:

$$z = x - iy, \quad z^* = x + iy;$$

$$\partial_z = \partial_x + i\partial_y, \quad \partial_z^* = \partial_x - i\partial_y;$$

and write the position and gradient in their terms:

$$x = \frac{1}{2}(z + z^*), \quad y = \frac{1}{2i}(z^* - z);$$

$$\partial_x = \frac{1}{2}(\partial_z + \partial_z^*), \quad \partial_y = \frac{1}{2i}(\partial_z - \partial_z^*).$$

It is straightforward to see that $x^2 + y^2 = zz^*$ and $\partial_x^2 + \partial_y^2 = \partial_z \partial_z^*$. Since $\hat{\mathbf{p}}^2 = -\hbar^2(\partial_x^2 + \partial_y^2)$, the Hamiltonian in the new coordinates attains the form:

$$\hat{H} = -\frac{\hbar^2}{2m^*}(\partial_z \partial_z^*) + \frac{1}{2}m^*\omega_h^2(zz^*) - \frac{1}{4}\hbar\omega_c(z\partial_z - z^*\partial_z^*). \quad (2.5)$$

Next step is to define a unit length characteristic for this potential. I take $\ell = \sqrt{\frac{\hbar}{2m^*\omega_h}}$. Note that in zero magnetic field $\omega_h = \omega_0$ and $\ell_{B=0} = \sqrt{\frac{\hbar}{2m^*\omega_0}}$. In the absence of the parabolic confinement, but in the presence of the magnetic field, I get $\ell_B = \sqrt{\frac{\hbar}{m^*\omega_c}}$ (the magnetic length). Let us now insert this unit length into the Hamiltonian. The new, dimensionless variables are: $z_{new} = z_{old}/\ell$ and $\partial_{z(new)} = \partial_{z(old)}\ell$. Dropping the label “new” I get:

$$\hat{H} = -\frac{\hbar^2}{2m^*\ell^2}(\partial_z \partial_z^*) + \frac{1}{2}m^*\omega_h^2\ell^2(zz^*) - \frac{1}{4}\hbar\omega_c(z\partial_z - z^*\partial_z^*) \quad (2.6)$$

(in the last term no new factors appear, since ℓ crosses out). If I insert the explicit forms of ℓ , I obtain

$$\hat{H} = \hbar\omega_h\left(\frac{1}{4}zz^* - \partial_z \partial_z^*\right) - \frac{1}{4}\hbar\omega_c(z\partial_z - z^*\partial_z^*). \quad (2.7)$$

Let us now introduce the raising and lowering operators:

$$\begin{aligned} a &= \frac{1}{2}\left(\frac{z}{\sqrt{2}} + \partial_z^* \sqrt{2}\right), & a^+ &= \frac{1}{2}\left(\frac{z^*}{\sqrt{2}} - \partial_z \sqrt{2}\right), \\ b &= \frac{1}{2}\left(\frac{z^*}{\sqrt{2}} + \partial_z \sqrt{2}\right), & b^+ &= \frac{1}{2}\left(\frac{z}{\sqrt{2}} - \partial_z^* \sqrt{2}\right). \end{aligned} \quad (2.8)$$

To examine their properties I check two out of six of their possible commutators.

1. Commutator $[a, a^+]$.

$$[a, a^+] = \frac{1}{4}\left\{\left(\frac{1}{2}zz^* - z\partial_z + \partial_z^* z^* - 2\partial_z^* \partial_z\right) - \left(\frac{1}{2}z^* z - \partial_z z + z^* \partial_z^* - 2\partial_z \partial_z^*\right)\right\}.$$

But z commutes with z^* and ∂_z commutes with ∂_z^* , so the respective “pure” products cross out. Further, the commutator $[\partial_z, z] = 2$ and $[\partial_z^*, z^*] = 2$, so

$$[a, a^+] = 1.$$

Similarly one can prove that

$$[b, b^+] = 1.$$

2. Commutator $[a, b^+]$.

$$[a, b^+] = \frac{1}{4} \left\{ \left(\frac{1}{2} z^2 - z \partial_z^* + \partial_z^* z - 2(\partial_z^*)^2 \right) - \left(\frac{1}{2} z^2 - \partial_z^* z + z \partial_z^* - 2(\partial_z^*)^2 \right) \right\}.$$

Again, the respective “pure” products cross out. Moreover, the commutator $[\partial_z^*, z] = 0$ and $[\partial_z, z^*] = 0$, so

$$[a, b^+] = 0.$$

Similarly one can prove that any commutator of a (a^+) with b (b^+) is zero.

Thus I have shown that the pairs of operators (a, a^+) and (b, b^+) are independent.

I shall express the Hamiltonian in terms of these operators. To this end I need to perform the inverse transformation:

$$\begin{aligned} z &= \sqrt{2}(a + b^+), & z^* &= \sqrt{2}(a^+ + b), \\ \partial_z &= \frac{1}{\sqrt{2}}(b - a^+), & \partial_z^* &= \frac{1}{\sqrt{2}}(a - b^+). \end{aligned} \quad (2.9)$$

Upon substitution into the Hamiltonian I obtain:

$$\begin{aligned} \hat{H} &= \frac{1}{2} \hbar \omega_h \left((a + b^+)(a^+ + b) - (b - a^+)(a - b^+) \right) \\ &- \frac{1}{4} \hbar \omega_c \left((a + b^+)(b - a^+) - (a^+ + b)(a - b^+) \right), \end{aligned} \quad (2.10)$$

and, after reduction,

$$\hat{H} = \hbar \omega_h \left(a^+ a + \frac{1}{2} \right) + \hbar \omega_h \left(b^+ b + \frac{1}{2} \right) + \frac{1}{2} \hbar \omega_c \left(a^+ a + \frac{1}{2} \right) - \frac{1}{2} \hbar \omega_c \left(b^+ b + \frac{1}{2} \right). \quad (2.11)$$

I can now define a pair of oscillator frequencies

$$\omega_{\pm} = \omega_h \pm \frac{1}{2} \omega_c, \quad (2.12)$$

and, in terms of these frequencies,

$$\hat{H} = \hbar \omega_+ \left(a^+ a + \frac{1}{2} \right) + \hbar \omega_- \left(b^+ b + \frac{1}{2} \right). \quad (2.13)$$

Thus I have obtained a Hamiltonian of two harmonic oscillators. In analogy to the linear harmonic oscillator [35], the eigenstates of this Hamiltonian can be written as

$$|nm\rangle = \frac{1}{\sqrt{n!m!}} (a^+)^n (b^+)^m |00\rangle, \quad (2.14)$$

with n, m being quantum numbers ($n, m = 0, 1, 2, \dots$). The lowering and raising operators acting on such state give

$$\begin{aligned} a|n, m\rangle &= \sqrt{n}|n-1, m\rangle, & a^+|n, m\rangle &= \sqrt{n+1}|n+1, m\rangle; \\ b|n, m\rangle &= \sqrt{m}|n, m-1\rangle, & b^+|n, m\rangle &= \sqrt{m+1}|n, m+1\rangle. \end{aligned} \quad (2.15)$$

I am now ready to write the formula for the energy of the eigenstate $|n, m\rangle$:

$$\varepsilon(n, m) = \hbar\omega_+ \left(n + \frac{1}{2}\right) + \hbar\omega_- \left(m + \frac{1}{2}\right). \quad (2.16)$$

Let us now include the Zeeman term, introduced in the beginning of this Section, but neglected afterwards. This term accounts for the fact that the electron also has the spin degree of freedom, and its eigenstate should be identified by three quantum numbers: $|nm\sigma\rangle$, where $\sigma = \pm\frac{1}{2}$ is the quantum number describing the z spin component. In this case the electronic eigenenergies are

$$\varepsilon(n, m, \sigma) = \hbar\omega_+ \left(n + \frac{1}{2}\right) + \hbar\omega_- \left(m + \frac{1}{2}\right) - g\mu_B B\sigma. \quad (2.17)$$

In Figure 2.1 I show a few lowest-lying energies $\varepsilon(n, m, \sigma)$ as a function of the magnetic field. In this calculation I take $\hbar\omega_0 = 6$ meV and the Landé factor $g = -4.4$. This value of $\hbar\omega_0$ is characteristic for the vertical dots in GaAs, but my Landé factor is one order of magnitude larger than that of GaAs ($g_{GaAs} = -0.44$). Thus the Zeeman energy $E_Z = |g\mu_B B|$ is artificially enhanced; I have done so in order to make the spin splitting visible on this energy scale.

At zero magnetic field I have $\omega_+ = \omega_- = \omega_0$ and

$$\varepsilon_{B=0}(n, m, \sigma) = \hbar\omega_0(n + m + 1), \quad (2.18)$$

i.e., the energy of all eigenstates with the same value of $n + m$ is the same. These are the degenerate *shells*; let us name a few of them here. The lowest one, called the s shell, consists of two states, both with $n = m = 0$, but with different σ (i.e., the s shell is doubly degenerate with respect to spin). The second one, called the p shell, consists of

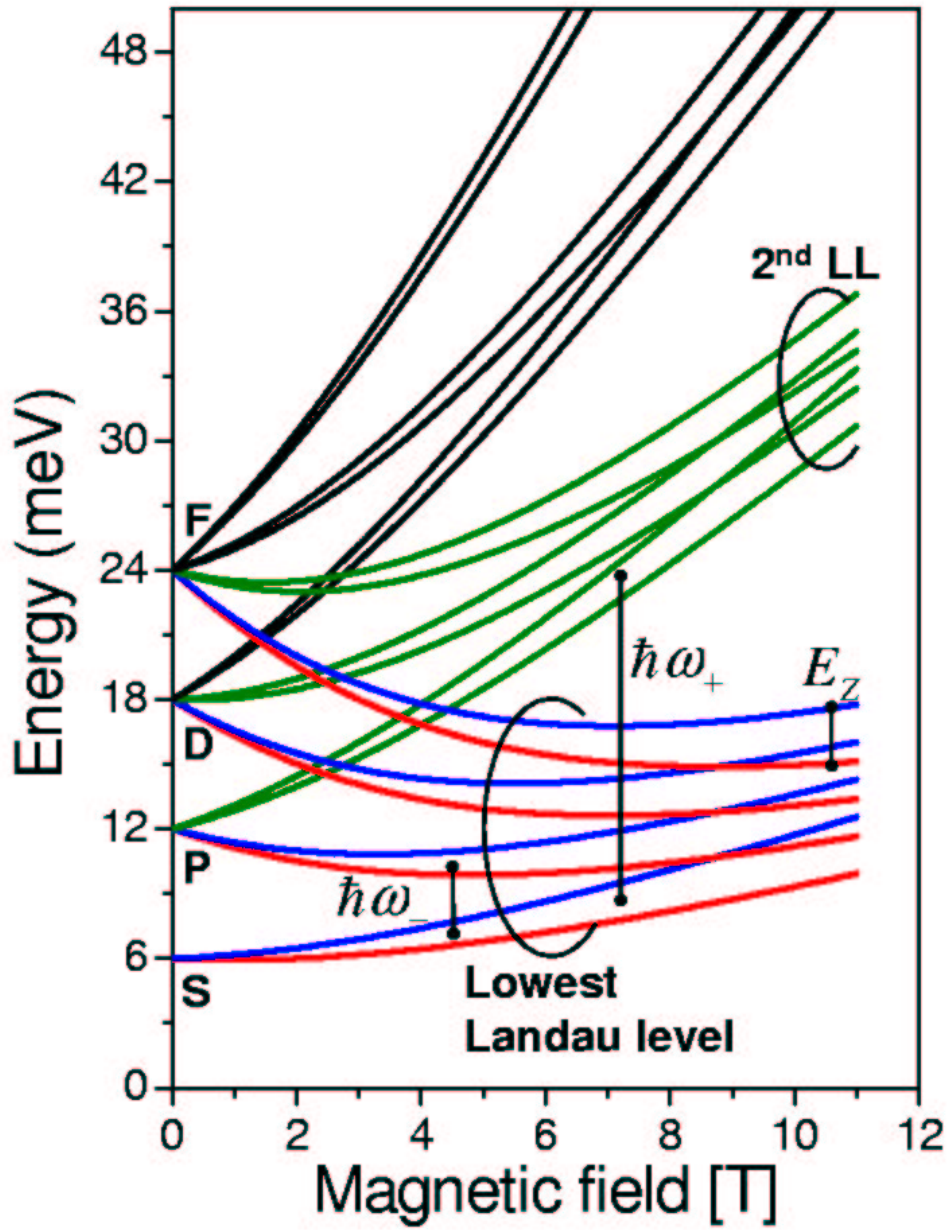


Figure 2.1: Energy spectrum of a single particle in a two-dimensional parabolic potential versus the magnetic field. I show the energies of twenty eigenstates which in the absence of the magnetic field form four lowest shells (see text for details). In this figure, the parabolic frequency $\hbar\omega_0 = 6$ meV, and the Landé factor $g = -4.4$.

states $(n, m) = (0, 1)$ and $(n, m) = (1, 0)$, both of them doubly degenerate with respect to spin. The third - d shell consists of states $(n, m) = (0, 2)$, $(1, 1)$, and $(2, 0)$, each of them spin-degenerate. Subsequent shells can be generated in analogous manner; the degeneracy of each next shell is greater by 2 than that of the previous shell (that includes the spin degeneracy). Moreover, the energy distance between consecutive shells is constant and equal to $\hbar\omega_0$.

As the magnetic field is increased, the frequency ω_+ increases, and the frequency ω_- decreases. Also, the Zeeman factor starts playing a role, causing the states with different spin orientations to differ in energies; this gap grows linearly with the magnetic field. Therefore, all degeneracies are removed, as seen in Fig. 2.1. In this Figure, in the lowest part of the spectrum I denote the spin-down states in red, and the spin-up states - in blue. This spin splitting occurs also for all higher states (accounted for in the graph, but not indicated with colours). Note that at certain values of the magnetic field (e.g., about 2 T and about 4 T) one sees crossings of levels belonging to different shells. In the absence of the Zeeman energy, this effect is observed whenever the ratio of frequencies $\omega_+/\omega_- = p/q$, where $p > q$ are nonzero integers.

For very large magnetic fields the frequency ω_- is very small (approaches zero), and the frequency ω_+ approaches the cyclotron frequency ω_c . At these fields the Landau level (LL) structure of the spectrum becomes particularly clear. The lowest Landau level (LLL) is composed of one pair of states from each shell (differing only by spin); these states are plotted in Fig. 2.1 in red and blue for spin down and up, respectively. A characteristic feature of all of these states is that all of them have the quantum number $n = 0$. The second LL (plotted in green) is composed again of one pair of states from each shell, but now with the exception of the s shell, whose states have already appeared in the LLL. All states here have the quantum number $n = 1$. In the Figure, one can also see a few lowest energies of states belonging to the third and fourth LLs, whose quantum numbers n are equal to 2 and 3, respectively. Each higher shell contributes to all LLs; I have presented

only four lowest shells for clarity. Since in the unmodified parabolic potential the number of shells is infinite, in reality each LL is composed of an infinite number of states. In this context let us note that the operators a , a^+ are associated with the frequency ω_+ , and therefore they are respectively inter-Landau-level lowering and raising operators. The difference of energies of two corresponding states (i.e., with the same m and σ) belonging to two consecutive LLs is thus equal to $\hbar\omega_+$. Analogously, b , b^+ are associated with the frequency ω_- , and are respectively intra-Landau-level lowering and raising operators. The splitting between two consecutive levels in one LL, neglecting the Zeeman splitting, is equal to $\hbar\omega_-$.

Finally let us express the z component of the angular momentum operator in the language of the lowering and raising operators:

$$\hat{l}_z = -\frac{\hbar}{2} (z\partial_z - z^*\partial_z^*) = -\hbar(b^+b - a^+a). \quad (2.19)$$

The states $|nm\sigma\rangle$ are thus also eigenstates of the operator l_z with eigenvalues $\hbar l = \hbar(n - m)$. The z component of the angular momentum is thus a good quantum number (the corresponding operator \hat{l}_z commutes with the Hamiltonian, and thus can be diagonalised together with it). In this context the degenerate structure of the p shell at zero magnetic field becomes more clear: the two doubly-spin-degenerate states have opposite angular momenta (1 and -1 , respectively), and their degeneracy simply reflects the axial symmetry of the potential. In the d shell, however, there are *three* doubly-spin-degenerate levels. The degeneracy of two of them, with angular momenta 2 and -2 , respectively, can be accounted for similarly to the states in the p shell. However, the third state, with angular momentum 0, does not fall into this category. Its degeneracy with the other two states in the d shell results from *dynamical* symmetries of the parabolic potential. These symmetries are similar to those in real atoms: atomic shells exhibit degeneracy which is higher than that due to the spherical symmetry of the system [35]. This is reflected in the fact that the energy of atomic levels depends only on one quantum number (the principal quantum number n).

The notion of angular momentum also allows for an interpretation of the raising and lowering operators: in acting on a state $|nm\rangle$ the operators a and a^+ respectively decrease and increase the angular momentum, thus they control the “counterclockwise” motion of an electron (to use a classical analogy). They also work against the magnetic field, which, in classical terms, accelerates the electron in the “clockwise” motion via the Lorenz force (this is because the magnetic field $\mathbf{B} = [0, 0, B]$ is parallel to the z axis and the electronic charge is negative). This is why Landau levels are composed of states with the same quantum number n : upon application of the operator a^+ the electron acquires one quantum of the “counterclockwise motion”, which transfers it one LL up.

2.2 Confinement of the quantum disk

In this Section I shall find the single-particle energy spectrum of an electron confined in a potential of a quantum disk with infinite walls. Let us denote the disk thickness by W and the disk radius by R . The Hamiltonian of the system in an external magnetic field $\mathbf{B} = [0, 0, B]$ takes the form

$$\hat{H} = \frac{1}{2m^*} \left(\hat{\mathbf{p}} + \frac{e}{c} \hat{\mathbf{A}} \right)^2 + \tilde{V}(x, y, z) - g\mu_B B \sigma, \quad (2.20)$$

with all the symbols defined in Section 2.1. The potential $\tilde{V}(x, y, z)$ equals zero inside the disk, and infinity outside it. When expressed in cylindrical coordinates (ϱ, θ, z) , this potential does not depend on the angle θ . Moreover, it can be separated into two parts:

$$\tilde{V}(\varrho, z) = \tilde{V}_R(\varrho) + \tilde{V}_Z(z), \quad (2.21)$$

each part dependent on one coordinate only. The potential \tilde{V}_Z is that of a square quantum well with infinite walls, and the potential \tilde{V}_R is that of a two-dimensional circular quantum well, also with infinite walls. Here I have assumed that the z axis coincides with the axis of rotational symmetry of the system.

At this point one can analytically obtain the energies and wave functions of an electron in the absence of the magnetic field, and this is what I shall do in the first part of this Section. The symmetry introduced by the magnetic field, however, turns out to be different than that of the disk potential, which makes it difficult to obtain an analytical solution in the presence of the magnetic field in a closed form. I shall therefore calculate the full single-particle energy spectrum as a function of the magnetic field using numerical methods. This procedure will be described in detail in the second part of this Section.

2.2.1 Quantum disk in the absence of the magnetic field

To simplify the notation, I will express all energies in units of the effective Rydberg, $\mathcal{R} = m^*e^4/2\varepsilon^2\hbar^2$, and all lengths in the units of the effective Bohr radius $a_B = \varepsilon\hbar^2/m^*e^2$ (ε is the dielectric constant of the QD material). For example, for GaAs $\varepsilon = 12.4$ and the effective mass of an electron $m^* = 0.067 m_0$, which yields $1 \mathcal{R} \approx 5.93$ meV and $1 a_B \approx 97.9$ Å. In these units the Hamiltonian (2.20) with $B = 0$ and written in cylindrical coordinates attains the following form:

$$\hat{H} = \left[-\frac{1}{\varrho^2} \left(\varrho \frac{\partial}{\partial \varrho} \varrho \frac{\partial}{\partial \varrho} + \frac{\partial^2}{\partial \theta^2} \right) - \frac{\partial^2}{\partial z^2} \right] + V_R(\varrho) + V_Z(z) \quad (2.22)$$

(note that the coordinates ϱ and z are now dimensionless). The above Hamiltonian can be separated into two parts, one describing the motion in z direction, and one describing the radial and angular motion. To take advantage of this fact, I shall seek the full wave function in the form

$$\Psi(\varrho, \theta, z) = \Phi(\varrho, \theta)\xi(z),$$

i.e., as a product of the in-plane and the z -dependent parts. In this case the Schrödinger equation written with the Hamiltonian (2.22) splits into two equations:

$$\left[-\frac{1}{\varrho^2} \left(\varrho \frac{\partial}{\partial \varrho} \varrho \frac{\partial}{\partial \varrho} + \frac{\partial^2}{\partial \theta^2} \right) \right] \Phi(\varrho, \theta) + V_R(\varrho)\Phi(\varrho, \theta) = E_R\Phi(\varrho, \theta), \quad (2.23)$$

$$-\frac{\partial^2}{\partial z^2}\xi(z) + V_Z(z)\xi(z) = E_Z\xi(z), \quad (2.24)$$

and the total energy $E = E_R + E_Z$.

Let us solve the equation (2.24) first. As I have already established, $V_Z(z)$ is the potential of a square quantum well with infinite walls. This problem is considered in many textbooks on quantum mechanics (see e.g. Ref [35]), and here I shall just write out its solution. For simplicity let us assume that the left wall of the well is positioned at $z = 0$, and the right wall - at $z = W$. In this case the normalised eigenstates of the equation (2.24) can be expressed by sines only (the wave functions do not contain cosine terms as they attain nonzero values at $z = 0$, i.e., at the edge of the well):

$$\xi_l(z) = \sqrt{\frac{2}{W}} \sin\left(\frac{l\pi}{W}z\right). \quad (2.25)$$

The corresponding eigenenergies are:

$$E_Z(l) = \frac{\pi^2}{W^2} l^2, \quad (2.26)$$

and the vertical quantum number $l = 1, 2, \dots$

Let us now move on to the equation (2.23). In this case one usually attempts to write the eigenfunction in the form

$$\Phi(\varrho, \theta) = R(\varrho)e^{im\theta}, \quad (2.27)$$

since the Hamiltonian of the planar motion contains elements of the z component of the angular momentum operator (m is the angular momentum quantum number). If one substitutes this wave function to Eq. (2.23), performs the differentiation and reduces the exponent on both sides, one obtains

$$\left[-\frac{1}{\varrho^2} \left(\varrho \frac{\partial}{\partial \varrho} \varrho \frac{\partial}{\partial \varrho} - m^2 \right) \right] R(\varrho) + V_R(\varrho) R(\varrho) = E_R R(\varrho). \quad (2.28)$$

This equation becomes the Bessel equation if $V_R(\varrho) \equiv 0$. Let us assume so, and include the potential V_R later on. In this case the analytical solution of this equation is possible [1], and the resulting unnormalised wave functions attain the form

$$R_m(\varrho) = J_m(\sqrt{E_R}\varrho), \quad (2.29)$$

where J_m are the Bessel functions of order m , and m is the angular momentum quantum number.

Let us now include the potential $V_R(\varrho)$. This potential is equal to zero inside the disk (i.e., for $\varrho < R$, where R is the disk radius), and infinity on the outside (i.e., for $\varrho \geq R$). Therefore the acceptable wave functions must have a node at $\varrho = R$, i.e.,

$$R_m(\sqrt{E_R}R) = 0.$$

This gives the quantisation condition for energy, which is

$$E_R(n, m) = \left(\frac{\alpha_m^n}{R}\right)^2. \quad (2.30)$$

Here α_m^n denotes the n -th node of the Bessel function J of order m . In other words, one obtains an additional radial (or nodal) quantum number $n = 1, 2, 3, \dots$, which, together with the angular momentum quantum number m , defines modes of the planar motion. The nodes α_m^n are obtained numerically.

The eigenenergies and normalised eigenfunctions of the total Hamiltonian (2.22) can now be written as:

$$E(n, m, l) = \left(\frac{\alpha_m^n}{R}\right)^2 + \frac{\pi^2}{W^2}l^2, \quad (2.31)$$

$$\langle \vec{r} | nml \rangle = \frac{\sqrt{2}}{R} \frac{1}{|J_{m+1}(\alpha_m^n)|} J_m\left(\frac{\alpha_m^n}{R}\varrho\right) \cdot \frac{1}{\sqrt{2\pi}} e^{im\theta} \cdot \sqrt{\frac{2}{W}} \sin\left(\frac{l\pi}{W}z\right). \quad (2.32)$$

Note that the quantum numbers n, m defining the eigenenergies and eigenvectors of the disk potential, although named with the same letters, have a *different* interpretation than the numbers n, m used in the case of parabolic confinements. Here, n_{disk} can be considered as the number of nodes in the radial direction, and $\hbar m_{disk}$ is the angular momentum of a given single particle state. In the parabolic case, n and m denoted the number of quanta of the “counterclockwise” and “clockwise” motion, respectively, and the angular momentum of a given state had to be calculated as $\hbar l = \hbar(n - m)$.

To complete the description of the case of zero magnetic field, let us briefly discuss the obtained energy spectrum. The formula (2.31) consists of two parts: first, corresponding

to the radial confinement, and second, corresponding to the vertical confinement. The first part scales as R^{-2} , and the second part as W^{-2} . Since the disk height W is usually much smaller than the disk radius R (for typical disk-shaped InAs/GaAs QDs, $R \approx 80 \text{ \AA}$ and $W \approx 20 \text{ \AA}$), the energy gaps between states with different numbers l , but the same n, m are much larger than the gaps between states with different numbers n, m , but the same l . Thus the spectrum consists of widely-spaced *subbands*, corresponding to different values of l , on top of which there are different modes of lateral motion, spaced much more closely. These modes are also organised in degenerate shells, and to demonstrate this let us write out values of $E_R(n, m)$ for several sets of quantum numbers (n, m) . Assuming that the disk radius $R = 1 a_B$, and using the values of Bessel zeros available in literature [1], one obtains: $E_R(0, 0) = 5.783 \mathcal{R}$ (s shell); $E_R(0, 1) = E_R(0, -1) = 14.682 \mathcal{R}$ (p shell); $E_R(0, 2) = E_R(0, -2) = 26.375 \mathcal{R}$ and $E_R(1, 0) = 30.471 \mathcal{R}$ (d shell). All these states are doubly degenerate with respect to spin. Note that here the p shell is also orbitally degenerate, as is the case with the parabolic potential. The d shell, on the other hand, is only partially orbitally degenerate. I shall discuss this and other properties of this spectrum at the end of this Section, together with effects introduced by the magnetic field.

2.2.2 Quantum disk in finite magnetic fields

Let us now consider the Hamiltonian (2.20) in nonzero magnetic field, but for now omitting the Zeeman term. If the vector potential \mathbf{A} is chosen in the symmetric gauge: $\mathbf{A} = [-By/2, Bx/2, 0]$, this Hamiltonian can be written as a sum

$$\hat{H}(B) = \hat{H}(0) + \frac{1}{8}m^*\omega_c^2 r^2 + \frac{1}{2}\omega_c \hat{l}_z, \quad (2.33)$$

where $\hat{H}(0)$ denotes the Hamiltonian (2.22) in the absence of the magnetic field, and the meaning of all other symbols is identical to that introduced in the case of the parabolic potential in Section 2.1. Thus, there are two terms dependent upon the magnetic field:

the first one depends on B quadratically, and the second one - linearly. To proceed further, let us write the above Hamiltonian in dimensionless units:

$$\hat{H}(B) = \hat{H}(0) + \frac{1}{16}\Omega_c^2 \varrho^2 - \frac{i}{2}\Omega_c \frac{\partial}{\partial \theta}, \quad (2.34)$$

where $\Omega_c = \hbar\omega_c/\mathcal{R}$ is the dimensionless cyclotron energy. Note that the terms dependent upon the magnetic field directed along the z axis do not depend on the z coordinate, but affect only the planar motion of the particle.

To find eigenenergies and eigenstates of the Hamiltonian (2.34), I shall use the exact diagonalisation procedure. This procedure involves: (i) choosing a basis of single-particle states, (ii) writing the Hamiltonian in matrix form in this basis, and (iii) diagonalising this Hamiltonian matrix numerically.

As for the choice of basis, the eigenstates $|nml\rangle$ (Eq. (2.32)) of the zero-field Hamiltonian $\hat{H}(0)$ seem to be natural candidates. But I do not have to build my basis out of states with all possible values of n , m and l ; I can divide my basis into subsets, containing functions with defined m and l , but with various n . To see why I can do that, let us check how the Hamiltonian (2.34) acts on a function $|nml\rangle$. I have $\hat{H}(0)|nml\rangle = E(n, m, l)|nml\rangle$, with $E(n, m, l)$ defined by Eq. (2.31), because these states are eigenstates of the zero-field Hamiltonian. Further, for the last term of the Hamiltonian (2.34) I get

$$-\frac{i}{2}\Omega_c \frac{\partial}{\partial \theta}|nml\rangle = \frac{m}{2}\Omega_c |nml\rangle,$$

which is readily seen from the form of the function $|nml\rangle$ (Eq. (2.32)). Finally, the action of the second term of $\hat{H}(B)$ on $|nml\rangle$ can be written in the operator form,

$$\frac{1}{16}\Omega_c^2 \varrho^2 |nml\rangle.$$

Let us now analyse the three expressions. In all three cases the part of the function describing the motion in z direction is left unchanged - in other words, the Hamiltonian $\hat{H}(B)$ does not couple states with different quantum numbers l . The angular part of the wave function is not affected either - $\hat{H}(B)$ does not couple states with different quantum

numbers m (in other words, the magnetic field directed along the z axis conserves the z component of the angular momentum of the particle). The only part of $|nml\rangle$ not conserved by $\hat{H}(B)$ is the radial part, and this is due only to the second term (the one containing ϱ^2). Therefore in choosing my basis I can preset the desired angular momentum m and the quantum number l , and take states with all possible radial quantum numbers n . Thus, my basis consists of states $\{|1ml\rangle, |2ml\rangle, |3ml\rangle, \dots\}$.

In the second step of the procedure, I write the Hamiltonian $\hat{H}(B)$ in matrix form in the chosen basis. The matrix elements of this Hamiltonian are

$$\langle lmn_1|\hat{H}(B)|n_2ml\rangle = E(n, m, l)\delta_{n_1, n_2} + \frac{1}{16}\Omega_c^2\langle lmn_1|\varrho^2|n_2ml\rangle + \frac{m}{2}\Omega_c\delta_{n_1, n_2}, \quad (2.35)$$

where δ_{n_1, n_2} is the Kronecker delta ($\delta_{n_1, n_2} = 1$ if $n_1 = n_2$, and zero otherwise). This expression is obtained by collecting all the terms considered earlier, when I analysed how $\hat{H}(B)$ acts on $|nml\rangle$, and taking into account the fact that the functions $|nml\rangle$ form an orthonormal set.

Note that the first and the third term appears only on the diagonal of the Hamiltonian matrix, while the second term introduces both diagonal and off-diagonal matrix elements. This term, written explicitly, has the form

$$\langle lmn_1|\varrho^2|n_2ml\rangle = \frac{2}{R^2} \frac{1}{|J_{m+1}(\alpha_m^{n_1})J_{m+1}(\alpha_m^{n_2})|} \int_0^R d\varrho \varrho^3 J_m\left(\frac{\alpha_m^{n_1}}{R}\varrho\right) J_m\left(\frac{\alpha_m^{n_2}}{R}\varrho\right).$$

This integration has to be carried out numerically.

Thus, I have defined my basis and I have calculated the Hamiltonian matrix elements in this basis. Before I can proceed to the proper diagonalisation, note that my basis is infinite, and therefore my Hamiltonian is also a matrix of infinite dimension. Thus, to be able to carry out calculations I need to restrict my basis to a finite set, or, in other words, limit the region of radial quantum numbers n . To decide how to do it, I invoke the rules of perturbation analysis [35] defining the subsequent corrections to the energy coming from mixing between basis states. These corrections are always in the form of a ratio, whose numerator contains the matrix elements of the perturbed Hamiltonian, and the denomina-

tor - respective differences of eigenenergies of the unperturbed Hamiltonian. This means in practice that in calculating the ground state energy of the Hamiltonian $\hat{H}(B)$ it is appropriate to choose a basis consisting of several low-lying levels $|nml\rangle$ of $\hat{H}(0)$; corrections from higher energies should give small contribution to the energy. Therefore, I choose the maximal quantum number n_{max} , which will be my cutoff, and the basis $\{|nml\rangle\}$ will now be finite and will contain only states with $1 \leq n \leq n_{max}$. There still remains a question of how much should n_{max} be to guarantee a well-converged result. The most straightforward method of establishing the cutoff value involves diagonalising the Hamiltonian in several bases (with different values of n_{max}) and performing the convergence study. This method will be used in my case.

I am now ready for the third step of the procedure - the diagonalisation of the Hamiltonian matrix. This is a standard operation of linear algebra, and many software packages capable of performing it are available. Calculations presented here are done using the Linear Algebra Package (LAPACK) [71] prepared as a FORTRAN software library.

For my model calculations I use a disk potential with thickness $W = 20$ Å and radius $R = 200$ Å. Note that the radius is taken to be more than two times larger than typical radii of indium-flashed InAs QDs on GaAs substrate (for these structures typically $R \approx 80$ Å), but comparable to the radii of InAs QDs grown on InP substrate. I took such a large radius of the structure to make the magnetic-field-induced effects more visible, since for small disks the field-dependent corrections in $\hat{H}(B)$ are small compared to the energy quantisation introduced by $\hat{H}(0)$.

First let us examine the convergence of the ground state energy in the channel $m = 0$, $l = 1$ (i.e., zero angular momentum, lowest subband of the vertical motion) as a function of the basis size. Since the magnetic terms in $\hat{H}(B)$ increase with increasing magnetic field, I perform my control calculations for a large field, e.g., for $B = 10$ T; if the result has converged for this field, it will also be well-converged for smaller fields. For my model structure at $B = 10$ T, I have performed calculations with n_{max} ranging from 1 to 20.

n_{max}	$E_{GS}(m = 0, l = 1, B = 10 \text{ T}) \text{ (eV)}$
1	1.41420722313
2	1.41406380561
3	1.41406291665
4	1.41406283691
5	1.41406282464
6	1.41406282195
7	1.41406282120
8	1.41406282095
9	1.41406282085
10	1.41406282081
15	1.41406282078
20	1.41406282077

Table 2.1: Convergence of the ground-state energy for angular momentum $m = 0$ and the vertical quantum number $l = 1$ of a quantum disk with $W = 20 \text{ \AA}$ and $R = 200 \text{ \AA}$

The ground-state energies with $m = 0$ and $l = 1$ obtained in each case are shown in Table 2.1. As can be seen, the convergence is achieved very rapidly, so that the result is fully converged already for $n_{max} = 20$. I choose this cutoff of the basis in my further calculations. Note that for a disk with $W = 20 \text{ \AA}$ and $R = 80 \text{ \AA}$ the convergence is expected to occur for even smaller n_{max} , since the quantisation introduced by the zero-field Hamiltonian $\hat{H}(0)$ is more than four times stronger than that with $R = 200 \text{ \AA}$ (indeed, the result is already fully converged for $n_{max} = 5$).

Using the exact diagonalisation procedure I have calculated several low-lying energy levels for my disk structure as a function of the magnetic field for $l = 1$ and in angular

momentum channels $m = 0, \pm 1, \pm 2, \pm 3$. Results of my calculations are shown in Fig. 2.2. I shall discuss the fundamental features seen in this graph by comparing it to Fig. 2.1, where I presented the spectrum corresponding to the parabolic potential.

Let us first focus on the case of zero magnetic field. As I already mentioned, the energy levels of the disk are organised in shells. The lowest shell - the s shell - is doubly degenerate with respect to spin, and the next shell - p - consists of four states, degenerate both orbitally and with respect to spin. These two shells behave identically as in the parabolic case, and the degeneracy of the p shell can be traced to the axial symmetry of the system. However, the d shell is only partially degenerate: the states with $m = \pm 2$ form a quadruplet, with both orbital and spin degeneracy present, but the doubly-spin-degenerate state with $m = 0$ lies at a slightly higher energy. Therefore, the disk potential does not exhibit the dynamical symmetries apparent in the parabolic confinement. The f shell is also split into two quadruplets: one with $m = \pm 3$ and one with $m = \pm 1$, all spin-degenerate. As can be seen, at zero magnetic field states with opposite angular momenta have the same energy, but there is *no* degeneracy of states with different angular momenta. Note also that the energy distance between consecutive shells in the case of my disk is larger than it is in the case of the parabolic system considered in Section 2.1. This is due to the fact that in the case of the disk the radial quantisation is stronger than that of the larger parabolic confinement. In fact, as I already mentioned, in more realistic approximations of indium-flashed quantum disks the radii are usually taken to be a factor of 2 smaller than the one I took. This makes the intershell gaps more than four times larger than those seen in Fig. 2.2. Also, all the energy levels on this graph correspond to states with the vertical quantum number $l = 1$. The states from the second subband are ignored, as their energies are much higher: due to the small disk width W one expects the second subband (containing states with $l = 2$) to start at energies of order of 5.6 eV.

Let us now move on to finite magnetic fields. Here I shall explicitly include the Zeeman term in the Hamiltonian, neglected up to now. Thus, I explicitly account for

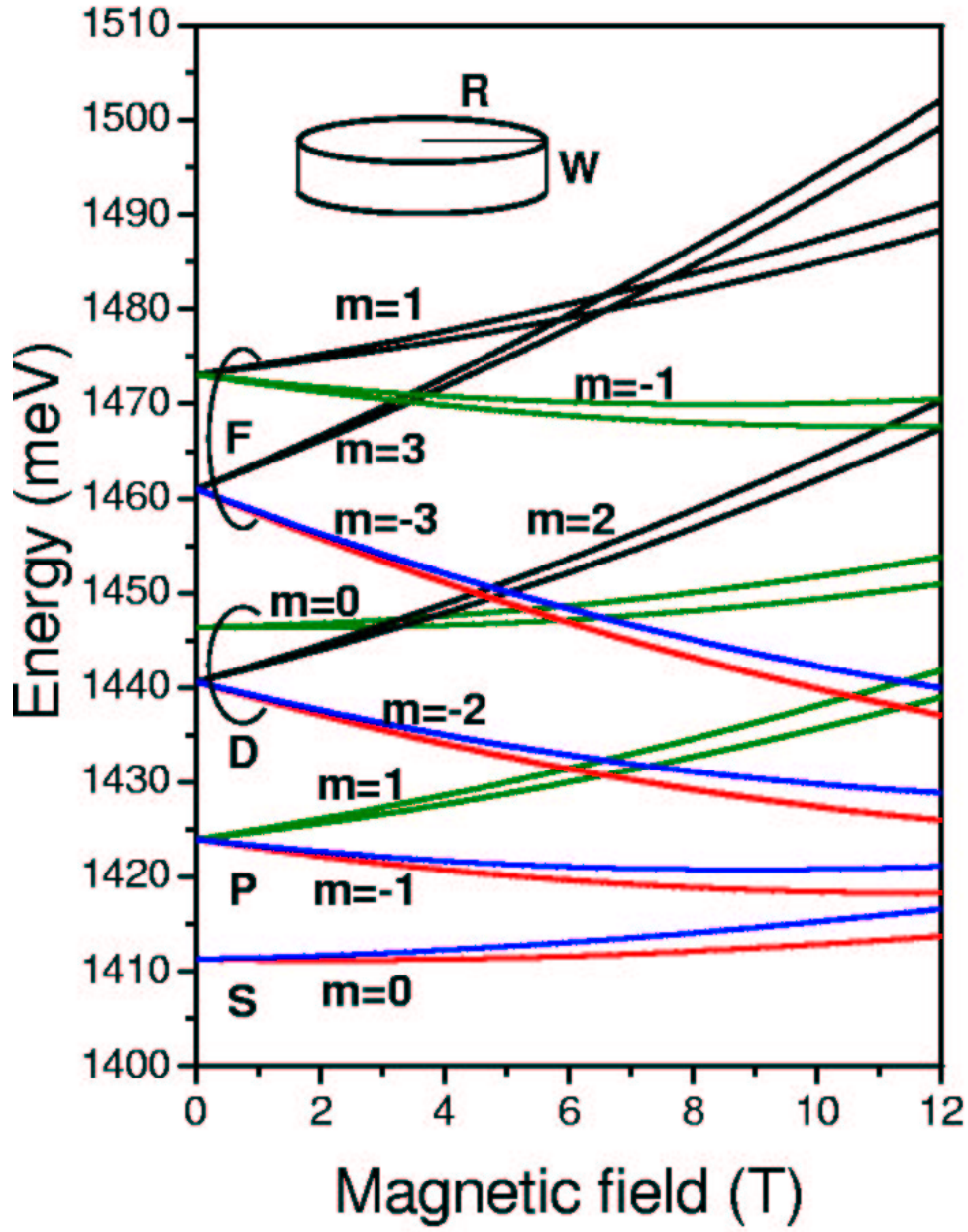


Figure 2.2: Energy spectrum of a single particle in a rigid-wall quantum disk potential versus the magnetic field. The width of the disk is $W = 20 \text{ \AA}$, and its radius is $R = 200 \text{ \AA}$. I show the energies of twenty eigenstates which in the absence of the magnetic field form four lowest shells (see text for details). In this figure the Landé factor $g = -4.4$. Inset shows the geometry of the disk confinement

the different possible values of electronic spin s_z ; the spin quantum number σ becomes an additional good quantum number. The qualitative behaviour of the levels in Fig. 2.2 is similar to that in the parabolic confinement: the shell degeneracy - both orbital and spin - is removed. As I did in Section 2.1, here also I artificially enhanced the Zeeman energy to make it visible on this energy scale. Compared to the parabolic confinement, in the case of quantum disk the magnetic field has a smaller effect: in Fig. 2.1, at $B = 11$ T the structure of Landau levels was already well established, while here the states belonging to different Landau levels are still interspersed. In Fig. 2.2, the states forming the lowest LL are drawn with red and blue lines (to denote the spin down and up, respectively), and the states belonging to the second LL - with green lines. The weaker effect of the magnetic field is due to the stronger zero-field quantisation of the disk confinement: the magnetic corrections in the softer parabolic potential of large gated QDs contribute more strongly to the energy spectrum. Calculations made for the more realistic disk potential (with $R = 80$ Å, not shown here) show that there the magnetic field has even less effect: even at fields as large as 12 T the structure of the spectrum resembles more the split zero-field shells than Landau levels.

2.3 Confinement of the quantum ring

I shall now move on to discussing the last “ideal” single-particle potential - a quantum ring. Let us write the Hamiltonian for this system in a general form:

$$\hat{H} = \frac{1}{2m^*} \left(\hat{\mathbf{p}} + \frac{e}{c} \mathbf{A} \right)^2 + V_R(x, y, z). \quad (2.36)$$

Henceforth I shall omit the Zeeman term, since, as I have already demonstrated, it changes the single-particle spectra only in a minor way. As for the quantum-ring potential $V_R(x, y, z)$, for simplicity I shall take it to be the ring-shaped quantum well with infinitesimal thickness and width, and infinite walls. In other words, $V_R(x, y, z) \equiv V_R(\varrho, \theta, z)$ restricts the motion of the electron only to the region defined by $\varrho = R$ and $z = 0$ (the

circumference of a circle, where R is its radius). Moreover, as usual, I take the magnetic field \mathbf{B} to be directed along the z axis, and the corresponding vector potential \mathbf{A} in the symmetric gauge. In this situation it is natural to work in polar coordinates, in which the electronic motion is described by only one independent coordinate - the angle θ .

If one expresses the Hamiltonian (2.36) in these coordinates, one obtains:

$$\hat{H} = -\frac{\hbar^2}{2m^*R^2} \frac{\partial^2}{\partial \theta^2} + \frac{1}{8}m^*\omega_c^2 R^2 - \frac{i}{2}\hbar\omega_c \frac{\partial}{\partial \theta}. \quad (2.37)$$

I now define the magnetic length as $\ell = \sqrt{\hbar/m^*\omega_c}$. This allows me to write the Hamiltonian in the form

$$\hat{H} = \frac{\hbar^2}{2m^*R^2} \left(-i\frac{\partial}{\partial \theta} + N_\phi \right)^2, \quad (2.38)$$

where N_ϕ is the number of magnetic flux quanta threading the ring. This quantity is defined as $N_\phi = \pi R^2/2\pi\ell^2$ and is the ratio of the area of the ring to the area defined by the magnetic length. Since the magnetic length $\ell \sim B^{-1/2}$, the number of flux quanta increases linearly with the magnetic field.

The eigenstates of the Hamiltonian (2.38) are

$$\Psi_m(\theta) = \frac{1}{\sqrt{2\pi R}} e^{im\theta}, \quad (2.39)$$

where the angular momentum quantum number $m = 0, \pm 1, \pm 2, \dots$. The corresponding eigenenergies are then $E(m) = \frac{\hbar^2}{2m^*R^2} (m + N_\phi)^2$, or in the effective Rydberg units, $E(m) = \frac{1}{R^2} (m + N_\phi)^2$ (now the ring radius R is expressed in the effective Bohr radii a_B). As can be seen from these formulae, the energy of a state with given angular momentum m depends quadratically on the magnetic field. This is seen in Fig. 2.3, where I show the quantity $E_m R^2$ as a function of the number of flux quanta N_ϕ for several angular momenta m . The colour lines show energies of states with definite angular momenta m (the values of m for each curve are given by the number on the graph). I deal thus with a series of parabolas, with minima at integer values of the number of flux quanta N_ϕ . These parabolas cross at half-integer values of N_ϕ . Therefore the single-electron ground-state energy, denoted in the graph by the black line, exhibits oscillations as a function of the

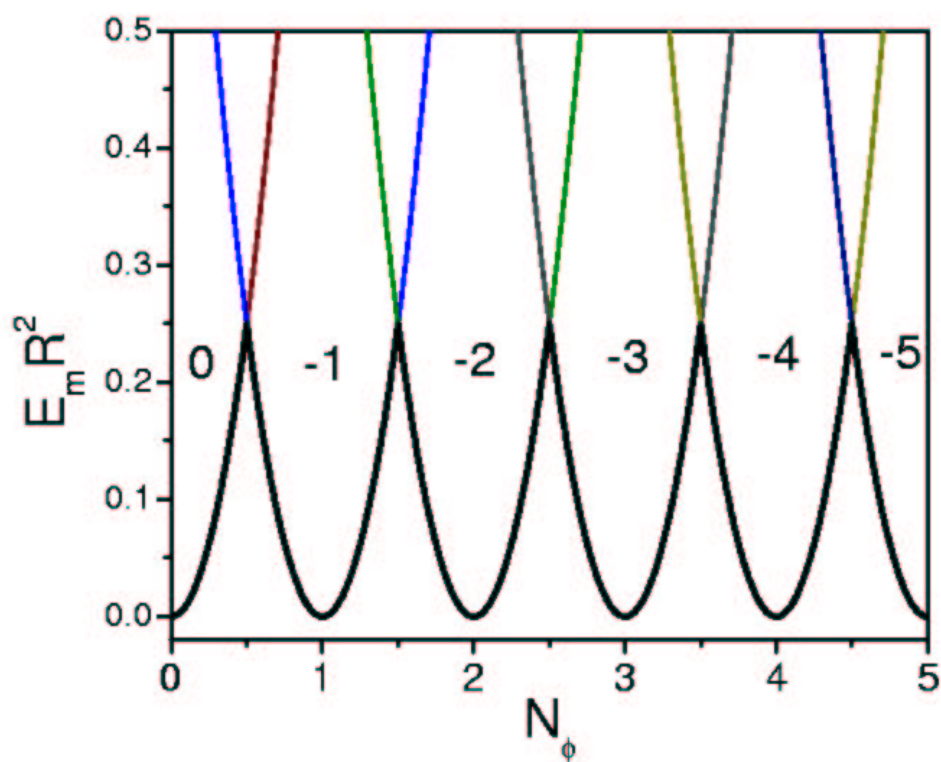


Figure 2.3: Energy of a single electron confined in a quantum-ring potential as a function of the number of flux quanta. The colour lines show energies of states with definite angular momenta m (given by numbers on the graph); the black line shows the ground-state energy

magnetic field. This is the Aharonov-Bohm effect. Note that at each maximum of the energy there is a transition in the ground state. At these points the angular momentum of the ground state changes by one unit (in the case of electrons it becomes more negative). This behaviour is fundamentally different from that observed in the energy spectra of the parabolic and the disk confinements. There the ground state was always the same (it was the state belonging to the s shell), and its energy depended monotonically on the magnetic field (see Figs. 2.1 and 2.2).

Chapter 3

Methods of analysis of confined many-particle systems

In the previous Chapter I have presented a detailed description of single-particle properties of nanostructures with various symmetries. It was the first, necessary step towards the main goal of this work - a description of the behaviour of *many particles* confined in these potentials, with a special emphasis put on correlation effects. To be able to achieve this goal, I have to develop methods capable of describing the systems of many interacting particles with sufficient accuracy. This Chapter contains a detailed presentation of my method of choice - the exact diagonalisation technique. I have chosen this method because, if properly used, it allows to account for all the interaction effects: direct and exchange Coulomb terms as well as particle-particle correlations, since the results it produces are *exact*.

My description will start with the mean-field Hartree-Fock approximation, accounting only for the direct and exchange Coulomb terms. Then I will begin the construction of the exact diagonalisation method by discussing two different ways of constructing the many-particle basis set: configurations of electrons distributed on single-particle states,

and configurations of quasiparticles distributed on Hartree-Fock orbitals. I shall also discuss possible optimisations of this basis set, obtained by explicitly accounting for all the symmetries of the system. I shall also compare this method with other approaches, more approximate and less controllable, but nevertheless capable of accounting for the correlations. These methods are the density functional theory in the local spin density approximation, and the quantum Monte Carlo method.

But before I move on to the methods, I will first formulate a general definition of the problem of many interacting particles confined by a QD potential.

3.1 The problem of many interacting particles in a QD confinement

3.1.1 The many-particle Hamiltonian

The Hamiltonian of N interacting electrons confined by the potential $U(\mathbf{r})$ of the nanostructure and in the presence of an external magnetic field can be written in the form:

$$\hat{H} = \sum_{i=1}^N \left[\frac{1}{2m^*} \left(\hat{\mathbf{p}}_i + \frac{e}{c} \mathbf{A}_i \right)^2 + U(\mathbf{r}_i) \right] + \frac{1}{2} \sum_{i \neq j}^N \frac{e^2}{\varepsilon |\mathbf{r}_i - \mathbf{r}_j|}, \quad (3.1)$$

where the notation corresponds to that introduced in Chapter 2. The first term in the above Hamiltonian introduces the single-particle QD spectrum for each confined particle, and has been considered in the previous Chapter. The second term is new - it describes the particle-particle Coulomb interactions.

The notation of my analysis will become particularly simple if I express the Hamiltonian in the language of the fermionic creation and annihilation operators. They will be denoted by $c_{i\sigma}^+$ and $c_{i\sigma}$, respectively. These operators create (annihilate) a particle on the single-particle orbital i with spin σ . Here i is a composite orbital index, denoting (n, m) in the case of the parabolic potential, (n, m, l) in the case of the quantum disk, and m in

the case of the quantum ring. In the language of these operators the Hamiltonian takes a simpler form

$$\hat{H} = \sum_{i\sigma} E(i, \sigma) c_{i\sigma}^+ c_{i\sigma} + \frac{1}{2} \sum_{ijkl\sigma\sigma'} \langle i\sigma, j\sigma' | V | k\sigma', l\sigma \rangle c_{i\sigma}^+ c_{j\sigma'}^+ c_{k\sigma'} c_{l\sigma}. \quad (3.2)$$

Now the summation extends over all single-particle orbitals.

Creation operators also allow for a concise notation regarding many-particle states. In their language, a configuration obtained by distributing N electrons on single-particle orbitals can be written as

$$|i_1\sigma_1, i_2\sigma_2, \dots, i_N\sigma_N\rangle = c_{i_1\sigma_1}^+ c_{i_2\sigma_2}^+ \dots c_{i_N\sigma_N}^+ |0\rangle, \quad (3.3)$$

where $|0\rangle$ denotes the vacuum. The equivalent of the above configuration, written in real space, is the Slater determinant built out of orbitals $i\sigma$. The antisymmetry of the state is guaranteed by the Fermionic anticommutation rules of the creation and annihilation operators:

$$\{c_i^+, c_j^+\} = \{c_i, c_j\} = 0; \quad \{c_i, c_j^+\} = \delta_{ij}. \quad (3.4)$$

The configurations constructed in such a way are not eigenstates of the many-body Hamiltonian (3.2), since these states are built out of the single-particle orbitals, and the Coulomb interaction can scatter particles between these orbitals. But the exact eigenstates of the interacting system can be written as *linear combinations* of many such configurations. The question of what these combinations should be is the central question of this thesis.

To complete my definition of the many-body problem, I have to define the Coulomb matrix element $\langle i, j | V | k, l \rangle$ appearing in the Hamiltonian (3.2). In general these matrix elements can be constructed by carrying out the real-space integration:

$$\langle i\sigma, j\sigma' | V | k\sigma', l\sigma \rangle = \frac{e^2}{\varepsilon} \int d\mathbf{r}_1 \int d\mathbf{r}_2 \frac{\Psi_{i\sigma}^*(\mathbf{r}_1) \Psi_{j\sigma'}^*(\mathbf{r}_2) \Psi_{k\sigma'}(\mathbf{r}_2) \Psi_{l\sigma}(\mathbf{r}_1)}{|\mathbf{r}_1 - \mathbf{r}_2|}. \quad (3.5)$$

In the remainder of this thesis I will be particularly interested in the matrix elements in the parabolic confinement. The orbitals $\Psi(\mathbf{r})$ are then the harmonic-oscillator states. In this case the matrix elements can be obtained analytically in a closed form. I shall present a detailed description of their evaluation in the next Section.

3.1.2 Coulomb matrix elements in the harmonic-oscillator basis

In this Section I calculate analytically the electron-electron Coulomb scattering matrix elements in the basis of the two-dimensional harmonic-oscillator orbitals. This calculation is similar to that presented in Ref. [127]. The final form of the Coulomb matrix elements in this basis was first given in Ref. [52], and later also reported in Ref. [34, 70].

In the units of effective Rydberg and effective Bohr radius (see Section 2.2) the part of the Hamiltonian (3.2) describing the electron-electron Coulomb scattering can be written as:

$$H_C = \frac{1}{2} \sum_{ijkl\sigma\sigma'} \langle i\sigma j\sigma' | v | k\sigma' l\sigma \rangle c_{i\sigma}^+ c_{j\sigma'}^+ c_{k\sigma'} c_{l\sigma}, \quad (3.6)$$

where

$$v(|\mathbf{r}_1 - \mathbf{r}_2|) = \frac{2}{|\mathbf{r}_1 - \mathbf{r}_2|}, \quad (3.7)$$

and the composite indices in the harmonic-oscillator basis $i = (n'_1, m'_1)$, $j = (n'_2, m'_2)$, $k = (n_2, m_2)$, $l = (n_1, m_1)$.

Further I will use the coordinates x and y of each particle written in the language of the harmonic-oscillator lowering and raising operators introduced in Section 2.1:

$$x = \frac{\ell}{\sqrt{2}} (a + a^+ + b + b^+), \quad y = \frac{i\ell}{\sqrt{2}} (a - a^+ - b + b^+). \quad (3.8)$$

Let us start the analysis by unfolding the Coulomb interaction into the basis of plane waves. In what follows I shall suppress the spin index σ of the orbitals, as it will play no role in this derivation.

$$\begin{aligned} \langle ij | v | kl \rangle &= \langle i | \langle j | \sum_q v_q e^{i\mathbf{q}(\mathbf{r}_1 - \mathbf{r}_2)} | k \rangle | l \rangle \\ &= \sum_q v_q \langle i | \langle j | e^{i\mathbf{q}(\mathbf{r}_1 - \mathbf{r}_2)} | k \rangle | l \rangle = \sum_q v_q \langle i | e^{i\mathbf{q}\mathbf{r}_1} | l \rangle \langle j | e^{-i\mathbf{q}\mathbf{r}_2} | k \rangle, \end{aligned} \quad (3.9)$$

with $v_q = \frac{4\pi}{q}$ being the Fourier transform of the Coulomb term. This transform is calculated in the following way:

$$v_q(q) = \int d\mathbf{r} \frac{2}{\mathbf{r}} e^{-i\mathbf{q}\mathbf{r}} = 2 \int_0^\infty r dr \int_0^{2\pi} d\phi_r \frac{1}{r} e^{-iqr \cos(\phi_r - \phi_q)}$$

$$\begin{aligned}
&= 2 \int_0^\infty dr \int_0^{2\pi} d\phi_r \sum_{m=-\infty}^{\infty} (-i)^m e^{-im(\phi_r - \phi_q)} J_m(rq) \\
&= 4\pi \int_0^\infty dr J_0(qr) = \frac{4\pi}{q}.
\end{aligned} \tag{3.10}$$

Let us calculate the first term of the sum (3.9). Substituting the equations (3.8) I get the form of the exponent:

$$\begin{aligned}
e^{i\mathbf{q}\mathbf{r}_1} &= e^{i\left(\frac{q_x\ell}{\sqrt{2}}(a_1+a_1^++b_1+b_1^+)+i\frac{q_y\ell}{\sqrt{2}}(a_1-a_1^+-b_1+b_1^+)\right)} \\
&= e^{iQ^*a_1^++iQa_1+iQb_1^++iQ^*b_1},
\end{aligned} \tag{3.11}$$

with $Q = \frac{\ell}{\sqrt{2}}(q_x + iq_y)$. To disentangle the operators I will use the Trotter-Suzuki formula:

$$e^{\hat{A}+\hat{B}} = e^{\hat{A}}e^{\hat{B}}e^{-\frac{1}{2}[\hat{A},\hat{B}]}, \tag{3.12}$$

applicable under condition $[\hat{A}, [\hat{A}, \hat{B}]] = [\hat{B}, [\hat{A}, \hat{B}]] = 0$. I have $[a_1^{(+)}, b_1^{(+)}] = 0$, and $[iQ^*a_1^+, iQa_1] = |Q|^2$ and also $[iQb_1^+, iQ^*b_1] = |Q|^2$, so the conditions for the applicability of the formula are satisfied for each pair of operators. I can now write

$$e^{iQ^*a_1^++iQa_1+iQb_1^++iQ^*b_1} = e^{-|Q|^2} e^{iQ^*a_1^+} e^{iQa_1} e^{iQb_1^+} e^{iQ^*b_1}. \tag{3.13}$$

Analogously, only with the exception to sign in the exponent, I can write for the second particle (second term in the sum (3.9)):

$$e^{-i\mathbf{q}\mathbf{r}_2} = e^{-|Q|^2} e^{-iQ^*a_2^+} e^{-iQa_2} e^{-iQb_2^+} e^{-iQ^*b_2}. \tag{3.14}$$

Let us continue with the first particle. I need to calculate the element

$$\begin{aligned}
M_1 &= \langle i|e^{-|Q|^2} e^{iQ^*a_1^+} e^{iQa_1} e^{iQb_1^+} e^{iQ^*b_1}|l\rangle \\
&= \frac{1}{\sqrt{n_1'!m_1'!n_1!m_1!}} \\
&\times \langle 00|b_1^{m_1'}a_1^{n_1'}e^{-|Q|^2} e^{iQ^*a_1^+} e^{iQb_1^+} \hat{\mathbf{1}} e^{iQa_1} e^{iQ^*b_1} (a_1^+)^{n_1} (b_1^+)^{m_1}|00\rangle
\end{aligned} \tag{3.15}$$

(there has been a slight rearrangement of order of operators - I can do that, since operators a and b commute). The unit operator

$$\hat{\mathbf{1}} = \sum_{p_1=0}^{\infty} \sum_{p_2=0}^{\infty} |p_1p_2\rangle \langle p_2p_1| = \frac{1}{p_1!p_2!} \sum_{p_1=0}^{\infty} \sum_{p_2=0}^{\infty} (a_1^+)^{p_1} (b_1^+)^{p_2} |00\rangle \langle 00| (b_1)^{p_2} (a_1)^{p_1}.$$

I will also unfold the exponential operators in Taylor series, e.g:

$$e^{iQa_1} = \sum_{s=0}^{\infty} \frac{(iQ)^s}{s!} a_1^s. \quad (3.16)$$

In this notation it is now clear that the indices p_1 and p_2 can change only from 0 to $\min(n_1, n'_1)$ and from 0 to $\min(m_1, m'_1)$, respectively. This is due to the fact that whenever these upper limits are exceeded, there will occur a situation when the lowering operator a or b will act on the lowest oscillator mode, giving zero as a result. Moreover, the matrix element will be nonzero only for certain powers of operators a , a^+ , b and b^+ :

$$\begin{aligned} M_1 &= \frac{1}{\sqrt{n'_1!m'_1!n_1!m_1!}} \sum_{p_1=0}^{\min(n_1, n'_1)} \sum_{p_2=0}^{\min(m_1, m'_1)} \frac{e^{-|Q|^2}}{p_1!p_2!} \\ &\times \langle 00 | b_1^{m'_1} a_1^{n'_1} \frac{(iQ^*)^{n'_1-p_1}}{(n'_1-p_1)!} (a_1^+)^{n'_1-p_1} \frac{(iQ)^{m'_1-p_2}}{(m'_1-p_2)!} (b_1^+)^{m'_1-p_2} (a_1^+)^{p_1} (b_1^+)^{p_2} | 00 \rangle \\ &\times \langle 00 | (b_1)^{p_2} (a_1)^{p_1} \frac{(iQ)^{n_1-p_1}}{(n_1-p_1)!} (a_1)^{n_1-p_1} \frac{(iQ^*)^{m_1-p_2}}{(m_1-p_2)!} (b_1)^{m_1-p_2} (a_1^+)^{n_1} (b_1^+)^{m_1} | 00 \rangle. \end{aligned} \quad (3.17)$$

From the above formula it can be seen why I chose these particular terms from the Taylor expansion of exponents - right now the operators are aligned exactly to take the state from $|00\rangle$ on the right-hand side to $|n'_1 m'_1\rangle$ (or $|n_1 m_1\rangle$) and back. This is also why the application of all these operators will result simply in multiplicative term $n'_1!m'_1!n_1!m_1!$. This is in accordance to the rules of application of the raising and lowering operators, laid out in Eq. (2.15). As a result one obtains:

$$\begin{aligned} M_1 &= \frac{e^{-|Q|^2}}{\sqrt{n'_1!m'_1!n_1!m_1!}} \sum_{p_1=0}^{\min(n_1, n'_1)} \sum_{p_2=0}^{\min(m_1, m'_1)} p_1!p_2! \binom{n'_1}{p_1} \binom{n_1}{p_1} \binom{m'_1}{p_2} \binom{m_1}{p_2} \\ &\times (iQ^*)^{n'_1-p_1} (iQ)^{m'_1-p_2} (iQ)^{n_1-p_1} (iQ^*)^{m_1-p_2}. \end{aligned} \quad (3.18)$$

The matrix element for the second particle, M_2 , can be calculated analogously, and will look similarly to M_1 , only wherever I have the imaginary constant i in M_1 , I will have $(-i)$ in M_2 . The formula for M_2 will also contain new indices of summation, p_3 and p_4 .

Now I am able to put all the elements together and calculate

$$\langle ij|v|kl\rangle = \frac{1}{4\pi^2} \int_0^\infty q dq \int_0^{2\pi} d\phi_q \frac{4\pi}{q} M_1 M_2$$

$$\begin{aligned}
&= \frac{1}{\sqrt{n'_1!m'_1!n_1!m_1!n'_2!m'_2!n_2!m_2!}} \sum_{p_1=0}^{\min(n_1, n'_1)} p_1! \binom{n'_1}{p_1} \binom{n_1}{p_1} \\
&\times \sum_{p_2=0}^{\min(m_1, m'_1)} p_2! \binom{m'_1}{p_2} \binom{m_1}{p_2} \sum_{p_3=0}^{\min(n_2, n'_2)} p_3! \binom{n'_2}{p_3} \binom{n_2}{p_3} \sum_{p_4=0}^{\min(m_2, m'_2)} p_4! \binom{m'_2}{p_4} \binom{m_2}{p_4} \\
&\times \frac{1}{\pi} I_{p_1 p_2 p_3 p_4}, \tag{3.19}
\end{aligned}$$

where the integral

$$\begin{aligned}
I_{p_1 p_2 p_3 p_4} &= \int_0^\infty dq \int_0^{2\pi} d\phi_q e^{-2|Q|^2} (iQ^*)^{n'_1-p_1} (iQ)^{m'_1-p_2} (iQ)^{n_1-p_1} (iQ^*)^{m_1-p_2} \\
&\times (-iQ^*)^{n'_2-p_3} (-iQ)^{m'_2-p_4} (-iQ)^{n_2-p_3} (-iQ^*)^{m_2-p_4}. \tag{3.20}
\end{aligned}$$

To solve this integral I take the following steps:

1. Change of variables: I have $Q = \frac{\ell}{\sqrt{2}}(q_x + iq_y)$. Let us write Q in the exponential form: $Q = |Q|e^{i\phi_q} = \frac{\ell}{\sqrt{2}}qe^{i\phi_q}$. I want then to set $|Q| = \frac{\ell}{\sqrt{2}}q$, so $dq = d|Q|\frac{\sqrt{2}}{\ell}$. The angle is not affected. Further I drop the modulus sign by $|Q|$.

2. Collect the moduli of Q (not including the sign) - I get

$$Q^{n'_1+m'_1+n_1+m_1+n'_2+m'_2+n_2+m_2-2p_1-2p_2-2p_3-2p_4},$$

3. Collect the phases of Q - I get $e^{i\phi_q(-n'_1+m'_1+n_1-m_1-n'_2+m'_2+n_2-m_2)}$

4. Collect the imaginary units i . I pick up all imaginary units (not including the sign)

$$\text{and I get } (i)^{n'_1+m'_1+n_1+m_1+n'_2+m'_2+n_2+m_2-2p_1-2p_2-2p_3-2p_4}.$$

5. And finally collect the factors (-1) appearing for the second particle - I get $(-1)^{n'_2+m'_2+n_2+m_2-2p_3-2p_4}$
 $= (-1)^{n'_2+m'_2+n_2+m_2}$, because the other two terms in exponent are even.

My integral separates now into two integrals - the one over Q and the one over ϕ_q . Let us carry out the second one first. I get

$$\int_0^{2\pi} d\phi_q e^{i\phi_q(-n'_1+m'_1+n_1-m_1-n'_2+m'_2+n_2-m_2)} = 2\pi \delta_{R_L, R_R}, \tag{3.21}$$

where $R_L = (m'_1 + m'_2) - (n'_1 + n'_2)$ is the angular momentum of the pair of particles on the left hand side of the matrix element (particles on orbitals i and j), and $R_R = (m_1 + m_2) - (n_1 + n_2)$ is the angular momentum of the pair on the right side (particles on orbitals k and l). I have formally obtained the **angular momentum conservation rule**.

From this rule I also obtain the identity $n_1 + n_2 + m'_1 + m'_2 = n'_1 + n'_2 + m_1 + m_2$. It means that the long sums in the exponents of Q and i can be written as $n'_1 + n'_2 + m'_1 + m'_2 + n_1 + n_2 + m_1 + m_2 - 2p_1 - 2p_2 - 2p_3 - 2p_4 = 2(n'_1 + n'_2 + m_1 + m_2 - p_1 - p_2 - p_3 - p_4) = 2p$. Now the integral

$$I_{p_1 p_2 p_3 p_4} = \frac{2\pi\sqrt{2}}{\ell} \int_0^\infty dQ e^{-2Q^2} (2Q)^{2p} \left(-\frac{1}{2}\right)^p (-1)^{n'_2 + m'_2 + n_2 + m_2} \quad (3.22)$$

(in passing I multiplied and divided by 2^p). Let us do another change of variables: $x = 2Q^2$, so that $dx = 4QdQ$ and $dQ = \frac{dx\sqrt{2}}{4\sqrt{x}}$. I get

$$\begin{aligned} I_{p_1 p_2 p_3 p_4} &= \frac{\pi}{\ell} \left(-\frac{1}{2}\right)^p (-1)^{n'_2 + m'_2 + n_2 + m_2} \int_0^\infty dx e^{-x} (x)^{p+1/2-1} \\ &= \frac{\pi}{\ell} \left(-\frac{1}{2}\right)^p (-1)^{n'_2 + m'_2 + n_2 + m_2} \Gamma(p + 1/2). \end{aligned} \quad (3.23)$$

The symbol Γ denotes the Gamma function, which is the generalised factorial [1]. Now I can collect everything together.

$$\begin{aligned} \langle n'_1 m'_1, n'_2 m'_2 | v | n_2 m_2, n_1 m_1 \rangle &= \frac{1}{\ell} \frac{\delta_{R_L, R_R} (-1)^{n'_2 + m'_2 + n_2 + m_2}}{\sqrt{n'_1! m'_1! n_1! m_1! n'_2! m'_2! n_2! m_2!}} \\ &\times \sum_{p_1=0}^{\min(n_1, n'_1)} p_1! \binom{n'_1}{p_1} \binom{n_1}{p_1} \sum_{p_2=0}^{\min(m_1, m'_1)} p_2! \binom{m'_1}{p_2} \binom{m_1}{p_2} \\ &\times \sum_{p_3=0}^{\min(n_2, n'_2)} p_3! \binom{n'_2}{p_3} \binom{n_2}{p_3} \sum_{p_4=0}^{\min(m_2, m'_2)} p_4! \binom{m'_2}{p_4} \binom{m_2}{p_4} \\ &\times \left(-\frac{1}{2}\right)^p \Gamma\left(p + \frac{1}{2}\right). \end{aligned} \quad (3.24)$$

As can be seen, the Coulomb scattering matrix element in the harmonic-oscillator basis can be expressed as a sum of generalised factorials. Let us write out explicitly some of these elements. The most important one is the one with all indices equal to 0, i.e.,

$$\langle 00, 00 | v | 00, 00 \rangle = \frac{\sqrt{\pi}}{\ell} \equiv E_0 = \frac{\mathcal{E}_0}{\sqrt{2}}. \quad (3.25)$$

Here \mathcal{E}_0 is the unit of exchange energy on the lowest Landau level, defined as

$$\mathcal{E}_0 = \sum_{m=0}^{\infty} \langle 00, 0m | v | 00, 0m \rangle = \frac{\sqrt{2\pi}}{\ell}. \quad (3.26)$$

I choose the quantity E_0 as the unit of Coulomb energy, and express all other Coulomb matrix elements in its terms. For example,

$$\langle 00, 01 | v | 01, 00 \rangle = 0.75 E_0;$$

$$\langle 00, 01 | v | 00, 01 \rangle = 0.25 E_0.$$

The first of these two elements is the direct Coulomb term describing the repulsion of two electrons, one occupying the orbital $(n, m) = (0, 0)$, and the other - the orbital $(n, m) = (0, 1)$. This repulsion term is always nonzero, even if these electrons have opposite spins. However, the second element describes the Coulomb *exchange* between the two electrons, and it is nonzero only if the electrons have parallel spins. These spin selection rules directly follow from the form of the matrix element shown e.g. in Eq. (3.5). The spin of the two “inner” orbitals (the ones described by j and k) must be the same, since these orbitals are integrated with respect to the same variable \mathbf{r}_2 . Difference in spins would lead to orthogonality of these orbitals, and would cause the matrix element to be zero. The same is true for the two “outer” orbitals (the ones described by i and l). These spin selection rules introduce another important symmetry of the Coulomb matrix elements. Not only do they conserve the total angular momentum of the two scattered particles, but also they conserve the z component of their total spin.

Here I shall also point out that the elements depend on the magnetic field only through the length ℓ in the constant E_0 . This is clearly a multiplicative constant, and Coulomb matrix elements in different magnetic fields and in potentials with different characteristic frequency ω_0 can be obtained by a simple rescaling. The fact that they do not have to be recalculated for each magnetic field and each potential makes these matrix elements very useful in large-scale calculations, as I shall demonstrate later in this work.

The last remark concerns the numerical stability of the elements $\langle i, j | v | k, l \rangle$. As can be seen from Eq. (3.24), these elements are long sums of factorials with alternating signs.

For higher harmonic-oscillator orbitals most of these factorial terms become very large in magnitude, but they have to reduce to a final value of order of 1 (and in practice even smaller, since the element $\langle 00, 00 | v | 00, 00 \rangle$ has the largest value of all the Coulomb elements). Since the present-day computers can only store a finite amount of significant digits per number, the matrix elements involving higher and higher orbitals will carry greater and greater error. Interestingly, the accumulation of this error tends to *lower* the total energy of the system. To avoid this spurious result, the matrix elements must be calculated using computers with higher precision capabilities (for instance, quadruple precision) or software packages capable of processing numbers with arbitrary precision (such as *Mathematica* or *Maple*). In my calculations I have used the C++ high-precision package called NTL, written by Victor Shoup [113].

3.2 The Hartree-Fock method

In Chapter 2 I have discussed the single-particle spectra of typical QD potentials, and in the previous Section I have shown how the Coulomb scattering matrix elements can be calculated for one of them - the parabolic lateral confinement. At this point all terms of the Hamiltonian (3.2), describing the system of many interacting particles confined in a QD, are known, and I may start analysing the properties of this system. However, as I have already mentioned, the many-body problem defined by the Hamiltonian (3.2) is very difficult to solve, and special methods have to be developed in order to account for all aspects of the Coulomb interactions. The rest of this Chapter will be devoted to describing these methods in detail.

I start the presentation of methods with the mean-field Hartree-Fock approximation. This effective mean-field approach accounts for the direct and exchange Coulomb interactions, but does not capture the correlation effects. In spite of that this method is of interest, for two main reasons. First, its results can be compared to those obtained using

more sophisticated approaches, which allows to isolate the effects introduced by correlations from those due to the direct and exchange terms. The second reason has to do with the form in which I write the exact eigenstates of my interacting system. In the beginning of this Chapter I have mentioned that the exact eigenstates of the Hamiltonian (3.2) can be written as linear combinations of configurations $c_{i_1\sigma_1}^+ c_{i_2\sigma_2}^+ \dots c_{i_N\sigma_N}^+ |0\rangle$, created using the single-particle orbitals. In the regime of strong interactions I deal with strong configuration mixing, which causes these linear combinations to involve many terms. However, instead of distributing the particles on single-particle orbitals, I can also build my configurations by distributing the quasiparticles dressed in interactions on the effective Hartree-Fock orbitals. Since these orbitals already partially account for Coulomb interactions, the configuration mixing in this case is weaker, and one may expect that good approximations of the eigenstates of the system will take the form of linear combinations with fewer terms.

The Hartree-Fock approximation is usually formulated in real space, and involves self-consistent solving for the renormalised orbitals of each electron in the presence of the external confinement and the effective potential created by the Coulomb direct and exchange interactions with all other electrons [19]. In my approach I use the language of creation operators, and write the wave function of the N -electron system as a single Slater determinant in the following form:

$$|\Psi\rangle = A_{i_1}^+ A_{i_2}^+ \dots A_{i_N}^+ |0\rangle. \quad (3.27)$$

The operators A_i^+ create a particle on the Hartree-Fock orbital i , and can be written in terms of the single-particle creation operators as

$$A_i^+ = \sum_{j\sigma} a_{j\sigma}^{*(i)} c_{j\sigma}^+. \quad (3.28)$$

The complex coefficients $a_{j\sigma}^{(i)}$ are variational parameters of the procedure. They are chosen so as to minimise the expectation value $\langle\Psi|H|\Psi\rangle$ of the Hamiltonian 3.2 under two

constraints: (i) that the state $|\Psi\rangle$ be normalised, and (ii) that the operators A_i, A_i^+ satisfy the Fermionic anticommutation rules.

In general, the Hartree-Fock operators defined in Eq. (3.28) can involve the single-particle creation operators of all orbitals j and both spin orientations. This approach is called the spin- and space-unrestricted Hartree-Fock method [17, 133, 134]. However, since the Hamiltonian (3.2) conserves both total angular momentum and projection of the total spin, in my calculations I use the spin- and space-restricted Hartree-Fock approach, in which the creation operators A^+ are written using the single-particle creation operators c^+ with the same angular momentum and spin. For the parabolic potential the single-particle angular momentum $l = n - m$, and, for $l \leq 0$,

$$A_{il\sigma}^+ = a_{0,-l,\sigma}^{*(i)} c_{0,-l,\sigma}^+ + a_{1,(-l+1),\sigma}^{*(i)} c_{1,(-l+1),\sigma}^+ + a_{2,(-l+2),\sigma}^{*(i)} c_{2,(-l+2),\sigma}^+ + \dots \quad (3.29)$$

For positive angular momenta the Hartree-Fock creation operators take a similar form:

$$A_{il\sigma}^+ = a_{l,0,\sigma}^{*(i)} c_{l,0,\sigma}^+ + a_{(l+1),1,\sigma}^{*(i)} c_{(l+1),1,\sigma}^+ + a_{(l+2),2,\sigma}^{*(i)} c_{(l+2),2,\sigma}^+ + \dots \quad (3.30)$$

Thus, the Hartree-Fock orbitals can renormalise only within a defined angular momentum and spin channel.

The coefficients $a_{nm\sigma}^*$ are determined by minimising the expectation value $\langle \Psi | H | \Psi \rangle$ of the many-body Hamiltonian. In the case of the spin- and space-restricted Hartree-Fock approach formulated in the language of creation operators, the minimisation procedure can be reduced to an eigenvalue problem of the Hartree-Fock Hamiltonian for each angular momentum-spin channel separately. I shall describe this procedure in detail in Chapter 5, where I use the Hartree-Fock approximation to analyse the properties of a N -electron parabolic quantum dot in an external magnetic field.

3.3 The exact diagonalisation approach

In the previous Section I have presented the Hartree-Fock method, capturing the direct and exchange Coulomb effects in its treatment of many confined interacting particles. I shall now move on to presenting a method that accounts for all aspects of Coulomb interactions, including electronic correlations, in an *exact* manner with controlled accuracy. This is the exact diagonalisation approach, formulated in the configuration-interaction framework.

In the configuration interaction (CI) method the Hamiltonian (3.2) is written in the matrix form in the basis of many-electron configurations. Unlike the correlated bases of Jastrow or Hylleraas functions, the configurations making up the basis do not include correlations among pairs of interacting particles, and so their repulsive interaction is not minimised. As a result, the choice and size of the CI basis affects the accuracy of the results, and, to obtain well-converged eigenenergies and eigenstates, it is usually necessary to consider very large basis sets.

In this Section I shall focus on the CI method applied to the system of N electrons confined in a parabolic quantum dot. My description starts with the choice of the many-particle basis. I shall consider two such bases, one built by distributing electrons on single-particle orbitals, and the second obtained by distributing quasiparticles on the Hartree-Fock orbitals. Then I shall move on to writing the Hamiltonian matrix in the chosen basis. I will show how the geometrical and dynamical symmetries of the single particle states, as well as the many-particle symmetries of the Hamiltonian can be exploited in order to divide the basis set into smaller, uncoupled subsets. This will allow for a reduced basis size and improved accuracy, which in turn allows for more reliable computations of many-body properties of my system in the regime of strong correlations. But, even using these reduced and optimised basis sets, the size of Hamiltonians that I need to consider is still very large (even of order of $10^6 \times 10^6$). Such matrices cannot be directly stored in the memory of the present-day computers, and special methods have to be developed

to diagonalise them. One such method - the conjugate gradient approach coupled with spectrum folding - will be presented in detail.

3.3.1 Notation and choice of basis

Configurations built out of single-particle orbitals

For clarity of the discussion let us start with rewriting the Hamiltonian of the system of N interacting electrons:

$$\hat{H} = \sum_{i\sigma} E(i, \sigma) c_{i\sigma}^+ c_{i\sigma} + \frac{1}{2} \sum_{ijkl\sigma\sigma'} \langle i\sigma, j\sigma' | V | k\sigma', l\sigma \rangle c_{i\sigma}^+ c_{j\sigma'}^+ c_{k\sigma'} c_{l\sigma}. \quad (3.31)$$

Because I shall now concentrate on the case of parabolic lateral confinement, the composite index i denotes the single-particle Fock-Darwin orbital quantum numbers (n, m) .

I construct the basis of my many-particle Hilbert space out of electronic configurations by distributing my N electrons on the single-particle Fock-Darwin states in all possible ways, however obeying the Pauli exclusion principle. In the language of creation operators compatible with the Hamiltonian (3.31), such configurations will take the form:

$$|n_1 m_1 \sigma_1, n_2 m_2 \sigma_2, \dots, n_N m_N \sigma_N\rangle = c_{n_1 m_1 \sigma_1}^+ c_{n_2 m_2 \sigma_2}^+ \dots c_{n_N m_N \sigma_N}^+ |0\rangle. \quad (3.32)$$

Such configurations are orthonormal, because the single-particle Fock-Darwin orbitals are orthonormal. The only question concerns the size of this basis.

As I have shown in Section 2.1, the single-particle Fock-Darwin spectrum consists of an infinite number of levels. To be able to perform computations, I thus need to restrict the basis size, similarly as I did in Section 2.2.2: Out of the infinite number of the Fock-Darwin states I only choose a finite number M of those with the lowest energies. In the simple case of the single electron confined in a disk in a magnetic field I only needed a small number of such states (in my model 20), but I clearly stated that such a fast convergence was due to the strong zero-field quantisation brought about by the small size of the disk. Here I deal with the parabolic potential, much softer compared to that

of the disk, and I need to compare the quantisation of the single-particle energy to the characteristic energies of the Coulomb interactions. As I shall show in the next Chapter, these two energy scales are comparable, which makes it necessary to consider more single-particle levels in order to obtain a well-converged result. I shall treat the number M as a parameter controlling my approximation - the *only* approximation in the method.

Let us now find the size of the many-particle basis. I have N electrons, of which N_{\uparrow} with spin up and N_{\downarrow} with spin down, and I have to distribute them on M single-particle orbitals. Since all M single-particle states are degenerate with respect to the electron spin, the full basis size is obtained as a product

$$\text{basis size} = \binom{M}{N_{\uparrow}} \binom{M}{N_{\downarrow}}, \quad (3.33)$$

in which I simply consider distributing the spin up electrons and the spin down electrons on M levels independently (one electron of each species can occupy the same Fock-Darwin orbital).

Configurations built out of the Hartree-Fock orbitals

The configurations constructed in the previous paragraph are Slater determinants built out of single-particle orbitals, and thus they do not include correlations between pairs of particles. Thus the particle-particle Coulomb repulsion is not minimised, which results in large diagonal and offdiagonal Hamiltonian matrix elements. This in turn entails the necessity of using very large basis sets in order to obtain accurate results.

Here I shall describe a different method of constructing the many-particle basis set: instead of distributing the electrons on the single-particle orbitals, I shall distribute the quasielectrons on the Hartree-Fock orbitals.

In Section 3.2, I have described the Hartree-Fock approximation in the language of effective creation and annihilation operators. In the space- and spin-restricted version of

the method these operators are written as

$$A_{1l\sigma}^+ = a_{n,m,\sigma}^{*(1)} c_{n,m,\sigma}^+ + a_{n+1,m+1,\sigma}^{*(1)} c_{n+1,m+1,\sigma}^+ + a_{n+2,m+2,\sigma}^{*(1)} c_{n+2,m+2,\sigma}^+ + \dots \quad (3.34)$$

$$A_{2l\sigma}^+ = a_{n,m,\sigma}^{*(2)} c_{n,m,\sigma}^+ + a_{n+1,m+1,\sigma}^{*(2)} c_{n+1,m+1,\sigma}^+ + a_{n+2,m+2,\sigma}^{*(2)} c_{n+2,m+2,\sigma}^+ + \dots \quad (3.35)$$

$$A_{3l\sigma}^+ = a_{n,m,\sigma}^{*(3)} c_{n,m,\sigma}^+ + a_{n+1,m+1,\sigma}^{*(3)} c_{n+1,m+1,\sigma}^+ + a_{n+2,m+2,\sigma}^{*(3)} c_{n+2,m+2,\sigma}^+ + \dots \quad (3.36)$$

with the angular momentum $l = n - m$, and coefficients a established in the Hartree-Fock minimisation. For each angular momentum and spin channel there is one-to-one correspondence between the effective creation operators A^+ (and the effective annihilation operators A) and the Fock-Darwin creation and annihilation operators c^+ and c , respectively. The transformation between one set of operators and the other can be seen simply as a rotation, and let us denote the rotation matrix as $U_{l\sigma}$: $A_{il\sigma}^+ = \sum_j U_{l\sigma}(i, j) c_{jl\sigma}^+$. This matrix may, in general, be different for each angular momentum and spin channel. Moreover, the operators A^+ and A can be constructed not only for occupied, but also for unoccupied orbitals. This operation is outside of the Hartree-Fock procedure itself; the corresponding sets of coefficients a are the eigenvectors obtained in the diagonalisation of the Hartree-Fock matrices for all angular momentum and spin channels (including those that do not contain electrons).

By performing the rotation $U_{l\sigma}$ I create a new, effective single-quasiparticle basis set, whose orbitals account for the direct and exchange interactions in the system. It is therefore advantageous to build my many-particle configurations in the new basis.

The construction of the many-particle basis set proceeds as follows. First I perform the Hartree-Fock procedure to find the Hartree-Fock ground state $|\Psi\rangle$, thereby establishing the rotation matrices $U_{l\sigma}$. Then I write my many-body Hamiltonian in the language of the effective creation and annihilation operators:

$$\begin{aligned} \hat{H} = & \sum_{k,k',l,\sigma} t_{kl\sigma,k'l\sigma} A_{kl\sigma}^+ A_{k'l\sigma} \\ & + \frac{1}{2} \sum_{k_1 k_2 k_3 k_4} \sum_{l_1 l_2 l_3 l_4} \sum_{\sigma \sigma'} \langle k_1 l_1 \sigma, k_2 l_2 \sigma' | V | k_3 l_3 \sigma', k_4 l_4 \sigma \rangle A_{k_1 l_1 \sigma}^+ A_{k_2 l_2 \sigma'}^+ A_{k_3 l_3 \sigma'} A_{k_4 l_4 \sigma}. \end{aligned} \quad (3.37)$$

Note that in the basis of the effective Hartree-Fock orbitals the energy term t is not diagonal, but couples different orbitals within the same angular momentum and spin channel. The Coulomb matrix elements in the new basis are obtained by a rotation:

$$\begin{aligned} \langle k_1 l_1, k_2 l_2 | V | k_3 l_3, k_4 l_4 \rangle &= \sum_{n_1 m_1} \sum_{n_2 m_2} \sum_{n_3 m_3} \sum_{n_4 m_4} \langle n_1 m_1, n_2 m_2 | V | n_3 m_3, n_4 m_4 \rangle \\ &\times U_{l_1}(k_1, (n_1 m_1)) U_{l_2}(k_2, (n_2 m_2)) U_{l_3}^+(k_3, (n_3 m_3)) U_{l_4}^+(k_4, (n_4 m_4)). \end{aligned} \quad (3.38)$$

The summation over the Fock-Darwin indices (nm) is done under constraints $n_1 - m_1 = l_1$, $n_2 - m_2 = l_2$, $n_3 - m_3 = l_3$ and $n_4 - m_4 = l_4$. At this point both the effective single-particle basis and the rotated Hamiltonian are known. I can proceed to distributing my quasiparticles on the Hartree-Fock orbitals and creating the configurations of the type

$$|k_1 l_1 \sigma_1, k_2 l_2 \sigma_2, \dots, k_N l_N \sigma_N\rangle = A_{k_1 l_1 \sigma_1}^+ A_{k_2 l_2 \sigma_2}^+ \dots A_{k_N l_N \sigma_N}^+ |0\rangle. \quad (3.39)$$

From this moment on, creation of the many-particle basis and diagonalisation of the Hamiltonian is carried out exactly in the same way as it is done for the case of non-renormalised single-particle orbitals.

An alternative way of constructing the manyparticle basis set is to start with the Hartree-Fock ground state $|\Psi\rangle$ and construct the basis vectors as quasielectron-quasihole pair excitations from this state. For example, the single-pair excitations are created as configurations of the type

$$A_{k_1 l_1 \sigma}^+ A_{k_2 l_2 \sigma'} |\Psi\rangle,$$

and can be constructed either with $(\sigma \neq \sigma')$ or without $(\sigma = \sigma')$ flipping the spin of the quasiparticle. Such excitations are thus obtained from the Hartree-Fock ground state by taking one quasiparticle (electron dressed in interactions) from below the Fermi energy, which creates a hole in the interior of the electronic droplet. The quasielectron is then put on one of the unoccupied Hartree-Fock orbitals above the Fermi energy. In this way I can create two- and multiple-pair excitations. Note that this approach allows to isolate the lower-lying excitations (two- and three-pair) from higher-lying ones (multiple-pair). In the exact-diagonalisation procedure the largest corrections to the energy of the

system are introduced by those basis states that are closest in energy to the ground state, as I have demonstrated in Section 2.2.2 on the example of the single-particle spectrum. Therefore it is advantageous to build my basis set from the vectors describing the few-pair excitations, as being more relevant for the accuracy of the result, and neglect the higher-pair excitations. I shall demonstrate the details of this procedure in Chapter 5, where I shall use the Hartree-Fock and exact diagonalisation methods to analyse the properties of the system of interacting electrons confined in a parabolic QD in an external magnetic field.

3.3.2 Exact diagonalisation method optimised for parabolic lateral confinements

From the formula (3.33) it is clear that this size grows factorially both with the number of single-particle states M and the number of electrons N . For instance, if I take six electrons, with $N_{\uparrow} = 3$ and $N_{\downarrow} = 3$, and distribute them in all possible ways on $M = 20$ orbitals, the total basis size is 1299600. This means that without further refinement I am unable to obtain any meaningful results with this method.

The optimisation of the basis set involves exploiting the symmetries of the system. I have demonstrated this idea at work already in Section 2.2.2, where I isolated subsets of the basis with definite angular momentum and definite vertical quantum number, and demonstrated that the Hamiltonian does not couple them. Because of that I could resolve the angular momentum-subband channels, and I performed the diagonalisation study in each such channel.

In the case of the many-particle system in the parabolic confinement I also have several symmetries, leading to a block-diagonal form of the Hamiltonian in the full configuration basis. The total Hamiltonian (3.31) in the basis of configurations built out of harmonic-oscillator single-particle basis conserves the total angular momentum L , total spin \mathbf{S} , and

total spin projection S_z of the system, and therefore I may classify the many-particle configurations into groups labelled by these three quantum numbers. The same is true for the Hamiltonian (3.38) in the basis of configurations built out of the effective Hartree-Fock orbitals calculated in the spin- and space-restricted approach. However, out of these two Hamiltonians only the first one exhibits an additional symmetry, stemming from the parabolic form of the confinement: it couples only the states with the same type of the centre-of-mass motion. This additional, fourth good quantum number allows to optimise the harmonic-oscillator many-particle basis set better than the one based on Hartree-Fock orbitals, and therefore in the rest of this Section I will focus on the former.

A detailed discussion of the optimisation steps applied to the many-particle basis set on the specific example of an N -electron parabolic quantum dot in a magnetic field is presented in the article “Configuration interaction method for Fock-Darwin states”, written by Andreas Wensauer, Marek Korkusiński, and Pawel Hawrylak, and published in Solid State Communications, vol. 130, page 115 (2004). This publication is an integral part of this thesis and is appended to the presented material. Here I will highlight its most important points.

Angular momentum

Let us start with the conservation of total angular momentum. The total angular momentum operator is defined as

$$\hat{L} = \sum_{nm\sigma} (n - m) c_{nm\sigma}^+ c_{nm\sigma}. \quad (3.40)$$

Since the parabolic confinement is circularly symmetric, each single-particle orbital has a definite angular momentum, and therefore the operator \hat{L} commutes with the single-particle energy term (consisting of the kinetic energy operator and the external confinement potential) of the Hamiltonian (3.31). Moreover, as I have demonstrated in Section 3.1.2, the Coulomb interactions conserve the total angular momentum of the scattered

pair of particles. Thus the operator \hat{L} commutes also with the interaction term in this Hamiltonian. This allows me to group my basis configurations into subspaces according to the total angular momentum.

Projection of the total spin

The second symmetry is the projection of the total spin S_z , whose corresponding operator is defined as:

$$\hat{S}_z = \sum_{nm\sigma} \sigma c_{nm\sigma}^+ c_{nm\sigma}. \quad (3.41)$$

In the Hamiltonian (3.31) there is only one term that couples to the spin of each electron: the single-particle Zeeman term in the single-particle energy operator. The Zeeman term, however, does not lead to spin flips, but lowers or increases the energy of a single-particle orbital depending on the magnetic field and the direction of the electronic spin. This means that the operator \hat{S}_z commutes with the total Hamiltonian, and all the configurations from each angular momentum subspace can be further grouped according to the value of their total spin projection S_z .

Total spin

Accounting for the conservation of the total spin \mathbf{S} of the system is more complicated. The total spin is a vector quantity, and to simplify my description I will focus on its square: the operator \hat{S}^2 . This operator, written in the language of creation and annihilation operators for N confined electrons, takes the form

$$\hat{S}^2 = \frac{N}{2} + \hat{S}_z^2 - \sum_{ij} c_{j\uparrow}^+ c_{i\downarrow}^+ c_{j\downarrow} c_{i\uparrow}. \quad (3.42)$$

The two first terms of the operator \hat{S}^2 are diagonal, and give the same values for all the N -electron configurations from the same angular-momentum and S_z -resolved basis set. The third term, however, couples many-particle configurations in such a way that it annihilates the particle on the orbital i and recreates it on the same orbital with the flipped spin;

the same is true for particle j . Note that for the two configurations to be coupled by \hat{S}^2 , they have to exhibit the same pattern of orbital quantum numbers, and only differ in the way the spin-up and spin-down electrons are distributed on these orbitals. For example, the operator \hat{S}^2 couples the configuration $|a\rangle = c_{00\uparrow}^+ c_{11\downarrow}^+ |0\rangle$ to $|b\rangle = c_{11\uparrow}^+ c_{00\downarrow}^+ |0\rangle$, but none of these configurations is coupled to $|c\rangle = c_{00\uparrow}^+ c_{33\downarrow}^+ |0\rangle$. Therefore it is possible to arrange the many-particle configurations into blocks with the same orbital pattern. I can then construct the matrix \hat{S}^2 in the basis of each of these blocks and diagonalise it numerically to obtain the eigenstates of the total spin operator. For example, in the basis of my two configurations $\{|a\rangle, |b\rangle\}$ the matrix of the operator \hat{S}^2 takes the form

$$\hat{S}^2 = \begin{bmatrix} 1 & -1 \\ -1 & 1 \end{bmatrix}, \quad (3.43)$$

and, upon the diagonalisation of this simple matrix one obtains the eigenstate $|S\rangle = \frac{1}{\sqrt{2}}(|a\rangle + |b\rangle)$ with the eigenvalue $S^2 = 0$, and the eigenstate $|T\rangle = \frac{1}{\sqrt{2}}(|a\rangle - |b\rangle)$ with the eigenvalue $S^2 = 2$. The first eigenstate is the spin singlet, and the second - the spin triplet. To enumerate these states, usually the eigenvalue of the total spin is used instead of the eigenvalue of \hat{S}^2 ; these two eigenvalues are connected via the relationship

$$\langle \hat{S}^2 \rangle = S(S + 1). \quad (3.44)$$

This means that the eigenvalue corresponding to the state $|S\rangle$ is $S = 0$, and the one corresponding to the state $|T\rangle$ is $S = 1$. The rotation to the basis of total spin eigenvectors becomes increasingly more complicated as the number of particles increases. The spin blocks are, however, fairly small, and are composed, e.g., of up to several hundred configurations for the system with $N = 6$ electrons. From this simple analysis it is clear that the many-particle basis with resolved total angular momentum, total spin, and total projection of the total spin will no longer consist of many-particle configurations, but will be composed of their linear combinations.

To illustrate how resolving the total spin as a good quantum number decreases the size of the many-particle basis, let us consider the system of $N = 6$ electrons, out of

which $N_{\uparrow} = 3$ are spin up and $N_{\downarrow} = 3$, distributed on the $M = 121$ single-particle orbitals (n, m) , for which $0 \leq n \leq 10$ and $0 \leq m \leq 10$. According to the formula (3.33), by distributing these electrons on these single-particle orbitals more than 8.29×10^{10} many-particle configurations can be generated. Out of those configurations there are 326120 configurations with total angular momentum $L = 0$. Further, if I resolve the total spin as a good quantum number, I obtain 92410 configurations with $S = 0$, 152460 configurations with $S = 1$, 70711 configurations with $S = 2$, and 10593 configurations with $S = 3$. Therefore, by resolving the two quantum numbers L and S I have reduced the size of the problem of six electrons with total spin projection $S_z = 0$ by five orders of magnitude.

Centre of mass

Let us now move on to describing the last symmetry, involving the centre-of-mass (CM) motion of the system. The parabolic confinement allows for a separation of the CM and relative motion of N interacting confined electrons, and so the real-space Hamiltonian of the system can be written as [51, 62]:

$$\hat{H} = \hat{H}_{CM}(\mathbf{R}, \mathbf{P}) + \hat{H}_{rel}(\varrho_1, \dots, \varrho_{N-1}, \pi_1, \dots, \pi_{N-1}). \quad (3.45)$$

Here, $N\mathbf{R} = \sum_{i=1}^N \mathbf{r}_i$ and $\mathbf{P} = \sum_{i=1}^N \mathbf{p}_i$ are the CM coordinate and momentum, respectively, and ϱ_i, π_i are, respectively, the position and momentum of the i -th relative particle, which can be written using Jacobi coordinates [62]. In the following I shall focus on the CM Hamiltonian, which, when written in the real-space representation, takes the form:

$$\hat{H}_{CM} = \frac{1}{2Nm^*} \mathbf{P}^2 + \frac{1}{2} Nm^* \omega_h \mathbf{R}^2 + \frac{1}{\omega_c} 2[\mathbf{R} \times \mathbf{P}]_z. \quad (3.46)$$

The notation used in this formula follows that introduced in the Section 2.1. I can now express the CM position and momentum by the single-particle raising and lowering operators a^+, b^+, a , and b , and write the CM Hamiltonian in the second quantisation as:

$$\hat{H}_{CM} = \hbar\omega_+ \left(\hat{A}_+^\dagger \hat{A}_+ + \frac{1}{2} \right) + \hbar\omega_- \left(\hat{A}_-^\dagger \hat{A}_- + \frac{1}{2} \right), \quad (3.47)$$

where the operators A_+^+ , A_+ , A_-^+ , and A_- are bosonic operators describing collective CM excitations of the system:

$$\hat{A}_+^+ = \frac{1}{\sqrt{N}} \sum_{nm\sigma} \sqrt{n+1} c_{(n+1)m\sigma}^+ c_{nm\sigma}; \quad (3.48)$$

$$\hat{A}_-^+ = \frac{1}{\sqrt{N}} \sum_{nm\sigma} \sqrt{m+1} c_{n(m+1)\sigma}^+ c_{nm\sigma}; \quad (3.49)$$

$$\hat{A}_+ = \frac{1}{\sqrt{N}} \sum_{nm\sigma} \sqrt{n} c_{(n-1)m\sigma}^+ c_{nm\sigma}; \quad (3.50)$$

$$\hat{A}_- = \frac{1}{\sqrt{N}} \sum_{nm\sigma} \sqrt{m} c_{n(m-1)\sigma}^+ c_{nm\sigma}. \quad (3.51)$$

These operators can be interpreted respectively as creation and annihilation operators for collective excitations of the system. The operator A_+^+ (A_+) increases (decreases) the total energy of the system by $\hbar\omega_+$, while the operator A_-^+ (A_-) increases (decreases) the total energy of the system by $\hbar\omega_-$. Note that these operators do not couple to the interaction term in the many-particle Hamiltonian. The CM operators can be now constructed using the four operators defined above as:

$$\hat{C}_+ = A_+^+ A_+ = \frac{1}{N} \sum_{n'm'\sigma'n m\sigma} \sqrt{n(n'+1)} c_{(n'+1)m'\sigma'}^+ c_{n'm'\sigma'} c_{(n-1)m\sigma}^+ c_{nm\sigma}, \quad (3.52)$$

$$\hat{C}_- = A_-^+ A_- = \frac{1}{N} \sum_{n'm'\sigma'n m\sigma} \sqrt{m(m'+1)} c_{n'(m'+1)\sigma'}^+ c_{n'm'\sigma'} c_{n(m-1)\sigma}^+ c_{nm\sigma}. \quad (3.53)$$

These two operators commute with the total Hamiltonian.

Let us focus, for example, on the operator \hat{C}_- . Note that this operator affects only the pattern of orbital quantum numbers m , leaving the number n of each electron unchanged. Therefore, similarly to the case of the total spin, I can arrange the configurations into blocks. The configurations belonging to each block have the same pattern of quantum numbers $n\sigma$, but differ in the patterns of the numbers m . To resolve the CM quantum numbers I build the matrix corresponding to the operator \hat{C}_- in each block and diagonalise it numerically. As a result I obtain the eigenvectors of the total centre-of-mass operator, together with the corresponding CM quantum numbers. For further processing it is sufficient to collect only those CM eigenstates with CM eigenvalues equal to zero; all other eigenstates can be generated simply by application of the CM raising operator A_-^+ .

In the paper we apply the basis reduction rules discussed in this Section to a model case of $N = 4 - 7$ interacting electrons confined by a parabolic potential in the absence of the magnetic field, and $N = 4$ electrons in the magnetic field. We show that the obtained results compare well with those obtained using the quantum Monte Carlo and stochastic-variational methods. We also point out that use of the optimised configuration-interaction approach allows to calculate reliably not only the ground state, but also the excited states of the system, an ability which the two other methods lack.

3.3.3 Creation of the Hamiltonian matrix

I have demonstrated how I create the basis of configurations and how I can optimise it to account for the symmetries of the system. Let us now move on to describing how the Hamiltonian is written in the matrix form in this basis.

I will describe the creation of the Hamiltonian matrix on a simple example of the system of $N = 3$ electrons, two with spin down and one with spin up. I shall restrict the number of the single-particle Fock-Darwin states available for my electrons to three: $(n, m) = (0, 0)$, $(n, m) = (0, 1)$, and $(n, m) = (1, 0)$. According to Eq. (3.33), in this case I can generate nine electronic configurations with different angular momenta. To optimise this basis I focus on the states with total angular momentum $L = -1$ only. This reduces my set to two configurations:

$$|a\rangle = c_{0,0,\downarrow}^+ c_{0,1,\downarrow}^+ c_{0,0,\uparrow}^+ |0\rangle; \quad (3.54)$$

$$|b\rangle = c_{0,1,\downarrow}^+ c_{1,0,\downarrow}^+ c_{0,1,\uparrow}^+ |0\rangle. \quad (3.55)$$

Note that in writing these two configurations I am using a convention, to which I shall adhere throughout this work: from left to right I write the creation operators first for spin-down, and then for spin-up electrons, and for each spin species I arrange the orbitals according to their energy in ascending order.

The configuration $|a\rangle$ is composed of two electrons with antiparallel spins occupying

the orbital $(0, 0)$ and one spin-down electron on the orbital $(0, 1)$. The configuration $|b\rangle$, on the other hand, consists of two electrons with antiparallel spins on the orbital $(0, 1)$ and one spin-down electron on the orbital $(1, 0)$. Both configurations have total spin $S = 1/2$, so my basis set $\{|a\rangle, |b\rangle\}$ is already composed of total spin eigenstates.

In my simple basis the Hamiltonian can be written as a 2×2 matrix in the following form:

$$\hat{H} = \begin{bmatrix} \langle a|H|a\rangle & \langle a|H|b\rangle \\ \langle b|H|a\rangle & \langle b|H|b\rangle \end{bmatrix}. \quad (3.56)$$

My task is to calculate the matrix elements $\langle a|H|a\rangle$, $\langle a|H|b\rangle = \langle b|H|a\rangle^*$, and $\langle b|H|b\rangle$ using the form of the Hamiltonian as in Eq. (3.31). To simplify the description, I shall write the total Hamiltonian as a sum of two operators:

$$\hat{H} = \hat{T} + \hat{H}_C, \quad (3.57)$$

where \hat{T} is the single-particle energy operator, describing the motion of each particle in the external confinement of the nanostructure, and \hat{H}_C is the Coulomb operator. I shall calculate the matrix elements of each of these two operators separately.

Single-particle energy operator

The single-particle energy operator written using the Fock-Darwin creation and annihilation operators takes the form:

$$\hat{T} = \sum_{nm\sigma} E(n, m, \sigma) c_{nm\sigma}^+ c_{nm\sigma}. \quad (3.58)$$

Let us calculate in detail the matrix element $T_{aa} = \langle a|\hat{T}|a\rangle$.

$$T_{aa} = \sum_{nm\sigma} E(n, m, \sigma) \langle 0|c_{0,0,\uparrow}c_{0,1,\downarrow}c_{0,0,\downarrow}|c_{nm\sigma}^+c_{nm\sigma}|c_{0,0,\downarrow}^+c_{0,1,\downarrow}^+c_{0,0,\uparrow}^+|0\rangle. \quad (3.59)$$

This matrix element has a form of a sum over the single-particle indices $nm\sigma$. Note that the operator $c_{nm\sigma}^+c_{nm\sigma} = n_{nm\sigma}$ is a number operator, returning the number of electrons on the orbital $nm\sigma$. Therefore the only nonzero terms in this sum will be those with the

indices $nm\sigma$ corresponding to the indices of one of the creation operators in the state $|a\rangle$; other orbitals contain zero electrons. Therefore, in this case

$$\begin{aligned} T_{aa} &= E(0, 0, \downarrow) \langle 0 | c_{0,0,\uparrow} c_{0,1,\downarrow} c_{0,0,\downarrow} | n_{0,0,\downarrow} c_{0,0,\downarrow}^+ c_{0,1,\downarrow}^+ c_{0,0,\uparrow}^+ | 0 \rangle \\ &+ E(0, 1, \downarrow) \langle 0 | c_{0,0,\uparrow} c_{0,1,\downarrow} c_{0,0,\downarrow} | n_{0,1,\downarrow} c_{0,0,\downarrow}^+ c_{0,1,\downarrow}^+ c_{0,0,\uparrow}^+ | 0 \rangle \\ &+ E(0, 0, \uparrow) \langle 0 | c_{0,0,\uparrow} c_{0,1,\downarrow} c_{0,0,\downarrow} | n_{0,0,\uparrow} c_{0,0,\downarrow}^+ c_{0,1,\downarrow}^+ c_{0,0,\uparrow}^+ | 0 \rangle. \end{aligned} \quad (3.60)$$

Since in each case the orbitals defined by the indices of the number operator contain one electron, all expectation values of \hat{n} will be equal to 1, and the matrix element

$$T_{aa} = E(0, 0, \downarrow) + E(0, 1, \downarrow) + E(0, 0, \uparrow). \quad (3.61)$$

Thus, the matrix element T_{aa} is equal to the sum of the single-particle energies of orbitals occupied by each electron. Similarly one can show that

$$T_{bb} = E(0, 1, \downarrow) + E(1, 0, \downarrow) + E(0, 1, \uparrow). \quad (3.62)$$

The off-diagonal matrix elements $\langle a | \hat{T} | b \rangle = \langle b | \hat{T} | a \rangle$ involve expectation values of the type $\langle a | n_{nm\sigma} | b \rangle$. Since the number operator \hat{n} cannot redistribute electrons, these expectation values will be zero. Thus, the single-particle energy operator in my basis is a diagonal matrix:

$$\hat{T} = \begin{bmatrix} T_{aa} & 0 \\ 0 & T_{bb} \end{bmatrix}. \quad (3.63)$$

Note that if the configurations are built out of the Hartree-Fock orbitals instead of the Fock-Darwin ones, this operator can contain nonzero off-diagonal elements, as can be seen from the form of the operator \hat{T} in Eq. (3.38).

Coulomb operator

Let us now focus on the Coulomb operator

$$\hat{H}_C = \frac{1}{2} \sum_{ijkl} \langle ij | v | kl \rangle c_i^+ c_j^+ c_k c_l, \quad (3.64)$$

where the composite index $i = nm\sigma$; the same applies to j , k , and l . In what follows I shall make use of the fact that my single-particle basis set is ordered according to the spin and single-particle energy, so, for instance, the notation $k > l$ will mean that the orbital k is higher up in the single-particle basis than the orbital l .

In the Coulomb operator (3.64) the composite indices run over all available single-particle orbitals. In particular, I need to consider terms with $k < l$ and $k > l$ (the term with $k = l$ is identically zero, since in this case the two annihilation operators would act on the same orbital).

I shall now demonstrate that I can reduce the number of terms in the sum in Eq. (3.64) using the Fermionic commutation rules for the operators c and c^+ written in Eq. (3.4).

Let us focus on the indices k and l first. I can separate the sum into two terms: one for $k < l$, and one for $k > l$:

$$\hat{H}_C = \frac{1}{2} \left(\sum_{i,j,k < l} \langle ij|v|kl \rangle c_i^+ c_j^+ c_k c_l + \sum_{i,j,k > l} \langle ij|v|kl \rangle c_i^+ c_j^+ c_k c_l \right). \quad (3.65)$$

In the second term I interchange the two annihilation operators, observing the Fermionic commutation rules: $c_k c_l = -c_l c_k$. I also rename the dummy indices: $k \rightarrow l$ and $l \rightarrow k$. This allows me to write the Coulomb operator in the form:

$$\hat{H}_C = \frac{1}{2} \sum_{i,j,k < l} (\langle ij|v|kl \rangle - \langle ij|v|lk \rangle) c_i^+ c_j^+ c_k c_l. \quad (3.66)$$

The first term in this sum is the Coulomb direct element. This matrix element attains a nonzero value only if the spin of the orbital $|i\rangle$ is the same as that of the orbital $|l\rangle$ and the spin of the orbital $|j\rangle$ is the same as that of the orbital $|k\rangle$, however, the spin of $|i\rangle$ can be different than that of $|j\rangle$. The second term in the sum is the Coulomb exchange element. This matrix element attains a nonzero value only if the scattered particles have the same spin.

I can perform a similar simplification for orbitals i and j . As a result, I will obtain another pair of matrix elements, one direct and one exchange, identical to the elements in Eq. (3.66). Upon their summation the factor $1/2$ in front of the sum is eliminated, and

the final form of the Coulomb operator is

$$\hat{H}_C = \sum_{i>j, k<l} (\langle ij|v|kl\rangle - \langle ij|v|lk\rangle) c_i^+ c_j^+ c_k c_l. \quad (3.67)$$

Let us now calculate the matrix elements of the Coulomb operator \hat{H}_C in my basis $\{|a\rangle, |b\rangle\}$ of the three-electron configurations, starting with the diagonal element $\langle a|\hat{H}_C|a\rangle = H_C^{aa}$.

$$H_C^{aa} = \sum_{i>j, k<l} (\langle ij|v|kl\rangle - \langle ij|v|lk\rangle) \langle 0|c_{0,0,\uparrow}c_{0,1,\downarrow}c_{0,0,\downarrow}|c_i^+c_j^+c_kc_l|c_{0,0,\downarrow}^+c_{0,1,\downarrow}^+c_{0,0,\uparrow}^+|0\rangle. \quad (3.68)$$

Note that the element $\langle 0|c_{0,0,\uparrow}c_{0,1,\downarrow}c_{0,0,\downarrow}|c_i^+c_j^+c_kc_l|c_{0,0,\downarrow}^+c_{0,1,\downarrow}^+c_{0,0,\uparrow}^+|0\rangle$ can be understood as the dot product of two vectors:

$$c_jc_ic_{0,0,\downarrow}^+c_{0,1,\downarrow}^+c_{0,0,\uparrow}^+|0\rangle \quad \text{and} \quad c_kc_lc_{0,0,\downarrow}^+c_{0,1,\downarrow}^+c_{0,0,\uparrow}^+|0\rangle, \quad (3.69)$$

with $i > j$ and $k < l$. It is now clear why I chose these boundaries in summation in Eq. (3.67): in each case, out of the two annihilation operators, the first one (i.e., c_i and c_l , respectively) removes an electron created deeper (farther to the right) in the sequence of operators c^+ as compared to the second annihilation operator (i.e., c_j and c_k , respectively). This simplifies the automatic computation of the matrix elements, since I do not have to check whether a given electron in the configuration has already been removed or not.

Let us now enumerate the possible sets of orbitals i, j and k, l , for which the vectors in Eq. (3.69) are nonzero. As for the pair i, j , there are three possibilities. One of them is $i = (0, 1, \downarrow)$, $j = (0, 0, \downarrow)$, which gives

$$c_{0,0,\downarrow}c_{0,1,\downarrow}c_{0,0,\downarrow}^+c_{0,1,\downarrow}^+c_{0,0,\uparrow}^+|0\rangle = -c_{0,0,\uparrow}^+|0\rangle.$$

The minus sign in the above expression is a phase factor, originating from the fact that in order to act with the operator $c_{0,1,\downarrow}$, I need to reverse the order of this operator and the first creation operator in the sequence. This introduces the minus sign due to the Fermionic commutation rules of these operators.

The second possible pair of orbitals i, j is $i = (0, 0, \uparrow)$, $j = (0, 0, \downarrow)$; upon their application I am left with the vector $+c_{0,1,\downarrow}^+|0\rangle$. Here the phase factor is positive because in order to act with $c_{0,0,\uparrow}$, I need to reverse the order of operators twice.

Finally, the third possible pair of orbitals is $i = (0, 0, \uparrow)$, $j = (0, 1, \downarrow)$. Their application gives $-c_{0,0,\downarrow}^+|0\rangle$, the negative phase being due to the three reversals of operators necessary to complete it.

Since the second vector in Eq. (3.69) is exactly the same as the first one, the possible pairs of orbitals k, l are identical to the pairs i, j described above. This gives $3 \times 3 = 9$ possible terms in the sum (3.68). The number of terms is further decreased by considering the dot products of the vectors from Eq. (3.69) for each combination of orbitals. These dot products will be nonzero only if the third electron (i.e., the electron that remains after the application of annihilation operators) is the same on either side. In the case of diagonal matrix elements of the Coulomb operator, and in particular for the element H_C^{aa} , this happens only if the orbitals $i = l$ and $j = k$. Thus the number of nonzero dot products is reduced to three, and the matrix element

$$\begin{aligned} H_C^{aa} &= (\langle 01, 00 | v | 00, 01 \rangle - \langle 01, 00 | v | 01, 00 \rangle) \\ &+ \langle 00, 00 | v | 00, 00 \rangle + \langle 00, 01 | v | 01, 00 \rangle. \end{aligned} \quad (3.70)$$

The term in braces corresponds to the orbitals $i = l = (0, 1, \downarrow)$, $j = k = (0, 0, \downarrow)$ and consists of the direct and exchange elements because the scattered electrons have the same spins. The two remaining terms in \hat{H}_C^{aa} correspond to the two other sets of orbitals and consist of direct elements only.

In an analogous fashion one can show that the second diagonal matrix element of the Coulomb operator is

$$\begin{aligned} H_C^{bb} &= (\langle 10, 01 | v | 01, 10 \rangle - \langle 10, 01 | v | 10, 01 \rangle) \\ &+ \langle 01, 01 | v | 01, 01 \rangle + \langle 01, 10 | v | 10, 01 \rangle. \end{aligned} \quad (3.71)$$

The off-diagonal matrix element \hat{H}_C^{ab} , on the other hand, consists of only one term:

$$H_C^{ab} = -\langle 00, 00 | v | 10, 01 \rangle. \quad (3.72)$$

This term corresponds to the following choice of orbitals: $i = (0, 0, \uparrow)$, $j = (0, 0, \downarrow)$, $k = (1, 0, \downarrow)$, $l = (0, 1, \uparrow)$. It has a negative phase, because the application of operators $c_j c_i$ requires two interchanges of operators, and application of the pair $c_k c_l$ requires three such interchanges. Thus the phase is $(-1)^{2+3} = (-1)$.

The full Hamiltonian

I am now ready to write my full Hamiltonian matrix in the basis $\{|a\rangle, |b\rangle\}$:

$$\hat{H} = \begin{bmatrix} T_{aa} + H_C^{aa} & H_C^{ab} \\ (H_C^{ab})^* & T_{bb} + H_C^{bb} \end{bmatrix}. \quad (3.73)$$

If I calculate the elements of the single-particle energy operator using the Fock-Darwin energies, and the elements of the Coulomb operator using the matrix elements $\langle ij | v | kl \rangle$ in the harmonic-oscillator basis, the resulting Hamiltonian matrix takes the form:

$$\hat{H} = \begin{bmatrix} \frac{3}{2}\hbar\omega_+ + \frac{5}{2}\hbar\omega_- + 2.25E_0 & -0.25E_0 \\ -0.25E_0 & \frac{5}{2}\hbar\omega_+ + \frac{7}{2}\hbar\omega_- + 1.875E_0 \end{bmatrix}, \quad (3.74)$$

where $E_0 = \sqrt{\pi}/\ell$. The eigenvalues of this simple matrix can be obtained analytically, and are

$$E_1 = 2\hbar\omega_+ + 3\hbar\omega_- + 2.0625E_0 + \frac{\sqrt{(\hbar\omega_+ + \hbar\omega_- 0.375E_0)^2 + 0.25E_0^2}}{2}, \quad (3.75)$$

$$E_2 = 2\hbar\omega_+ + 3\hbar\omega_- + 2.0625E_0 - \frac{\sqrt{(\hbar\omega_+ + \hbar\omega_- 0.375E_0)^2 + 0.25E_0^2}}{2}. \quad (3.76)$$

In this model calculation I assumed a very simple, two-element basis set. Later on I shall use much larger basis sets of configurations, however in all such cases the rules of constructing the Hamiltonian matrix remain the same.

The last step of the exact diagonalisation approach involves numerical diagonalisation of the Hamiltonian matrix. To this end I could use the numerical procedures appropriate

for full matrices, requiring that the entire matrix be stored in the memory of the computer. This, however, would be limiting, since the matrix of order of about 11000×11000 with elements encoded using 8-byte numbers (standard double-precision format) occupies about 1 gigabyte of memory; I would be thus restricted to the sizes of the basis set no larger than a few tens of thousands. I am, however, interested in much larger bases, composed of millions of configurations. Processing of such large Hamiltonian matrices can be accomplished only by exploiting the fact that they are *sparse*.

A matrix is sparse if the majority of its off-diagonal matrix elements is equal to zero. In my Hamiltonian the off-diagonal elements can only be due to the Coulomb operator. This operator has two important properties: each term in the sum (3.67) has to conserve the angular momentum of the scattered pair of electrons, and the dot product of the two vectors obtained after the application of operators $c_j c_i$ and $c_k c_l$ has to be nonzero. These properties impose stringent conditions on the pairs of vectors that can be coupled by \hat{H}_C , and lead to vanishing of typically about 80% of off-diagonal elements. Thus my Hamiltonian matrix is typically sparse, and I can save the computer memory by storing only its nonzero elements. This, however, prevents me from using the most popular linear algebra packages, such as LAPACK [71], since they are not compatible with such a packed matrix storage. Therefore I need to develop a numerical diagonalisation algorithm which is designed specifically to handle sparse matrices. I describe two such algorithms in the next Section.

3.3.4 Diagonalisation of large and sparse matrices

In the previous Section I have shown how I can decrease the size of the many-particle basis of configurations of N electrons distributed on M single-particle levels by accounting for the symmetries of the system. But the accuracy of the results of the configuration-interaction method is still affected by the choice of the cutoff M chosen to limit the number of single-particle orbitals: in order to obtain reliable results, the number M

should be as large as possible. Therefore, by exploiting the symmetries of the system I have not eliminated the problem of large matrices; I just replaced them by ones, whose diagonalisation will yield results which are much more accurate than those obtained using the unoptimised basis set of the same size. These matrices still have sizes at least of $10^5 \times 10^5$, and special techniques must be used to diagonalise them. In my research I employ the iterative conjugate gradient method combined with spectrum folding. I shall describe these techniques in this Section.

In discussing the conjugate gradient method of matrix diagonalisation I shall first focus on a simpler technique - the steepest descent method - in which the entire principle of iterative minimisation is not obscured by optimisation details. I will assume that the Hamiltonian matrix H is real and symmetric, which guarantees real eigenvalues. This applies directly to the many-body problem, since the many-body Hamiltonian matrix is real in the basis of configurations. The method can, however, be easily generalised to treat complex Hermitian matrices as well.

Both the steepest descent and the conjugate gradient methods are of iterative nature, and their general premise is to “generate” a guess vector and then “purify” it according to some algorithm. This purification process aims at obtaining the exact eigenvector corresponding to the *lowest eigenvalue* of H . The process is executed with the constraint that the vector being processed be normalised to 1.

The steepest descent and conjugate gradient methods presented here are special cases of the general steepest descent and conjugate gradient methods, which deal with finding a minimum of a multivariable function. The only thing that makes them special is the normalisation constraint mentioned before. The general methods are constructed with the assumption that the user supplies the multidimensional function $f(x_1, x_2, \dots, x_N)$ to be minimised. The first step is to generate a random starting point (the “guess vector”) $\vec{u}_0 = [x_1^{(0)}, x_2^{(0)}, \dots, x_N^{(0)}]$, whose coordinates are chosen using a random number generator. This point, in general, is away from the minimum of the function f . Now I calculate the

gradient of the function f at the point \vec{u}_0 :

$$\nabla f(\vec{u})|_{\vec{u}=\vec{u}_0} = \left[\frac{\partial f}{\partial x_1}, \frac{\partial f}{\partial x_2}, \dots, \frac{\partial f}{\partial x_N} \right] \Big|_{\vec{u}=\vec{u}_0}. \quad (3.77)$$

This vector shows the direction of the steepest increase of the function, and the vector $-\nabla f(\vec{u})|_{\vec{u}=\vec{u}_0}$ shows the direction of the steepest descent. I can then take a step of some length from the point \vec{u}_0 along the direction of the steepest descent, and this hopefully will shift me closer to the global (or local) minimum of the function f . At the new point, \vec{u}_1 , I do the same, i.e., calculate the direction of the steepest descent and take the next step. I expect that after a sufficiently large number of steps I will descend to the actual minimum of f . This is the method of the steepest descent.

Sophisticated methods have been developed to calculate the desirable length of the step mentioned above. Also, sometimes steps are taken not along the direction of the steepest descent, but along a set of “conjugate” directions. The idea of “conjugacy” involves creating the next direction of the step based not only on the gradient, but also on previous step directions. In this way one never steps along the same direction twice.

To better visualise these techniques, let us consider a simple two-dimensional problem of a long and deep potential valley. My goal is to find the lowest point (minimum) in this valley, but for now without any normalisation constraints. If I choose a random starting point, say, on one of the walls of the valley, and then take a step along the direction of steepest descent, I may end up somewhere on the opposite wall of this valley. If the shape of the potential valley is strongly asymmetric (the valley is very long and narrow), in the next iteration I may return close to the starting point (the subsequent directions of steepest descent will be nearly parallel). I will, most likely, ultimately find a minimum, but this convergence can take place after a large number of steps. I can limit the number of steps taken in the steepest descent procedure by imposing additional requirements on subsequent directions in which I step - make them conjugate. In such procedure, the first step is always taken along the direction of steepest descent. However, if my function f depends only on two variables, it is possible to construct a conjugate direction that

already in the second step of the iteration will take me directly to the minimum of the function if the function is a quadratic polynomial, or very close to the minimum, if the function is more complicated. For a detailed description of the general steepest descent and conjugate gradient methods I refer the reader to Ref. [109].

Now I set out to adopt the technique described above to find the lowest eigenvalue of the matrix H . To this end I define my function f as the expectation value of the Hamiltonian in the state $|u\rangle$:

$$f(\vec{u}) = \langle u|H|u\rangle, \quad (3.78)$$

where $|u\rangle = \vec{u} = [x_1, x_2, \dots, x_N]$. This vector is understood as a shorthand notation of a many-particle state of the system. This state is a linear combination of many-particle configurations, from which I constructed my basis set. To make the notation compact, I simply retain the coefficients that correspond to each configuration in this combination. Here I also assumed that the size of the basis, and the dimension of the Hamiltonian H , is N (in this Section, this symbol does not denote the number of electrons).

Therefore, I have a function of N variables, defined as an expectation value of the Hamiltonian H , but with the normalisation constraint: $\langle u|u\rangle = x_1^2 + x_2^2 + \dots + x_N^2 = 1$. The above function is a long sum of terms such as $u_i u_j H_{kl}$, so if it was not for the constraint, it would be a quadratic function in the variables (a quadratic form). The additional constraint complicates the picture, since one of the variables becomes dependent on all other variables, and can be eliminated from the function f . However, in this approach I shall not carry out this elimination explicitly. I will only be interested in finding the set of variables x_1, x_2, \dots, x_N giving the smallest possible value of the function f , while still fulfilling the normalisation condition. Note that the minimum thus found does not necessarily correspond to the unconstrained global minimum of the function f . It is rather a *conditional* minimum of f , the condition being, of course, the normalisation. Thus, as an output from this method I shall obtain the smallest eigenvalue of the matrix H , and the corresponding eigenvector, and I have reduced the diagonalisation problem to the

minimisation of a function f .

The reader will find a detailed review of methods, by means of which this problem can be solved, in Ref. [95]. In this article, Payne *et al.* describe a wide variety of techniques, including molecular dynamics, Car-Parinello techniques, etc. Among them I also find the steepest descend and conjugate gradient approaches, however, Payne *et al.* give only a general description of principles on which these methods operate. The specific algorithm presented in detail in this Section has been created and implemented by the author of this Thesis.

I have chosen these two methods for an important reason. As I mentioned in the previous Section, the sizes of Hamiltonian matrices that I typically encounter are of order of hundreds of thousands, and it is not possible to store these matrices in full form in computer memory. The two iterative methods are designed to circumvent this obstacle: they do not require the full matrix H as input, but rather the result of the matrix-vector multiplication. This gives the user a great flexibility in the choice of matrix storage mechanism: the user can store only nonzero matrix elements, use some symmetries of the matrix H characteristic for the problem at hand, or even calculate the matrix elements on the fly. The fundamental object being processed in each method is the vector itself, and one needs to provide a workspace consisting of several such vectors. Therefore, one never handles the object of the size of $N \times N$, only a few objects of the size of N . Unfortunately, this great advantage comes at a cost: the methods can only calculate one - the lowest - eigenvalue of the matrix at a time. To obtain other eigenvalues and eigenvectors one needs to employ additional techniques, such as reorthogonalisation. Later on in this Section I shall describe one such technique - the spectrum folding method, which is very stable numerically and simple to implement.

Let us start the presentation with the description of the **steepest descent method**. Below I shall enumerate the steps which must be taken in the iterative procedure.

1. As mentioned before, I start with a guess vector $|u\rangle_0$. This vector is generated at

random, and *should not* be initialised by assigning identical values to all its entries. This is because in doing so one might accidentally impose a symmetry on the vector which is different from the symmetry of the actual eigenvector corresponding to the lowest eigenvalue. In such situation the procedure might converge to one of the excited states, which is uncontrollable, and thus discouraged. One cannot count on this phenomenon as a possible way of implementing the finding of the excited states, because the imposed symmetry can be broken due to the buildup of the computational error incurred in each iteration. The vector generated at random will, on the other hand, contain elements of all possible symmetries, and it will be possible to purify it to the symmetry of the ground state.

Once initialised, the guess vector $|u\rangle_0$ should be normalised to 1, so that $\langle u|u\rangle = 1$. Now I can calculate the first value of my function: $E_0 = f(|u\rangle_0) = {}_0\langle u|H|u\rangle_0$.

2. Now I need to find the direction of steepest descent. To this end let us make an explicit use of the fact that the vector $|u\rangle$ must be normalised to 1 at each step of iteration. Therefore, the next approximation of the eigenvector can be achieved only by a rotation of the current vector by a certain angle, i.e.,

$$|u\rangle_1 = \cos(\alpha)|u\rangle_0 + \sin(\alpha)|g\rangle_0, \quad (3.79)$$

where the auxiliary vector $|g\rangle_0$ must be normalised to 1 and orthogonal to $|u\rangle_0$. This orthogonality is required, because without it I would change the norm of $|u\rangle$: if $|g\rangle_0$ has a component parallel to $|u\rangle_0$, I would add some length to the vector $|u\rangle_0$, which must be avoided. To prove that, let us consider explicitly the normalisation:

$${}_1\langle u|u\rangle_1 = \cos^2(\alpha) {}_0\langle u|u\rangle_0 + \sin^2(\alpha) {}_0\langle g|g\rangle_0 + 2 \sin(\alpha) \cos(\alpha) {}_0\langle g|u\rangle_0. \quad (3.80)$$

The above norm equals 1 only if both vectors are normalised (from the first two terms I get $\cos^2(\alpha) + \sin^2(\alpha) = 1$) and orthogonal (the third term vanishes). The angle α will be defined afterwards, now I will focus on generating the vector $|g\rangle_0$.

Let us postulate it in the form:

$$|g\rangle_0 = (H - E_0 I)|u\rangle_0. \quad (3.81)$$

As defined above, $E_0 = {}_0\langle u|H|u\rangle_0$ is the zeroth approximation to the sought energy, calculated with the guess vector $|u\rangle_0$, and I is the unit matrix. Now I shall prove that the vector $|g\rangle_0$ is orthogonal to $|u\rangle_0$:

$${}_0\langle u|g\rangle_0 = {}_0\langle u|H - E_0 I|u\rangle_0 = {}_0\langle u|H|u\rangle_0 - E_0 {}_0\langle u|u\rangle_0 = E_0 - E_0 = 0, \quad (3.82)$$

from the definition of E_0 and because the vector $|u\rangle_0$ is normalised to 1.

Let us now use the vector $|g\rangle_0$, henceforth called “gradient”, to rotate the guess vector $|u\rangle_0$. I have shown how this is accomplished in Eq. (3.79); now I only have to define the angle α . To do that, let us calculate the next approximation to the eigenvalue:

$$E_1(\alpha) = {}_1\langle u|H|u\rangle_1 = \cos^2(\alpha)E_0 + \sin^2(\alpha) {}_0\langle g|H|g\rangle_0 + 2\sin(\alpha)\cos(\alpha) {}_0\langle g|H|u\rangle_0. \quad (3.83)$$

Note that all matrix-vector multiplications appearing in the above equation can be carried out explicitly, because the only unknown here is α . I choose its value so that $E_1(\alpha)$ is minimal, and I can do it analytically by calculating the derivative $dE_1(\alpha)/d\alpha$ and equating it to zero. I obtain, after elementary calculations,

$$\tan(2\alpha) = \frac{2 {}_0\langle g|H|u\rangle_0}{E_0 - {}_0\langle g|H|g\rangle_0}; \quad \alpha = \frac{1}{2}\arctan\left(\frac{2 {}_0\langle g|H|u\rangle_0}{E_0 - {}_0\langle g|H|g\rangle_0}\right). \quad (3.84)$$

In reality the trigonometric equation $dE_1(\alpha)/d\alpha = 0$ has two solutions in the domain $0 \leq \alpha \leq 2\pi$: α as written above, and $\alpha + \pi/2$; one solution corresponds to the maximum, and one - to the minimum. I do not know a priori which solution to take. I therefore need to calculate both $E_1(\alpha)$ and $E_1(\alpha + \pi/2)$ and compare them. The argument corresponding to the smaller value of E_1 is taken for further calculations. Using this α I can get the next approximation to the vector $|u\rangle_1$ and the energy E_1 explicitly.

The last step is to normalise $|u\rangle_1$ manually. Of course, if all the steps described above were performed with infinite precision, this step would not be necessary. However, I deal with finite-precision calculations, and the machine error will accumulate with each iteration. I circumvent this problem by renormalising the vector $|u\rangle_1$.

3. I repeat the procedure described in item 2, only treating the vector $|u\rangle_1$ and eigenvalue E_1 as known, and using them to calculate the next vector, $|u\rangle_2$, and the next eigenvalue, E_2 . I do so iteratively in a loop, until the relative difference between two consecutive approximations of the eigenvalue is smaller than the predefined accuracy factor:

$$\left| \frac{E_{i+1} - E_i}{E_i} \right| \leq EPS. \quad (3.85)$$

The value EPS is defined by the user, but it should not be smaller than the respective machine accuracy (typically 10^{-16}). Note that the user does not have to preset the number of iterations, which would decrease the generality of the method. The iterative procedure should be self-terminating - upon fulfilment of the accuracy condition (3.85).

Let us now move on to the optimised version of the steepest descent approach - the **conjugate gradient method**. The goal of the optimisation is to limit the number of iterations necessary to reach convergence. I shall attempt to accomplish this by influencing the choice of auxiliary vectors $|g\rangle_i$ in each iteration. This will be, however, the only difference distinguishing this algorithm from the steepest descent method.

As described above, the directions generated in the steepest descent method are completely defined by the matrix H and the current vector $|u\rangle_i$, without any correlation with any previous gradients $|g\rangle_j$ or vectors $|u\rangle_j$ with $j < i$. In particular, the gradient in step i , $|g\rangle_i$, does not have to be orthogonal to the gradient in the step j , $|g\rangle_j$, which means that I will rotate the vector $|u\rangle$ (at least partially) in the same direction in both steps. It would be best, however, not to repeat the rotation direction that has already been used.

The idea here is to orthogonalise the gradient vector in step i , $|g\rangle_i$, to all the previous gradients, i.e. to define a *direction* $|d\rangle_i$, which is equal to the gradient $|g\rangle_i$, but with all previous gradients $|g\rangle_j$ projected out of it. That way each new direction will be orthogonal to all previous ones, and I will never retrace the steps already taken. It can be proved, however, that the problem posed in this way is over-constrained [109]: the construction of a sequence of steps along these lines requires the prior knowledge of the solution, which I seek.

However, instead of enforcing *orthogonality* of directions, I can enforce their *conjugacy*. Two vectors, $|x\rangle$ and $|y\rangle$ are conjugate if they fulfill the condition

$$\langle x|H|y\rangle = 0. \quad (3.86)$$

(note that the orthogonality condition is $\langle x|y\rangle = 0$ and does not involve the Hamiltonian matrix H). As I shall describe, it is possible to create a set of conjugate vectors recursively, retaining in memory only two immediately preceeding vectors (the generation of an orthogonal set requires knowledge of *all* previous vectors).

The procedure starts by simply taking the gradient $|d\rangle_0 = |g\rangle_0$ as the zeroth direction. I use this gradient to establish the next approximation to the eigenvector and eigenvalue, precisely as it was done in the steepest descent method.

In the first step of the algorithm I already have two objects: the gradient $|g\rangle_1$, and the direction from the previous step $|d\rangle_0$, and I can use these two. The direction in this step, $|d\rangle_1$ is written as

$$|d\rangle_1 = |g\rangle_1 + \beta_1 |d\rangle_0. \quad (3.87)$$

Note that the two vectors on the right-hand side of this equation are known; I only have to establish the value of the parameter β_1 . I do it by requiring that $|d\rangle_1$ be conjugate to the previous direction, $|d\rangle_0$:

$${}_0\langle d|H|d\rangle_1 = 0; \quad \beta_1 = -\frac{{}_0\langle d|H|g\rangle_1}{{}_0\langle d|H|d\rangle_0}. \quad (3.88)$$

Now I look for the next approximation of the eigenvector and the eigenvalue using the direction $|d\rangle_1$ rather than the gradient $|g\rangle_1$ itself.

In each next step of the algorithm I generate the new direction in an analogous way:

$$|d\rangle_i = |g\rangle_i + \beta_i |d\rangle_{i-1}. \quad (3.89)$$

Note that I only use the current gradient and the previous direction in this process. The parameter β_i is calculated by requiring that $|d\rangle_i$ be conjugate to $|d\rangle_{i-1}$, and is

$$\beta_i = -\frac{{}_{i-1}\langle d|H|g\rangle_i}{{}_{i-1}\langle d|H|d\rangle_{i-1}}. \quad (3.90)$$

In the case of the general conjugate method, i.e., the one in which I do not require the normalisation of the guess vector, it can be proved [109] that by this construction each direction is conjugate not only to the immediately previous one, but to all previous directions. In the current algorithm, in order to maintain the normalisation constraint, I introduce a new element: at each step the direction $|d\rangle_i$ is additionally manually orthogonalised to the previous vector $|u\rangle_i$, before the new vector $|u\rangle_{i+1}$ is obtained. This is aimed at conserving the normalisation of $|u\rangle$, as was already explained for the steepest descent, but it upsets the conjugacy. The new direction $|d\rangle_i$ will be conjugate to the previous direction, and nearly conjugate to the one before that, but the conjugacy with earlier directions will be preserved to a lesser and lesser degree. This is a drawback, since it leads only to a local improvement of the rate of convergence. However, the loss of conjugacy does not cause the algorithm to diverge, nor converge to a wrong value; the algorithm will simply converge slower, but always to the correct eigenvalue.

Having understood the idea of conjugacy I shall now formulate the minimisation algorithm that employs it.

1. First I generate the guess vector $|u\rangle_0$ and normalise it to 1; I also calculate E_0 as described above.
2. I find the gradient $|g\rangle_0$, normalise it, and using it I find the appropriate parameter

α as I did in the steepest descent algorithm. This parameter α is then used to generate the next approximation $|u\rangle_1$ and E_1 .

3. This step is unique to the conjugate gradient algorithm. I generate the next gradient, $|g\rangle_1 = H|u\rangle_1 - E_1|u\rangle_1$, but I am not using it in the rotation of the vector. Instead, I use the direction $|d\rangle_1^* = |g\rangle_1 + \beta_1|d\rangle_0$, with the parameter $\beta_1 = -\frac{o\langle d|H|g\rangle_1}{o\langle d|H|d\rangle_0}$. In general, the vector $|d\rangle_1^*$ generated this way will not be orthogonal to $|u\rangle_1$. In order to preserve the norm of my approximate eigenvector $|u\rangle$, I need to perform the orthogonalisation manually, e.g., by taking a single step of the well-known Gram-Schmidt orthogonalisation: $|d\rangle_1 = |d\rangle_1^* - \frac{1\langle u|d\rangle_1^*}{1\langle u|u\rangle_1}|u\rangle_1$. Of course, the above expression can be written in a simpler form - without the denominator, since the approximate eigenvector $|u\rangle_1$ is normalised. If execution time is absolutely crucial, the denominator can then be simply set to 1, as it should be in theory. However, this may not be so in practice due to the computer roundoff errors.
4. Now that I have the old approximate vector $|u\rangle_1$ and the new direction $|d\rangle_1$, I can generate the new approximate vector $|u\rangle_2$ in precisely the same way as I did for the steepest descent - writing it as a rotation and calculating the appropriate angle α . Thus I obtain $|u\rangle_2$ and the corresponding approximate eigenvalue E_2 .
5. I repeat the step 3 until the convergence is reached.

To compare the performance of the two algorithms, I take the model Hamiltonian matrix describing a two-dimensional quantum well with rigid walls, discretised on a mesh of points. The continuous Schrödinger equation in the effective Rydberg units takes here the form

$$\left[-\frac{\partial^2}{\partial x^2} - \frac{\partial^2}{\partial y^2} \right] \phi(x, y) = E\phi(x, y), \quad (3.91)$$

where $0 \leq x \leq 1$ and $0 \leq y \leq 1$ (the length of the sides of the square well is equal 1 a_B , and the walls are infinite). Elementary analytical calculations show that the ground-state energy in such a well is $E_0 = 2\pi^2$ Rydbergs. The discretisation scheme involves replacing

the continuous function $\phi(x, y)$ by the function $\phi(x_i, y_j)$ defined on a mesh of discrete points. For the model calculation, let us assume that I have discretised the system in such a way that there are $M + 2$ points along each wall of the well, numbered from 0 (the first point has number 0, the second - number 1, and so on, until the last, $M + 2$ -nd point which has the number $M + 1$). Therefore the distance between points along each coordinate axis is $\Delta x = \Delta y = \frac{1}{M+1}$. The first and last of the mesh points coincide with the wall of the well, and therefore I expect the wave function to be equal to zero on those points. The function may assume nonzero values only on the mesh inside the well, and this mesh comprises M^2 points.

I also need to discretise the second derivatives in the Schrödinger equation:

$$\left. \frac{\partial^2}{\partial x^2} \phi(x, y) \right|_{x_i, y_j} \approx \frac{\phi(x_{i-1}, y_j) - 2\phi(x_i, y_j) + \phi(x_{i+1}, y_j)}{(\Delta x)^2}, \quad (3.92)$$

and similarly for the derivative over the coordinate y . Upon this discretisation, the continuous Schrödinger equation (3.91) can be written as a set of linear equations of the type

$$-\phi(x_{i-1}, y_j) - \phi(x_i, y_{j-1}) + 4\phi(x_i, y_j) - \phi(x_{i+1}, y_j) - \phi(x_i, y_{j+1}) = (\Delta x)^2 E \phi(x_i, y_j) \quad (3.93)$$

for each of the points in the mesh, i.e., for $1 \leq i \leq M$ and $1 \leq j \leq M$. Whenever the above equation requires the value of the function ϕ on any of the walls of the well (i.e., for $i = 0$ or $i = M + 1$ or $j = 0$ or $j = M + 1$), the value 0 is explicitly introduced instead. I also order the equations in such a way that in the first one I have $i = j = 1$, in the second - $i = 2$ and $j = 1$, etc, until I reach $i = M, j = 1$. After that I begin again with $i = 1$ but this time $j = 2$. I continue this sequence until I reach the equation with $i = j = M$.

Such a set of equations can be written in a matrix form, with a penta-diagonal matrix H of order $M^2 \times M^2$. All the diagonal elements of this matrix are equal to 4, and on the immediate upper and lower diagonal I put -1 , except for each $M + 1$ -st element along it, which is set to zero (this is due to the rigid wall of the well, positioned next to this point on the mesh). Also, this matrix possesses a remote upper- and lower-diagonal, filled with

values -1 , beginning respectively in the $M + 1$ -st column and the $M + 1$ -st row. Upon diagonalisation of this matrix I obtain the eigenvalues ε , which can be converted to the values of energy by rescaling $E = \varepsilon/(\Delta x)^2$.

In these model calculations I assume $M = 50$ so that the simple Hamiltonian is of the size 2500×2500 . The target eigenvalue - the ground-state energy that I should obtain in the diagonalisation - is $\varepsilon_0 = \frac{2\pi^2}{51 \times 51} = 0.0075890845$. Of course, I should not expect to obtain this value exactly, as the factor $2\pi^2$ in this formula corresponds to the true solution of the continuous equation (3.91).

The steepest descent method applied to the matrix H converged to the value of 0.007586685051830517 after 3392 iterations. The relative error EPS , as calculated in the algorithms, was decreasing systematically in the progress of the calculation, attaining the value of about $7.16 \cdot 10^{-6}$ after first 500 iterations, about $7.82 \cdot 10^{-9}$ after first 1000 iterations, and $1.41 \cdot 10^{-11}$ after 2000 iterations. Thus I deal with a long convergence tail. As for the conjugate gradient applied to the same matrix, it converged to the value of 0.007586685051823797 after only 174 iterations. A comparison of relative errors EPS of both methods as a function of the number of iterations is shown in Fig. 3.1. Note that the line corresponding to the steepest descent method exhibits some oscillatory behaviour just before reaching the convergence. The line corresponding to the conjugate gradient method does exhibit such behaviour as well, but to a much smaller degree. This performance comparison shows clearly the superiority of the conjugate gradient method over the steepest descent. The latter converged after taking more steps than the order of the matrix itself, whereas the conjugate gradient method converged after the number of steps equal to about 7% of the order of the matrix.

Both the steepest descent and conjugate gradient methods are capable of finding the ground state eigenvector and eigenenergy only. The last issue that I need to address is the use of the iterative methods in finding not only the ground, but also the excited states of the system. To this end I employ a technique called the **spectrum folding**

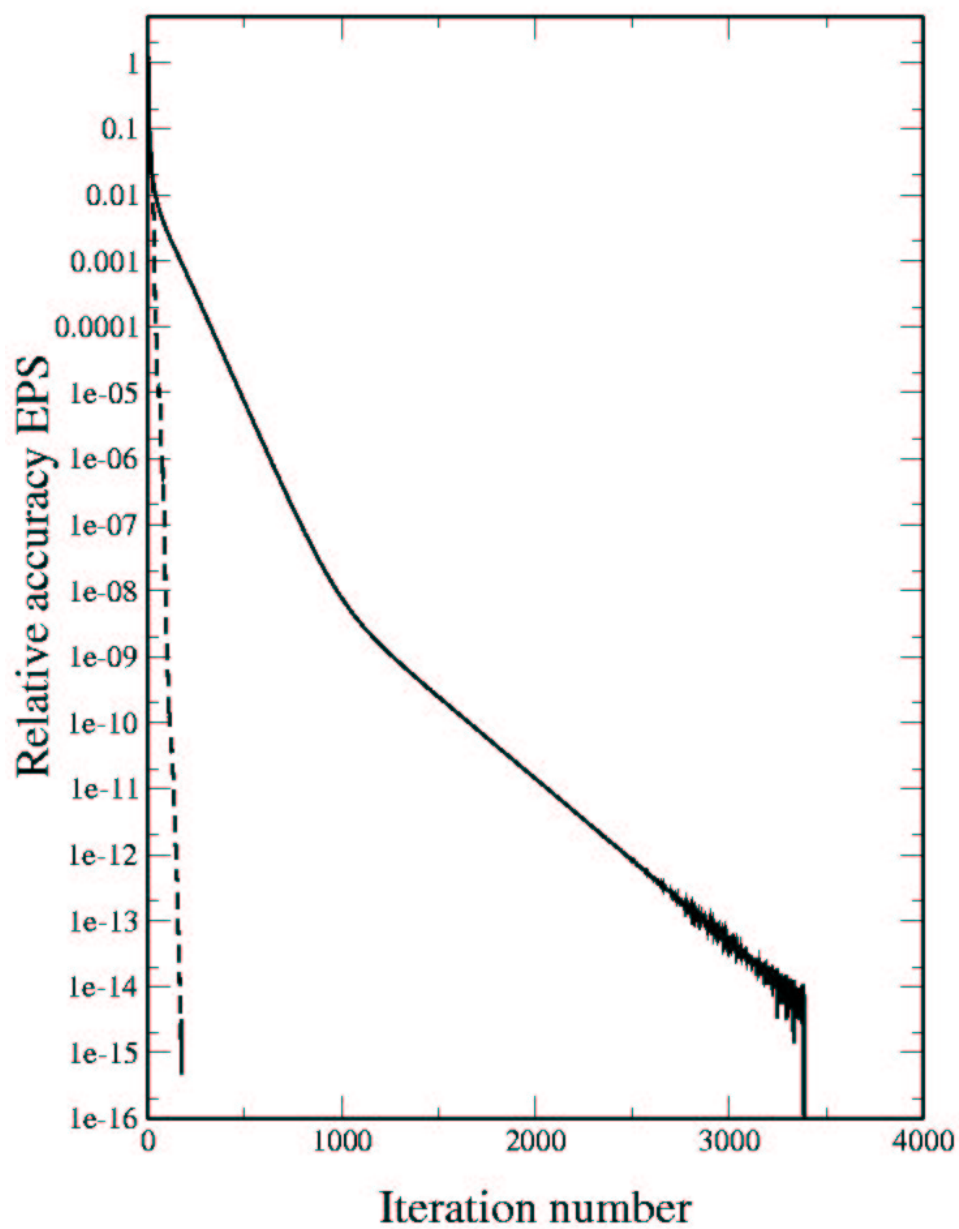


Figure 3.1: Relative error of the steepest descent (solid line) and the conjugate gradient (dashed line) methods as a function of the iteration number.

method, used extensively in large computations, e.g., by the group of Alex Zunger [28]. Preparation and implementation of the spectrum folding algorithm in the form described below, and coupling it with the conjugate gradient method is an original work of the author of this Thesis.

The spectrum folding method involves constructing a new Hamiltonian H_2 , whose ground-state eigenvector is identical to the eigenvector corresponding to one of the excited states of the original Hamiltonian H . The new Hamiltonian is postulated in the form:

$$H_2 = (H - \varepsilon I)^2, \quad (3.94)$$

where ε is a user-supplied number with dimension of energy, and I is the unit matrix. Let us explain the meaning of the number ε later. First I shall look at the eigenvectors of H_2 . Let us assume that the vector $|v\rangle$ is one of the eigenvectors of the original Hamiltonian H with the eigenvalue E , i.e.,

$$H|v\rangle = E|v\rangle. \quad (3.95)$$

I have

$$H_2|v\rangle = (H - \varepsilon I)(H - \varepsilon I)|v\rangle = (E - \varepsilon)^2|v\rangle,$$

which means that the vector $|v\rangle$ is also an eigenvector of H_2 , but with eigenvalue $(E - \varepsilon)^2$. Thus, in transition from the Hamiltonian H to H_2 the eigenvectors are unchanged, and the energies are transformed quadratically: $E_i \rightarrow (E_i - \varepsilon)^2$. To see what this gives me, let us assume for a moment that the original Hamiltonian H has both positive and negative eigenvalues, and let us take $\varepsilon = 0$. Clearly, upon transformation to the Hamiltonian H_2 all the eigenvalues will be squared, so that all the negative eigenvalues will acquire the positive sign. Thus, by transforming H to H_2 , I have parabolically “folded” the spectrum of the original Hamiltonian H . Note that the ground state of the Hamiltonian H_2 will be *different* than the ground state of H - in fact, the ground state of H_2 will be one of the excited states of H , the one, whose absolute value of eigenenergy was originally closest to zero. Now, if I tune the parameter ε , I can additionally shift the energy spectrum of H ,

which gives an ability to bring the eigenenergy of the chosen excited state of H to zero. This guarantees that the chosen excited state will become the ground state of H_2 , and I can find it using the conjugate gradient algorithm. By appropriate tuning of ε I can thus find all the eigenstates of H , and the eigenenergies that correspond to them.

The last issue I shall address here is the choice of the most efficient way of tuning the shift ε . In principle, one could simply change it in some small steps over a chosen region of values. That would, however, require a long time, necessary to perform such a large number of iterative diagonalisations. There is also a danger that the eigenvalues of H can be clustered in such a way that the gaps between them are smaller than the step taken in tuning the shift ε ; such eigenvalues would be impossible to resolve with this procedure. To circumvent these obstacles, I propose a more efficient tuning scheme, involving partial reorthogonalisation of the guess vector. I proceed in the following way:

1. Find the ground-state eigenvector and eigenvalue of the original Hamiltonian H . To this end, I do not have to fold the spectrum, since the conjugate gradient method is constructed to find the lowest eigenvalues of matrices. The ground-state eigenvector found in this step is stored for further processing.
2. Find the *approximate* first-excited-state eigenvector and eigenvalue by performing the conjugate gradient minimisation with the original Hamiltonian H , but imposing an additional constraint on the guess vector $|u\rangle$ in each iteration: not only does it have to be normalised, but also orthogonal to the ground-state eigenvector found and stored in the previous step. The orthogonalisation is accomplished by means of the Gram-Schmidt procedure.
3. Use the approximate eigenvalue of the first excited state - found in the previous step - as the shift ε . Use this shift to construct the Hamiltonian H_2 , and perform the conjugate gradient procedure with it. The shift causes the first excited state of H to be the ground state of H_2 with corresponding eigenvalue equal to zero. The

eigenvector found this way is stored for further processing.

4. Repeat steps 2 and 3 for higher and higher states of H , “guessing” the approximate eigenvalue corresponding to each of them by performing the conjugate-gradient minimisation with reorthogonalisation to all eigenstates previously found, and use this approximate eigenvalue as the shift in H_2 . The reorthogonalisation procedure is not used in this step.

Note that this shifting-and-reorthogonalisation procedure allows to resolve even those eigenstates of H , whose eigenvalues are degenerate. Unfortunately, I pay for this functionality by extended storage requirements - I need to store all the eigenvectors found in subsequent steps. This may make it impossible to find *all* the eigenvalues and eigenvectors of H , but in my calculations I will be interested in resolving only the ground and several excited states of the system anyway. The most important feature of the proposed method is the fact that the numerical error, accumulating in the reorthogonalisation, *does not affect* the eigenvalues, since the reorthogonalisation steps are taken only in evaluating the optimal shift, and not the final result.

3.4 Other methods accounting for electronic correlations

In this Chapter I have built the optimised exact diagonalisation technique for many-body systems confined in QD potentials, and I have demonstrated its operation on a system of several interacting electrons confined in a two-dimensional parabolic potential. As I have shown, this method involves building a basis set out of electronic configurations, constructing the Hamiltonian matrix in this basis and diagonalising it numerically. This approach treats all aspects of the Coulomb interaction on equal footing (without any approximations), and therefore the results it gives are, in principle, *exact*. However, as I

have shown, the basis of many-particle configurations in a parabolic confinement is infinite, and, to be able to perform computations, I need to restrict it by considering only a finite number M of single-particle states, on which I distribute my electrons. This is, in fact, the only approximation of this method, and I can control it by performing convergence studies, in which I examine the ground-state energies of the system as a function of the parameter M . In Section 3.3 I have shown that even with the cutoff the number of electronic configurations necessary to obtain a well-converged result increases factorially both with the number of electrons N and the number of single-particle states M . This makes the method extremely unwieldy for larger electron numbers; using present-day computers I was only able to treat at most nine interacting particles.

But often of interest are properties of larger systems, and in these cases the configuration-interaction method can only be used to form general intuitions about their properties, as the limitation of the basis to manageable sizes prevents me from reaching convergence. In these cases other - approximate - methods must be used. Here I shall briefly describe two of such methods - the spin density functional theory (SDFT) and the quantum diffusion Monte Carlo method (QDMC) - which are also capable of resolving correlation effects, albeit in an approximate manner. The main point of this presentation is the fact that the results obtained with these methods can be compared to those of the exact diagonalisation for systems in which the performance of the latter technique is adequate. This allows to control the approximations made in SDFT and QDMC, so that, when these methods are applied to larger systems, their results are more reliable.

My description of SDFT and QMC methods will be limited to fundamentals only, as I shall not use them in the rest of this work. My goal here is to inform the reader of their existence and provide the appropriate literature context.

3.4.1 Spin density functional theory

In this Section I shall describe the fundamentals of the spin density functional theory. This description will be based on original papers of the contributors to this theory, but the reader can find excellent reviews of the subject in Refs. [116, 127]. To ensure consistency I shall use the notation proposed in these publications.

The development of the density functional theory (DFT) was started by P. Hohenberg and W. Kohn in 1964, who proved [60] that the energy of a system of interacting particles in an external potential is a unique functional of electronic density. In their work they introduced the following notation:

$$\hat{T} = -\frac{\hbar^2}{2m^*} \int d\mathbf{r} \Psi^\dagger(\mathbf{r}) \nabla^2 \Psi(\mathbf{r}); \quad (3.96)$$

$$\hat{V} = \int d\mathbf{r} V(\mathbf{r}) \Psi^\dagger(\mathbf{r}) \Psi(\mathbf{r}); \quad (3.97)$$

$$\hat{W} = \frac{1}{2} \frac{e^2}{\varepsilon} \int d\mathbf{r} \int d\mathbf{r}' \frac{1}{|\mathbf{r} - \mathbf{r}'|} \Psi^\dagger(\mathbf{r}) \Psi^\dagger(\mathbf{r}') \Psi(\mathbf{r}') \Psi(\mathbf{r}). \quad (3.98)$$

Here, \hat{T} is the kinetic energy operator, \hat{V} is the operator introducing the external potential $V(\mathbf{r})$, \hat{W} is the operator introducing the Coulomb interactions. The Hamiltonian of the system can be written as a sum of all these operators:

$$\hat{H} = \hat{T} + \hat{V} + \hat{W}. \quad (3.99)$$

Moreover, $\Psi(\mathbf{r})$ are the field operators; with their use the electronic density operator can be written as

$$\hat{n}(\mathbf{r}) = \Psi^\dagger(\mathbf{r}) \Psi(\mathbf{r}). \quad (3.100)$$

The Hohenberg-Kohn formalism treats the electronic density $n(\mathbf{r})$ as the central quantity, by means of which all properties of the system can be described completely. In fact, even the electronic wave functions $|\Psi[n]\rangle$ are functionals of the density. Now, the expectation value of any observable \hat{O} can be expressed as $O = \langle \Psi[n] | \hat{O} | \Psi[n] \rangle$, and, in particular, the energy

$$E[n] = \langle \Psi[n] | \hat{H} | \Psi[n] \rangle \quad (3.101)$$

is a unique functional of density. This *exact* result is the Hohenberg-Kohn theorem.

The formula for energy as a functional of the electronic density can be used to find the ground-state energy E_{GS} of the system. Hohenberg and Kohn prove that $E_{GS} = E[n_0(\mathbf{r})]$ if the density $n_0(\mathbf{r})$ fulfils two conditions: first, it minimises the functional $E[n]$, and second, it is normalised to give

$$N[n] = \int d\mathbf{r} n(\mathbf{r}) = N, \quad (3.102)$$

where N is the number of electrons in the system. The greatest strength of the Hohenberg-Kohn theorem is the fact that it allows to work with a three-dimensional electronic density instead of the $3N$ -dimensional electronic wave function. As I shall show, this allows to treat electronic systems far larger than those treatable by the exact diagonalisation method provided that one is able to correctly minimise the energy functional for these systems.

In treating the electronic density up to now I have neglected the spin degree of freedom. This quantum number is, however, essential for systems of interest, as I have already demonstrated in Section 3.3.2. The inclusion of electronic spin into the DFT formalism in early 1970s led to the development of the spin density functional theory (SDFT) [13, 100]. In SDFT, the electronic density $n(\mathbf{r})$ is replaced by a pair of densities, $n_\uparrow(\mathbf{r})$ and $n_\downarrow(\mathbf{r})$, corresponding to electrons spin up and spin down, respectively. Therefore the field operators Ψ acquire an additional index, and are denoted as $\Psi_\sigma(\mathbf{r})$, and in the definitions (3.96), (3.97), (3.98) of energy operators the integration over coordinates must be supplemented by the summation over spins. Now the total energy of the system is a functional of the two densities,

$$E[n_\uparrow, n_\downarrow] = \langle \Psi[n_\uparrow, n_\downarrow] | \hat{H} | \Psi[n_\uparrow, n_\downarrow] \rangle, \quad (3.103)$$

and the ground state energy $E_{GS}[n_\uparrow, n_\downarrow]$ can be obtained by minimising the above functional with respect to both densities under constraints

$$\int d\mathbf{r} n_\uparrow(\mathbf{r}) = N_\uparrow, \quad (3.104)$$

$$\int d\mathbf{r} n_{\downarrow}(\mathbf{r}) = N_{\downarrow}, \quad (3.105)$$

$$N_{\uparrow} + N_{\downarrow} = N, \quad (3.106)$$

where N_{\uparrow} (N_{\downarrow}) is the number of electrons spin up (down).

The latest density-functional theories include an additional term in the Hamiltonian, accounting for the interaction of currents, created by orbiting electrons, with the magnetic field. This is the so-called current-spin density functional theory, developed by Vignale and Rasolt [125]. However, the current corrections - at least in the quantum-dot systems - have been shown to be very small [116, 127], and I shall not describe them further.

I have defined the object on which I need to work: the total energy as a functional of the electronic densities. Let us now briefly describe the minimisation procedure of this functional, used to obtain the ground state energy and density of the system. This procedure was developed by W. Kohn and L. Sham in 1965 [67]. To simplify the description, let us follow their notation and drop the spin index in densities and functionals; all the derivations presented below can be naturally extended to resolve the spin degree of freedom. To arrive at the famous Kohn-Sham equations, let us introduce an additional density functional

$$F[n] = \langle \Psi[n] | \hat{T} + \hat{W} | \Psi[n] \rangle, \quad (3.107)$$

being the expectation value of the Hamiltonian without the external potential \hat{V} . It is further convenient to isolate the so-called exchange-correlation energy:

$$E_{XC}[n] = F[n] - T[n] - \frac{1}{2} \frac{e^2}{\epsilon} \int d\mathbf{r} \int d\mathbf{r}' \frac{n(\mathbf{r})n(\mathbf{r}')}{|\mathbf{r} - \mathbf{r}'|}. \quad (3.108)$$

Thus, E_{XC} is obtained by subtracting from the functional F the kinetic energy functional T and the direct Coulomb energy functional (the last term in the above equation). E_{XC} carries only the effects of exchange and electronic correlations. Hohenberg and Kohn proved [60] that if the densities $n_{\sigma}(\mathbf{r})$ are slowly varying functions, the exchange-correlation energy can be written as

$$E_{XC}[n] = \int d\mathbf{r} n(\mathbf{r}) \epsilon_{XC}[n(\mathbf{r})], \quad (3.109)$$

where ϵ_{XC} in a uniform electron gas is the exchange-correlation energy per electron.

Now the total energy functional can be minimised with respect to the density. To this end, the energy functional (3.103) is functionally differentiated with respect to the density and this derivative is equated to zero. One obtains [67]

$$\int d\mathbf{r} \delta n(\mathbf{r}) \left\{ \frac{\delta T[n]}{\delta n(\mathbf{r})} + V(\mathbf{r}) + \frac{e^2}{\epsilon} \int d\mathbf{r}' \frac{n(\mathbf{r}')}{|\mathbf{r} - \mathbf{r}'|} + \mu_{XC}[n(\mathbf{r})] \right\} = 0, \quad (3.110)$$

with the constraint

$$\int d\mathbf{r} \delta n(\mathbf{r}) = 0. \quad (3.111)$$

In the above equations, $\mu_{XC}[n(\mathbf{r})] = d(n\epsilon_{XC}[n(\mathbf{r})])/dn(\mathbf{r})$ is the exchange-correlation contribution to the chemical potential for the electron gas.

Solving the above equation for the density $n(\mathbf{r})$ is equivalent to solving the single-particle Schrödinger equation

$$\left\{ -\frac{\hbar^2}{2m^*} \Delta + V(\mathbf{r}) + \frac{e^2}{\epsilon} \int d\mathbf{r}' \frac{n(\mathbf{r}')}{|\mathbf{r} - \mathbf{r}'|} + \mu_{XC}[n(\mathbf{r})] \right\} \phi_i(\mathbf{r}) = E_i \phi_i(\mathbf{r}) \quad (3.112)$$

for each electron. Thus, each electron moves in the mean field created by the external potential $V(\mathbf{r})$, the direct Coulomb repulsion with all other electrons, and the potential μ_{XC} taking into account the exchange and correlation effects of the electronic system. The wave function $\phi_i(\mathbf{r})$ is the ground state of the electron in this effective potential (the Kohn-Sham orbital).

Since the effective potential experienced by each electron depends on the behaviour of all other electrons, the equation (3.112) must be solved self-consistently. The process starts by assuming some initial density $n(\mathbf{r})$ (e.g., constant), and calculating the wave functions $\phi_i(\mathbf{r})$ for each electron. Next, the electronic density is recalculated as follows:

$$n(\mathbf{r}) = \sum_{i=1}^N |\phi_i(\mathbf{r})|^2, \quad (3.113)$$

and the new density is used to solve for the ground state wave functions of each electron. The procedure is repeated until the density profile $n(\mathbf{r})$ converges, i.e., subsequent steps

do not change the density any more. The final density can be further used to calculate the total energy of the system via the energy functional $E[n]$.

As I mentioned before, extension of the Kohn-Sham equations to include spin is straightforward. The only modification is due to the fact that now the exchange-correlation potential μ_{XC} depends on the spin σ , and one formulates separate set of Kohn-Sham equations for electrons spin up and for electrons spin down. As a result, one obtains Kohn-Sham orbitals with additional spin quantum number, and by summing their squared moduli as presented above one arrives at the densities of electrons spin up and spin down.

The Kohn-Sham equations (3.112) have been derived without any approximations, and so they describe the electronic properties of the system in the *exact* manner. However, I cannot solve them yet, since the exact form of the exchange-correlation functional $\mu_{XC}[n(\mathbf{r})]$ is not known. Unfortunately, this functional cannot be obtained from first principles. The forms most commonly used in this context are postulated on the basis of extrapolations from the few exact results available. Frequently one assumes that the exchange-correlation potential μ_{XC} can be locally approximated by the potential for an infinite system at constant density [104]. This is the “local spin density approximation”. The parametrisation of choice, commonly used in the context of parabolic two-dimensional quantum dots, is that of Tanatar and Ceperley [120]. These authors obtained the exchange-correlation functional of the two-dimensional gas as a Padé approximant. This approximant is constructed by fitting to the available quantum Monte Carlo results obtained for selected values of electronic density.

This necessity of postulating the exchange-correlation functional unfortunately makes the SDFT only an approximate theory. Nevertheless, it is widely used to examine the properties of many-electron quantum dots with electron numbers far exceeding the capabilities of the exact diagonalisation method. In Section 1.5 I have discussed some of the applications of the SDFT method to electronic QDs. For references and reviews of this field, I refer the reader to Refs. [11, 59, 75, 102, 104, 111, 128]. The density-functional

approach with the Thomas-Fermi-Dirac-von Weizsäcker energy functional can also be applied to arrays of quantum dots; for instance, the magnetoplasmon excitations in such arrays were analysed in Ref. [132]. In the context of comparing the SDFT method with the exact diagonalisation approach the work by Wensauer [127] is particularly interesting: the author attempts to extract the *exact* form of the exchange-correlation potential from the results of the exact diagonalisation for systems with few electrons, in which both methods can be applied with the same accuracy.

3.4.2 Monte Carlo methods

Let us now describe a different approach to the many-body problem, involving random sampling of the parameter space of the system and analysing the results obtained this way by statistical methods. Due to this random sampling process, this approach is widely known as the quantum Monte Carlo method (QMC). In reality one can name several quantum Monte Carlo methods, differing in the definition of the parameter space being sampled. A review of these methods can be found in several papers by D. Ceperley [29], in which the author presents the main principles of the variational QMC, path integral QMC, Green's function QMC and the diffusion QMC. Each of these techniques is usually used in a slightly different context. For instance, in the variational QMC one defines a trial variational wave function of the system, and, using the variational principle, one tries to find the minimum of the expectation value of the Hamiltonian in this state. The wave function usually depends on several parameters, whose optimal values must be found, and the calculation of the expectation value of the energy usually involves calculating a multi-dimensional integral. Both tasks can be accomplished using Monte Carlo sampling. In path-integral QMC all the possible paths the system can take in its evolution are explored, usually using the rejection algorithm of Metropolis *et al.* [84]. Here, however, I shall focus only on the quantum diffusion Monte Carlo technique (QDMC), because it is frequently used to study the properties of systems of many interacting electrons confined

in quantum dots.

Perhaps the best introduction to the subject can be found in Ref. [3], where Anderson describes the application of QDMC to study the properties of the H_3^+ molecule, composed of three protons localised in the corners of an equilateral triangle, and two interacting electrons with antiparallel spins moving in their potential. The description starts with the simple one-dimensional time-dependent Schrödinger equation, written for a single particle moving in a potential $V(x)$:

$$-i\hbar \frac{\partial \psi(x, t)}{\partial t} = \frac{\hbar^2}{2m^*} \frac{\partial^2 \psi(x, t)}{\partial x^2} - V(x)\psi(x, t). \quad (3.114)$$

The key point of the method consists in introducing the imaginary time τ , defined as

$$\tau = i \frac{t}{\hbar}. \quad (3.115)$$

The Schrödinger equation written in terms of this parameter takes the form

$$\frac{\partial \psi(x, \tau)}{\partial \tau} = \frac{\hbar^2}{2m^*} \frac{\partial^2 \psi(x, \tau)}{\partial x^2} - V(x)\psi(x, \tau). \quad (3.116)$$

Clearly, the above differential equation can be easily integrated over the imaginary time, and its solution will have the form

$$\psi(x, \tau) = \psi(x) e^{-E\tau}, \quad (3.117)$$

where the orbital part $\psi(x)$ of the wave function and the energy E must be obtained by solving the stationary Schrödinger equation, defined by the right-hand side of Eq. (3.116).

Note that the form of Equation (3.116) is similar to that of the diffusion equation in real time:

$$\frac{\partial C}{\partial t} = \mathcal{D} \frac{\partial^2 C}{\partial x^2} - kC, \quad (3.118)$$

where \mathcal{D} is the diffusion constant, C is the distribution of diffusing particles, and k is a rate term, describing the decay of the population of diffusing particles. The idea of the QDMC technique is to use this analogy, and model the imaginary-time evolution of the system as the game of chance, using “ ψ particles” as random walkers.

By mapping the equation (3.116) onto the equation (3.118) one sees immediately that for each random walker ψ situated at the position x the “diffusion constant” $\mathcal{D} = \frac{\hbar^2}{2m^*}$, and the “rate term” $k = V(x)$, i.e., it is equal to the value of the potential V at the point where the random walker is. The simulation is organised in such a way that the imaginary time τ is advanced in steps $\Delta\tau$, and during this time interval the random walker changes its position by Δx . These quantities are, of course, not independent; according to the Einstein relation [94]

$$\frac{1}{2} \frac{(\Delta x)^2}{\Delta\tau} = \mathcal{D}. \quad (3.119)$$

In the absence of the rate term k the diffusion equation can be solved analytically, and the probability that the random walker takes the step of length Δx in time interval $\Delta\tau$ exhibits a Gaussian distribution:

$$W(\Delta x) = \frac{1}{\sqrt{2\pi}\sigma} \exp\left(-\frac{(\Delta x)^2}{2\sigma^2}\right) \quad (3.120)$$

where the parameter $\sigma = \sqrt{2\mathcal{D}\Delta\tau}$. This is why in this game of chance after each time step $\Delta\tau$ one moves the random walkers by distances Δx selected at random according to the Gaussian distribution, and accounts for the rate term (i.e., the existence of the external potential) by conditional *deaths* or *births* of random walkers.

I can now formulate the general QDMC algorithm for my problem, posed by defining the Schrödinger equation for a M -particle system

$$\frac{\partial\psi}{\partial\tau} = \left[\sum_{i=1}^M \frac{\hbar^2}{2m_i} \Delta_i - (V - V_{ref}) \right] \psi = -(E - V_{ref})\psi. \quad (3.121)$$

1. In the first, preparatory step, one creates N random walkers distributed randomly in real space. If the problem has a single-particle nature in three dimensions, each random walker will be remembered as a triplet of numbers, defining its coordinates. If the problem involves more particles, say M , each random walker will have $3M$ coordinates, defining the position of each particle in space.
2. Now the simulation time is advanced by $\Delta\tau$ (this time interval is chosen by the user). All coordinates of each random walker are changed by the step Δx selected

at random with the Gaussian distribution as described above. Of course, steps for each coordinate of each random walker are chosen independently, so that in each case we deal with the real random walk in $3M$ -dimensional space.

3. Next one accounts for the rate term k . In this simulation, as already mentioned, the value of this rate term equals to the value of the potential at coordinates of each random walker, and is clearly different for each walker. In general, it is not just the confinement potential, but it also contains all relevant particle-particle interactions. For instance, for my interacting electrons the rate term will comprise both the value of the parabolic potential corresponding to a given distribution of electrons in space, but also all Coulomb interactions between each pair of electrons.

The probability of birth or death is calculated by comparing the full potential V of a given walker to a certain reference potential V_{ref} , used to control the population of walkers; I shall define this potential later. Here let us only state that the probability of birth for each walker is

$$P_B = -(V - V_{ref})\Delta\tau \quad \text{if } V < V_{ref},$$

$$P_B = 0 \quad \text{if } V \geq V_{ref},$$

and the probability of death is

$$P_D = (V - V_{ref})\Delta\tau \quad \text{if } V > V_{ref},$$

$$P_D = 0 \quad \text{if } V \leq V_{ref}.$$

For each walker one select at random a number from the region $(0, 1)$ (with uniform distribution) and compares it to the above probabilities. If this number is smaller than P_B , another, new walker is introduced at the position of the current one (birth), and if it is smaller than P_D , the current walker is removed from the population. Note that by doing so I, in general, change the number N of random walkers.

4. The procedure outlined in points 2 and 3 is repeated until the population of random walkers reaches the steady state distribution.

I must now develop tools allowing me to derive meaningful physical information from the random walk procedure. First of all, let us define the reference potential V_{ref} as

$$V_{ref} = V_{avg} - \frac{N - N_P}{N_P \Delta\tau}. \quad (3.122)$$

The number N_P is the target number of random walkers. If the current population N is smaller than N_P , the reference potential will favour births of walkers; if $N > N_P$, the reference potential will favour their deaths. In the above formula, V_{avg} is the average potential of random walkers, calculated by adding the potential of each walker and dividing by the current number of walkers N . Second, it can be proved [3] that upon reaching the steady-state distribution, the total energy of the system is simply $E = V_{avg}$.

The procedure I have just described contains no approximations, and therefore should give *exact* results within the numerical accuracy of the algorithm. In practice, in order to be able to perform a meaningful statistical study, it is advisable to take large population of walkers and small time steps $\Delta\tau$. Another improvement in the efficiency of this algorithm can be introduced by the so-called *importance sampling* [3]. In real systems the random walkers are usually distributed nonuniformly, reflecting the fact that usually the probability of finding the particles is larger in some areas, and smaller in others. Therefore, it is not efficient to sample all these regions in the same way: regions, where the wave function is expected to assume the largest values, should be sampled preferentially. To introduce this importance sampling, one usually prepares a trial function, reflecting the expected steady-state distribution of walkers, and one modifies the QDMC algorithm so that only the *difference* between the actual and the trial distributions is calculated.

The quantum diffusion Monte Carlo algorithm can be applied directly to single particle problems, and problems of many interacting bosons. However, in the case of many interacting fermions it is necessary to modify the approach in order to account for the antisymmetry of the wave function of the system. From the above description it is clear that the distribution of the random walkers is a measure of the wave function distribution in the system, but the method cannot yield negative distributions. But for many-fermion

systems there must be regions, where the total wave function of the system assumes positive values, and other regions, where it is negative. The QDMC algorithm in such cases is constructed in such a way that the motion of random walkers is constrained to areas, where the function is positive, and, at the same time, only those areas that are not connected via the permutation operator. This is an important difficulty, since in order to be able to execute the algorithm, one must know in advance where the nodes of the total wave function are so that the motion of walkers can be restricted only to the appropriate regions between nodal surfaces. To achieve this goal, several techniques were developed, usually involving some kind of trial wave function ψ_T as an input [3, 23]. The trial function can be prepared, e.g., by performing the SDFT calculation first, arranging the Kohn-Sham orbitals in a single Slater determinant, and determining the nodal surfaces of such many-particle function [22, 49].

Another difficulty appears in treatments of interacting fermions in the presence of an external magnetic field. Since in such cases the real-space Hamiltonian exhibits a broken time-reversal symmetry, the wave functions are usually complex, and the magnetic field usually couples to their phase [93]. In this case it is possible to write the complex Schrödinger equation as a set of two coupled real equations: one for the modulus, and one for the phase of the wave function, and the equation for the modulus is already of the bosonic nature, i.e., does not suffer from the sign problem. The procedure here is to make a choice for the phase, and solve for the modulus exactly (that is, exactly within this particular choice of the phase) using the diffusion algorithm.

The QDMC and other Monte Carlo techniques are extensively used in the context of many-electron quantum-dot systems [22, 40]. In the paper discussing the exact diagonalisation method optimised for the harmonic-oscillator basis set (Section 3.3.2), we have briefly presented a comparison of energies obtained with this method and with QDMC, and shown an excellent agreement of the results of these two techniques. However, it is clear that the QDMC method is capable of handling much larger systems than the

exact diagonalisation. The only real difficulty arises in constructing the fixed-node or fixed-phase schemes, whose level of complexity increases with the increase of the number of electrons.

Chapter 4

Electronic correlations as a function of the confinement energy

In Chapter 2 I have found the single-particle spectra of the most important classes of QD potentials, and in Chapter 3 I have formulated the problem of many interacting particles confined in QDs. In order to solve this problem, I have introduced the exact diagonalisation method with optimised many-particle basis set. I have demonstrated that this method treats all aspect of particle-particle interactions on equal footing, and, within the assumed cutoff of the single-particle basis, delivers the exact eigenenergies of the system. In the following chapters I shall use the theoretical tools thus constructed to analyse the properties of systems of many interacting particles confined by nanostructures with various geometry, with special attention devoted to the manifestations of particle-particle correlation effects.

My presentation starts with the description of properties of N electrons confined in a parabolic quantum dot at zero magnetic field. This description is given in the paper “Designing quantum systems in self-assembled quantum dots”, by M. Korkusiński, W. Sheng, and P. Hawrylak, published in *Physica Status Solidi (b)*, vol. 238, page 246

(2003). This publication is an integral part of this thesis and is appended to the presented material. Below I shall highlight the most important points of this work.

Let us start by comparing the energy scale of the single-particle energy quantisation with that of Coulomb interactions. For a parabolic dot the fundamental scale of the single-particle energy quantisation is introduced by the characteristic oscillator energy $\Omega_0 = \hbar\omega_0/\mathcal{R}$ (see Section 2.1; \mathcal{R} is the effective Rydberg). As for the interactions, their strength can be measured, e.g., by the magnitude of the fundamental Coulomb matrix element described in Section 3.1.2:

$$\langle 00, 00 | v | 00, 00 \rangle = E_0 = \frac{\sqrt{\pi}}{\ell}, \quad (4.1)$$

where the oscillator length ℓ at zero magnetic field, when expressed in the effective Bohr radii, is simply $\ell = 1/\sqrt{\Omega_0}$. Therefore, the characteristic energy $E_0 = \sqrt{\pi\Omega_0}$.

Let us now compare these two energy scales. The single-particle energy quantisation scales linearly with the oscillator energy, while the interactions scale as square root of Ω_0 . Then, as I tune Ω_0 - by changing the dot size in the case of SADs, or by tuning the gate voltage in the case of gated devices - I can change the ratio of these two energies. The characteristic single-particle energy becomes equal to that of interactions when $\Omega_0 = \pi$. If the confinement is stronger (Ω_0 larger), then the single-particle energy quantisation is larger than interactions, and if the confinement is softer ($\Omega_0 < \pi$), the situation is reversed.

Thus, when considering the system of many interacting particles one expects to find two regimes. In QDs with strong confinement the single-particle energy quantisation dominates, and one can construct the ground state of the system just by distributing the particles on the single-particle levels with the lowest energies, seeing only that the Pauli exclusion principle is satisfied. The total energy of the system can be then calculated perturbatively. On the other hand, for QDs with sufficiently soft confinement the interactions will dominate the energy landscape of the system. One expects strong configuration mixing, and so one can no longer anticipate the ground-state configuration reliably: it

has to be calculated. It is possible that the ground states of the systems in each of the regimes will be different.

To demonstrate this, I shall now consider a system of three electrons in a parabolic quantum dot with two single-particle shells. As I demonstrated in Section 2.1, the lowest, s shell in the parabolic potential consists of one doubly-spin-degenerate state with single-particle angular momentum $l = 0$. The second, p shell, on the other hand, consists of two doubly-spin-degenerate states, one with angular momentum $l = -1$, and one with angular momentum $l = +1$. This simple structure of the single-particle energy levels is presented in Figure 4.1 (a) and (b).

Let us now distribute my three electrons on the three orbitals. If I were to assume that the particles do not interact, the natural choice of the candidate for the ground state of the system would be that shown in Fig. 4.1 (a), since it has the lowest total energy. This configuration is built out of two electrons with opposite spins distributed on the s shell, and the third electron on the p shell. The total angular momentum of this state is $0 + 0 + (-1) = -1$, the total spin $S = 1/2$, and the projection of the total spin $S_z = -1/2$. One can construct another state with the same energy by putting the third electron on the other orbital of the p shell. This configuration would have the same total spin and projection as the previous one, but the total angular momentum of $+1$. Since the angular momenta of the two configurations are different, the Hamiltonian does not couple them, and they can be considered independently. Moreover, due to the symmetry of the system at zero magnetic field, the energy levels corresponding to these two configurations are degenerate, so it is sufficient to consider just one of them. The configuration $|L, S_z\rangle = |-1, -1/2\rangle$ shown in Fig. 4.1 (a) is not the only configuration that can be generated with this particular suite of quantum numbers. Another one would involve leaving the s shell completely empty, and putting one electron on the orbital with $l = 1$, and two electrons - with opposite spins - on the orbital $l = -1$. Therefore, the configuration I have chosen is not the exact many-body state of the system since

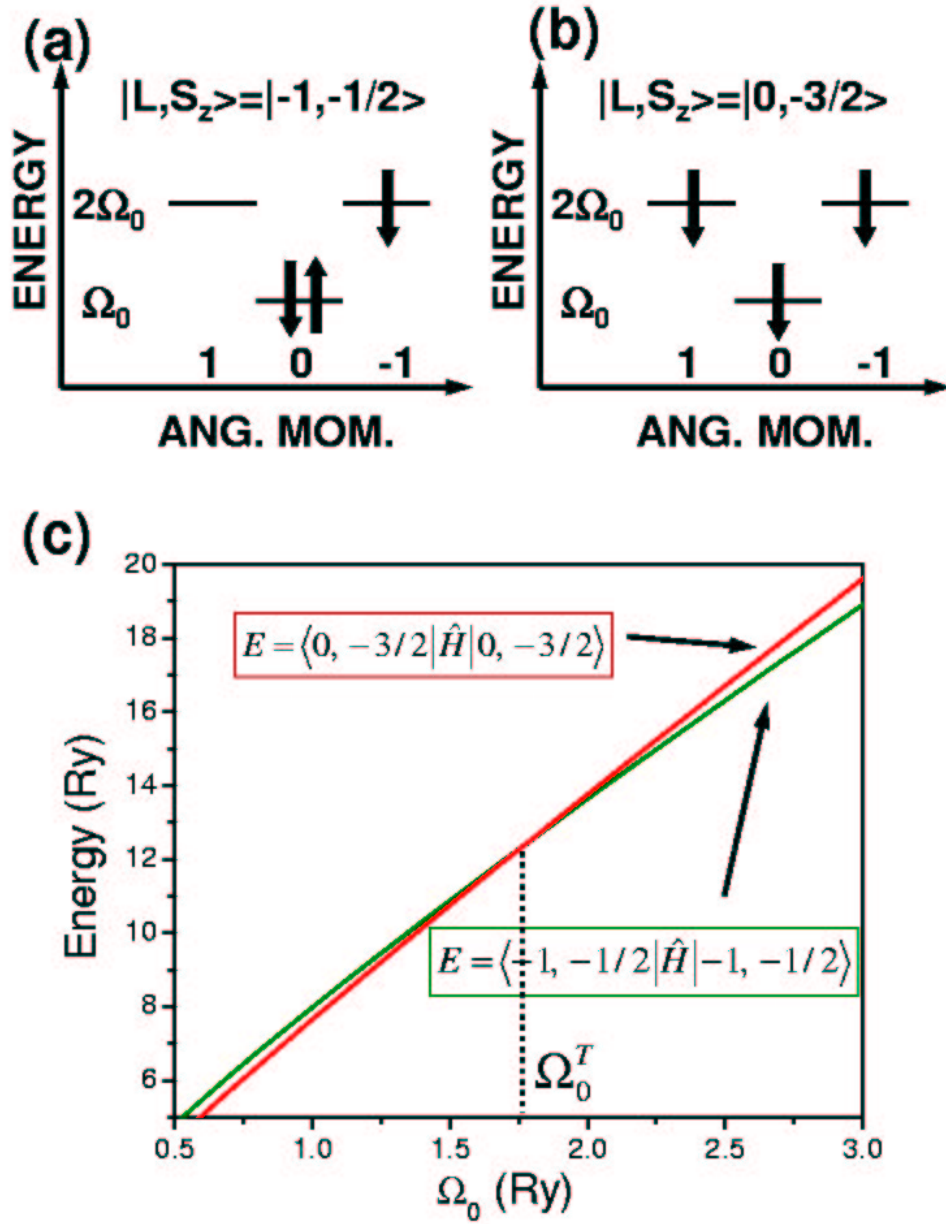


Figure 4.1: The configuration of the three-electron system with quantum numbers $|L, S_z\rangle = |-1, -1/2\rangle$ (a) and $|0, -3/2\rangle$ (b). The graph (c) shows the expectation values of the total energy of the system as a function of the confinement energy Ω_0 for the low-spin state (green line) and the high-spin state (red line)

it is mixed with the other one by Coulomb interactions. I shall include the effects of configuration mixing later on.

Let us now consider a different configuration, presented in Fig. 4.1 (b). This is the only way of distributing the three electrons on single-particle states if I require that all of them have the same spin. The total angular momentum of this configuration is zero, the total spin $S = 3/2$, and the projection of the total spin $S_z = -3/2$. This configuration, further referred to as $|L, S_z\rangle = |0, -3/2\rangle$, is the only configuration in its suite of quantum numbers, and is thus an *exact* many-body state in the two-shell approximation.

Let us now compare the energies of these two states as a function of Ω_0 . The corresponding total energy in each case is calculated as the expectation value of the full many-body Hamiltonian

$$\hat{H} = \sum_{i\sigma} E(i, \sigma) c_{i\sigma}^\dagger c_{i\sigma} + \frac{1}{2} \sum_{ijkl\sigma\sigma'} \langle i\sigma, j\sigma' | V | k\sigma', l\sigma \rangle c_{i\sigma}^\dagger c_{j\sigma'}^\dagger c_{k\sigma'} c_{l\sigma}. \quad (4.2)$$

Using the energies of single-particle states $E(nm\sigma) = \Omega_0(n+m+1)$ obtained in Section 2.1 and the Coulomb matrix elements calculated in Section 3.1.2, I can express these energies in the following form:

$$E_{-1, -1/2} = 4\Omega_0 + 2.25\sqrt{\pi\Omega_0}; \quad (4.3)$$

$$E_{0, -3/2} = 5\Omega_0 + 1.5\sqrt{\pi\Omega_0}. \quad (4.4)$$

The low-spin state has lower orbital energy, but higher interaction energy as compared to the high-spin state. Therefore, for strong confinements (large Ω_0) one may expect the low-spin state to be lower in energy than the high-spin state, and for small Ω_0 the situation may be reversed. This is indeed the case, as can be seen in Fig. 4.1 (c). In this graph I present the above energies as a function of the confinement energy Ω_0 . For strong confinement the low-spin configuration is the ground state of the system. But as Ω_0 is decreased, the two energies cross, and a transition to the high-spin state occurs. This transition takes place at a critical value of confinement energy, further referred to as Ω_0^T . Note that this transition is due entirely to the interplay between the single-particle

(orbital) energy quantisation and direct and exchange Coulomb terms. In this simple model correlations play no role, since I have not considered the interaction mixing effects in the low-spin subspace.

To include the correlation effects in a controllable fashion, let us perform the exact diagonalisation study as a function of the confinement energy Ω_0 and the number of confined shells N_S . This time I fully account for *all* configurations possible within each subspace. Thus, the basis sets of the low-spin and the high-spin subspace no longer contain just one configuration, but the sizes of these sets grow factorially with N_S . This is shown in Fig. 4.2 (a), where I give the number of configurations in the low-spin (green bars) and high-spin subspace (red bars) as a function of N_S ; inset to this figure shows the ratio of these numbers. Note that for all values of N_S except for $N_S = 3$ this ratio is approximately 2 : 1, while for $N_S = 3$ it is almost 3 : 1.

With these basis sets I have performed the exact diagonalisation studies as a function of the number of shells, and in most cases have observed the low-spin-high-spin transition. The characteristic value of confinement energy Ω_0^T as a function of N_S is shown in Fig. 4.2 (b). I see, in general, that as I increase the number of shells, the transition occurs for lower and lower confinements, with the exception of $N_S = 3$, where the transition does not occur at all (the ground state is the low-spin state for all values of Ω_0). This behaviour can be understood in the context of the number of available configurations in each subspace. As can be seen in Fig. 4.2 (a), for all N_S there are more low-spin configurations than the high-spin configurations. This is due to the fact that in the case of low spin one can distribute two electrons on the same orbital, while for spin-polarised configurations this is forbidden by the Pauli principle. The low-spin states, although not favoured by the direct and exchange Coulomb terms, have a correlation advantage over the high-spin states due to larger correlation mixing effects. It is particularly visible in the case of $N_S = 3$, where the low-spin basis set is particularly large as compared to the high-spin set, and the correlation advantage thus gained causes the low-spin state to be the ground state of the

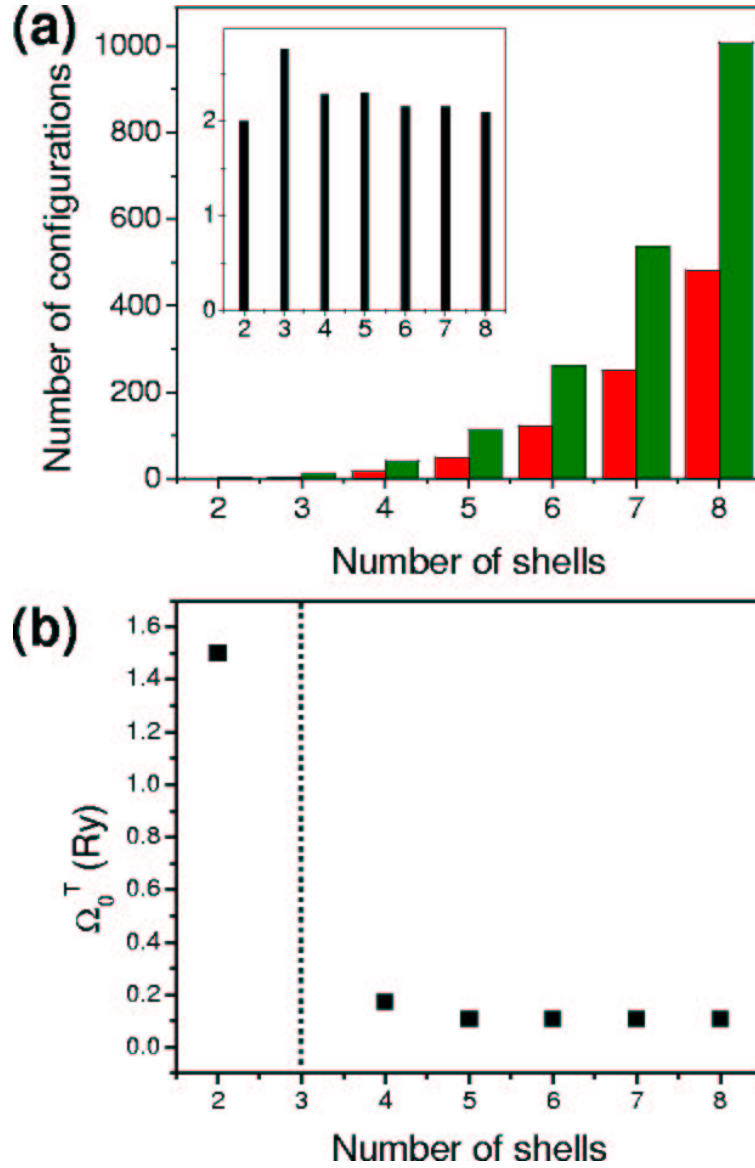


Figure 4.2: (a) Number of configurations in the low-spin subspace ($L = -1$, $S_z = -1/2$ - green bars) and in the high-spin subspace ($L = 0$, $S_z = -3/2$ - red bars) for a three-electron system as a function of the number of single-particle shells N_S . Inset shows ratios between these numbers. (b) Critical confinement energies Ω_0^T marking the low-spin - high-spin transition as a function of the number of shells N_S . For $N_S = 3$ there is no transition

system for all confinement energies. The progressive increase in basis sizes also causes the critical value Ω_0^T to decrease with the increase of N_S , and saturate around $N_S = 5$, where the convergence of the low-energy configurations is already achieved (at this stage further increase of N_S supplements the basis sets only with high-energy configurations, having a negligible effect on the lowest-energy states). As can be seen, by changing the number of available single-particle shells one can tune the electronic correlations. This tuning can be realized in the case of self-assembled quantum dots by engineering these nanostructures to contain only a desired number of single-particle orbitals.

The paper invoked in the beginning of this Chapter describes similar evolution of the system with the number of shells and confinement energy for up to eight confined electrons. The most important aspect of this work is the fact that one can create magnetic moments in quantum dots by appropriately engineering its single-particle and many-particle properties: the shell spacing, the number of confined shells, and the number of electrons distributed on them. For instance, in the case of $N_S = 4$ shells the electrons tend to align their spins as the confinement energy Ω_0 is lowered, which means that the Hund's rules and the magnetic moments associated with half-filled shells are not valid in the regime of strong interactions.

Chapter 5

Electronic correlations as a function of the magnetic field

In Chapter 4 I have described the effects of electron-electron correlations in the system of N interacting electrons confined in a parabolic potential with no external fields. Let us now move on to discussing the properties of the system in the presence of a magnetic field.

Let us compare the orbital energy quantisation and characteristic interaction energies as a function of the magnetic field. As I have shown in Section 2.1, the single-particle energy spectrum in the presence of the field is characterised by two frequencies,

$$\omega_{\pm} = \sqrt{\omega_0^2 + \frac{1}{4}\omega_c^2} \pm \frac{1}{2}\omega_c, \quad (5.1)$$

where the cyclotron frequency ω_c increases linearly with the magnetic field. Thus, in large fields the frequency ω_+ approaches the cyclotron frequency, while the frequency ω_- approaches zero. Interactions, on the other hand, scale as

$$E_0 = \frac{\sqrt{\pi}}{\ell} = \sqrt{\pi} \left(\omega_0^2 + \frac{1}{4}\omega_c^2 \right)^{1/4}, \quad (5.2)$$

i.e., they increase with the magnetic field. Thus, for sufficiently large ω_0 , in low magnetic

field the single-particle orbital energy quantisation will dominate, while the regime of large magnetic fields is the regime of strong interactions.

5.1 Collapse of the $\nu = 2$ phase of the quantum Hall droplet

I start my presentation by summarising the most important points of the paper “Theory of spin-singlet filling factor $\nu = 2$ quantum Hall droplet”, published by Andreas Wensauer, Marek Korkusiński, and Pawel Hawrylak in Physical Review B, vol. 67, page 035325 (2003). This publication is an integral part of this thesis and is appended to the presented material.

In this paper we discuss the stability of the $\nu = 2$ phase of the quantum Hall droplet composed of an even number of $2N$ electrons in a parabolic confinement and in the magnetic field. First let us explain what the $\nu = 2$ phase is by distributing the $2N$ electrons on the levels of the single-particle parabolic energy spectrum, presented in Figure 5.1 (a). In this Figure I show several single-particle orbitals $(0, m, \sigma)$ forming the lowest Landau level, and two orbitals $(1, 0, \sigma)$ belonging to the second Landau level (for discussion of Landau levels in parabolic confinement, see Section 2.1). The confinement energy of the quantum dot $\hbar\omega_0 = 6$ meV, and the Zeeman energy is artificially enhanced for better visibility. In finite magnetic fields there exists a ladder of low-energy states $(0, m, \sigma)$ whose energy is lower than that of the lowest-energy orbital $(1, 0, \sigma)$ of the second Landau level. Such a ladder is denoted in the Figure 5.1 (a) by the black bars. If one distributes the $2N$ electrons on these states, they will form spin-singlet pairs and occupy the single-particle orbitals with increasing quantum number m , as shown in Figure 5.1 (b) for eight electrons. This spin-singlet state of the electronic droplet is called the $\nu = 2$ phase in the terminology of the integer quantum Hall effect.

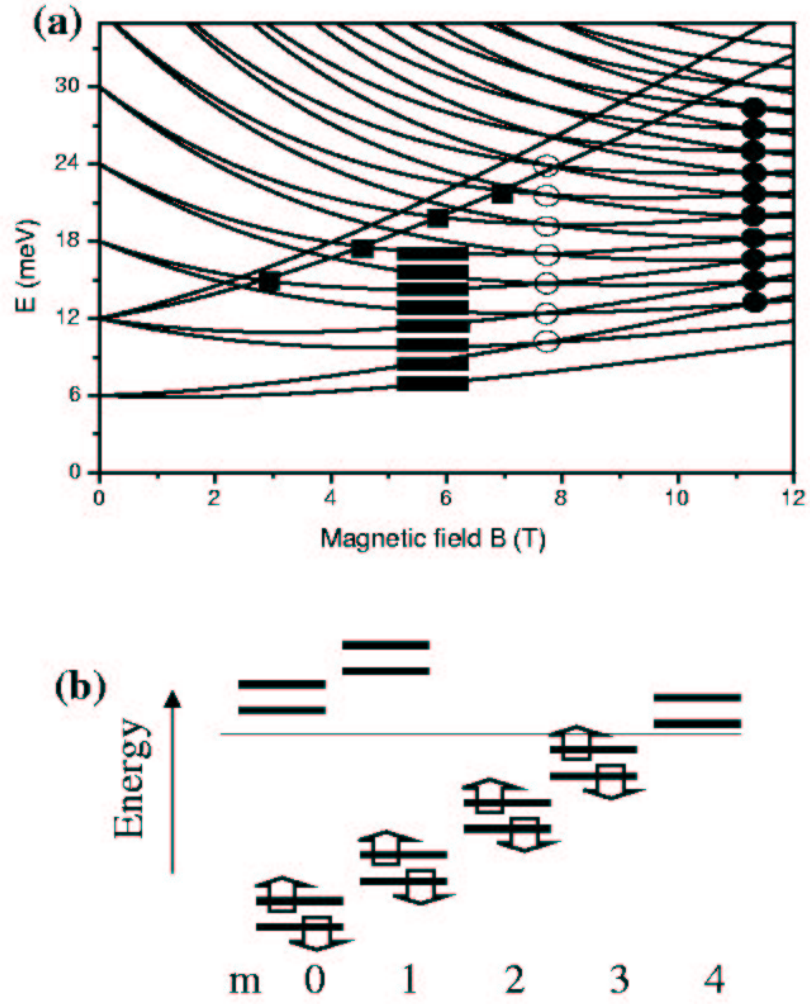


Figure 5.1: (a) Magnetic field evolution of the single-particle spectrum of the parabolic quantum dot (Zeeman energy artificially enhanced). Circles denote the edge spin flip of a droplet with even (empty) and odd (full) number of electrons; squares denote the centre spin flip. (b) Configuration of noninteracting electrons corresponding to the $\nu = 2$ phase

Let us now analyse the behaviour of this configuration as a function of the magnetic field. If the field is low enough, the states from the second Landau level may become lower in energy than the last occupied orbital on the lowest Landau level. These states are presented in Figure 5.1 (b) as empty levels with $m = 0$ and $m = 1$ above the Fermi energy, denoted by the black line. Due to the presence of the Zeeman energy, the electron on the last occupied orbital on the lowest Landau level $(0, 3)$ has spin up, while the lowest-energy state belonging to the second Landau level can contain the electron spin-down. Therefore, if the magnetic field is lowered sufficiently, a spin-flip transition will take place: the electron spin-up at the edge of the droplet will flip its spin and occupy the orbital $(1, 0, \downarrow)$ in the centre of the dot. These spin flips for different numbers of electrons are denoted in Figure 5.1 (a) with black squares.

If the magnetic field is increased, the separation between the consecutive orbitals of the lowest Landau level with the same spin (equal to $\hbar\omega_-$) decreases, and the Zeeman splitting increases linearly. For sufficiently high magnetic fields these two energies become equal: in Figure 5.1 (b) the lowest, empty, spin-down orbital with $m = 4$ becomes degenerate with the orbital with $m = 3$ occupied by the spin-up electron. This degeneracy will occur for the same magnetic field for all orbitals on the lowest Landau level; it is denoted with empty circles in Figure 5.1 (a). If the magnetic field is further increased, it becomes energetically favourable for the spin-up electron at the edge to flip its spin and move to the next orbital. Thus, the $\nu = 2$ phase is unstable against the centre spin-flip transition in low magnetic fields, and the edge spin-flip transition in high magnetic fields. Note that as more and more single-particle orbitals are populated with electrons, the range of magnetic fields in which the $\nu = 2$ phase is stable becomes narrower and narrower. It disappears completely for a critical number of electrons, for which the two spin-flip transitions occur at the same magnetic field (the last empty circle in Figure 5.1(a)). In this single-particle description the $\nu = 2$ phase diagram is thus finite, both as a function of the magnetic field and the number of electrons. However, due to the small value of

the Zeeman energy the predicted edge spin-flip transitions terminating the stability of the $\nu = 2$ phase would take place at magnetic fields of hundreds of Tesla while such transitions are observed experimentally for fields of order of a few Tesla. This discrepancy is due to my assumption of the absence of interactions. Our paper is devoted to understanding how the direct and exchange Coulomb interactions as well as electronic correlations modify the phase diagram of the system.

Let us start the analysis by considering the system in the lowest-Landau-level approximation (LLL). I write the wave function of the $\nu = 2$ phase as a product of two spin-polarised droplets:

$$|GS(2N)\rangle = \prod_{m=0}^{N-1} c_{0,m,\uparrow}^+ \prod_{m=0}^{N-1} c_{0,m,\downarrow}^+ |0\rangle. \quad (5.3)$$

The total energy of the $\nu = 2$ state is calculated as the expectation value $\langle GS(2N) | H | GS(2N) \rangle$ of the many-body Hamiltonian (3.2) analysed in Chapter 3. Now the particles are quasi-electrons dressed in interactions, and for further discussion it is convenient to define the selfenergy $\Sigma(n, m, \sigma)$, measuring the total interaction energy of the electron on orbital (n, m, σ) with all other electrons:

$$\Sigma(n, m, \sigma) = \sum_{m'=0}^{N-1} (2\langle nm, 0m' | V | 0m', nm \rangle - \langle nm, 0m' | V | nm, 0m' \rangle). \quad (5.4)$$

Note that in this case this selfenergy does not depend on spin.

The centre and edge spin-flip configurations can now be expressed as excitations from the $\nu = 2$ state $|GS\rangle$. The wave function and corresponding energy of the centre configuration is

$$|C(2N)\rangle = c_{1,0,\downarrow}^+ c_{0,(N-1),\uparrow} |GS(2N)\rangle; \quad (5.5)$$

$$\begin{aligned} E(C) &= E_{\nu=2} + \Omega_+ - (N-1)\Omega_- - E_z \\ &+ \Sigma(1, 0) - \Sigma(0, N-1) - \langle 0, (N-1); 1, 0 | V | 1, 0; 0, (N-1) \rangle. \end{aligned} \quad (5.6)$$

The energy $E(C)$ is calculated with respect to the energy $E_{\nu=2}$ of the $\nu = 2$ configuration. One quasielectron with spin up is taken off from the orbital $(0, N-1)$, and therefore the

appropriate orbital energy and selfenergy has to be subtracted from $E_{\nu=2}$. Then this quasielectron is put on the orbital $(1, 0)$, and the orbital energy and selfenergy corresponding to this orbital has to be added. Further the spin of the particle is flipped, which results in the gain of Zeeman energy. The last term is the vertex correction, accounting for the attractive interaction of the quasielectron with the quasihole, which was created by removing the particle from the droplet.

As for the edge configuration, the corresponding wave function and energy are created in an analogous way:

$$|E(2N)\rangle = c_{0,N,\downarrow}^+ c_{0,(N-1),\uparrow} |GS(2N)\rangle, \quad (5.7)$$

$$\begin{aligned} E(E) &= E_{\nu=2} + \Omega_- - E_z \\ &+ \Sigma(0, N) - \Sigma(0, N-1) - \langle 0, (N-1); 0, N | V | 0, N; 0, (N-1) \rangle. \end{aligned} \quad (5.8)$$

Both these energies indicate that the spin-flip transitions take place as a result of the competition between the single-particle orbital energy and the interaction energy. For example, the interactions favour the edge spin-flip phase, because the edge spin-flip transition leads to (i) a redistribution of the last electron leading to a decrease of the direct repulsive Coulomb term, and (ii) an increase of the spin of the system, which leads to an increase of the exchange term, additionally lowering the energy. This is why in the case of the edge spin-flip transition the interactions play a role similar to that of the Zeeman energy in the noninteracting picture, but are strong enough to cause this transition in the magnetic fields of order of several Tesla. In the case of the centre spin-flip configuration the interplay of energies is more complicated: the spin is flipped, gaining the exchange energy, but the electron is put in the centre of the dot, which increases the Coulomb repulsion. The net result of this interplay drives the spin-flip transition to lower magnetic fields.

In order to be able to address the experimental spectra one needs to calculate the electrochemical potential of the $2N$ -electron droplet: $\mu(2N) = E(2N+1) - E(2N)$. To

this end I also need to find the phase diagram of the $2N + 1$ -electron droplet. I do that by treating the extra particle as a quasielectron added to the state $|GS(2N)\rangle$ of the $2N$ -electron droplet. This allows to calculate the energies of the system in a simple way, analogous to that described above.

For the $2N + 1$ -electron system I focus on a phase analogous to the $\nu = 2$, built out of the spin-singlet configuration for $2N$ particles as presented in Figure 5.1 (b), with the extra electron spin down on the next available orbital on the lowest Landau level (in this case, the orbital $(n, m) = (0, 4)$). As the magnetic field is lowered, this unpaired electron is transferred to the central orbital $(n, m) = (1, 0)$ of the second Landau level (without the spin flip). On the other hand, as the magnetic field is increased, the last edge electron with spin up (the electron on the orbital $(0, N)$; in Fig. 5.1 this electron occupies the orbital $(0, 3)$) is transferred over the unpaired electron to the orbital $(0, 5)$, and its spin is flipped. This transition leaves the system in a state with three unpaired spin-down electrons at the edge. These transitions occur at magnetic fields different than those corresponding to the centre and edge spin-flips of the $2N$ -electron droplet. As a result, the electrochemical potential $\mu(2N)$ calculated as a function of the magnetic field is expected to exhibit a characteristic pattern of kinks. This pattern is indeed measured experimentally.

To improve the understanding of the role of direct and exchange Coulomb interactions, the $2N$ -electron droplet is analysed using the spin- and space-restricted Hartree-Fock approach, as described in Section 3.2. For the $\nu = 2$ phase the variational Hartree-Fock wave function is written as

$$|GS(2N)\rangle = \prod_{\sigma} \prod_{m=0}^{N-1} (a_{0,m,\sigma}^* c_{0,m,\sigma}^{\dagger} + a_{1,m+1,\sigma}^* c_{1,m+1,\sigma}^{\dagger}) |0\rangle, \quad (5.9)$$

i.e., the Hartree-Fock orbitals is constructed with definite angular momentum and spin out of the single-particle states from the two lowest Landau levels. The minimisation of the expectation value $\langle GS(2N) | H | GS(2N) \rangle$ with respect to the variational parameters a is written as an eigenvalue problem of the Hartree-Fock Hamiltonian within each angular

momentum and spin channel. The Hartree-Fock matrix is of order of 2×2 , and is composed of the diagonal orbital energy terms, and both diagonal and offdiagonal self-consistent Hartree-Fock fields. A similar variational wave function is also constructed for the edge configuration $|E(2N)\rangle$ and the centre configuration $|C(2N)\rangle$, in the latter case allowing for the mixing of the second-Landau-level centre orbital $(1, 0)$ with the orbital $(2, 1)$ from the third Landau level. To calculate the phase diagram in this approximation, I compare the total energies calculated self-consistently for each of these three configurations as a function of the magnetic field and the number of electrons.

Finally, I attempt to account for the effects of electronic correlations. I do that using three different approaches: (i) single quasielectron-quasihole pair excitations from the Hartree-Fock $\nu = 2$ ground state, (ii) the exact diagonalisation, and (iii) the spin density functional theory.

As I have discussed in Section 3.3, the first approach involves calculating self-consistently the Hartree-Fock ground state $GS(2N)\rangle$ as expressed in Eq. (5.9), and use the optimal variational coefficients to construct the new creation and annihilation operators A^+ , A , such that

$$A_{1l\sigma}^+ = a_{0l\sigma}^{*(1)} c_{0l\sigma}^+ + a_{1,l+1,\sigma}^{*(1)} c_{1,l+1,\sigma}^+, \quad (5.10)$$

$$A_{2l\sigma}^+ = a_{0l\sigma}^{*(2)} c_{0l\sigma}^+ + a_{1,l+1,\sigma}^{*(2)} c_{1,l+1,\sigma}^+. \quad (5.11)$$

The two sets of coefficients a are obtained in the eigenvalue problem of the Hartree-Fock Hamiltonian for each angular momentum and spin channel, even if the channel does not contain any electrons. Further the many-body Hamiltonian is rotated from the basis of operators c^+ , c to the basis of operators A^+ , A . The next step is to construct the basis set by distributing the quasiparticles on the Hartree-Fock orbitals. Here the basis is restricted to contain single quasielectron-quasihole pairs only, and therefore this basis set is composed of states of the type $A_{k,l+\delta l,\uparrow}^+ A_{0l\downarrow} |\nu = 2\rangle_{HF}$. Note that in this way one only generates the electron-hole pair triplet excitations on the two lowest Landau levels. I am interested in the triplet states only, since both the centre and edge spin-flip configurations

are spin triplets. My pair excitations have a definite angular momentum $L_{\nu=2} + \delta l$, where $L_{\nu=2}$ is the angular momentum of the $\nu = 2$ state. Therefore I can group my pair excitations into subsets according to their angular momentum, and diagonalise the Hamiltonian matrix in each subset separately. Using this technique I am able to calculate the phase diagram of the electronic droplet containing even 30 electrons.

In the full exact diagonalisation approach I distribute my electrons on the single-particle orbitals, without rotating them into the Hartree-Fock basis. I generate all possible configurations of $2N$ electrons on two Landau levels, for all allowed values of total spin, and for total angular momenta from $L_{\nu=2} - 5$ to $L_{\nu=2} + 5$. Unfortunately now the total size of the basis, even after resolving the total angular momentum, total spin, and the projection of total spin, is so large that I am only able to analyse the magnetic field evolution of the system with 6 and 8 electrons.

The third approach to include correlations is the spin density functional theory in the local spin density approximation. Due to its effective single-particle character this approach allows to construct the phase diagram of the system for an arbitrary number of electrons. To remain consistent with the two other treatments in the calculation the Kohn-Sham orbitals are constructed only from the single-particle states belonging to the two lowest Landau levels.

In Figure 5.2 I present the phase diagrams of the $\nu = 2$ phase as a function of the number of electrons and magnetic field calculated using the five methods: the LLL approximation, the Hartree-Fock method on two Landau levels, the single quasielectron-quasihole pair excitations, the exact diagonalisation, and the SDFT. All phase diagrams were prepared using the GaAs material parameters assuming the same parabolic confinement energy $\hbar\omega_0 = 6$ meV. This is the central result of this work. In each diagram the $\nu = 2$ phase is stable only over a finite region of magnetic fields. Also, the four methods capable of treating large electron numbers reveal the existence of a critical number of electrons N_c , beyond which the $\nu = 2$ phase is not stable for any magnetic field. Differences

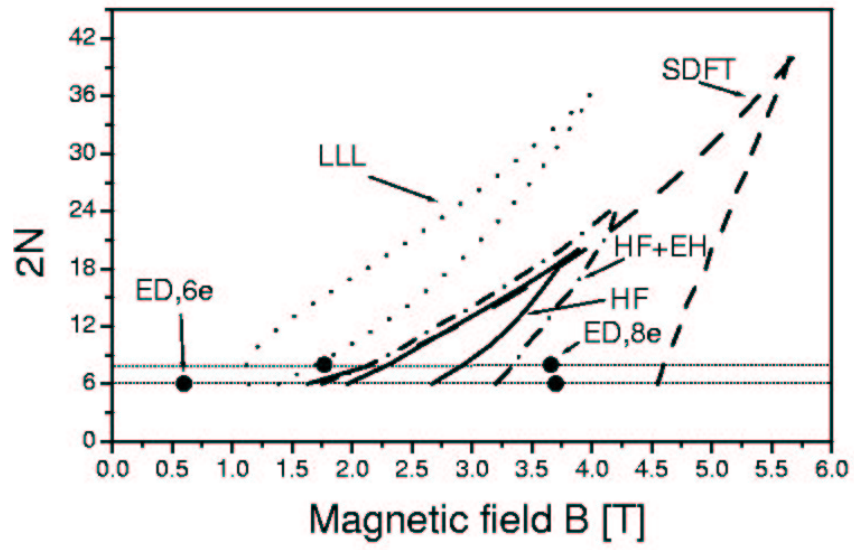


Figure 5.2: Phase diagrams obtained in the lowest Landau level approximation (dotted lines), using the Hartree-Fock approximation (solid lines), from single electron-hole pair excitation spectre (dot-dashed lines), using the SDFT approach (dashed lines), and from exact diagonalisation study (full circles)

between the phase diagrams lie only in positions of phase boundaries.

The LLL approximation predicts the occurrence of both spin-flip transitions at magnetic fields lower than those obtained with the other methods. This can be understood considering the fact that the spin flips are driven by interactions. In the LLL method the interactions were particularly strong, since the Hilbert space for each phase consisted of only one configuration. Other methods involved either self-consistent renormalisation of electronic orbitals (Hartree-Fock and SDFT) or writing the total wave function as a linear combination of many Slater determinants (single-pair excitations and exact diagonalisation). As a result, the electrons were allowed to redistribute in order to lower their repulsive Coulomb energy. This shifted the spin-flip transitions to larger magnetic fields.

Let us now compare the result of the Hartree-Fock method, accounting for the Coulomb direct and exchange interactions only, to that of the single-pair excitation approach, which partially includes the effects of correlations as well. The low-field phase boundary (i.e., the centre spin-flip) in both approaches is established by considering only one configuration, since in the pair excitation approach only one quasielectron-quasihole pair could be generated in the subspace of the centre spin-flip configuration. That is why the low-field boundaries predicted by each method almost coincide. On the other hand, the edge spin-flip state calculated in the pair excitation approach is correlated with the configurations involving occupation of the second Landau level, while in the Hartree-Fock theory it is approximated again by one configuration only. The phase boundaries predicted by these two approaches do not coincide; inclusion of correlations leads to an increase in stability range of the $\nu = 2$ phase. This is confirmed by the results of exact diagonalisation for 6 and 8 electrons, and SDFT for up to 42 electrons. Note that the SDFT calculation predicts a broader stability range of the spin-singlet phase towards higher magnetic fields than that obtained by exact diagonalisation. This is due to a slight overestimation of exchange effects in the SDFT procedure with the variational space reduced to two Landau levels. The regions of stability of the $\nu = 2$ phase obtained with the two approaches are much

larger than those predicted by the Hartree-Fock theory, both in magnetic fields (SDFT and exact diagonalisation) and in electron numbers (SDFT). Thus, electronic correlations counteract the exchange, and this is due to the fact that the exchange effects lower only the energy of the spin-polarised states, while correlation effects provide a mechanism to decrease the ground-state energies for the spin-singlet configurations as well.

In experiments the phase diagram is mapped out by analysing the addition spectrum obtained by measuring the electrochemical potential $\mu(2N) = E(2N+1) - E(2N)$. I have briefly presented this experimental procedure in Section 1.4. Such experiment is clearly sensitive both to the initial state of the N -electron droplet and the final state of the $N+1$ -electron droplet. As I have already discussed, the spin-flip transitions manifest themselves in the addition spectra as series of kinks, and for low electron number it is possible to find the kinks corresponding to the centre spin-flip and the edge spin-flip transitions. However, for electron numbers larger than the critical number N_c the $\nu = 2$ phase is no longer stable. In this regime the centre-edge transition involves transfer of the spin-down electron from the centre orbital on the second Landau level directly to the first unoccupied orbital at the edge of the droplet (without spin flip). The experimental signature of this transition is similar to the transition from the $\nu = 2$ phase to the edge configuration for lower electron numbers, and the high-electron-number kinks appear as a continuation of the line of $\nu = 2$ -edge transitions. Therefore, the collapse of the $\nu = 2$ phase is not revealed in the positions of the addition peaks. However, various alignments of stability regions can be probed by the spin-polarised tunnelling current due to the spin blockade phenomenon. In the experiment, the electrons tunnelling through the system are predominantly spin-down, and the current cannot flow if the spin of the final state of the $N+1$ -electron droplet is not equal to the spin of the initial state of the N -electron droplet plus one electronic spin down. Therefore, changes of the order of phases from centre- $\nu = 2$ -edge (triplet-singlet-triplet) to centre-edge (triplet-triplet) are visible in the amplitude pattern of the addition peaks: the sequence of amplitudes of peaks as a function of the magnetic field for $2N < N_c$

is different than that for $2N > N_c$. The amplitude patterns of addition peaks is studied as a function of the parameters of the system (Zeeman energy and electron number). This amplitude reversal is almost not recovered if the approximation used overestimates exchange or correlations. In such cases the phase boundaries of the $\nu = 2$ and spin-triplet phases are shifted, which leads to their misalignment with respect to the phases of the $N + 1$ -electron droplet. It is only when a proper balance between all interaction terms is found (e.g., by using an enhanced Zeeman energy in the SDFT calculations) that the reversal of amplitudes is obtained for a range of electron numbers.

5.2 Pairing of spin excitations in high magnetic fields

Up to now I have focused on the properties of the system of many electrons confined in a parabolic quantum dot in the region of stability of the $\nu = 2$ spin-singlet phase. In this Section I shall extend this discussion to higher magnetic fields. Research on this subject is presented in the paper “Pairing of spin excitations in lateral quantum dots”, by Marek Korkusiński, Pawel Hawrylak, Mariusz Ciorga, Michel Pioro-Ladrière and Andrew S. Sachrajda, submitted for publication in Physical Review Letters. This publication is an integral part of this thesis and is appended to the presented material.

I shall present the analysis on the model system of eight electrons in a parabolic quantum dot. Let us first consider the magnetic-field evolution of the droplet within the lowest-Landau-level approximation. I have already shown that there exists a range of magnetic fields, in which the ground state of the system is the spin-singlet $\nu = 2$ state, shown schematically in Fig. 5.3 (a). As the magnetic field is increased, one sees a transition to the edge spin-triplet configuration, or the first spin-flip phase, shown in Fig. 5.3 (b). The value of the magnetic field corresponding to this transition is determined by the competition of the orbital energy, decreasing with the increase of the field, against Coulomb direct and exchange interactions, which increase with the field. If the magnetic

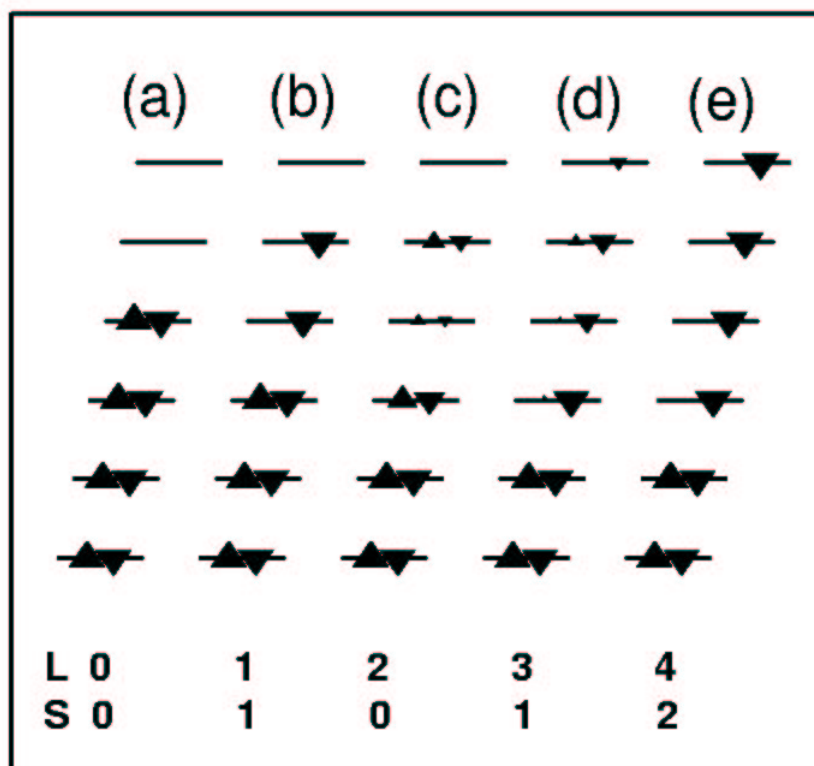


Figure 5.3: Charge distribution corresponding to the $\nu = 2$ phase (a), the first spin-flip configuration (b), the correlated biexciton (c), the internal spin-flip phase (d) and the second spin-flip configuration for an eight-electron parabolic dot

field is increased even further, one observes the second spin-flip transition - a transition from the configuration (b) to the configuration (e) in Fig. 5.3. As a result of this transition the droplet becomes even more spin-polarised (the second spin-flip phase has total spin 2), which increases the exchange energy, and the electrons are redistributed farther apart from one another, lowering the direct Coulomb repulsion. This sequence of spin flips continues until the dot becomes completely spin-polarised (this is the so-called maximum density droplet).

Note that the angular momentum of the first spin-flip configuration (b) is larger than that of the $\nu = 2$ phase by one: $L_{1SF} = L_{\nu=2} + 1$, and the angular momentum of the second spin-flip configuration (e) is $L_{2SF} = L_{\nu=2} + 4$. As can be seen, the sequence of spin flips predicted just by considering the direct and exchange interactions leaves the subspaces with angular momenta $L_{\nu=2} + 2$ and $L_{\nu=2} + 3$ unexplored.

I have analysed these unexplored subspaces within a simple exact-diagonalisation scheme, and found that by distributing the eight electrons on the single-particle orbitals of the lowest Landau level one can generate several electronic configurations with these angular momenta: there exist three singlet and two triplet configurations with $L = L_{\nu=2} + 2$ and five singlet and five triplet configurations with $L = L_{\nu=2} + 3$. The Hamiltonian matrix is diagonalised in these spin- and angular momentum-resolved basis sets. The resulting eigenstates are found have correlated character. In the subspace with $L = L_{\nu=2} + 2$ there are more singlets than triplets, and this correlation advantage causes the lowest singlet state to have lower energy than the lowest triplet. In the subspace with $L = L_{\nu=2} + 3$, on the other hand, the numbers of configurations with either spin are equal, and singlets do not have the correlation advantage. As a result, the lowest eigenstate of the Hamiltonian in this subspace is a spin triplet, since, being more spin-polarised, it has the exchange advantage over the singlets.

When the eigenenergies in the two subspaces are compared to the energies of the $\nu = 2$, first, and second spin-flip configurations, it turns out that for some regions of magnetic

fields the correlations lower the energies of the new states sufficiently for them to become ground states of the system.

Thus one obtains a new phase diagram, with two new phases occurring between the first and second spin-flip transitions. The distribution of the electronic charge of the first new correlated phase on the single-particle orbitals is shown in Fig. 5.3(c). It is a spin singlet, and it exhibits a spin-biexcitonic character, since its charge distribution clearly expresses a signature of a double hole below the $\nu = 2$ Fermi energy, and double electron above it. The second correlated phase, whose charge distribution is shown in Fig. 5.3(d), is a spin-triplet, and is predicted to become the ground state of the system just before the second spin flip. This phase can be described as a spin flip in the interior of the spin-biexciton phase. The last transition in the sequence is the second spin-flip, which terminates the correlated phases, and brings the system back to the weakly correlated ground state (e) in Fig. 5.3.

Note that the analysis accounting only for the direct and exchange interactions predicted a steplike increase of the total spin of the system: from the singlet $\nu = 2$ phase, through the triplet first spin-flip configuration, to the second spin-flip state with $S = 2$. Inclusion of correlations leads to the appearance of low-spin phases, having a correlation advantage over the high-spin configurations. As a result, the total spin exhibits an oscillatory character as a function of the magnetic field.

In Figure 5.4 I show the phase diagram of the even-electron system as a function of the magnetic field and the number of electrons. As I have shown earlier, the $\nu = 2$ phase has a finite stability region both in the magnetic field and in the number of electrons. For all the electron numbers for which $\nu = 2$ is stable I find a similar progression of phases as the magnetic field is increased: the $\nu = 2$ phase becomes unstable against the first spin-flip transition, which, in turn, is followed by the correlated biexciton, and finally the second spin-flip. The spin biexciton is stable even for very large electron numbers (of order of 30). In the phase diagram, I also find the correlated internal spin-flip phase, however it

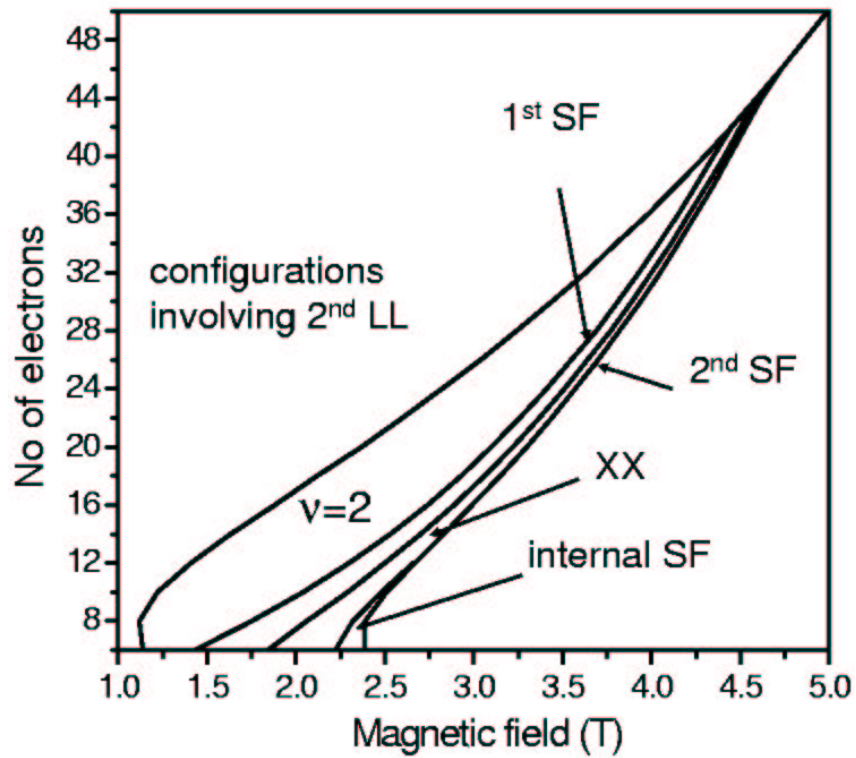


Figure 5.4: Phase diagram of the even-electron droplet as a function of the number of electrons and the magnetic field. In this calculation $\hbar\omega_0 = 6$ meV and the Zeeman energy $E_Z = 0$.

has a much smaller region of stability (this phase is no longer present for the number of electrons $N > 12$). Thus, both correlated phases should be visible in the experimental addition spectra measured for a QD with a sufficiently low number of electrons. The experimental evidence for the correlated phases is indeed found in the results of recent measurements of A.S. Sachrajda and his group at the NRC Institute for Microstructural Sciences. They have measured the addition spectra of the eighth electron into the seven-electron quantum dot in the high source-drain voltage mode. As discussed in Section 1.4, in this mode one can map not only the ground, but also the excited states of the system. The signatures of correlated phases in the vicinity of the second spin-flip are indeed found, and, to the best of my knowledge, this is the first experimental observation of correlated phases in a quantum dot with known and precisely controlled number of electrons. The correlated phases appear first as excited states, descend in energy with the increase of the magnetic field, and then some of them briefly become the ground states of the system.

Chapter 6

Correlations in a coupled quantum-dot molecule

In the two previous Chapters I have discussed the manifestations of correlations in a system of N electrons confined by a parabolic quantum dot. In this Chapter I shall move on to considering correlation effects in more complicated systems, composed of electrons and holes confined in self-assembled quantum dots.

My approach to the electronic systems involved distributing the electrons on the single-particle levels of the parabolic potential and analysing how the configurations thus created are coupled by Coulomb interactions of the carriers. I demonstrated that the strength of interactions relative to characteristic single-particle energies could be tuned by changing either the confinement energy Ω_0 or the external magnetic field. Such tuning is more difficult in the case of SADs. In Section 2.2 I have shown that for these structures the orbital energy quantisation is so strong that even the magnetic fields of magnitudes of order of 10 T modify the spectra only slightly. The only way of influencing the ratio of single-particle orbital to interaction energies is thus the manipulation of the QD confinement. In this Chapter I shall move from weakly to strongly interacting systems not by changing Ω_0 of

a single QD, but by changing the separation between two coupled quantum disks.

A schematic diagram of the system of two vertically coupled quantum disks is presented in Fig. 6.1 (a). The disks have the same height H and are horizontally aligned in such a way that they share the axis of rotational symmetry. The disk radii are denoted as R_1 (bottom disk) and R_2 (top disk); in general, $R_1 \neq R_2$. Each disk is formed on a thin wetting layer, and the thickness of the tunnelling barrier between disks is controlled by the distance D between these layers. The quantum-mechanical coupling between the two dots leads to formation of quantum-dot molecular orbitals analogous to those found in diatomic molecules. Energies corresponding to these orbitals are sensitive to the distance between dots, and therefore by tuning the distance D one can tune the single-particle energy spectrum of the system.

6.1 Single-particle states of the QD molecule

Before I can consider the system of many particles confined in the double-dot molecule, I first have to analyse its single-particle energy spectrum. This analysis is presented in the paper “Electronic structure of vertically stacked self-assembled quantum disks”, published by M. Korkusiński and P. Hawrylak in Physical Review B, vol. 63, page 195311 (2001). This publication is an integral part of this thesis and is appended to the presented material. Here I shall summarise its most important points.

Let us start with a simple model of a single electron confined by the molecule composed of two identical disks. Let us also assume that the single-particle energy spectrum of each individual disk consists of a single orbital, whose energy will be denoted as E_s . Since the disks are identical, the energy E_s of the top disk is equal to that of the bottom disk. In the absence of interdisk tunnelling, the electron can occupy either the bottom disk (say, disk 0) or the top disk (disk 1). Its state can therefore be labelled by the quantum-dot layer index, or isospin: $|0\rangle$ or $|1\rangle$.

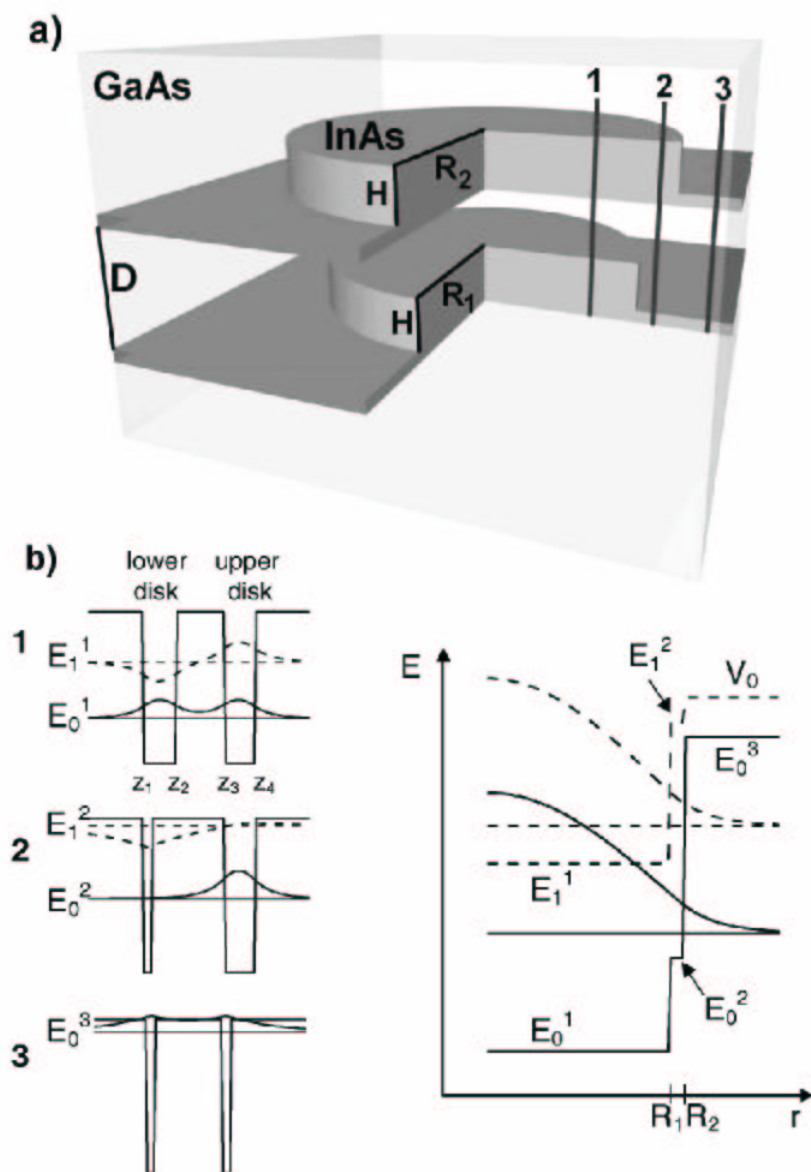


Figure 6.1: (a) Schematic picture of the vertically coupled double-dot molecule; (b) illustration of effective potentials in the adiabatic calculation of electronic states for the vertical motion (left-hand panel) and for the planar motion (right-hand panel) (see text for details)

Let us now include the tunnelling. The Hamiltonian of this simple double-dot molecule written in the basis of the isospin states takes the form

$$\hat{H} = \sum_{i=0}^1 E_s c_i^\dagger c_i - t(c_0^\dagger c_1 + c_1^\dagger c_0), \quad (6.1)$$

or, in a matrix form,

$$H = \begin{bmatrix} E_s & -t \\ -t & E_s \end{bmatrix}. \quad (6.2)$$

Diagonalisation of this simple matrix yields the molecular eigenstates and eigenenergies: the symmetric (or bonding) orbital $|+\rangle = \frac{1}{\sqrt{2}}(|0\rangle + |1\rangle)$ with energy $E_+ = E_s - t$, and the antisymmetric (or antibonding) orbital $|-\rangle = \frac{1}{\sqrt{2}}(|0\rangle - |1\rangle)$ with energy $E_- = E_s + t$. These energy levels are split by $2t$, and the value of this splitting depends on the thickness of the tunnelling barrier between disks, measured by the QD layer distance D . If D is large, the tunnelling matrix element t is small, and the two molecular orbitals are nearly degenerate. On the other hand, if D is decreased, then the splitting between the energies E_\pm increases.

Let us now present a more realistic calculation for a pair of coupled self-assembled InAs quantum disks embedded in the GaAs barrier material. The calculation is done within the effective mass approximation. The single-particle Hamiltonian of the system, written in cylindrical coordinates and in the effective units of energy and length (Section 2.2) takes the form:

$$\hat{H} = -\frac{1}{r^2} \left(r \frac{\partial}{\partial r} r \frac{\partial}{\partial r} + \frac{\partial^2}{\partial \theta^2} \right) - \frac{\partial^2}{\partial z^2} + V(r, z), \quad (6.3)$$

where $V(r, z)$ is the double-disk potential.

In Sections 2.2 and 2.3 I have considered similar Hamiltonians, with the quantum disk and quantum ring confinement potentials, and I assumed that these potentials have barriers of infinite height. In the case of the quantum disk this assumption led to the separation of the Hamiltonian into two operators: one describing the vertical motion, and the other - the lateral motion of the particle. The two resulting Schrödinger equations could be then solved analytically.

But in order to account for the quantum-mechanical coupling in my double-disk system I need to consider a potential $V(r, z)$ whose walls are of finite height. This complicates the analysis in that now the Hamiltonian (6.3) is not separable into two operators, and the corresponding Schrödinger equation cannot be solved analytically even at zero magnetic field. To gain insight into the properties of the single-particle spectrum of the double-disk potential without resorting to numerical treatment, we have proposed a semi-analytical adiabatic approximation, involving an artificial separation of the motion in z direction from the motion in the plane. This method is fast and portable, and allows to obtain energies and wave functions of bound states as a function of the distance between disks with minimal computational effort even if the disks are not identical (they can vary both in width and radius).

In the adiabatic approximation the electronic wave functions are sought in the following form:

$$\psi(r, \theta, z) = \frac{1}{\sqrt{2\pi}} e^{im\theta} \times g_r^\nu(z) \times f_m^\nu(r). \quad (6.4)$$

The first term in this formula is the angular wave function. Isolating it from the rest of the total wave function is not an approximation, since the system is rotationally symmetric, and all electronic orbitals have a well-defined angular momentum m . The approximate character of the method lies in writing the rest of the wave function ψ in the form of a product of the function g dependent on the z coordinate and the function f dependent on the radial coordinate. The Schrödinger equation constructed with the Hamiltonian (6.3) and the wave function as above can be formally separated into two coupled equations:

$$\left[-\frac{\partial^2}{\partial z^2} + V(r, z) \right] g_r^\nu(z) = E_\nu g_r^\nu(z), \quad (6.5)$$

$$\left[-\frac{1}{r^2} \left(r \frac{\partial}{\partial r} r \frac{\partial}{\partial r} - m^2 \right) \right] f_m^\nu(r) = (E - E_\nu(r)) f_m^\nu(r). \quad (6.6)$$

Let us now describe how the two equations were solved.

The equation (6.5) is solved first. It describes the vertical motion of an electron in the potential $V(r, z)$ for a given value of the radial coordinate r . In Figure 6.1 (a) and (b) I

show that, depending on the coordinate r , one deals with three different potentials $V(r, z)$: if $r < R_1$ I have two wide quantum wells, each of width equal to the height H of the disk plus the width W of the wetting layer; if $R_1 < r < R_2$ I have one wide well, corresponding to the top disk, and one narrow well, corresponding to the wetting layer, and finally for $r > R_2$ I have a double-well structure composed of the two wetting layers. I solve for the motion of the electron in each of these cases using the transfer-matrix method, described in detail in the paper. For further analysis I retain two lowest energies, $E_\nu = E_0$ and $E_\nu = E_1$ and the two corresponding orbitals g^0 and g^1 . The energy E_0 is the energy of the symmetric solution, corresponding to the bonding quantum-molecular orbital, and the energy E_1 is the antisymmetric solution, corresponding to the antibonding quantum-molecular orbital. The corresponding wave functions in each radial region are drawn in the left-hand panel of Fig. 6.1 (b). Their symmetric and antisymmetric character is apparent in the first region, where the confining potential is a pair of identical quantum wells. In the second region the potential is no longer symmetric, and therefore here the bonding and antibonding orbitals do not have a definite symmetry. This symmetry is restored in the third region, when I again deal with two identical quantum wells. However here the wells are narrow, and only the bonding orbital is confined.

The energies E_ν are different in each region. Out of them I build the effective potential $E_\nu(r)$ for the lateral motion of the electron, which is illustrated in the right-hand panel of Fig. 6.1(b). This effective potential is built for each subband ν separately and inserted into the equation (6.6). The radial equation for each subband is solved using the transfer-matrix method, presented in detail in the paper. The energies E obtained as a result of the calculation form the single-particle spectrum of the system.

The adiabatic effective-mass approximation requires two parameters as input: the effective mass m^* of the carrier and the depth V_0 of the confining potential $V(r, z)$. They determine how many bound states there are in the single-particle spectrum, and how sensitive this spectrum is to the change of the interdisk distance. Thus I need to establish

the parameters m^* and V_0 for existing double-dot systems.

In Chapter 1 I have described the techniques of fabrication of stacked InAs disks embedded in the GaAs barrier material. The depth of confinement V_0 in such systems is determined by the alignment of band edges of the constituent materials. If the bulk properties of GaAs and InAs is used, the conduction band edge of the dot material is about 1 eV below the conduction band edge of the barrier, and the confinement in the degenerate heavy- and light-hole subbands of the valence band is of order of 85 meV. However, strain present in the system modifies these confinement depths dramatically: the confinement of electrons is in reality of order of 600 meV. Moreover, the hole subbands are split, the heavy-hole confinement is enhanced, and the light-hole confinement is decreased. The strain-induced modifications to the confinement potential can be calculated using the Bir-Pikus formalism [21]. I will show the results of such calculations below.

The effective mass m^* of the carriers is also influenced by the strain, but in the framework of the effective mass approximation we are not able to assess this influence quantitatively. Therefore the effective mass is treated as the fitting parameter in the electronic calculations, and it can be adjusted to obtain agreement with more sophisticated microscopic calculations or with the experiment.

Let us now demonstrate how the presence of strain can be accounted for in the calculations of electronic structure of the system. This discussion is presented briefly in the paper; here I shall provide some supplementary details [56].

Let us start by calculating the distribution of strain in my system. The strain is due to the mismatch of lattice constants of the dot and barrier materials; in this InAs/GaAs system this mismatch is of order of 7%. The degree of strain is quantitatively described with strain tensor matrix elements

$$\varepsilon_{ij}(\mathbf{r}) = \frac{1}{2} \left(\frac{\partial u_i(\mathbf{r})}{\partial x_j} + \frac{\partial u_j(\mathbf{r})}{\partial x_i} \right), \quad (6.7)$$

where $\mathbf{u}(\mathbf{r})$ is a vector describing the displacement of a small element of the system at coordinate \mathbf{r} from its equilibrium position. The distribution of these strain elements in

this system can be calculated using several methods (for reviews see Refs. [56, 99]). I use the continuous elasticity theory, in which the total elastic energy of the system is written as

$$\begin{aligned}
 E = & \int d^3r \left\{ \frac{1}{2} C_{11}(\mathbf{r}) (\varepsilon_{xx}^2 + \varepsilon_{yy}^2 + \varepsilon_{zz}^2) + C_{12}(\mathbf{r}) (\varepsilon_{xx}\varepsilon_{yy} + \varepsilon_{xx}\varepsilon_{zz} + \varepsilon_{yy}\varepsilon_{zz}) \right. \\
 & \left. + 2C_{44}(\varepsilon_{xy}^2 + \varepsilon_{xz}^2 + \varepsilon_{yz}^2) - \alpha\varepsilon_0(\varepsilon_{xx} + \varepsilon_{yy} + \varepsilon_{zz}) \right\}. \quad (6.8)
 \end{aligned}$$

Here C_{11} , C_{12} , and C_{44} are the material-specific elastic constants, and $\varepsilon_0 = (a_{dot} - a_{barrier})/a_{barrier}$ is the relative difference between the lattice constants a of the dot and the barrier, respectively. The parameter $\alpha = C_{11} + 2C_{12}$ in the dot material, and zero in the barrier. The calculation of strain distribution involves discretising the system on a grid of points and minimising the above total elastic energy with respect to displacements of grid nodes $\mathbf{u}(\mathbf{r})$. In the paper (Figure 3 (a), (b), (c), and (d)), I show, respectively, the distributions of the strain matrix elements ε_{xx} , ε_{yy} , ε_{zz} , and the hydrostatic strain $\varepsilon_h = \varepsilon_{xx} + \varepsilon_{yy} + \varepsilon_{zz}$ on the vertical plane through the centre of both disks assuming the disk radii $R_1 = 8$ nm, $R_2 = 8.5$ nm, disk thicknesses $H = 2$ nm and the QD layer distance $D = 4$ nm. To supplement this presentation, I show again the distribution of the hydrostatic strain $\varepsilon_h = \varepsilon_{xx} + \varepsilon_{yy} + \varepsilon_{zz}$ and the biaxial strain $\varepsilon_B = \varepsilon_{zz} - \frac{1}{2}(\varepsilon_{xx} + \varepsilon_{yy})$ in Figure 6.2 (a) and (b), respectively. From Fig. 6.2 one can see that as we move along the symmetry axis through the centre of both disks, the hydrostatic strain remains negative (compressive) throughout, but the sign of the biaxial strain changes on the dot-barrier interfaces: it is positive inside the disks and negative in the barrier.

As the unit cell of the crystal is deformed by strain, the bond lengths and angles change, and this in turn influences the band structure. The attempt to describe this effect within the $\vec{k} \cdot \vec{p}$ formalism was undertaken by Bir and Pikus [21] for the diamond-type lattices. Bahder [12] extended their approach to the zinc-blende binary semiconductor alloys using

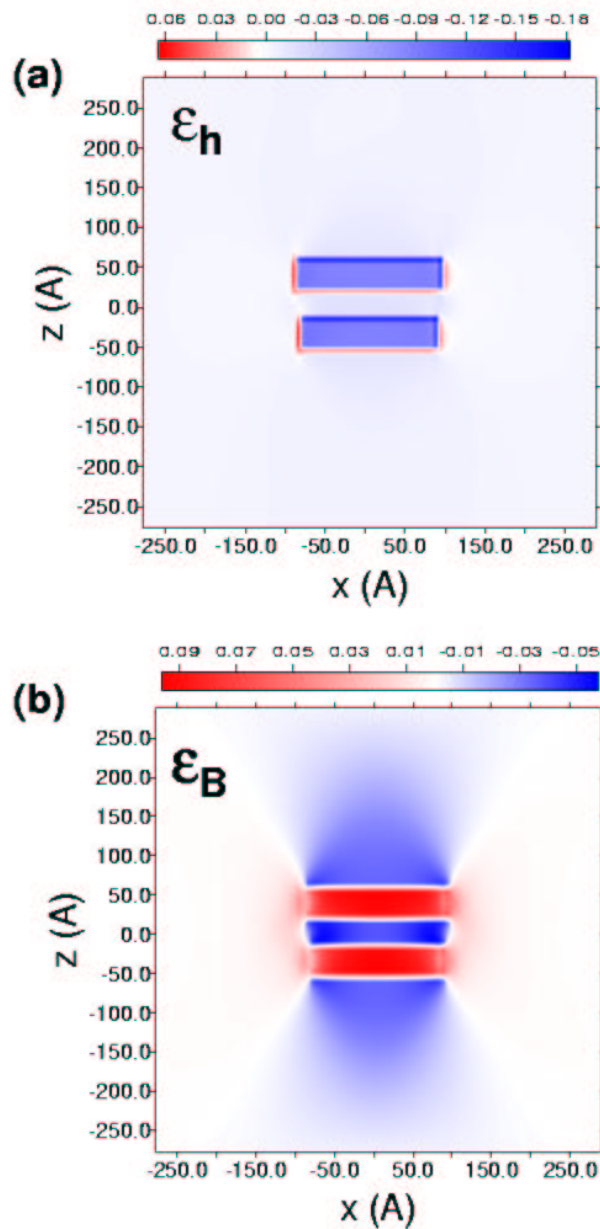


Figure 6.2: Vertical cross section of the spatial variation of hydrostatic (a) and biaxial (b) strain components through the centre of the double-disk InAs/GaAs system

the Löwdin perturbation theory and obtained the following eight-band $\vec{k} \cdot \vec{p}$ Hamiltonian:

$$\hat{H}_{\text{strain}} = \begin{pmatrix} a_c \varepsilon_h & 0 & -v^* & 0 & -\sqrt{3}v & \sqrt{2}u & u & -\sqrt{2}v^* \\ 0 & a_c \varepsilon_h & \sqrt{2}u & \sqrt{3}v^* & 0 & v & -\sqrt{2}v & -u \\ -v & \sqrt{2}u & -p+q & -s^* & r & 0 & \sqrt{3/2}s & -\sqrt{2}q \\ 0 & \sqrt{3}v & -s & -p-q & 0 & r & -\sqrt{2}r & \sqrt{1/2}s \\ -\sqrt{3}v^* & 0 & r^* & 0 & -p-q & s^* & \sqrt{1/2}s^* & \sqrt{2}r^* \\ \sqrt{2}u & v^* & 0 & r^* & s & -p+q & \sqrt{2}q & \sqrt{3/2}s^* \\ u & -\sqrt{2}v^* & \sqrt{3/2}s^* & -\sqrt{2}r^* & \sqrt{1/2}s & \sqrt{2}q & -a_v \varepsilon_h & 0 \\ -\sqrt{2}v & -u & -\sqrt{2}q & \sqrt{1/2}s^* & \sqrt{2}r & \sqrt{3/2}s & 0 & -a_v \varepsilon_h \end{pmatrix}, \quad (6.9)$$

where

$$\begin{aligned} p &= a_v \varepsilon_h, \\ q &= b \left[\varepsilon_{zz} - \frac{1}{2}(\varepsilon_{xx} + \varepsilon_{yy}) \right], \\ r &= \frac{\sqrt{3}}{2} b (\varepsilon_{xx} - \varepsilon_{yy}) - i d \varepsilon_{xy}, \\ s &= -d (\varepsilon_{xz} - i \varepsilon_{yz}), \\ u &= -\frac{i}{\sqrt{3}} P_0 \sum_j \varepsilon_{zj} \partial_j, \\ v &= -\frac{i}{\sqrt{6}} P_0 \sum_j (\varepsilon_{xj} - i \varepsilon_{yj}) \partial_j, \end{aligned} \quad (6.10)$$

with the parameters a_c , a_v , b and d being the material-dependent deformation potentials, and P_0 being the imaginary valence-conduction band coupling.

The above formula is written in the notation of Pryor *et al.* [99]. I can use it to calculate the local band edge profiles at each point of the grid used previously in the strain calculations. To this end, however, one can set the parameters u and v to zero, as I am only interested in the band structure at the Γ point of the Brillouin zone. Then, from Eq. (6.9) one can easily see that the conduction band is not coupled to the valence band, and that the strain-induced modification of the conduction band edge consists only of a shift proportional to the hydrostatic strain. The valence band, on the other hand, is

much more complicated. I will focus here mainly on understanding the diagonal elements of the matrix H_{strain} . It can be readily seen that all heavy- and light-hole band edges are shifted by $-p$, which is proportional to the hydrostatic strain. Further, the strain introduces a splitting between the heavy and light hole band edges equal to $2q$, if the off-diagonal elements are disregarded. As can be seen from Eq. (6.10), the parameter q is proportional to the biaxial strain, and depends on the deformation potential b , which is negative for most semiconductors. That means that if the biaxial strain is negative (compressive), the heavy hole band edge will lie above the light hole band edge (i.e., from the viewpoint of the holes, the heavy hole band will have a lower energy). If the biaxial strain is positive, the situation is reversed.

Now I input the calculated distributions of strain tensor matrix elements into the Bir-Pikus Hamiltonian (6.9) and, for each point of the structure, diagonalise it numerically to obtain the strain-modified profiles of band edges. The result of these calculations is shown in Fig. 6.3. This figure is similar to the Figure 4 from the paper and differs only in the valence band. Figure 6.3 indicates that the edge of the heavy-hole subband (green line) crosses the edge of the light-hole subband (blue line) at all dot-barrier interfaces. This is the correct picture; the assignment of bands in Figure 4 from the paper is erroneous. The crossing of light-hole and heavy-hole band edges is due to the fact that the biaxial strain changes sign at the barrier dot interfaces. Since the biaxial strain controls the splitting between the heavy- and light-hole bands, the change of sign of this strain component leads to the reversal of bands. This effect has also been reported, e.g., in Ref. [112].

The strain calculations coupled to the Bir-Pikus formalism suggest that the parameter V_0 in my InAs/GaAs system is reduced to 600 meV. Using this confinement depth and treating the effective mass m^* as a fitting parameter, the electronic spectra were fitted to those obtained with a similar system within the eight-band $\vec{k} \cdot \vec{p}$ formalism. As a result of this fitting, the electronic effective mass was found to be $m^* = 0.053 m_0$.

With the adiabatic effective mass approximation fully defined and parametrised I

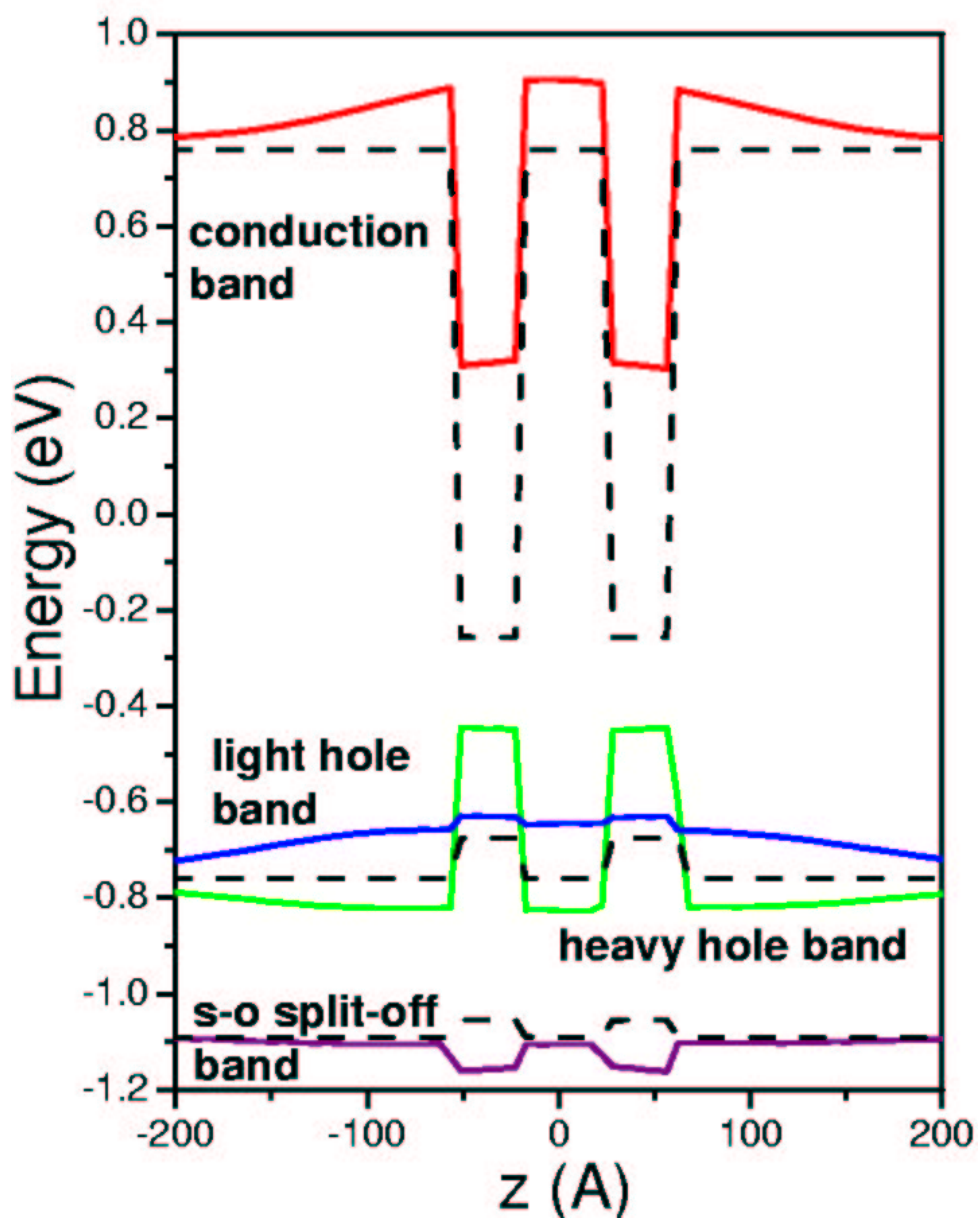


Figure 6.3: Band edge alignment along the symmetry axis of the system (dotted lines - unstrained, solid lines - with strain)

have calculated the electronic spectra of the vertically coupled double-disk InAs/GaAs molecule. The spectrum for the double-disk structure with radii of $R_1 = 8$ nm, $R_2 = 8.5$ nm and height of each disk of $H = 2$ nm is shown in Fig. 6.4. Due to the finite depth of the confinement potential there are only a few bound electronic states. These states possess a new characteristic property due to the double-dot potential: they are either symmetric or antisymmetric in the direction along the axis of rotational symmetry. These symmetry properties are analogous to those of bonding and antibonding states in diatomic molecules. The energies of these states change as a function of the distance between disks, as shown in Fig. 6.4. At large interdisk distances the symmetric and antisymmetric states associated with the same radial and angular modes (i.e., characterised by the same quantum numbers n and m) are almost degenerate - one deals essentially with two uncoupled quantum disks. Small splittings between these levels are due to the fact that the disks are not identical. Of course, for each vertical symmetry I find the ladder of levels with different quantum numbers n and m , as I did in the case of the single disk in Section 2.2.

As the two disks are shifted closer together, the tunnelling through the interdisk barrier causes the symmetric and antisymmetric states to split. This splitting increases exponentially as the distance between disks is decreased, and can become as large as the energy gap between two adjacent shells of each disk (which is of order of 30 meV), so that a symmetric state of, say, the p shell can become degenerate with the antisymmetric state of the s shell (this situation corresponds to the QD layer distance of 45 Å). Thus I deal with a situation distinctly different from that of the single disk: there, the vertical energy quantisation introduced the largest energy scale of the system; here this energy scale is typically the smallest. For all interdisk distances the ladder of lateral modes built on top of each vertical mode exhibits the shell structure characteristic for the disk confinement (I covered it in detail in Section 2.2).

In the paper we also discuss the case of nonzero magnetic field, however, unlike in Section 2.2 for a single quantum disk, the field is now perpendicular to the axis of rota-

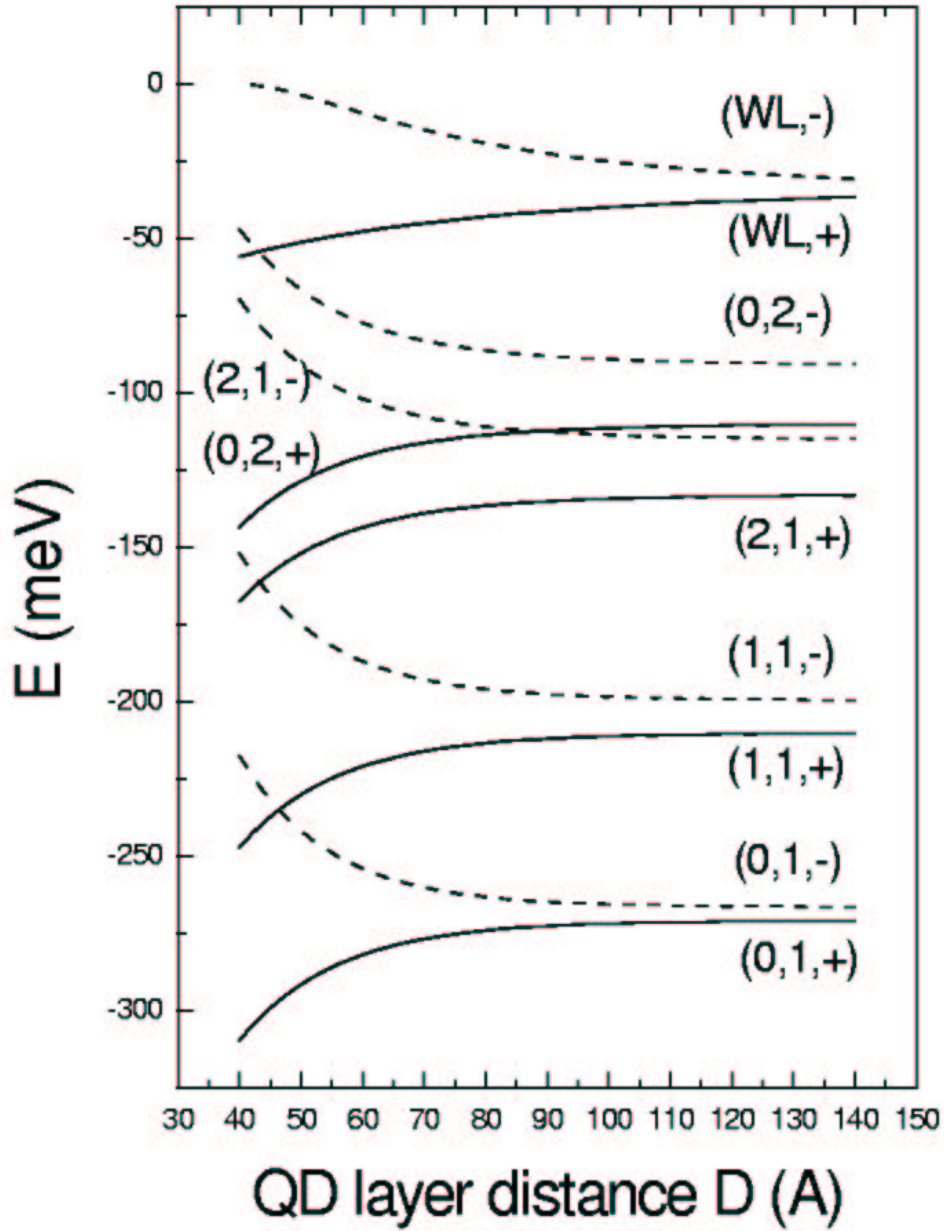


Figure 6.4: Electronic energy levels for a double-disk structure with confinement $V_0 = 600$ meV and electronic effective mass $m^* = 0.053 m_0$. WL denotes the states of the wetting layer. Numbers in braces denote quantum numbers (n, m, l) of the states. $l = +$ denotes a symmetric state (solid lines), while $l = -$ denotes an antisymmetric state (dashed lines)

tional symmetry. We have chosen this alignment, since, as I have shown in Section 2.2, the magnetic field aligned in parallel to the rotational axis has relatively little effect on the spectrum even at fields of order of 10 T. The second reason is the fact that the magnetic field directed perpendicularly to the rotational axis couples the symmetric and the antisymmetric states, and can lead to anticrossing of shells which originally had opposite symmetries. This is clearly seen in Figure 7 in the paper, where we show this anticrossing behaviour as a function of the interdisk distance e.g., for the antisymmetric s shell and the symmetric p shell (the anticrossing is seen for the distance between disks of 45 Å, i.e., at the point where at zero magnetic field the two states cross).

6.2 Entangled states of an electron-hole complex in the QD molecule

Let us now discuss the properties of a single electron-hole pair confined in the double-disk quantum molecule. I focus on discussing the structure of the states of the electron-hole pair in the context of entanglement, being a special kind of particle-particle correlations.

The results of this work were published in the paper “Entangled states of electron-hole complex in a single InAs/GaAs coupled quantum dot molecule”, by Marek Korkusiński, Pawel Hawrylak, Manfred Bayer, Gerhard Ortner, Alfred Forchel, Simon Fafard, and Zbigniew Wasilewski, published in *Physica E*, vol. 13, page 610 (2002). This publication is an integral part of this thesis and is appended to the presented material.

The notion of entanglement is of particular importance in quantum computing, where the information is stored in quantum bits. Quantum phenomena must be also used to process this information, and the simplest object capable of doing so is the quantum logic gate. The operation of such gate relies on the existence of entangled states of constituent qubits, i.e., states which cannot be obtained by individual qubit rotation. If I were to

change the state of one qubit in the entangled system, I would nontrivially affect the state of the entire system.

In the paper, we have proposed a model of a quantum logic gate composed of two qubits - an electron and a hole - confined in a vertically coupled pair of disk-shaped self-assembled quantum dots. Since we deal with an electron-hole pair - an exciton, such a system can be examined optically - by the photoluminescence experiment. My goal is to predict the luminescence spectra of the exciton and, in these spectra, find features proving the existence of entangled states.

In this simple analysis, I return to my original description of the single-particle molecular orbitals in the language of isospin states, and assume that the two quantum disks are identical. In the absence of the interdisk tunnelling, the particle can be localised either on the bottom disk (isospin state $|0\rangle$) or on the top disk (isospin state $|1\rangle$), and these states are identified as the states of the qubit. Tunnelling through the barrier between disks leads to mixing of isospin states, i.e., rotation of the qubit. One observes the formation of molecular orbitals $|\pm\rangle = \frac{1}{\sqrt{2}}(|0\rangle \pm |1\rangle)$ and their energies E_{\pm} are split by $2t$. The tunnelling matrix element t is the only free parameter; its value for each interdot distance can be easily established from the single-particle spectra calculated using the adiabatic effective-mass approximation.

Let us now introduce the second qubit - the hole - into the system, and let us assume for the moment that the two carriers do not interact. In the absence of the tunnelling, the wave function of the pair can be written as a product of the isospin states of each qubit separately. There are four possible configurations: $|0\rangle_e|0\rangle_h$, $|1\rangle_e|1\rangle_h$, $|0\rangle_e|1\rangle_h$, and $|1\rangle_e|0\rangle_h$. Upon the inclusion of tunnelling the qubits will rotate independently, and now the exact wave functions of the system can be written as $|+\rangle_e|+\rangle_h = \frac{1}{2}(|0\rangle_e + |1\rangle_e)(|0\rangle_h + |1\rangle_h)$, and analogously $|-\rangle_e|-\rangle_h$, $|+\rangle_e|-\rangle_h$ and $|-\rangle_e|+\rangle_h$. Thus, the total wave function of the system can be written as a simple product of the electron wave function and the hole wave function, which means that the qubits are not entangled.

Inclusion of the electron-hole Coulomb interaction changes this picture: now the qubits are no longer independent. The Hamiltonian of the system of two interacting qubits in the basis of the quantum-molecular orbitals takes the form:

$$\hat{H} = \sum_i E_i^e c_i^\dagger c_i + \sum_i E_i^h h_i^\dagger h_i - \sum_{ijkl} \langle ij|V|kl \rangle c_i^\dagger h_j^\dagger h_k c_l, \quad (6.11)$$

where the index $i = +$ or $-$, similarly j, k , and l , and the operators h_i^\dagger (h_i) create (annihilate) a hole on the orbital i . I construct the basis set out of configurations created by distributing the electron and hole on the molecular orbitals: $\{|+\rangle_e |+\rangle_h, |-\rangle_e |-\rangle_h, |+\rangle_e |-\rangle_h, |-\rangle_e |+\rangle_h\}$.

In a PL experiment only the two first states, i.e., $|+\rangle_e |+\rangle_h$ and $|-\rangle_e |-\rangle_h$ can be addressed optically due to their symmetry; the two remaining states with mixed symmetry are dark.

In this basis the Hamiltonian matrix takes the form

$$H = \begin{bmatrix} E_{++} + V_{++++} & V_{++--} & 0 & 0 \\ V_{--++} & E_{--} + V_{----} & 0 & 0 \\ 0 & 0 & E_{+-} + V_{-++-} & V_{-+-+} \\ 0 & 0 & V_{+-+-} & E_{+-} + V_{-+-+} \end{bmatrix} \quad (6.12)$$

(details of calculations of the Coulomb matrix elements are given in the paper). This matrix has a block-diagonal form, because the Coulomb interaction mixes only states with the same overall symmetry. In particular, the Hamiltonian matrix does not mix the optically active states with the dark states, and in what follows I will only focus on the top left-hand segment of the matrix,

$$H_A = \begin{bmatrix} E_{++} + V_{++++} & V_{++--} \\ V_{--++} & E_{--} + V_{----} \end{bmatrix}. \quad (6.13)$$

Upon diagonalisation of this simple matrix I obtain the optically active eigenstates of the system of two interacting qubits. If recast in terms of the isospin states, they can be written as

$$|a\rangle = \alpha_1(|0\rangle_e |0\rangle_h + |1\rangle_e |1\rangle_h) + \beta_1(|0\rangle_e |1\rangle_h + |1\rangle_e |0\rangle_h), \quad (6.14)$$

$$|b\rangle = \alpha_4(|0\rangle_e |0\rangle_h + |1\rangle_e |1\rangle_h) + \beta_4(|0\rangle_e |1\rangle_h + |1\rangle_e |0\rangle_h). \quad (6.15)$$

Thus, the states of the pair of interacting qubits cannot be written as simple products of the states of individual qubits, and so the Coulomb electron-hole interaction leads to entanglement of my qubits. The energies corresponding to these two wave functions are composed of orbital and interaction terms. Without interactions the splitting between them would be equal to $E_{++} - E_{--}$, and, for large interdisk distances D , would approach zero. However, due to the off-diagonal matrix element V_{+-} , which changes only weakly with the interdisk distance, the energies of the two optically active states will be split even for large D . This splitting is thus the signature of the entangled states of my qubits. Since both eigenstates, $|a\rangle$ and $|b\rangle$, are optically active, the splitting should be visible in the photoluminescence experiment.

The PL experiment on the InAs/GaAs quantum-disk molecules with varying interdisk distance was performed by the group of Alfred Forchel and Manfred Bayer at Würzburg University. The author of this Thesis, not being involved in the measurements, refers the reader interested in the experimental details to the attached paper. Here let us only state that the splitting of the PL lines due to the recombination of excitons on states $|a\rangle$ and $|b\rangle$ is indeed observed even for the interdisk separations as large as 8 nm. To the best of my knowledge, this is the first successful observation of the PL spectra of an entangled electron-hole pair confined in a double-disk quantum-dot molecule.

Chapter 7

Negatively charged exciton on a quantum ring

The last system I am going to consider is the electron-hole system confined in a quantum ring. The results of the treatment of a single electron, an exciton and a negatively charged exciton in the quantum-ring potential and in an external magnetic field can be found in two papers: “Negatively charged exciton on a quantum ring”, by Marek Korkusiński, Pawel Hawrylak, and Manfred Bayer, published in *Physica Status Solidi (b)*, vol. 234, page 274 (2002), and “Optical detection of the Aharonov-Bohm effect on a charged particle in a nanoscale quantum ring”, by Manfred Bayer, Marek Korkusiński, Pawel Hawrylak, Thomas Gutbrod, M. Michel, and Alfred Forchel, published in *Physical Review Letters*, vol. 90, page 186801 (2003). Both these publications are integral parts of this thesis and are appended to the presented material.

In Section 2.3 I have described the single-particle energy spectrum of a single electron confined in a quantum ring, and subject to an external magnetic field directed along the axis of rotational symmetry of the system. I have shown that the single-particle ground-state energy exhibits Aharonov-Bohm oscillations as a function of the number of

flux quanta threading the ring. In this Chapter I consider the behaviour of an electron-hole pair (a single exciton) and a complex composed of two electrons and one hole (a negatively charged exciton, X^-) confined in such ring. I show that correlations between particles may lead to measurable effects, manifesting themselves in a complete or partial suppression of the Aharonov-Bohm oscillations in the total energy of these systems.

As in Section 2.3, I assume that the ring is infinitesimally thin and narrow, which allows to describe the motion of each particle just by one coordinate (the angle ϕ). The ring is therefore fully characterised by its radius R , and, as I will show, the single-particle energy and the Coulomb interactions scale differently with R : for small rings the single-particle (orbital) energy quantisation dominates, while for large rings the behaviour of the system is strongly affected by interactions. I analyse the properties of the systems in both regimes.

I start the analysis with a single exciton. I write the Schrödinger equation of the system using the centre-of-mass and relative coordinates, which reduces the two-body problem to two single-body problems:

$$\hat{H}_{CM} = -\frac{\hbar^2}{2M_X R^2} \frac{\partial^2}{\partial \phi_{CM}^2}; \quad (7.1)$$

$$\hat{H}_{rel} = \frac{\hbar^2}{2\mu R^2} \left(-i \frac{\partial}{\partial \phi_{rel}} + N_\phi \right)^2 - \frac{e^2}{2R\epsilon} \frac{1}{\sqrt{d^2 + \sin^2(\phi_{rel}/2)}}. \quad (7.2)$$

Here $M_X = m_e + m_h$ is the total mass of the exciton, $\mu = m_e m_h / (m_e + m_h)$ is the reduced mass of the relative particle, and the parameter d is introduced to account for the finite width of the ring and to prevent the Coulomb interactions from diverging. N_ϕ is the number of flux quanta threading the ring; its definition was given in Section 2.3.

As can be seen from Eq. (7.1), the motion of the centre-of-mass particle is not affected by the magnetic field, as is expected, considering the fact that the exciton as a whole is a charge-neutral object. The energy of the centre-of-mass particle does not exhibit the Aharonov-Bohm oscillations, and does not carry any signature of the electron-hole interactions.

On the other hand, the orbital energy operator of the relative particle (first term in Eq. (7.2)) is that of a single charged particle with the reduced mass μ . It conserves the angular momentum k of the relative particle, and via its quadratic dependence on the number of flux quanta N_ϕ it introduces the Aharonov-Bohm oscillations to the energy spectrum of the particle. The relative Hamiltonian (7.2) also contains the Coulomb term, introducing a residual attractive potential of a fixed point charge. This potential mixes the states of the relative particle with different angular momenta, and thus leads to averaging out of the Aharonov-Bohm oscillations in the spectrum. Thus, the behaviour of the particle in the magnetic field depends on the relative strength of these two terms. I study the energy spectrum of the exciton in the regime of both weak and strong interactions using the exact diagonalisation method in the basis of states $\{|k\rangle\}$ of the relative particle, where the angular momentum $k = -10, -9, \dots, 10$.

For small disks, the single-particle (orbital) energy quantisation dominates and the symmetry breaking introduced by the Coulomb term is weak. The energy of the relative particle, and thus also the total energy of the exciton, exhibits Aharonov-Bohm oscillations. Thus, in this regime, the electron and the hole move almost independently, and the oscillations of each carrier add to produce Aharonov-Bohm oscillations of the total energy of the system.

For large disks, the interactions dominate the energy landscape of the system. The Coulomb term in the relative Hamiltonian strongly couples the configurations with different angular momenta, which causes the oscillations to be averaged out. The total energy of the system changes monotonically with the magnetic field (exhibits the diamagnetic shift). In this regime the electron and the hole are strongly correlated and move as one, charge-neutral object.

In analysing the negatively charged exciton X^- , composed of two electrons and one hole moving on the ring, I use a similar formalism of centre-of-mass and relative coordinates. In these coordinates the Hamiltonian of the system separates into the centre-

of-mass Hamiltonian, composed only of the orbital energy operator, and the relative Hamiltonian, describing the motion of two interacting relative particles:

$$\hat{H}_{CM} = \frac{\hbar^2}{2MR^2} \left(-i\frac{\partial}{\partial\phi_{CM}} + N_\phi \right)^2, \quad (7.3)$$

$$\begin{aligned} \hat{H}_{rel} = & \sum_{i=1}^2 \frac{\hbar^2}{2\mu R^2} \left(-i\frac{\partial}{\partial\phi_i} + N_\phi \right)^2 - \frac{e^2}{2R\varepsilon} \frac{1}{\sqrt{d^2 + \sin^2(\phi_i/2)}} \\ & + \frac{e^2}{2R\varepsilon} \frac{1}{\sqrt{d^2 + \sin^2((\phi_1 - \phi_2)/2)}} + \frac{\hbar^2}{m_h R^2} \left(-i\frac{\partial}{\partial\phi_1} \right) \left(-i\frac{\partial}{\partial\phi_2} \right) \\ & - \frac{2\sigma}{1 + 2\sigma} \frac{\hbar^2}{2\mu R^2} N_\phi^2, \end{aligned} \quad (7.4)$$

where $\sigma = m_e/m_h$, and $M = 2m_e + m_h$ is the mass of the entire X^- complex. I solve for the centre-of-mass motion analytically, and use an exact diagonalisation approach to analyse the motion of relative particles.

Since now the entire complex carries an effective negative electron charge, the centre-of-mass particle is charged as well. That is why the centre-of-mass Hamiltonian contains terms dependent upon the magnetic field, and the single-particle (orbital) energy of the centre-of-mass particle exhibits Aharonov-Bohm oscillations. However, the amplitude of these oscillations is small compared to that of a single electron because of the large mass M of the centre-of-mass particle.

As for the two relative particles, they are light and charged, and they move in the additional residual attractive potential of a fixed point charge, similar to the one obtained in the case of the exciton. The particles interact via Coulomb potential and a pairwise momentum interaction, appearing as a result of the transformation of the system's kinetic energy operator into relative coordinates. The last term in the relative Hamiltonian is proportional to N_ϕ^2 and contributes to the diamagnetic shift.

The single-particle orbital energy operators for the relative particles introduce the Aharonov-Bohm oscillations. Both pairwise interaction terms conserve the total angular momentum of the pair, and therefore do not lead to the suppression of these oscillations. However, the residual single-body attractive potential mixes the states of the pair with

different angular momenta, and can lead to the suppression of the oscillations, similarly as it did in the case of the single exciton. Quantitative calculations for the pair of relative particles are carried out using the configuration-interaction method, in the basis of configurations $|k_1 k_2\rangle$ created as Slater determinants of single-particle orbitals with definite angular momentum. To optimise the basis, I rotate the set constructed with configurations to the set consisting of eigenvectors of the total spin operator. Since I deal with two particles only, this rotation allows to separate the spin singlet and spin triplet states, and to perform the exact diagonalisation in each subspace separately.

Based on this analysis, I find that the total energy of the X^- complex always oscillates in the magnetic field, but, depending on the disk radius, these oscillations can have larger or smaller amplitude. For small disks the symmetry breaking introduced by the residual potential in the relative Hamiltonian is small, the three particles move almost independently, and their total energy oscillates with a large amplitude. On the other hand, for large disks the configurations of relative particles are strongly mixed, and their oscillations average out. The total energy is modulated only weakly by oscillations of the heavy centre-of-mass particles, and exhibits the diamagnetic shift. In this case, the X^- complex is composed of strongly correlated particles and moves in the magnetic field as one object.

Since both the exciton and the X^- are composed of carriers of both types, the electron-hole recombination process can occur resulting in an emission of one photon, which can be further detected. As I discussed in Section 1.4, the energy of this photon is equal to the difference between the initial state (before the recombination) and the final state of the system (after the recombination). In this way, one can directly measure the energy of the exciton, but in the case of the X^- one will detect the energy difference between the total energy of the complex and the energy of the final-state electron. These energies have indeed been measured experimentally by means of photoluminescence spectroscopic techniques. The ring used in the experiment was large enough for the system to be

in the strongly interacting regime, where, as I have explained, the excitonic complexes are expected to behave as strongly correlated entities. This behaviour is indeed seen in the experimental data. The photoluminescence line attributed to the single exciton on the ring exhibits only a diamagnetic shift as a function of the magnetic field while the line attributed to the X^- complex is strongly modulated. Since in this regime the oscillations of the total energy of X^- are almost suppressed, the modulation seen in the experiment can only be due to the final state electron. This is confirmed by the characteristic shape of the photoluminescence trace, similar to the inverted sequence of single-electron oscillations. Thus, one directly observes the Aharonov-Bohm oscillations of a *single* electron, which is possible due to the correlated character of the initial-state X^- complex.

Chapter 8

Conclusions

In this Thesis I have presented an overview of the field of research on electronic correlations in nanostructures. I have started with a general introduction to quantum dots and compared their fundamental properties to those of natural atoms. I have shown that both classes of systems - QDs and natural atoms - possess many common characteristics to the extent that the QDs are often called “artificial atoms”. However, these two systems exhibit several important differences, and perhaps the most important of them in the context of correlations is the strong atomic quantisation of single-particle (orbital) energy contrasted with much weaker, and tunable, QD confinement. This soft QD confinement allows to build confined systems, in which the quantisation of orbital energy introduces the same energy scale as Coulomb carrier-carrier interactions. For this reason, theoretical and experimental study of properties of QDs allows to gain insight into the correlated behaviour of strongly interacting carriers.

To introduce the reader into the subject of QD physics and technology, I have presented the most important methods of fabrication of QDs. I have divided these methods into three groups. In the first technique the lateral confinement is created electrostatically by means of gates, locally depleting the two-dimensional gas. Such dots allow to study electronic systems only. Another technique, utilising the Stranski-Krastanow phase tran-

sition in the epitaxial growth of heterostructures, yields dots with relatively small sizes, capable of confining both electrons and holes. Both types of carriers can be also confined in quantum rings, fabricated by lithography and etching. I have also summarised the most important experimental techniques used to probe the properties of many-particle systems confined in QDs.

But the main focus of this thesis is a fundamental research into the properties of correlated systems confined in nanostructures. I started my detailed discussion of these properties by defining mathematical methods and computational tools used in my work. I described the single-particle spectra of several idealised confinement potentials, approximating the actual QD systems, and used these spectra as an input in the many-body problem.

The problem of many interacting particles confined in the lateral confining potential of nanostructures was defined in the language of fermion creation and annihilation operators. To be complete, this formulation requires the single-particle spectrum, established before, and also the Coulomb scattering matrix elements. These elements have been calculated analytically in the case of the two-dimensional parabolic lateral confinement.

Further I have discussed the possible mathematical and computational methods that could be used to solve the many-body problem. I needed a method capable of treating the correlation effects on equal footing with the direct and exchange Coulomb interactions. I have reviewed three such methods, the exact diagonalisation technique, the spin density functional theory and the quantum diffusion Monte Carlo approach. However, for my research I have chosen the exact-diagonalisation configuration-interaction method, because only this method allows to obtain *exact* description of the system, albeit only for relatively small number of particles.

In my detailed description of the configuration-interaction approach, I have described how the symmetries of the system could be exploited in order to reduce the size of the many-particle basis set and achieve greater computational accuracy. I have also shown

that special tools are needed in order to diagonalise these optimised, but still very large Hamiltonian matrices. My tool of choice was the conjugate gradient minimisation technique combined with the spectrum folding method. By use of this computational tool I could find the ground and several lower excited states of matrices with size of order of $10^5 \times 10^5$ and larger, i.e., objects so large that they could not be stored all at once in the computer memory.

Having completely defined the many-body problem and the methods of solving it I have analysed the correlation effects in parabolic quantum dots with or without the magnetic fields, containing electrons only, and coupled quantum dot and quantum ring systems confining both electrons and holes. My presentation of this material was comprised of a series of articles, integrated into the text.

In my analysis of parabolic many-electron quantum dots, I have carefully distinguished the effects due to electronic correlations from those brought about by the direct and exchange Coulomb terms. I showed that the latter terms favourize more spin-polarised systems, and are counteracted by correlations whose essence lies in configuration mixing. This is due to the fact that the low-spin subspaces usually have much larger basis sets than the high-spin ones, and therefore acquire a correlation advantage additionally lowering their energy. This correlation advantage can lead not only to shifts in phase boundaries of the system, but also to the appearance of entirely new phases whose presence is verified by experimental data. In particular, I have demonstrated the composite nature of the second spin-flip transition in the eight-electron droplet. I have shown that in the evolution of the system with the magnetic field, the region of stability of the second-spin-flip configuration is preceded by strongly correlated, spin-unpolarised phases. This prediction was confirmed experimentally in the high source-drain voltage tunnelling spectroscopy. This was - to the best of my knowledge - the first experimental observation of correlated states in electronic QDs with known and controlled number of electrons in the presence of a magnetic field.

Further I have analysed the electron-hole systems. I have shown that the Coulomb

interactions between an electron and a hole confined in a vertically coupled double-disk structure lead to the entanglement of states of the two carriers, which can be viewed as a particular manifestation of correlations. I have also shown that the electron-hole correlations strongly influence the behaviour of an exciton and a charged exciton on a quantum ring, and may lead to the suppression of Aharonov-Bohm oscillations of their energy. As a result, the photoluminescence spectrum of the charged complex is dominated by the energy of the final state electron. This allows to observe the Aharonov-Bohm oscillations of a single electron directly in the photoluminescence spectra.

Bibliography

- [1] Abramowitz, M. and Stegun, I., *Handbook of mathematical functions* (Dover, New York, 1972).
- [2] Ancilotto, F., Austing, D.G., Barranco, M., Mayol, R., Muraki, K., Pi, M., Sasaki, S., and Tarucha, S., Phys. Rev. B **67**, 205311 (2003).
- [3] Anderson, J.B., J. Chem. Phys. **63**, 1499 (1975); *ibid.* **65**, 4121 (1976); *ibid.* **86**, 2839 (1987).
- [4] Austing, D.G., Honda, T., and Tarucha, S., Semicond. Sci. Technol. **11**, 388 (1996); Tarucha, S., Austing, D.G., and Honda, T., Superlatt. Microstruct. **18**, 121 (1995).
- [5] Anders, S., Rebohle, L., Schrey, F.F., Schrenk, W., Unterrainer, K., and Strasser, G., Appl. Phys. Lett. **82**, 3862 (2003).
- [6] Apalkov, V.M. and Chakraborty, T., Appl. Phys. Lett. **78**, 1820 (2001).
- [7] Ashcroft, Neil W., and Mermin, David N., *Solid State Physics* (Saunders College, Philadelphia, 1976).
- [8] Ashoori, R.C., Nature (London) **379**, 413 (1996).
- [9] Ashoori, R.C., Störmer, H.L., Weiner, J.S., Pfeiffer, L.N., Pearton, S.J., Baldwin, K.W., and West, K., Phys. Rev. Lett. **68**, 3088 (1992); Ashoori, R.C., Störmer, H.L., Weiner, J.S., Pfeiffer, L.N., Baldwin, K.W., and West, K., *ibid.* **71**, 613 (1992).

- [10] Aslan, B., Liu, H.C., Korkusinski, M., Cheng, S.-J., and Hawrylak, P., Appl. Phys. Lett. **82**, 630 (2003).
- [11] Austing, D.G., Sasaki, S., Tarucha, S., Reimann, S.M., Koskinen, M., and Manninen, M., Phys. Rev. B **60**, 11514 (1999).
- [12] Bahder, T.B., Phys. Rev. B **41**, 11992 (1990); *ibid.* **45**, 1629 (1992).
- [13] von Barth, U. and Hedin, L., J. Phys. C **5**, 1629 (1972).
- [14] Bayer, M., Hawrylak, P., Hinzer, K., Fafard, S., Korkusiński, M., Wasilewski, Z.R., Stern, O., and Forchel, A., Science **291**, 451 (2001).
- [15] Bayer, M., Korkusiński, M., Hawrylak, P., Gutbrod, T., Michel, M., and Forchel, A., Phys. Rev. Lett. **90**, 186801 (2003).
- [16] Bayer, M., Stern, O., Hawrylak, P., Fafard, S., and Forchel, A., Nature **405**, 923 (2000).
- [17] Bednarek, S., Szafran, B., and Adamowski, J., Phys. Rev. B **59**, 13036 (1999).
- [18] Bennett, C.H., and Brassard, G., in: *Proceedings of IEEE International Conference on Computers, Systems, and Signal Processing, Bangalore, India* (IEEE, New York, 1984), p. 175.
- [19] Bethe, H.A. and Jackiw, R., *Intermediate Quantum Mechanics* (Benjamin-Cummings, Menlo Park, 1986).
- [20] Bimberg, D., Grundmann, M., and Ledentsov, N.N., *Quantum Dot Heterostructures* (Wiley, New York, 1999).
- [21] Bir, G.L. and Pikus, G.E., *Symmetry and Strain-Induced Effects in Semiconductors* (Wiley, New York, 1974); Pikus, G.E., and Bir, G.L., Sov. Phys. - Solid State **1**, 1502 (1960).

- [22] Bolton, F., Phys. Rev. B **54**, 4780 (1996); Siljamäki, S., Harju, A., Nieminen, R.M., Sverdlov, V.A., and Hyvönen, P., Phys. Rev. B **65**, 121306 (2002) and references therein; Pederiva, F., Umrigar, C.J., and Lipparini, E., Phys. Rev. B **62**, 8120 (2000).
- [23] Bolton, F., Solid-State Electron. **37**, 1159 (1994).
- [24] Brassard, G., Lütkenhaus, N., Mor, T., and Sanders, B.C., Phys. Rev. Lett. **85**, 1330 (2000).
- [25] Brunner, K., Bockelmann, U., Abstreiter, G., Walther, M., Böhm, G., Tränkle, G., and Weimann, G., Phys. Rev. Lett. **69**, 3216 (1992).
- [26] Bryant, G. and Jaskólski, W., Physica E **11**, 72 (2001); Klimeck, G., Oyafuso, F., Boykin, T.B., Bowen, R.C., and von Allmen, P., Computer Model. Engin. Sci. **3**, 601 (2002); Sun, S.J. and Chang, Y.-C., Phys. Rev. B **62**, 13631 (2000).
- [27] Büttiker, M., Imry, Y., and Landauer, R., Phys. Lett. **96A**, 365 (1983); Aronov, A.G. and Sharvin, Yu.V., Rev. Mod. Phys. **59**, 755 (1987); Chakraborty, T., and Pietiläinen, P., Phys. Rev. B **50**, 8460 (1994).
- [28] Canning, A., Wang, L.W., Williamson, A.J., and Zunger, A., J. Comp. Phys. **160**, 29 (2000); Williamson, A.J. and Zunger, A., Phys. Rev. B **59**, 15819 (1999); *ibid.* **58**, 6724 (1998) and references therein.
- [29] Ceperley, D.M. and Adler, B., Science **231**, 555 (1986); Ceperley, D.M., Rev. Mod. Phys. **67**, 279 (1995).
- [30] Chakraborty, T., Comments Condens. Matter Phys., **16**, 35 (1992).
- [31] Ciorga, M., Sachrajda, A.S., Hawrylak, P., Gould, C., Zawadzki, P., Feng, Y., and Wasilewski, Z., Physica E **11**, 35 (2001); Sachrajda, A.S., Hawrylak, P., Ciorga, M., Gould, C., and Zawadzki, P., *ibid.* **10**, 493 (2001).

- [32] Ciorga, M., Sachrajda, A.S., Hawrylak, P., Gould, C., Zawadzki, P., Jullian, S., Feng, Y., and Wasilewski, Z., Phys. Rev. B **61**, R16315 (2000).
- [33] Ciorga, M., Wensauer, A., Pioro-Ladrière, M., Korkusiński, M., Kyriakidis, J., Sachrajda, A.S., and Hawrylak, P., Phys. Rev. Lett. **88**, 256804 (2002).
- [34] Cheng, S.-J., Sheng, W., and Hawrylak, P., Phys. Rev. B **68**, 235330 (2003); Raymond, S., Studenikin, S., Sachrajda, A., Wasilewski, Z., Cheng, S.-J., Sheng, W., Hawrylak, P., Babinski, A., Potemski, M., Ortner, G., and Bayer, M., Phys. Rev. Lett. **92**, 187402 (2004).
- [35] Cohen-Tannoudji, C., Diu, B., and Laloë, B., *Quantum mechanics* (Wiley, New York, 1977).
- [36] Creffield, C.E., Häusler, W., Jefferson, J.H., and Sarkar, S., Phys. Rev. B **59**, 10719 (1999); Reimann, S.M., Koskinen, M., and Manninen, M., *ibid.* **62**, 8108 (2000).
- [37] Darwin, C.G., Proc. Cambridge Phil. Soc. **27**, 86 (1931).
- [38] Demel, T., Heitmann, D., Grambow, P., Ploog, K., Phys. Rev. Lett. **64**, 788 (1990).
- [39] DiVincenzo, D.P., Bacon, D., Kempe, J., Burkard, G., and Whaley, K.B., Nature **408**, 339 (2000).
- [40] Egger, R., Häusler, W., Mak, C.H., and Grabert, H., Phys. Rev. Lett. **82**, 3320 (1999); Filinov, A.V., Bonitz, M., and Lozovik, Y.E., *ibid.* **86**, 3851 (2001).
- [41] Fafard, S., Leonard, D., Merz, J.L., and Petroff, P.M., Appl. Phys. Lett. **65**, 1388 (1994).
- [42] Arakawa, Y., and Sasaki, H., Appl. Phys. Lett. **40**, 939 (1982); Fafard, S., Hinzer, K., Raymond, S., Dion, M., McCaffrey, J., Feng, Y., and Charbonneau, S., Science **22**, 1350 (1996); Maximov, M.V., Shernyakov, Yu.M., Tsatsul'nikov, A.F., Lunev, A.V.,

- Sakharov, A.V., Ustinov, V.M., Egorov, A. Yu., Zhukov, A.E., Kovsh, A.R., Kop'ev, P.S., Asryan, L.V., Alferov, Zh.I., Ledentsov, N.N., Bimberg, D., Kosogov, A.O., and Werner, P., *J. Appl. Phys.* **83**, 5561 (1998); Ledentsov, N.N., Ustinov, V.M., Shchukin, V.A., Kop'ev, P.S., Alferov, Zh.I., and Bimberg, D., *Semiconductors* **32**, 343 (1998); Fafard, S., Wasilewski, Z.R., Allen, C. Ni., Hinzer, K., McCaffrey, J.P., and Feng, Y., *Appl. Phys. Lett.* **75**, 986 (1999);
- [43] Feynman, R.P., *Foundations of Physics* **16**, 507 (1986); Steane, A., *Rep. Prog. Phys.* **61**, 117 (1998); Bennet, C.H. and DiVincenzo, D.P., *Nature* **404**, 247 (2000); Awschalom, D.D. and Kikkawa, J.M., *Physics Today* **6**, 33 (1999).
- [44] Fock, V., *Z. Phys.* **47**, 446 (1928).
- [45] Fukui, T., Ando, S., Tokura, Y., and Toriyama, T., *Appl. Phys. Lett.* **58**, 2018 (1991).
- [46] Gérard, J.-M. and Gayral, B., *J. Lightwave Technol.* **17**, 2089 (1999).
- [47] Goldhaber-Gordon, D., Shtrikman, H., Mahalu, D., Abusch-Magder, D., Meirav, U., and Kastner, M.A., *Nature* **391**, 156 (1998); Choi, M.-S., Sanchez, D., and Lopez, R., *Phys. Rev. Lett.* **92**, 056601 (2004).
- [48] Goldmann, E., and Renn, S.R., *Phys. Rev. B* **60**, 16611 (1999).
- [49] Güclü, A.D., Wang, J.-S., and Guo, H., *Phys. Rev. B* **68**, 035304 (2003).
- [50] Hawrylak, P., *Phys. Rev. B* **60**, 5597 (1999).
- [51] Hawrylak, P., *Phys. Rev. Lett.* **71**, 3347 (1993).
- [52] Hawrylak, P., *Solid State Commun.* **88**, 475 (1993).
- [53] Hawrylak, P., Fafard, S., and Wasilewski, Z.R., *Condens. Matter News* **7**, 16 (1999).

- [54] Hawrylak, P., Gould, C., Sachrajda, A.S., Feng, Y., and Wasilewski, Z., Phys. Rev. B **59**, 2801 (1999) and references therein.
- [55] Hawrylak, P., and Korkusiński, M., Nonlinear Optics **29**, 329 (2002).
- [56] Hawrylak, P., and Korkusiński, M., in: *Single Quantum Dots: Fundamentals, Applications, and New Concepts*, Peter Michler (Ed.) (Springer, Berlin, 2003).
- [57] Hawrylak, P., Narvaez, G.A., Bayer, M., and Forchel, A., Phys. Rev. Lett. **85**, 389 (2000); Narvaez, G.A. and Hawrylak, P., Phys. Rev. B **61**, 13753 (2000); Wójs, A. and Hawrylak, P., Phys. Rev. B **55**, 13066 (1997); *ibid.* **53**, 10841 (1996).
- [58] Hawrylak, P., Potemski, M., Lockwood, D.J., Labbe, H.J., Kamada, H., Weman, H., Temmyo, J., and Tamamura, T., Physica E **2**, 652 (1998).
- [59] Hirose, K., and Wingreen, N.S., Phys. Rev. B **59**, 4604 (1999).
- [60] Hohenberg, P. and Kohn, W., Phys. Rev. **136**, B864 (1964).
- [61] Imamura, H., Aoki, H., and Maksym, P.A., Phys. Rev. B **57**, R4257 (1998).
- [62] Jacak, L., Hawrylak, P., and Wojs, A., *Quantum Dots* (Springer, Berlin, 1998).
- [63] The webpage of Marc A. Kastner's group at MIT is
<http://rleweb.mit.edu/rlestaff/p-kast.htm>.
- [64] Kastner, M.A., Nature **389**, 667 (1997).
- [65] Kastner, M.A., Phys. Today **46**, 23 (1993).
- [66] The webpage of Klaus von Klitzing's group at MPI Stuttgart is
<http://www.mpi-stuttgart.mpg.de/klitzing/>.
- [67] Kohn, W. and Sham, L.J., Phys. Rev. **140**, A1133 (1965).

- [68] The webpage of Leo Kouwenhoven's group at Delft is
<http://vortex.tn.tudelft.nl/grkouwen/kouwen.html>.
- [69] Kouwenhoven, L.P., Marcus, C.M., McEuen, P.L., Tarucha, S., Westervelt, R.M., and Wingreen, N.S., "Electron transport in quantum dots", in: *Mesoscopic electron transport, NATO ASI Conference Proceedings*, L.L. Sohn, L.P. Kouwenhoven, and G. Schön, Eds. (Kluwer, Dordrecht, 1997).
- [70] Kyriakidis, J., Pioro-Ladrière, M., Ciorga, M., Sachrajda, A.S., and Hawrylak, P., *Phys. Rev. B* **66**, 035320 (2002).
- [71] The LAPACK software library together with full documentation is available at
<http://www.lapack.org>.
- [72] Laughlin, R.B., *Phys. Rev. B* **27**, 3383 (1983); *Phys. Rev. Lett.* **50**, 1395 (1983).
- [73] Lebens, J.A., Tsai, C.S., Vahala, K.J., and Kuech, T.F., *Appl. Phys. Lett.* **56**, 2642 (1990).
- [74] Levine, B.F., *J. Appl. Phys.* **74**, R1 (1993).
- [75] Lin, J.C. and Guo, G.Y., *Phys. Rev. B* **65**, 035304 (2002).
- [76] Liu, H.C., Aslan, B., Korkusinski, M., Cheng, S.-J., and Hawrylak, P., *Infrared Physics and Technology* **44**, 503 (2003).
- [77] Liu, H.C., Capasso, F., eds., *Intersubband Transitions in Quantum Wells: Physics and Device Applications I* (Academic, San Diego, 2000).
- [78] Lorke, A., Luyken, R.J., Govorov, A.O., and Kotthaus, J.P., *Phys. Rev. Lett.* **84**, 2223 (2000); Warburton, R.J., Schäfflein, C., Haft, D., Bickel, F., Lorke, A., Karrai, K., Garcia, J.M., Schoenfeld, W., and Petroff, P.M., *Nature* **405**, 926 (2000).
- [79] Loss, D., and DiVincenzo, D., *Phys. Rev. A* **57**, 120 (1998).

- [80] MacDonald, A.H., Yang, S.R.E., and Johnson, M.D., Aust. J. Phys. **46**, 345 (1993).
- [81] The webpage of Charles Marcus's group at Harvard University is
<http://marcuslab.harvard.edu/>.
- [82] Marzin, J.-Y., Gérard, J.-M., Izraël, A., Barrier, D., Bastard, G., Phys. Rev. Lett. **73**, 716 (1994).
- [83] Maksym, P.A. and Chakraborty, T., Phys. Rev. Lett. **65**, 108 (1990); Eto, M., J. Phys. Soc. Jpn. **66**, 2244 (1997); Yang, S.R.E., MacDonald, A.H., and Johnson, M.D., Phys. Rev. Lett. **71**, 3194 (1993); Palacios, J.J., Martin-Moreno, L., Chiappe, G., Louis, E., and Tejedor, C., Phys. Rev. B **50**, 5760 (1994); Oaknin, J.H., Martin-Moreno, L., Palacios, J.J., and Tejedor, C., Phys. Rev. Lett. **74**, 5120 (1995); Wójs, A. and Hawrylak, P., Phys. Rev. B **56**, 13227 (1997) and references therein.
- [84] Metropolis, N., Rosenbluth, A.W., Rosenbluth, M.N., Teller, A.H., and Tellet, E., J. Chem. Phys. **21**, 1087 (1953).
- [85] Michler, P. (Ed.), *Single Quantum Dots: Fundamentals, Applications, and New Concepts* (Springer, Berlin, 2003).
- [86] Michler, P., Kiraz, A., Becher, C., Schoenfeld, W.V., Petroff, P.M., Zhang, L., Hu, E., and Imamoglu, A., Science **290**, 2282 (2000).
- [87] Mikhailov, S.A., Phys. Rev. B **65**, 115312 (2002); Phys. Rev. B **66**, 153313 (2002).
- [88] Moreau, E., Robert, I., Manin, L., Thierry-Mieg, V., Gérard, J.M., and Abram, I., Phys. Rev. Lett. **87**, 183601 (2001).
- [89] Murthy, G., and Shankar, R., Rev. Mod. Phys. **75**, 1101 (2003).
- [90] Müller, H.-M. and Koonin, S.E., Phys. Rev. B **54**, 14532 (1996).
- [91] Oaknin, J.H., Martin-Moreno, L., and Tejedor, C., Phys. Rev. B **54**, 16850 (1996).

- [92] Oosterkamp, T.H., Janssen, J.W., Kouwenhoven, L.P., Austing, D.G., Honda, T., and Tarucha, S., Phys. Rev. Lett. **82**, 2931 (1999);
- [93] Ortiz, G., Ceperley, D.M., and Martin, R.M., Phys. Rev. Lett. **71**, 2777 (1993); Melik-Alaverdian, M., Bonesteel, N.E., and Ortiz, G., *ibid.* **79**, 5286 (1997).
- [94] Pathria, R.K., *Statistical mechanics* (Butterworth-Heinemann, Oxford, 1996).
- [95] M.C. Payne, M.P. Teter, D.C. Allan, T.A. Arias, and J. D. Joannopoulos, Rev. Mod. Phys. **64**, 1045 (1992).
- [96] Pioro-Ladrière, M., Ciorga, M., Lapointe, J., Zawadzki, P., Korkusiński, M., Hawrylak, P., and Sachrajda, A.S., Phys. Rev. Lett. **91**, 026803 (2003).
- [97] Petroff, P.M., in: *Single Quantum Dots: Fundamentals, Applications, and New Concepts*, Peter Michler (Ed.) (Springer, Berlin, 2003); Lundstrom, T., Schoenfeld, W. Lee, H., and Petroff, P.M., Science **286**, 2312 (1999).
- [98] Petroff, P.M., and DenBaars, S.P., Superlatt. Microstruct. **15**, 15 (1994).
- [99] Pryor, C., Pistol, M.-E., and Samuelson, L., Phys. Rev. B **56**, 10404 (1997); Pryor, C., *ibid.* **57**, 7190 (1998); Pryor, C., Phys. Rev. Lett. **80**, 3579 (1998); Tadić, M., Peeters, F.M., Janssens, K.L., Korkusiński, M., and Hawrylak, P., J. Appl. Phys. **92**, 5819 (2002); Schliwa, A., Stier, O., Heitz, R., Grundmann, M., Bimberg, D., Phys. Stat. Sol. (b) **224**, 2232 (2001) and references therein.
- [100] Rajagopal, A.K. and Callaway, J., Phys. Rev. B **7**, 1912 (1973).
- [101] Raymond, S., Fafard, S., Poole, P.J., Wójs, A., Hawrylak, P., Charbonneau, S., Leonard, D., Leon, R., Petroff, P.M., and Merz, J.L., Phys. Rev. B **54**, 11548 (1996).
- [102] Räsänen, E., Saarikoski, H., Puska, M.J., and Nieminen, R.M., Phys. Rev. B **67**, 035326 (2003); Akbar, S. and Lee, I.-L., *ibid.* **63**, 165301 (2001); Austing, D.G.,

- Sasaki, S., Tarucha, S., Reimann, S.M., Koskinen, M., and Manninen, M., *ibid.* **60**, 11514.
- [103] Reed, M.A., Bate, R.T., Bradshaw, K., Duncan, W.M., Frensley, W.M., Lee, J.W., Smith, H.D., J. Vacuum Sci. Technol. B **4**, 358 (1986).
- [104] Reimann, S.M. and Manninen, M., Rev. Mod. Phys. **74**, 1283 (2002).
- [105] Riel, B.J., Hinzer, K., Moisa, S., Fraser, J., Finnie, P., Piercy, P., Fafard, S., and Wasilewski, Z.R., J. Cryst. Growth **236**, 145 (2002).
- [106] Rontani, M., Amaha, S., Muraki, K., Manghi, F., Molinari, E., Tarucha, S., and Austing, D.G., Phys. Rev. B **69**, 085327 (2004).
- [107] Sachrajda, A., Hawrylak, P., and Ciorga, M., “Nano-spintronics with lateral quantum dots”, in: *Transport in Quantum Dots*, J.Bird, Editor (Kluwer, 2003).
- [108] Santori, C., Pelton, M., Solomon, G., Dale, Y., and Yamamoto, Y., Phys. Rev. Lett. **86**, 1502 (2001).
- [109] J.R. Schewchuk, *An Introduction to the Conjugate Gradient Method Without the Agonizing Pain*, <http://www-2.cs.cmu.edu/jrs/jrspapers.html> (1994)
- [110] Schiff, L.I., *Quantum Mechanics* (McGraw-Hill, New York, 1955).
- [111] Serra, Ll., Barranco, M., Emperador, A., Pi, M., and Lipparini, E., Phys. Rev. B **59**, 15290 (1999); Ferconi, M., and Vignale, G., *ibid.* **56**, 12108 (1997); Stoof, T.H. and Bauer, G.E.W., Phys. Rev. B **52**, 12143 (1995).
- [112] Sheng, W. and Leburton, J.-P., Phys. Rev. B **67**, 125308 (2003); Phys. Rev. Lett. **88**, 167401 (2002).
- [113] Shoup, V., *NTL - a Library for doing Number Theory*, <http://www.shoup.net/>.

- [114] Shtrichman, I., Metzner, C., Gerardot, B.D., Schoenfeld, W.V., and Petroff, P.M., Phys. Rev. B **65**, 081303 (2002).
- [115] Sikorski, C., Merkt, U., Phys. Rev. Lett. **62**, 2164 (1989).
- [116] Steffens, O., *Künstliche Atome im Magnetfeld. Strom-Spin-Dichtenfunktional-Rechnungen für Halbleiterquantenpunkte* (Ph.D. Dissertation, Universität Regensburg, 1999).
- [117] Stopa, M., van der Wiel, W.G., Franceschi, S.D., Tarucha, S., and Kouwenhoven, L.P., Phys. Rev. Lett. **91**, 046601 (2003).
- [118] Stranski, I.N., von Krastanow, L., Sitzungsber K. Preuss. Akad. Wiss., Phys. Math. K1, **146**, 797 (1937).
- [119] Szafran, B., Peeters, F.M., Bednarek, S., and Adamowski, J., Phys. Rev. B **69**, 125344 (2004).
- [120] Tanatar, B. and Ceperley, D.M., Phys. Rev. B **39**, 5005 (1989).
- [121] Tarucha, S., Austing, D.G., Honda, T., van der Hage, R.J., and Kouwenhoven, L.P., Phys. Rev. Lett. **77**, 3613 (1996).
- [122] Tarucha, S., Austing, D.G., Tokura, Y., van der Wiel, W.G., and Kouwenhoven, L.P., Phys. Rev. Lett. **84**, 2485 (2000).
- [123] Tokura, Y., Kouwenhoven, L.P., Austing, D.G., and Tarucha, S., Physica B **83**, 246 (1998).
- [124] Tsui, D.C., Störmer, H.L., and Gossard, A.C., Phys. Rev. Lett. **48**, 1559 (1982).
- [125] Vignale, G. and Rasolt, M., Phys. Rev. Lett. **59**, 2360 (1987); Phys. Rev. B **37**, 10685 (1988).

- [126] Wasilewski, Z.R., Fafard, S., and McCaffrey, J.P., J. Cryst. Growth **201**, 1131 (1999).
- [127] Wensauer, A., *Quantenpunkte im Magnetfeld* (Ph.D. Dissertation, Universität Regensburg, 2003).
- [128] Wensauer, A., Steffens, O., Suhrke, M., and Rössler, U., Phys. Rev. B **62**, 2605 (2000); Wensauer, A., Kainz, J., Suhrke, M., and Rössler, U., phys. stat. sol. (b) **224**, 675 (2001); Steffens, O. and Suhrke, M., Phys. Rev. Lett. **82**, 3891 (1999).
- [129] The webpage of Robert Westervelt's group at Harvard University is <http://meso.deas.harvard.edu/>.
- [130] Williams, R.L., Aers, G.C., Poole, P.J., Lefebvre, J., Chithrani, D., and Lamontagne, B., J. Cryst. Growth **223**, 321 (2001); Williams, R.L., Aers, G.C., Lefebvre, J., Poole, P.J., and Chithrani, D., Physica E **13**, 1200 (2002).
- [131] Wingreen, N.S. and Stafford C.A., IEEE J. Quant. Electron. **33**, 1170 (1997).
- [132] van Zyl, B.P., Zaremba, E., and Hutchinson, D.A.W., Phys. Rev. B **61**, 2107 (2000).
- [133] Yannouleas, C., and Landmann, U., Phys. Rev. B **69**, 113306 (2004); Reusch, B., Häusler, W., and Grabert, H., Phys. Rev. B **63**, 113313 (2001); Phys. Rev. B **68**, 045309 (2003).
- [134] Yannouleas, C., and Landmann, U., Phys. Rev. Lett. **82**, 5325 (1999).

Appendix A

Curriculum Vitae

Marek Korkusiński

Institute for Microstructural Sciences, National Research Council of Canada

1200 Montreal Road, Ottawa, Canada K1A 0R6

tel. ++1 (613) 991 5341; elm. marek.korkusinski@nrc.ca

and

Physics Department

150 Louis Pasteur

University of Ottawa, Ottawa, Canada

Main areas of interest:

Theoretical condensed matter physics, Optical and electronic properties of semiconductor nanostructures, Correlations in electronic and electron-hole systems, Quantum computing.

Education

M. Sc. (with Honors) – Technical University of Wrocław, Poland, 1998;

Ph.D – University of Ottawa, Canada (2000 – present); supervisor: Dr. P. Hawrylak.

Professional Experience

2000–2004 — teaching assistant at the University of Ottawa (Teaching Assistant of the Year Award in 2001),

2003 — short visit to the Autonomous University of Madrid, Spain, working with Prof. Carlos Tejedor on a single quantum dot in a photonic cavity,

2001 — short visit to the Department of Natural Sciences, Antwerp University (Belgium), working with Prof. F. Peeters on strain in self-assembled quantum dots,

1999 – short visit to the Institute of Physics, Chair of Technical Physics, University of Würzburg, working with Dr. P. Hawrylak on Lanczos recursive methods in numerical simulations of the electronic structure of solids,

1998 – three-month visit to the Institute of Semiconductor Technology, Technical University of Braunschweig, working with Prof. A. Schlachetzki on optical spectra and gain of quantum cascade and quantum wire lasers.

Computer Skills

Programming Languages: Extensive experience in FORTRAN and C/C++, beginning 80x86 Assembler;

Operating Systems: Windows 95/98/XP: advanced user/administrator; SuSE and Red Hat Linux: advanced user, beginning administrator.

Extensive experience in numerical calculations of material properties, in particular quantum dots: multimillion-atom strain, piezoelectric and tight-binding electronic structure calculations, configuration-interaction methods for interacting confined carriers.

Conference presentations

1. Contributed talk “Electron and hole states in vertically coupled self-assembled In-GaAs quantum dots” given at the 2004 March Meeting of the American Physical Society (Montreal, 2004);

2. Seminar “Exchange and correlations in lateral quantum dots” given at the Dalhousie University (Halifax, August 2003);
3. Seminar “Nano-spintronics: Single and coupled spin transistor” given at the workshop of the National Research Council of Canada (St-Sauveur, 2002) ;
4. Oral presentations at the Congress of the Canadian Association of Physicists: “Coupling and entangling of electron and hole states in a quantum dot molecule” (Victoria, 2001), “Exchange and correlations in a few-electron quantum dot” (Quebec City, 2002), and “Optical detection of Aharonov-Bohm oscillations of a single electron on a quantum ring” (Charlottetown, 2003);
5. Cross Border Workshop “Controlling Matter with Light and Light with Matter” – poster presentation “Quantum dot in a photonic cavity” (May 2001);
6. 10th International Conference on Modulated Semiconductor Structures, contributed talk “Entangled states of electron-hole complex in a single InAs/GaAs coupled quantum dot molecule” (Linz, Austria, 2001).

Personal

Born February 4, 1975, Wrocław, Poland, single, no children. Citizenship: Polish.

References

1. Dr. Pawel Hawrylak
Principal Research Officer, Group Leader
Quantum Theory Group, Institute for Microstructural Sciences
National Research Council of Canada
Ottawa, Ontario, Canada, K1A 0R6
elm: pawel.hawrylak@nrc.ca

2. Dr. Jordan Kyriakidis

Assistant Professor, Condensed Matter Theory

Dept. of Physics and Atmospheric Science

Dalhousie University Halifax, Nova Scotia, Canada, B3H 3J5

elm: jordan.kyriakidis@dal.ca

3. Dr. Robin Williams

Senior Research Officer

Quantum Physics Group, Institute for Microstructural Sciences

National Research Council of Canada

Ottawa, Ontario, Canada, K1A 0R6

elm: robin.williams@nrc.ca

4. Dr. Andrew S. Sachrajda

Principal Research Officer, Group Leader

Quantum Physics Group, Institute for Microstructural Sciences

National Research Council of Canada

Ottawa, Ontario, Canada, K1A 0R6

elm: andy.sachrajda@nrc-cnrc.gc.ca

List of Publications**Main Papers**

1. M. Korkusiński, P. Hawrylak, M. Ciorga, M. Pioro-Ladrière, and A. S. Sachrajda, “Pairing of spin excitations: correlated electron states in lateral quantum dots”, submitted to Phys. Rev. Lett.
2. A. Wensauer, M. Korkusiński, and P. Hawrylak, “Configuration interaction method for Fock-Darwin states”, Solid State Comm. **130**, 115 (2004).
3. M. Ciorga, M. Korkusiński, M. Pioro-Ladriere, P. Zawadzki, P. Hawrylak, and A.S.

- Sachrajda, “Simple spin textures in a quantum dot”, *phys. stat. sol. (b)* **238**, 325 (2003).
4. M. Korkusiński, W. Sheng, and P. Hawrylak, “Designing quantum systems in self-assembled quantum dots”, *phys. stat. sol. (b)* **238**, 246 (2003).
 5. M. Pioro-Ladrière, M. Ciorga, J. Lapointe, P. Zawadzki, M. Korkusiński, P. Hawrylak, and A. S. Sachrajda, “Spin-Blockade Spectroscopy of a Two-Level Artificial Molecule”, *Phys. Rev. Lett.* **91**, 026803 (2003).
 6. M. Bayer, M. Korkusiński, P. Hawrylak, T. Gutbrod, M. Michel, and A. Forchel, “Optical Detection of the Aharonov-Bohm Effect on a Charged Particle in a Nanoscale Quantum Ring”, *Phys. Rev. Lett.* **90**, 186801 (2003).
 7. A. Wensauer, M. Korkusiński, and P. Hawrylak, “Theory of the spin-singlet filling factor $\nu = 2$ quantum Hall droplet”, *Phys. Rev. B* **67**, 035325 (2003).
 8. M. Korkusiński, P. Hawrylak, and M. Bayer, “Negatively Charged Exciton on a Quantum Ring”, *phys. stat. sol. (b)* **234**, 273 (2002).
 9. M. Ciorga, A. Wensauer, M. Pioro-Ladriere, M. Korkusiński, J. Kyriakidis, A.S. Sachrajda, and P. Hawrylak, “Collapse of the Spin-Singlet Phase in Quantum Dots”, *Phys. Rev. Letters* **88**, 256804 (2002).
 10. M. Korkusiński, P. Hawrylak, M. Bayer, G. Ortner, A. Forchel, S. Fafard, Z. Wasilewski, “Entangled states of electron-hole complex in a single InAs/GaAs coupled quantum dot molecule”, *Physica E* **13**, 610 (2002).
 11. M. Korkusiński and P. Hawrylak, “Electronic structure of vertically stacked self-assembled quantum disks”, *Phys. Rev. B* **63**, 195311 (2001).

Secondary Papers

1. A. Olaya-Castro, M. Korkusiński, P. Hawrylak, and M. Yu. Ivanov, “Effective Bloch equations for strongly driven modulation-doped quantum wells”, *Phys. Rev. B* **68**, 155305 (2003).
2. H.C. Liu, B. Aslan, M. Korkusiński, S.-J. Cheng, and P. Hawrylak, “Detailed characterization of a systematic set of quantum dot infrared photodetectors”, *Infrared Physics and Technology* **44**, 503 (2003).
3. B. Aslan, H.C. Liu, M. Korkusinski, S.-J. Cheng, and P. Hawrylak, “Response spectra from mid- to far-infrared, polarization behaviors, and effects of electron numbers in quantum-dot photodetectors”, *Appl. Phys. Lett.* **82**, 630 (2003).
4. P. Hawrylak and M. Korkusiński, “Excitonic artificial atoms in a semiconductor quantum dot for single photon sources”, *Nonlinear Optics* **29**, 329 (2002).
5. M. Tadić, F.M. Peeters, K.L. Janssens, M. Korkusiński, and P. Hawrylak, “Strain and band edges in single and coupled cylindrical InAs/GaAs and InP/InGaP self-assembled quantum dots”, *J. Appl. Phys.* **92**, 5819 (2002).
6. P. Hawrylak, M. Korkusiński, S. Fafard, R. Dudek, H.C. Liu, “Photo-current spectroscopy of modulation-doped InAs self-assembled quantum dots”, *Physica E* **13**, 246 (2002).
7. M. Bayer, G. Ortner, A. Larionov, V. Timofeev, A. Forchel, P. Hawrylak, K. Hinzer, M. Korkusiński, S. Fafard, and Z. Wasilewski, “Entangled exciton states in quantum dot molecules”, *Physica E* **12**, 900 (2002).
8. K. Hinzer, M. Bayer, J.P. McCaffrey, P. Hawrylak, M. Korkusiński, O. Stern, Z.R. Wasilewski, S. Fafard, and A. Forchel, “Optical Spectroscopy of Electronic States in a Single Pair of Vertically Coupled Self-Assembled Quantum Dots”, *phys. stat. sol.* **224**, 385 (2001).

9. K. Hinzer, P. Hawrylak, M. Korkusiński, S. Fafard, M. Bayer, O. Stern, A. Gorbunov, and A. Forchel, “Optical spectroscopy of a single AlInAs/AlGaAs quantum dot”, *Phys. Rev. B* **63**, 075314 (2001).
10. M. Bayer, P. Hawrylak, K. Hinzer, S. Fafard, M. Korkusiński, Z.R. Wasilewski, O. Stern, A. Forchel, “Coupling and Entangling of Quantum States in Quantum Dot Molecules”, *Science* **291**, 451 (2001).
11. L. Jacak, J. Krasnyj, M. Korkusiński, “Quantum Dots”, *Proceedings of International Conference on Symmetry and Structural Properties of Condensed Matter (SSPCM)*, Zajaczkowo, Poland, T. Lulek, et al. eds, World Scientific, 1999.
12. L. Jacak, J. Krasnyj, M. Korkusiński, and A. Wójs “Theory of radiative recombination from the metastable excited states of quantum dots”, *Phys. Rev. B* **57**, 9069 (1998).

Book Chapters

1. P. Hawrylak and M. Korkusiński, “Electronic Properties of Self-Assembled Quantum Dots”, in: P. Michler (Ed.), “Single Quantum Dots, Fundamentals, Applications and New Concepts” (Springer, Berlin, 2003).